

An Evidence for Spectral Distortion of Reactor Anti-Neutrinos
and
A Study of Three Flavor Neutrino Oscillation

Ph.D. thesis

Itaru Shimizu

Department of Physics, Tohoku University

Sendai 980-8578, Japan

November 2004

Abstract

Results of the KamLAND (Kamioka Liquid Scintillator Anti-Neutrino Detector) experiment are presented based on data collected from March 9, 2002 to January 11, 2004. In the absence of anti-neutrino disappearance, we expect 365.2 ± 23.7 (syst) events above 2.6 MeV for the 766.3 ton-year (515.1 days) data set, however, the observed number of events is only 258. The average $\bar{\nu}_e$ survival probability ($\frac{N_{\text{obs}} - N_{\text{BG}}}{N_{\text{expected}}}$) is $0.658 \pm 0.044(\text{stat}) \pm 0.047(\text{syst})$, confirming $\bar{\nu}_e$ disappearance at 99.998% C.L. The neutrino oscillation gives rise to not only the disappearance of $\bar{\nu}_e$ but also to energy spectrum distortion. The scaled no oscillation $\bar{\nu}_e$ spectrum is excluded by a χ^2 test at 99.78% C.L independently of the $\bar{\nu}_e$ rate. This is the first evidence for spectral distortion in the $\bar{\nu}_e$ spectrum. Moreover, two alternative hypotheses for neutrino disappearance, neutrino decay and decoherence, are strongly disfavored. A global oscillation analysis based on the solar neutrino, KamLAND, CHOOZ, atmospheric and K2K experiments is performed in three flavor neutrino oscillation scheme. The Δm_{21}^2 , θ_{12} , and θ_{13} is limited to $7.3 \sim 8.7 \times 10^{-5}$ eV², $29^\circ \sim 36^\circ$ and $< 11^\circ$ at 95% C.L., respectively.

Acknowledgments

First of all, I would like to express my great appreciation to Prof. Atsuto Suzuki, the spokesperson of the KamLAND experiment. He introduced me to experimental physics and encouraged me to study. I always got many significant words from him. His excellent guidance were very valuable to me.

I would like to be thankful to my advisor, Prof. Kunio Inoue. He provided me a lot of precious guidance, and always found the time to help me. Without his continuous encouragement and suggestions for my study, this thesis would never have been completed. The smooth sailing in this thesis owed to his support.

I also would like to deeply thank Asso. Prof. Junpei Shirai, Asso. Prof. Fumihiko Suekane and Asso. Prof. Masayuki Koga. I often had useful discussions with them about the experiment. Without their excellent works, this experiment would never have been a great success.

I would like to thank all of people in Research Center for Neutrino Science (RCNS) at Tohoku university. Especially, Prof. Toshio Kitagaki, Prof. Akira Yamaguchi, Prof. Hitoshi Yamamoto, Asso. Prof. Tomoki Hayashino, Dr. Tadashi Nagamine, Dr. Takuya Hasegawa, Dr. Yasuhiro Kishimoto, Dr. Tadao Mitsui, Dr. Koichiro Furuno, Dr. Kengo Nakamura, Dr. Masakazu Motoki, Dr. Jean-Stephane Ricol and Dr. Yoshihito Gando. I often had useful discussion with them about physics. I also would like to thank all members of the secretarial, technical and other staffs for their kindly support. I also would like to thank all the KamLAND collaboration for the successful construction and operation of the experiment. I gratefully acknowledge the cooperation of the Kamioka Mining and Smelting Company and financial support of the Japan Society of the Promotion of Science.

I would like to thank Sanshiro Enomoto, Hideki Watanabe, Haruo Ikeda, Yuichi Matsuda, Yoshinari Mikami, Kyo Nakajima, Yosuke Yusa, Manabu saigo, Yotaro Koseki, Kentaro Owada, Ryosuke Yamauchi and other postgraduate students. We had discussions about physics and unrelated to physics.

Special appreciation goes to Dr. Kenji Ishihara, Dr. Toshiyuki Iwamoto, Dr. Hiroshi Ogawa and Dr. Osamu Tajima, my seniors, currently in other universities or research institutes. They gave me many valuable advice about experimental physics. Special thanks to Dr. Patrick Decowski for his advice about English as well as physics.

Finally, I thank my parents, Motoichi and Michiko Shimizu, and brother, Takashi Shimizu for their unfailing support in my life.

Contents

1	Introduction	1
1.1	The Neutrino	3
1.2	Neutrino Oscillation	4
1.2.1	Vacuum Oscillation	4
1.2.2	Neutrino Oscillation in Matter (MSW Effect)	5
1.3	Neutrino Oscillation Experiment	7
1.3.1	Solar Neutrinos	7
1.3.2	Atmospheric Neutrinos	16
1.3.3	Accelerator Neutrinos	19
1.3.4	Reactor Neutrinos	21
1.4	Neutrino Mass Measurement	23
1.4.1	Cosmological Data	23
1.4.2	Semileptonic Decay	23
1.4.3	Supernova 1987A	24
1.4.4	Double Beta Decay	24
1.5	Motivation	27
2	Detector	29
2.1	KamLAND Detector	29
2.1.1	Design	29
2.1.2	Anti-Neutrino Detection	31
2.2	Purification System	33
2.3	Liquid Scintillator and Buffer Oil	34
2.4	PMT	35
2.5	Front-End Electronics	38
2.6	Trigger System	39
2.7	Calibration System	41
3	Event Reconstruction and Detector Calibration	43
3.1	Waveform Analysis	44
3.1.1	Algorithm of Waveform Analysis	45
3.1.2	Calibration of Time Bin Width	45
3.2	Timing Calibration	45

3.3	Gain Calibration	50
3.4	Bad Channel Selection	50
3.5	Vertex Reconstruction	53
3.5.1	Algorithm of Vertex Reconstruction	53
3.5.2	Reconstruction Performance	56
3.5.3	Fiducial Volume Uncertainty	56
3.6	Energy Reconstruction	61
3.6.1	Algorithm for Position Dependence Correction	61
3.6.2	Basic Corrections	62
3.6.3	Dark Hit Subtraction	63
3.6.4	Photon Yield Efficiencies	65
3.6.5	Uncertainty of Energy Scale	68
3.7	Muon Track Reconstruction	78
3.7.1	Selection Criteria	78
3.7.2	Algorithm for Muon Track Reconstruction	78
3.7.3	Tracking Performance	80
3.8	Reconstruction Quality	84
3.8.1	Noise Event Selection	84
3.8.2	Flasher Event Selection	84
3.8.3	Estimation of Reconstruction Quality	89
4	Background Estimation	105
4.1	Backgrounds for Single Events	107
4.2	Spallation Study	111
4.2.1	Spallation Neutron	111
4.2.2	Spallation Products	116
4.2.3	Radioactivity in Liquid Scintillator	122
4.3	Backgrounds for Electron Anti-Neutrino	130
4.3.1	Accidental Coincidence	130
4.3.2	$^8\text{He}/^9\text{Li}$	130
4.3.3	Fast Neutron	135
4.3.4	(α, n)	137
4.3.5	(γ, n)	143
4.3.6	Spontaneous Fission	143
4.3.7	Atmospheric Neutrino	145
4.3.8	Geo Neutrino	146
5	Reactor Anti-Neutrino Estimation	147
5.1	Reactor Anti-Neutrino Flux	148
5.2	Number of Targets	155
5.3	Cross-Section	155
5.4	Live Time Calculation	155
5.4.1	Deadtime	156
5.4.2	Vetotime	157

5.4.3	Livetime	158
5.5	Detection Efficiency and Systematic Uncertainties	159
5.5.1	Space Correlation	163
5.5.2	Time Correlation	163
5.5.3	Delayed Energy	163
5.6	Expected Reactor Anti-Neutrino Events	168
5.6.1	No Oscillation Case	168
5.6.2	Oscillation Case	170
5.7	Final Sample	170
5.7.1	Selection Criteria for Electron Anti-Neutrinos	170
5.7.2	Event Reduction	171
6	Significance of Neutrino Oscillation	182
6.1	Hypothesis Test	182
6.1.1	Significance of Neutrino Disappearance	182
6.1.2	Significance of Spectral Distortion	184
6.2	Null Oscillation Probability	186
6.3	Two Generation Neutrino Oscillation Analysis	188
6.4	Test for Non-Standard Models of Neutrino Disappearance	191
6.4.1	Neutrino Decay	191
6.4.2	Neutrino Decoherence	191
6.5	Discussion	193
7	Oscillation Analysis	194
7.1	Global Analysis	196
7.1.1	Solar Neutrino Experiments	196
7.1.2	KamLAND	199
7.1.3	CHOOZ	203
7.1.4	Supernova 1987A	206
7.1.5	Global three generation analysis	210
8	Summary	216
A	Trigger Types	218
B	Decay chain of ^{238}U and ^{232}Th	223
B.1	^{238}U	223
B.2	^{232}Th	224
C	Nuclear Level Diagrams	225
C.1	^{203}Hg	225
C.2	^{68}Ge	226
C.3	^{65}Zn	226
C.4	^{60}Co	227

D	Am-Be source	228
E	Analytical calculation of neutrino propagation	232
F	Supernova Neutrino Emission	238

List of Figures

1.1	Feynman diagrams of neutrino interaction in matter	6
1.2	pp-chain	9
1.3	CNO cycle	9
1.4	Solar neutrino spectrum from pp chain predicted by the SSM	10
1.5	Production points of neutrinos as a function of the solar radius	11
1.6	Predicted versus measured sound speeds	11
1.7	Comparisons of neutrino event rates between SSM prediction and experimental measurements	12
1.8	Flux of ^8B solar neutrinos from active neutrinos other than ν_e vs that from ν_e deduced from the three neutrino reactions in SNO	15
1.9	Zenith angle distribution of μ -like events e-like events and multi-ring events for sub-GeV and multi-GeV sample, upward stopping muons and upward through-going muons	17
1.10	Ratio of the data to the MC events without neutrino oscillation (dots) as a function of the reconstructed L/E	18
1.11	Allowed regions for two flavor $\nu_\mu \leftrightarrow \nu_x$ oscillations	18
1.12	Reconstructed neutrino energy distribution for 1 ring μ -like sample at the K2K experiment	19
1.13	Allowed regions of oscillation parameters at the K2K experiment	20
1.14	Ratio of measured to expected $\bar{\nu}_e$ flux from reactor experiments	22
1.15	Schematic view of the neutrino mass hierarchy for the case of the normal and inverted	26
1.16	Effective Majorana mass $\langle m_{\beta\beta} \rangle^2$ as a function of the lightest neutrino for the case of the normal hierarchy and inverted hierarchy	26
1.17	Sensitivity of the JHF-Kamioka experiment	27
1.18	Sensitivity for CP violation at the long baseline experiment JHF-Kamioka	28
2.1	The KamLAND detector and experimental site	30
2.2	Schematic diagram of the KamLAND detector	31
2.3	Total cross section of the inverse β -decay reaction $\bar{\nu}_e + p \rightarrow e^+ + n$	33
2.4	Schematic view of the purification system	34
2.5	Wavelength-dependence of the index of refraction of liquid scintillator, buffer oil and acrylic boards at 14°C	36
2.6	Schematic view of the 17-inch and 20-inch PMTs	37

2.7	Quantum efficiency of the KamLAND PMTs	37
2.8	Schematic diagram of the Front-End Electronics readout system	38
2.9	The prompt trigger efficiency within 5.5-m-radius fiducial volume	40
2.10	The delayed trigger efficiency within 5.5-m-radius fiducial volume	40
2.11	Layouts of various calibration sources	42
2.12	Layout of the dye-laser diffusion ball and the deployment system	42
3.1	Typical waveform of a two photon signal	46
3.2	Clock test pulse for the calibration of time bin width	46
3.3	Schematic view of the timing calibration system	47
3.4	Typical correlation between time and charge for a channel of 17 inch PMT in the timing calibration data	48
3.5	Correlation between the time and charge for a typical channel of 20 inch PMT in the timing calibration data	48
3.6	Time distribution of 17 inch PMT hits	49
3.7	Time distribution of 20 inch PMT hits	49
3.8	Single photo-electron distributions for the typical 17 inch PMT and 20 inch PMT	50
3.9	Time variation of the mean 1 p.e. charge	51
3.10	Time variation of the number of bad channels	52
3.11	Measured speed of light for calibration sources	54
3.12	Correlation between t and dt/dx , dt/dy , dt/dz , q (charge)	55
3.13	Deviations of reconstructed vertex along z-axis for various radioactivities	56
3.14	Miss reconstructed probability of the ^{60}Co events	57
3.15	Fiducial volume error for the 5.5-m radius	58
3.16	R^3 distribution of 2.2 MeV neutron capture γ 's and β -decay events from $^{12}\text{B}/^{12}\text{N}$ (>4 MeV) spallation products	59
3.17	R distribution for various radioactivities	60
3.18	Time variation of the balloon edge R using various radioactivities.	60
3.19	Algorithm of the energy reconstruction	62
3.20	Timing distribution of PMTs hits after the correction for time of flight	64
3.21	Time variation of the dark charge for 17 inch PMTs and temperature of the outer buffer oil	64
3.22	Correction of shadow effect from the balloon and its rope	67
3.23	Effective light attenuation length in the liquid scintillator and the buffer oil	67
3.24	Position dependence of visible energy for neutron capture gamma events	70
3.25	Deviation of reconstructed energy at various positions on z-axis for various sources	71
3.26	Correlation of the resolution σ/E at various positions on z-axis for various sources	72
3.27	^{40}K γ peak	73
3.28	Time variation of spallation neutrons which were captured on protons	73
3.29	Deviation of reconstructed energy at the center of the detector for various sources	74
3.30	Time variation of the resolution σ/E at the center of the detector for various sources	75
3.31	Variation of the energy resolution (17 inch PMTs + 20 inch PMTs) as a function of the combining factor α	76

3.32	Combined energy (17 inch PMTs + 20 inch PMTs) linearity as a function of the energy	76
3.33	Uncertainty in the parameters for the nonlinearity calibration	77
3.34	Non-linearity correction and uncertainty in the energy	77
3.35	Time difference from muon to muon and Charge distribution of muons	79
3.36	Cherenkov photons and scintillation photon	81
3.37	Correlations between the total charge in the inner detector and the muon track length	81
3.38	Normalized charge by reconstructed muon track length (dQ/dX)	82
3.39	Correlation between the total charge in the inner detector and the distance from the center to muon track (impact parameter)	83
3.40	Distribution of various classified events with the total charge sum	85
3.41	Noise event selection criteria	86
3.42	Ringing events selected by the $n_{hit} > 600$	87
3.43	Event display of a typical noise event and ringing event	87
3.44	Event display of a typical flasher event	88
3.45	Flasher event selection criteria	88
3.46	^{60}Co (2γ , 1.173 + 1.333 MeV) at the center position	91
3.47	^{60}Co (2γ , 1.173 + 1.333 MeV) at $z = -5.25$ m	92
3.48	^{65}Zn (1γ , 1.11552 MeV) at the center position	93
3.49	^{65}Zn (1γ , 1.11552 MeV) at $z = -5.75$ m	94
3.50	^{68}Ge (2γ , 0.511×2 MeV) at the center position	95
3.51	^{68}Ge (2γ , 0.511×2 MeV) at $z = -5.5$ m	96
3.52	^{203}Hg (1γ , 0.279197 MeV) at the center position	97
3.53	^{203}Hg (1γ , 0.279197 MeV) at $z = -5.5$ m	98
3.54	Explanation of criteria of the reconstruction quality check	99
3.55	Reconstruction quality of a typical neutrino coincidence event	100
3.56	Reconstruction quality of a typical Am-Be source coincidence event	101
3.57	Reconstruction quality of a typical noise coincidence event	102
3.58	Reconstruction quality of a typical ringing coincidence event	103
3.59	Reconstruction quality of a typical flasher coincidence event	104
4.1	Correlation of the energy spectrum with fiducial radius	108
4.2	Vertex distributions of various energy events in the whole volume	109
4.3	Single spectrum with the 5 m fiducial radius	110
4.4	NsumMax distribution of neutron capture events on protons or ^{12}C	113
4.5	Visible energy spectra after muons with the cuts $150 < \Delta T_{muon} < 1000 \mu\text{sec}$. . .	113
4.6	Time correlation from last muons to spallation neutron capture events with a simple cut $350 < \text{NsumMax} < 550$	114
4.7	Neutron production rate in the KamLAND liquid scintillator	115
4.8	Time correlation and energy spectrum of spallation products within 500 msec . .	117
4.9	Time correlation and energy spectrum of spallation products within 10 sec	118
4.10	$\Delta\chi^2$ profiles projected onto the production ratio of ^{12}N to $^{12}\text{B} + ^{12}\text{N}$	119
4.11	$\Delta\chi^2$ profile projected onto the production ratio of ^8B to $^8\text{Li} + ^8\text{B}$	119

4.12	Time correlation, energy spectrum and space correlation of spallation products within 300 sec	120
4.13	Time correlation, energy spectrum and space correlation of spallation products within 300 min	121
4.14	^{214}Bi - ^{214}Po coincidence events	124
4.15	^{212}Bi - ^{212}Po coincidence events	125
4.16	Time variation of the event rate of ^{214}Bi - ^{214}Po and ^{212}Bi - ^{212}Po coincidence . . .	126
4.17	Time variation of the event rate of ^{214}Bi - ^{214}Po in the center cylindrical region with radius 2 m	126
4.18	Visible energy spectrum of the low energy backgrounds	128
4.19	Delayed coincidence events of the ^{85}Kr β -decay	129
4.20	Accidental time and energy spectrum for 5.5 m fiducial volume	131
4.21	Time correlation between these delayed coincidence events and muons	132
4.22	Allowed region from extended likelihood analysis for the number of ^8He and ^9Li events vs the ratio of ^9Li	133
4.23	Track correlation of spallation neutron events for non-showering muons	133
4.24	Prompt energy spectrum of ^8He and ^9Li events within 500 msec following showering muons	134
4.25	Fast neutron events selected by the triple coincidence	136
4.26	Total cross sections of (α, n) reactions for various target nuclei	138
4.27	Neutron energy vs alpha energy in forward(0°), right(90°), backward(180°) scattering angles in the $^{13}\text{C}(\alpha, n)^{16}\text{O}$ reaction	140
4.28	Angular distribution of neutron expressed by a Legendre-polynomial	141
4.29	Cross section of $^{13}\text{C}(\alpha, n)^{16}\text{O}$, stopping power, neutron energy distribution, energy distribution	142
4.30	Atmospheric anti-neutrino fluxes with the BGS model	145
4.31	Expected geo-neutrino energy spectrum for 16 TW intensity	146
5.1	Contribution to the expected $\bar{\nu}_e$ events from distant reactors	147
5.2	The locations of Japanese nuclear reactors and KamLAND	150
5.3	Energy spectra of $\bar{\nu}_e$ flux from nuclear fissions, ^{235}U , ^{238}U , ^{239}Pu and ^{241}Pu . . .	153
5.4	Uncertainties of neutrino spectra from four isotopes	153
5.5	Fission rate of each isotopes, ^{235}U , ^{238}U , ^{239}Pu and ^{241}Pu	154
5.6	Time variation of $\bar{\nu}_e$ flux from reactors	154
5.7	$\bar{\nu}_e$ energy spectra from long-lived nuclei (^{106}Ru , ^{144}Ce)	154
5.8	Ratio of indistinct deadtime in percentage	157
5.9	Ratio of livetime/runtime for each run	158
5.10	Space correlation between prompt and delayed events generated by the MC and efficiency for the delayed vertex	164
5.11	Delayed coincidence calibration using the Am-Be source at the center of the detector	165
5.12	Efficiencies of the neutron capture event within 200 cm in the Am-Be source calibration	166
5.13	Time difference from muons to spallation neutron capture candidates	167
5.14	Expected spectrum in the no oscillation case	169

5.15	Visible energy spectrum for the single events and the delayed coincidence in the whole volume	173
5.16	Prompt energy and delayed energy distribution	174
5.17	Vertex distribution of the delayed coincidence events	175
5.18	Profiles of $\bar{\nu}_e$ candidates (Prompt Energy, Delayed Energy, Space Correlation, Time Difference)	176
5.19	Profiles of $\bar{\nu}_e$ candidates (Prompt Energy vs Delayed Energy, Time Difference vs Delayed Energy, Space Correlation vs Delayed Energy, Space Correlation vs Time Difference)	177
5.20	Badness of $\bar{\nu}_e$ candidates	178
5.21	Reconstruction quality of the worst event of all candidates	179
5.22	Correlation coefficients of $\bar{\nu}_e$ candidates	180
5.23	Expected time variation of the reactor $\bar{\nu}_e$ flux, and observed $\bar{\nu}_e$ rate versus expected rate	181
6.1	Excluded region for neutrino oscillation parameters, using the KamLAND rate analysis above 2.6 MeV analysis threshold	183
6.2	Distortion from the energy scale uncertainty in the case of no oscillation	185
6.3	Distortion from the (α, n) background uncertainty in the case of no oscillation	185
6.4	Scaled no oscillation spectrum compared with the observed data	187
6.5	Allowed region from shape only analysis for the data set above 2.6 MeV	189
6.6	Allowed region from rate + shape analysis for the data set above 2.6 MeV	190
6.7	No oscillation spectrum and the best fit	190
6.8	Allowed region in pure neutrino decay case	192
6.9	Allowed region in pure neutrino decoherence case	192
6.10	Ratio of the observed $\bar{\nu}_e$ spectrum to the expectation for no-oscillation versus L_0/E	193
7.1	Allowed region from solar data in two generation analysis	198
7.2	Allowed region from solar data in the $(\sin^2 \theta_{12}, \Delta m_{21}^2)$ plane for 3 n.d.f.	200
7.3	Allowed region from KamLAND data for 3 n.d.f.	201
7.4	Allowed region from KamLAND data and solar data for 2 n.d.f.	202
7.5	Ratio of the observed $\bar{\nu}_e$ spectrum to the expectation for no-oscillation versus L_0/E for various $\sin^2 \theta_{13}$	202
7.6	Excluded region of neutrino oscillation parameters from CHOOZ	205
7.7	Observed supernova events in Kamiokande II and IMB detector within the first 13 sec	207
7.8	Schematic view of level crossing for the supernova neutrino	207
7.9	Allowed regions in the $(T_{\bar{\nu}_e}, \sin^2 \theta_{13})$ plane for 2 n.d.f from the combined analysis of Kamiokande II and IMB with the supernova 1987A data	209
7.10	Allowed regions in the $(\sin^2 \theta_{13}, \Delta m_{31}^2)$ plane for 2 n.d.f from CHOOZ data alone and CHOOZ + solar + KamLAND data	211
7.11	$\Delta\chi^2$ profiles projected onto the $\sin^2 \theta_{13}$ axis for solar, KamLAND, solar + KamLAND, atmospheric + K2K + CHOOZ	212

7.12	Projections of the allowed regions onto the $(\sin^2 \theta_{12}, \Delta m_{21}^2)$ plane from KamLAND, solar, and KamLAND + solar for 2 n.d.f.	214
7.13	Projection of the allowed regions onto the $(\sin^2 \theta_{12}, \Delta m_{21}^2)$ plane from the global oscillation data	215
B.1	Decay chain of ^{238}U	223
B.2	Decay chain of ^{232}Th	224
C.1	Level diagram for ^{203}Hg	225
C.2	Level diagram for ^{68}Ge	226
C.3	Level diagram for ^{65}Zn	226
C.4	Level diagram for ^{60}Co	227
D.1	Geometry of Am-Be source moderator	228
D.2	Primary neutron spectrum of a ^{241}Am - ^9Be source	229
D.3	Prompt energy spectrum of Am-Be source (no moderator) in the visible energy scale	230
D.4	Level diagram for ^{12}C and $^9\text{Be} + \alpha - \text{n}$	231
E.1	Section of the earth showing the relevant shell	235
E.2	Electron density profile $N(r)$ from the parameterization	236
F.1	Energy spectra of ν_e , $\bar{\nu}_e$ and ν_x of the numerical supernova model	240
F.2	Schematic view of neutrino processes in each stage of the collapse-driven supernova explosion	241

List of Tables

1.1	Experimental limits on neutrino masses	3
1.2	The relation between the electron density and the mixing angle in matter	7
1.3	Neutrino-producing reactions in the sun	10
1.4	Results of the solar neutrino experiments	13
1.5	Result of the atmospheric neutrino experiments	17
1.6	Experimental limits on effective neutrino mass contributing to $0\nu\beta\beta$	25
2.1	Liquid scintillator parameters	35
3.1	Reconstructed visible energies for various gamma sources	68
4.1	Summary of Backgrounds for $\bar{\nu}_e$ (events / data-set)	107
4.2	Concentration of radioactivities in the balloon and suspending rope	108
4.3	Concentration of radioactivities in the liquid scintillator	110
4.4	Summary of the spallation products (not neutron emitter)	116
4.5	Summary of detection efficiency of ^{214}Bi - ^{214}Po coincidence	122
4.6	Summary of systematic uncertainty of ^{214}Bi - ^{214}Po selection	122
4.7	Summary of detection efficiency of ^{212}Bi - ^{212}Po coincidence	123
4.8	Summary of systematic uncertainty of ^{212}Bi - ^{212}Po selection	123
4.9	Summary of the low energy backgrounds below 1 MeV	128
4.10	Summary of the nuclei which emit neutron after β decays	132
4.11	Target nuclei of (α, n) reaction [82, 83]	137
4.12	Summary of (α, n) Backgrounds (events / data-set)	140
4.13	Target nuclei of (γ, n) reaction	143
4.14	Spontaneous fission nuclei and neutron emitters in the U/Th/Ac/Np series	144
5.1	Contributions from world reactors and long-lived nuclei at the HAT (2.6 MeV analysis threshold)	149
5.2	Japanese and Korean reactors - part 1 -	151
5.3	Japanese and Korean reactors - part 2 -	152
5.4	Summary of data-set	159
5.5	$\bar{\nu}_e$ detection efficiency (period I + II)	160
5.6	$\bar{\nu}_e$ detection efficiency (period III)	160
5.7	Systematic uncertainties of $\bar{\nu}_e$ detection (period I + II)	161
5.8	Systematic uncertainties of $\bar{\nu}_e$ detection (period III)	162

7.1	Summary of the Chooz data acquisition cycle	203
7.2	Observed positron yields	204
7.3	Summary of the limit on $\sin^2 \theta_{13}$	212
7.4	Summary table of the best fit and error (1 n.d.f.) of the oscillation parameters from all neutrino oscillation experiments	213
A.1	Trigger types as recorded by the trigger - part I -	221
A.2	Trigger types as recorded by the trigger - part II -	222
D.1	Moderator size of Am-Be source in each calibration.	229
D.2	Branchings of decays [108]	230
E.1	Coefficients of the electron density parameterization $N_j(r) = \alpha_j + \beta_j r^2 + \gamma_j r^4$ (mol/cm ³), for the j-th shell range $[r_{j-1}, r_j]$. The radial distance r is normalized to the earth radius.	234

Chapter 1

Introduction

The neutrino was introduced by W. Pauli [1] in 1930 to reconcile an anomaly of energy and spin conservation in nuclear β decay. This elementary particle has remarkable characteristics compared to other elementary particles, since it has no electric charge, spin 1/2 and very small mass. It was discovered in the 1950s by F. Reines and C. L. Cowan in their reactor neutrino experiments via the reaction $\bar{\nu}_e + p \rightarrow e^+ + n$ [2]. As the neutrino interacts with other particles only via the weak interaction, its cross section is very small. This neutrino property allows us to observe neutrinos from distant sources, such as the sun, the atmosphere entry and from distant reactor.

Solar neutrinos were detected by R. Davis and his colleagues [3] for the first time, by making use of the capture reaction on ^{37}Cl . They observed solar neutrinos for about 30 years, but the number of detected neutrino was only one third of the theoretical prediction. This is the so-called 'Solar Neutrino Problem'. Successive observations confirmed the significant deficit of solar neutrinos. The most plausible solution for this anomaly is the neutrino oscillation, which was suggested by Maki, Nakagawa and Sakata [4] in 1962. Similar to the quark sector, neutrino oscillation describes neutrino flavor changing while the neutrino propagates. Massless particles cannot change their state, thus neutrinos that undergo oscillation are massive. Recently, the SNO group observed neutrino flavor transformation from neutral current (NC) interactions and confirmed that the total flux of all neutrino types is conserved [5]. In terms of two neutrino oscillation, current solar neutrino data yield various solutions. These solutions are called 'Large Mixing Angle solution' (LMA), 'Low Δm^2 ' solution for the Large Mixing Angle (Low), 'Small Mixing Angle solution' (SMA) and 'Vacuum Oscillation solution' (VAC). The LMA solution is favored from the combined analysis of all solar neutrino experiments.

In 1998, Super-Kamiokande (SK) detected the atmospheric neutrino anomaly and reported evidence for neutrino oscillations [6]. However, the most significant characteristic of neutrino oscillation, oscillatory behavior of survival probability, has not been observed yet. Discrimination of neutrino oscillation from other disappearance hypotheses, such as neutrino decay [7] and neutrino decoherence [8] was still difficult, although they give different spectrum shapes. In 2002, the first result of KamLAND [9] revealed a significant deficit of the electron anti-neutrinos from distant power reactors and excluded all solar neutrino solutions but the LMA solution in the context of two neutrino oscillation with CPT invariance. However, the spectrum shape was

almost consistent with the no oscillation shape, because of low statistics. The detection of evident spectral distortion is essential to confirm neutrino oscillation. Furthermore, the determination of the oscillation parameter set is the last subject for neutrino oscillation physics.

In this thesis, the distortion of the energy spectrum is investigated by using 515.1 days of data first. Next, the neutrino oscillation parameters are analyzed in two neutrino oscillation. Lastly, the analysis is extended from two neutrinos to three neutrinos. This thesis is arranged as follows,

Chapter 1 :

A detailed description of neutrino oscillation physics is given in this chapter. At the last section, the motivation of this thesis is described.

Chapter 2 :

The detection method is described in this chapter. The detailed description of the KamLAND detector is also given.

Chapter 3 :

The event reconstruction and detector calibration are described in this chapter. The fiducial volume is extended relative to earlier KamLAND measurement by improving the event reconstruction, vertex fit and energy estimation. Systematic uncertainties of reconstruction are also discussed.

Chapter 4 :

Backgrounds for the detection of reactor $\bar{\nu}_e$ are estimated in this chapter. Those are dominated by the (α, n) and $^8\text{He}/^9\text{Li}$ backgrounds. The muon induced spallation events are also studied.

Chapter 5 :

The reactor $\bar{\nu}_e$ flux and the detection efficiency are calculated in this chapter. The selection of reactor $\bar{\nu}_e$ candidates is also shown.

Chapter 6 :

The significance of neutrino oscillation is given in this chapter. The observed data are compared with its expectation for both rate and shape. A neutrino oscillation analysis is carried out in two neutrino oscillation. The non-standard models of neutrino disappearance, neutrino decay and decoherence are also discussed.

Chapter 7 :

The oscillation analysis is appropriately extended from two neutrinos to three neutrinos in this chapter. All neutrino oscillation experiments are considered.

Chapter 8 :

Summary of this thesis.

1.1 The Neutrino

The existence of the neutrino first introduced by W. Pauli [1] in 1930 was confirmed by F. Reines and C. L. Cowan [2]. They used reactor electron anti-neutrinos to study neutrino properties via the inverse β decay reaction

$$\bar{\nu}_e + p \rightarrow e^+ + n \quad (1.1)$$

followed by the γ -rays from neutron capture on the Cadmium nucleus. Another flavor of neutrino ν_μ , was discovered at Brookhaven National Laboratory in 1962 [10]. The τ particle was discovered at the Stanford Linear Accelerator Center in 1975 [11] and its associated ν_τ was discovered by the DONUT Collaboration in 2000 [12]. The structure of the weak interaction (V-A interaction) was established by T. Lee and C. Yang [13] via the possible parity violation, which explains the result of K^+ decay, and it was confirmed by C. Wu [14] using ^{60}Co β decay in 1957. The intermediate bosons, W^\pm and Z^0 , were directly detected at the CERN $p\bar{p}$ collider experiment in 1983 [15]. The precise measurement of the decay width of Z^0 in e^+e^- colliders, LEP at CERN [16], constrains the number of light visible neutrino families to 3.

In the Standard Model, the elementary particles which have spin 1/2 are organized in 2 types, 6 leptons and 6 quarks, as follows.

$$\begin{array}{ccc} \begin{pmatrix} \nu_e \\ e \end{pmatrix} & \begin{pmatrix} \nu_\mu \\ \mu \end{pmatrix} & \begin{pmatrix} \nu_\tau \\ \tau \end{pmatrix} & \text{leptons} \\ \begin{pmatrix} u \\ d \end{pmatrix} & \begin{pmatrix} c \\ s \end{pmatrix} & \begin{pmatrix} t \\ b \end{pmatrix} & \text{quarks} \end{array}$$

The elementary particles and their interactions are expressed in a $SU(3) \times SU(2) \times U(1)$ gauge theory within the framework of the Standard Model. The neutrino has zero mass, zero charge and spin 1/2 in the Standard Model. However, there is no compelling reason that forbids finite masses of neutrinos. Table 1.1 shows the recent experimental limits on neutrino masses. There is no established evidence for finite neutrino masses from direct measurements. Another limit on neutrino masses comes from cosmology. The amplitude of fluctuations of the cosmic microwave background is suppressed if neutrinos are massive. In the condition that the three neutrino flavors are degenerate, the upper limit of neutrino mass is $m_\nu < 0.23$ eV at 95% C.L [17].

Table 1.1: Experimental limits on neutrino masses [18, 19, 20]

neutrino flavor	mass limit
ν_e	2.5 eV (95% C.L.)
ν_μ	0.17 MeV (90% C.L.)
ν_τ	18.2 MeV (95% C.L.)

The small neutrino masses cannot be explained naturally by the standard model. That solution may be given by a new physics beyond the Standard Model, such as the ‘See-saw mechanism’ [21, 22, 23]. The See-saw mechanism explains small neutrino masses in relation to the existence of new physics at a much higher energy scale.

1.2 Neutrino Oscillation

1.2.1 Vacuum Oscillation

The neutrino oscillation was suggested by Maki, Nakagawa and Sakata in 1962 [4]. For massive neutrinos, the flavor eigenstates, ν_e, ν_μ, ν_τ are not necessarily the same as the mass eigenstates, ν_1, ν_2, ν_3 . Generally, the flavor eigenstates can be expressed as a linear combination of the mass eigenstates.

$$|\nu_\alpha\rangle = \sum_{i=1}^3 U_{\alpha i} |\nu_i\rangle \quad (\alpha = e, \mu, \tau) \quad (1.2)$$

where the unitary matrix U is defined by the mixing angle, $\theta_{12}, \theta_{23}, \theta_{13}$ and a CP phase δ .

$$U = \begin{pmatrix} 1 & 0 & 0 \\ 0 & c_{23} & s_{23} \\ 0 & -s_{23} & c_{23} \end{pmatrix} \begin{pmatrix} c_{13} & 0 & s_{13}e^{-i\delta} \\ 0 & 1 & 0 \\ -s_{13}e^{i\delta} & 0 & c_{13} \end{pmatrix} \begin{pmatrix} c_{12} & s_{12} & 0 \\ -s_{12} & c_{12} & 0 \\ 0 & 0 & 1 \end{pmatrix} \quad (1.3)$$

$$= \begin{pmatrix} c_{12}c_{13} & s_{12}c_{13} & s_{13}e^{-i\delta} \\ -s_{12}c_{23} - c_{12}s_{23}s_{13} & c_{12}c_{23} - s_{12}s_{23}s_{13}e^{i\delta} & s_{23}c_{13} \\ s_{12}s_{23} - c_{12}c_{23}s_{13} & -c_{12}s_{23} - s_{12}c_{23}s_{13}e^{i\delta} & c_{23}c_{13} \end{pmatrix} \quad (1.4)$$

where, $s_{ij} = \sin \theta_{ij}$, $c_{ij} = \cos \theta_{ij}$ ($i, j = 1, 2, 3$). Majorana phases (Section 1.4.4) have no effect on neutrino oscillation and are neglected here. Time evolution of the mass eigenstates are given by

$$i \frac{d}{dt} |\nu_i\rangle = E_i |\nu_i\rangle \quad (1.5)$$

where E_i is the energy of ν_i , and so the wave function can be written as,

$$|\nu_i(t)\rangle = e^{-iE_i t} |\nu_i(0)\rangle \quad (1.6)$$

For flavor eigenstates, using Eq. (1.2), Eq. (1.5) and Eq. (1.6),

$$i \frac{d}{dt} |\nu_\alpha\rangle = \sum_{i=1}^3 U_{\alpha i} E_i U_{i\alpha}^\dagger |\nu_\alpha\rangle \quad (1.7)$$

$$|\nu_\alpha(t)\rangle = \sum_{i=1}^3 U_{\alpha i} e^{-iE_i t} U_{i\alpha}^\dagger |\nu_\alpha(0)\rangle. \quad (1.8)$$

If ν_α is produced at $t = 0$, the probability of being flavor β at $t = t$ is

$$P(\nu_\alpha \rightarrow \nu_\beta) = |\langle \nu_\beta(t) | \nu_\alpha(0) \rangle|^2 \quad (1.9)$$

$$= \sum_{i=1}^3 \left| \langle \nu_\beta(t) | U_{\alpha i} e^{-iE_i t} U_{i\alpha}^\dagger | \nu_\alpha(0) \rangle \right|^2 \quad (1.10)$$

$$= \delta_{\alpha\beta} - 4 \sum_{i>j} \text{Re} (U_{\alpha i}^* U_{\beta i} U_{\alpha j} U_{\beta j}^*) \cdot \sin^2 \Phi_{ij} \\ \pm 2 \sum_{i>j} \text{Im} (U_{\alpha i}^* U_{\beta i} U_{\alpha j} U_{\beta j}^*) \cdot \sin^2 2\Phi_{ij} \quad (1.11)$$

where

$$\Phi_{ij} \equiv \frac{\Delta m_{ij}^2 L}{4E_\nu} = \frac{1.27 \Delta m_{ij}^2 [\text{eV}^2] L [\text{m}]}{E_\nu [\text{MeV}]} \quad (1.12)$$

$\Delta m_{ij}^2 = m_i^2 - m_j^2$, L is the flight distance, and E_ν is the neutrino energy. The \pm sign in the third term is the CP violation effect, $-$ for neutrinos and $+$ for anti-neutrinos. Because $\Delta m_{21}^2 + \Delta m_{31}^2 + \Delta m_{13}^2 = 0$, there exist only two independent Δm^2 for 3 species of neutrinos. Thus three generation neutrino oscillation can be described by two Δm^2 , three angles (θ_{12} , θ_{23} , θ_{13}) and one phase (δ).

To simplify the discussion, only two flavors are considered from here onwards,

$$\begin{pmatrix} \nu_e \\ \nu_x \end{pmatrix} = \begin{pmatrix} \cos \theta & \sin \theta \\ -\sin \theta & \cos \theta \end{pmatrix} \begin{pmatrix} \nu_1 \\ \nu_2 \end{pmatrix} \quad (1.13)$$

where θ is the mixing angle in vacuum between ν_e and ν_x . And the survival probability ($\alpha = \beta$) Eq. (1.11) is simplified to,

$$P(\nu_\alpha \rightarrow \nu_\alpha) = 1 - \sin^2 2\theta \sin^2 \Phi \quad (1.14)$$

$$= 1 - \sin^2 2\theta \sin^2 \left(\frac{1.27 \Delta m^2 [\text{eV}^2] L [\text{m}]}{E [\text{MeV}]} \right) \quad (1.15)$$

1.2.2 Neutrino Oscillation in Matter (MSW Effect)

A resonance effect of Neutrino oscillations in matter was first suggested by Mikheyev and Smirnov based [24] on the theory advocated by Wolfenstein [25]. Therefore, it is called the MSW effect. The phase factor of neutrino propagation is modified from ipx to $ipnx$, where n is a refractive index,

$$p(n-1) = \frac{2\pi N_e}{p} f(0) = -\sqrt{2} G_F N_e \quad (1.16)$$

where N_e is an electron density, $f(0)$ is the forward scattering amplitude in $\nu_e e \rightarrow \nu_e e$, and G_F is the Fermi constant. In matter, all neutrinos (electron, muon, tau type) can interact with an electron, a proton or a neutron via the neutral current interaction. The MSW effect is caused by the fact that only electron neutrinos can interact with an electron via a charged

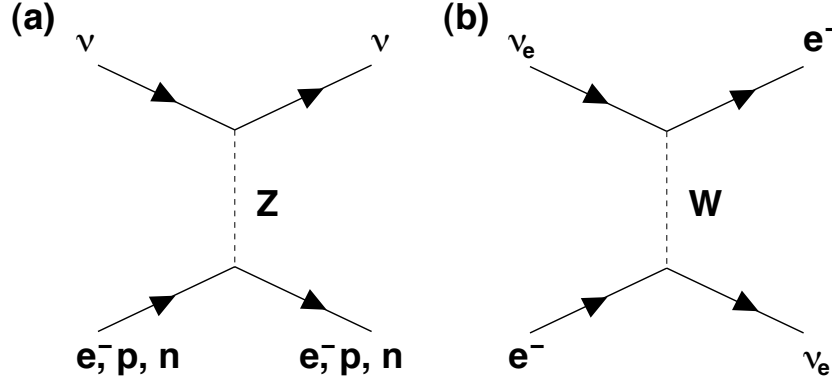


Figure 1.1: Feynman diagrams of neutrino interaction in matter. (a) indicates neutral current interaction with Z boson exchange between a neutrino and an electron, a proton or neutron. (b) indicates charged current interaction with W boson exchange between an electron neutrino and an electron.

current interaction while other neutrino flavors cannot (Figure 1.1). This causes a difference in $f(0)$ between electron neutrinos and other neutrinos. This effect was applied to the solar neutrino problem and a possibility of resonant enhancement of neutrino oscillations in the sun was pointed out.

$$i \frac{d}{dt} \begin{pmatrix} \nu_e \\ \nu_x \end{pmatrix} = \left[U \begin{pmatrix} E_1 & 0 \\ 0 & E_2 \end{pmatrix} U^\dagger + \begin{pmatrix} \sqrt{2}G_F N_e & 0 \\ 0 & 0 \end{pmatrix} \right] \begin{pmatrix} \nu_e \\ \nu_x \end{pmatrix} \quad (1.17)$$

$$= \frac{1}{2} \left[(\Sigma + \sqrt{2}G_F N_e) + \begin{pmatrix} -\Delta_V \cos 2\theta_V + \sqrt{2}G_F N_e & \Delta_V \sin 2\theta_V \\ \Delta_V \sin 2\theta_V & \Delta_V \cos 2\theta_V - \sqrt{2}G_F N_e \end{pmatrix} \right] \begin{pmatrix} \nu_e \\ \nu_x \end{pmatrix} \quad (1.18)$$

where $\Sigma = (m_2^2 + m_1^2)/2E$, $\Delta_V = (m_2^2 - m_1^2)/2E$, $m_{1,2}$ are the neutrino masses, θ_V is the vacuum mixing angle.

After discarding the diagonal term $(\Sigma + \sqrt{2}G_F N_e)$ in Eq. (1.18), which doesn't contribute to the oscillation pattern, the eigenvalues can be given by

$$\pm \Delta_M/2 \quad (1.19)$$

where

$$\Delta_M = [(\Delta_V \cos 2\theta_V - \sqrt{2}G_F N_e)^2 + \Delta_V^2 \sin^2 2\theta_V]^{1/2} \quad (1.20)$$

and its eigenstates are

$$\begin{pmatrix} \nu_{1M} \\ \nu_{2M} \end{pmatrix} = \begin{pmatrix} \cos \theta_M & -\sin \theta_M \\ \sin \theta_M & \cos \theta_M \end{pmatrix} \begin{pmatrix} \nu_e \\ \nu_x \end{pmatrix} \quad (1.21)$$

and θ_M is the neutrino mixing angle in matter, given by

$$\tan 2\theta_M = \frac{\Delta_V \sin 2\theta_V}{-\sqrt{2}G_F N_e + \Delta_V \cos 2\theta_V} \quad (1.22)$$

or, equivalently

$$\sin^2 2\theta_M = \frac{(\Delta_V \sin 2\theta_V)^2}{\Delta_M^2}. \quad (1.23)$$

From the above equation, a large electron density provides a larger mixing angle in the matter, as shown in Table 1.2. When the electron density satisfies

$$N_e^{resonance} = \frac{\Delta_V \cos 2\theta_V}{\sqrt{2}G_F}, \quad (1.24)$$

the resonance occurs and neutrino mixing is at maximum.

Table 1.2: The relation between the electron density and the mixing angle in matter

N_e	0	...	$N_e^{resonance}$...	∞
θ_M	θ_V	...	$\pi/4$...	$\pi/2$

1.3 Neutrino Oscillation Experiment

1.3.1 Solar Neutrinos

The sun is a main-sequence star at the stage of stable hydrogen burning. The SSM (standard solar model) [26] predicts that over 98.4% of solar energy is generated from the pp-chain (proton-proton) reaction (Figure 1.2) and a small fraction is from the CNO (carbon-nitrogen-oxygen) cycle (Figure 1.3). The overall reaction is given by



Positron annihilate with electrons. Therefore, when considering the solar thermal energy generation, the relevant expression is

$$4p + 2e^- \rightarrow {}^4\text{He} + 2\nu_e + 26.73\text{MeV} - E_\nu \quad (1.26)$$

where E_ν represents the energy taken away by neutrinos, with an average value of $\langle E_\nu \rangle \sim 0.6$ MeV. The neutrino producing reactions which are at work inside the sun are enumerated in the first column in Table 1.3. The second column in Table 1.3 shows the abbreviation for these reactions. Neutrino energy spectra are shown in Figure 1.4. The neutrino production points are different for every reaction (Figure 1.5) because each reaction rate depends on the composition of atoms, temperature and density. The neutrino flux is calculated using solar models. The

calculation of a model begins with the description of a main sequence that has a homogeneous composition. Hydrogen burns in the stellar core, supplying both the radiated luminosity and the thermal pressure that supports the star against the force of gravity. Successive models are calculated by allowing for composition changes caused by nuclear reactions, as well as the mild evolution of other contribution inside the star. A satisfactory solar model is a solution of the evolutionary equations that satisfies boundary conditions in both space and time.

The SSM accuracy was verified by Helioseismology. Figure 1.6 shows the excellent agreement between the calculated sound speeds for the SSM (BP2000) and the helioseismologically measured (Sun) sound speeds [28]. The calculated sound speeds and the measured sound speeds agree everywhere in the sun at 0.1% accuracy. The estimation of solar neutrino flux uncertainties is based on the SSM precision. The pp neutrino flux, which has the largest contribution to the pp chain, is not determined by the solar luminosity, even if the CNO fusion reaction is ignored. The primary uncertainty is caused by an uncertainty in the branch of the solar fusion reaction determining whether the pp neutrino is produced once or twice when four protons are burned. The reaction ${}^3\text{He}({}^3\text{He}, 2p){}^4\text{He}$ makes two protons, which produces one pp neutrino again. On the other hand the reaction ${}^3\text{He}({}^4\text{He}, \gamma){}^7\text{Be}$ ends up with one ${}^7\text{Be}$ or ${}^8\text{B}$ neutrino production. The ratio of ${}^3\text{He} + {}^4\text{He}$ to ${}^4\text{He} + {}^4\text{He}$ reactions can be calculated from the neutrino flux

$$R \equiv \frac{\langle {}^3\text{He} + {}^4\text{He} \rangle}{\langle {}^3\text{He} + {}^3\text{He} \rangle} = \frac{2 [\phi({}^7\text{Be}) + \phi({}^8\text{B})]}{\phi(pp) - [\phi({}^7\text{Be}) + \phi({}^8\text{B})]}, \quad (1.27)$$

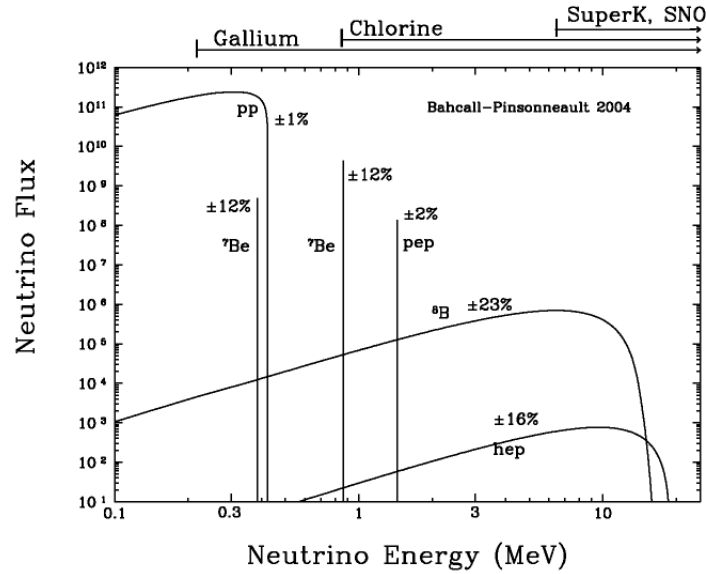
and the SSM (BP2004) predicts $R = 0.178$. The ${}^3\text{He} + {}^4\text{He}$ cross section directly affects the ${}^7\text{Be}$ neutrino flux. The ${}^8\text{B}$ neutrino production strongly depends on the ${}^7\text{Be}(p, \gamma){}^8\text{B}$ cross section $S({}^7\text{Be} + p) = 20.6 \pm 0.8 \text{ eV b}$ [26], which has been determined in laboratory measurements. Currently, the largest uncertainty in the ${}^8\text{B}$ neutrino flux is caused by the heavy element to hydrogen ratio Z/X uncertainty.

As a well-defined neutrino source, the sun also provides extremely important opportunities to investigate nontrivial neutrino properties such as nonzero mass and mixing, because of the wide range of matter density and the great distance from the sun to the earth, $1.5 \times 10^{11} \text{ m}$. A pioneering solar neutrino experiment by R. Davis and his colleagues [3] using ${}^{37}\text{Cl}$ started in the late 1960's. From the very beginning of the solar neutrino observation, it was recognized that the observed flux was significantly smaller than the SSM prediction, indicating that something happens to the electron neutrinos after they are created in the solar interior. This deficit has been called the ‘Solar Neutrino Problem’.

The solar neutrinos have been detected in various methods, such as radiochemical procedures and real-time measurements with Cherenkov imaging detectors. All solar neutrino experiments showed the deficit of solar neutrinos. In 2002 however, the SNO experiment [5] showed that the NC (sensitive to all active neutrinos) rate is consistent with the SSM prediction (Figure 1.7). This strongly indicates the neutrino flavor conversion of solar neutrinos. The results of the solar neutrino experiments are summarized in Table 1.4.

Table 1.3: Neutrino-producing reactions in the sun [26, 27]

Reaction	Abbr.	Flux [$\text{cm}^{-2}\text{sec}^{-1}$] (BP2004)
<i>pp</i> chain		
$pp \rightarrow de^+\nu$	<i>pp</i>	$5.94 (1.00^{+0.01}_{-0.01}) \times 10^{10}$
$pe^-p \rightarrow d\nu$	<i>pep</i>	$1.40 (1.00^{+0.02}_{-0.02}) \times 10^8$
${}^3\text{He } p \rightarrow {}^4\text{He } e^+\nu$	<i>hep</i>	$7.88 (1.00^{+0.16}_{-0.16}) \times 10^3$
${}^7\text{Be } e^- \rightarrow {}^7\text{Li } \nu + (\gamma)$	${}^7\text{Be}$	$4.86 (1.00^{+0.12}_{-0.12}) \times 10^9$
${}^8\text{B} \rightarrow {}^8\text{Be}^* e^+\nu$	${}^8\text{B}$	$5.82 (1.00^{+0.23}_{-0.23}) \times 10^6$
CNO cycle		
${}^{13}\text{N} \rightarrow {}^{13}\text{C } e^+\nu$	${}^{13}\text{N}$	$5.71 (1.00^{+0.37}_{-0.35}) \times 10^8$
${}^{15}\text{O} \rightarrow {}^{15}\text{N } e^+\nu$	${}^{15}\text{O}$	$5.03 (1.00^{+0.43}_{-0.39}) \times 10^8$
${}^{17}\text{F} \rightarrow {}^{17}\text{O } e^+\nu$	${}^{17}\text{F}$	$5.91 (1.00^{+0.44}_{-0.44}) \times 10^6$

Figure 1.4: Solar neutrino spectrum from *pp* chain predicted by the SSM [28].

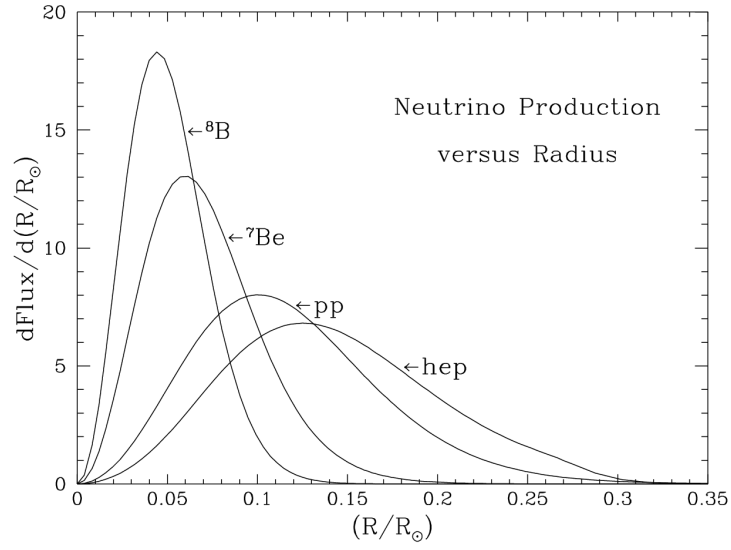


Figure 1.5: Production points of neutrinos as a function of the solar radius [28].

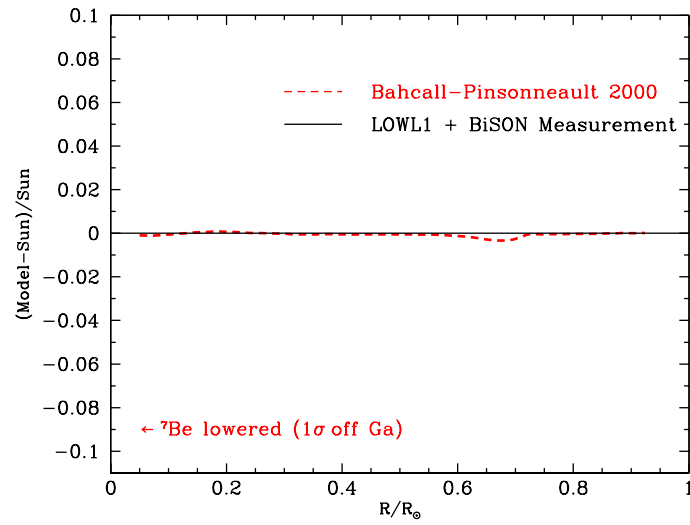


Figure 1.6: Predicted versus measured sound speeds [28].

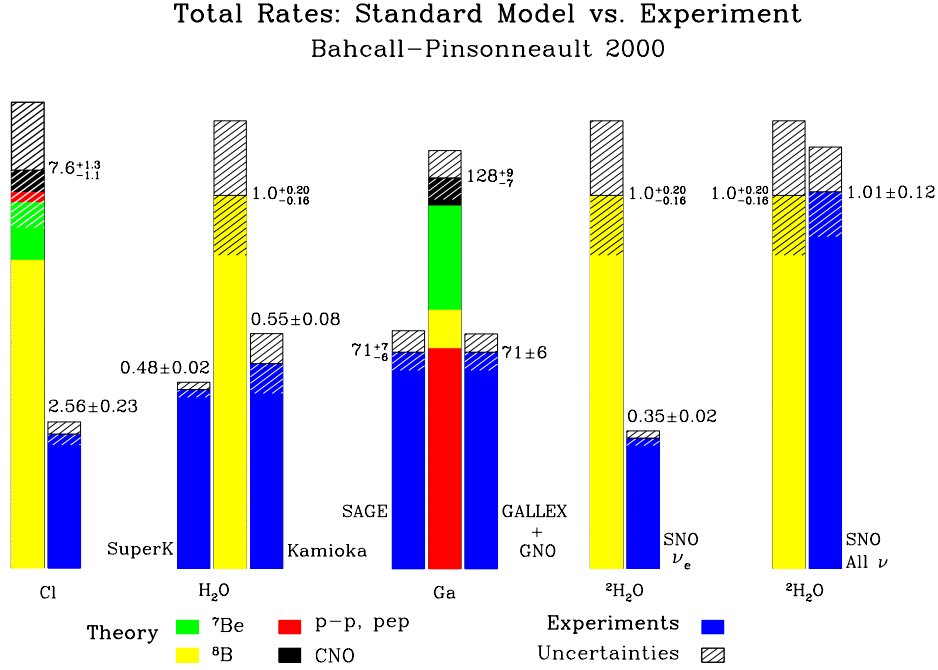


Figure 1.7: Comparisons of neutrino event rates between SSM prediction and experimental measurements [28].

Homestake

Solar neutrino observation by the Homestake experiment started in 1967 [3]. The detector consisted of a horizontal steel tank, 6.1 m in diameter and 14.6 m long, containing 615 m³ of C₂Cl₄. It was located 1500 m underground (4100 m water equivalent) in the Homestake Gold Mine in Lead, South Dakota, USA. The solar neutrinos are detected via the capture reaction of ³⁷Cl

$$\nu_e(E_\nu > 0.814\text{MeV}) + {}^{37}\text{Cl} \rightarrow e^- + {}^{37}\text{Ar}, \quad (1.28)$$

where the detected ν_e 's are mainly ⁸B neutrinos. The expected event rate from BP2001 is $7.6^{+1.3}_{-1.1}$ SNU, where SNU is the number of interactions per 10³⁶ targets per second. The observed capture rate is [29]

$$R_{obs}^{\text{Cl}} = 2.56 \pm 0.16(\text{stat}) \pm 0.16(\text{syst}) \quad \text{SNU}. \quad (1.29)$$

The ratio of the observed rate to the SSM prediction is 0.30 ± 0.07 .

GALLEX/GNO and SAGE

The GALLEX and SAGE use the neutrino capture reaction on ⁷¹Ga

$$\nu_e(E_\nu > 0.233\text{MeV}) + {}^{71}\text{Ga} \rightarrow e^- + {}^{71}\text{Ge}, \quad (1.30)$$

and its low energy threshold made it possible for the experiment to observe *pp* neutrinos.

Table 1.4: Results of the solar neutrino experiments

experiment	measurement	SSM (BP2004 [26, 27])	measurement/SSM
Homestake [29]			
$^{37}\text{Cl} \rightarrow ^{37}\text{Ar}$ (SNU)	$2.56 \pm 0.16 \pm 0.16$	$8.5^{+1.8}_{-1.8}$	0.30 ± 0.07
GALLEX/GNO [30, 31]			
$^{71}\text{Ga} \rightarrow ^{71}\text{Ge}$ (SNU)	$69.3 \pm 4.1 \pm 3.6$	131^{+12}_{-10}	0.53 ± 0.06
SAGE [32]			
$^{71}\text{Ga} \rightarrow ^{71}\text{Ge}$ (SNU)	$66.9 \pm 3.9 \pm 3.6$	131^{+12}_{-10}	0.51 ± 0.06
Kamiokande [33]			
^8B ν flux ($10^6 \text{cm}^{-2}\text{s}^{-1}$)	$2.80 \pm 0.19 \pm 0.33$	$5.82 (1.00^{+0.23}_{-0.23})$	0.48 ± 0.13
Super-Kamiokande [34]			
^8B ν flux ($10^6 \text{cm}^{-2}\text{s}^{-1}$)	$2.35 \pm 0.03^{+0.07}_{-0.06}$	$5.82 (1.00^{+0.23}_{-0.23})$	0.40 ± 0.09
SNO (NaCl in D_2O) [35]			
CC			
^8B ν flux ($10^6 \text{cm}^{-2}\text{s}^{-1}$)	$1.59^{+0.08+0.06}_{-0.07-0.08}$	$5.82 (1.00^{+0.23}_{-0.23})$	0.27 ± 0.07
NC			
^8B ν flux ($10^6 \text{cm}^{-2}\text{s}^{-1}$)	$5.21 \pm 0.27 \pm 0.38$	$5.82 (1.00^{+0.23}_{-0.23})$	0.90 ± 0.22
ES			
^8B ν flux ($10^6 \text{cm}^{-2}\text{s}^{-1}$)	$2.21^{+0.31}_{-0.26} \pm 0.10$	$5.82 (1.00^{+0.23}_{-0.23})$	0.38 ± 0.15

The GALLEX experiment was started in 1991 and ended in 1997, and the GNO experiment resumed in 1998 [36, 37]. The detector is located at a depth of 3000 m water equivalent in the Gran Sasso Underground Laboratory in Italy. The target consists of 101 tons (53.5 m^3) of GaCl_3 , of which 12 tons is ^{71}Ga .

The SAGE experiment was started in 1990 [38]. The detector was situated in a tunnel in the Northern Causaus Mountains in southern Russia at a depth of 4800 m water equivalent. The target was 30 tons (\sim July 1991) and 57 tons (August 1991 \sim) of metallic gallium.

The expected event rate from BP2004 is 131^{+12}_{-10} SNU, and the observed capture rate from Ga experiments are [30, 31, 32]

$$R_{obs}^{\text{GALLEX/GNO}} = 69.3 \pm 4.1(\text{stat}) \pm 3.6(\text{syst}) \quad \text{SNU} \quad (1.31)$$

$$R_{obs}^{\text{SAGE}} = 66.9 \pm 3.9(\text{stat}) \pm 3.6(\text{syst}) \quad \text{SNU}, \quad (1.32)$$

and the combined rate is [39]

$$R_{obs}^{\text{Ga}} = 68.1 \pm 3.75 \quad \text{SNU}. \quad (1.33)$$

The ratio of the observed rate to the SSM prediction is 0.52 ± 0.06 .

Kamiokande and Super-Kamiokande

Kamiokande and Super-Kamiokande are real-time experiments measuring neutrinos via νe scattering

$$\nu_x + e^- \rightarrow \nu_x + e^- \quad (x = e, \mu, \tau) \quad (1.34)$$

using a ring imaging Cherenkov detector. The reaction is sensitive to all active neutrinos, but the sensitivity to ν_μ, ν_τ , is smaller than to ν_e by a factor of ~ 0.16 . There is directional correlation between the incoming neutrino and the recoil electron, it helps clear separation of the solar neutrino signal from background. Due to the high thresholds (7 MeV in Kamiokande and 5 MeV in Super-Kamiokande), these experiments only observe ^8B and *hep* solar neutrinos.

The Kamiokande experiment started solar neutrino observation in April 1987 and ended in 1995 [33]. The detector was located in the Kamioka mine in Gifu Prefecture, Japan. Purified water of 3000 m³ was contained in a steel tank of 15.6 m diameter and 16.1 m high. The inner detector contained 2140 m³ of purified water and was viewed by 946 50 cm PMTs.

The Super-Kamiokande started neutrino observation in April 1996 [40]. The detector is located near Kamiokande. Purified water of 50 kton is contained in a stainless steel tank of 39.3 m diameter and 42 m high. The inner detector contained 32 kton of purified water and is viewed by 11,146 inward-facing 50 cm PMTs.

The observed ^8B neutrino fluxes for the two experiments are [33, 34]

$$\Phi_{^8\text{B(ES)}}^{\text{Kamiokande}} = 2.80 \pm 0.19(\text{stat}) \pm 0.33(\text{syst}) \times 10^6 \text{ cm}^{-2}\text{sec}^{-1} \quad (1.35)$$

$$\Phi_{^8\text{B(ES)}}^{\text{Super-Kamiokande}} = 2.35 \pm 0.03(\text{stat})_{-0.06}^{+0.07}(\text{syst}) \times 10^6 \text{ cm}^{-2}\text{sec}^{-1} \quad (1.36)$$

The ratio of the observed rate to the SSM prediction is 0.40 ± 0.09 from the Super-Kamiokande result.

SNO

The Sudbury Neutrino Observatory (SNO) is a ring imaging Cherenkov detector that started data-taking in 1999. The detector is located at a depth of 2070 m underground (6100 m water equivalent) in the INCO, Ltd. Creighton mine near Sudbury, Ontario, Canada. The detector uses 1000 tons of ultra-pure heavy water D₂O, which is contained in a transparent acrylic spherical vessel (12 m in diameter). Cherenkov light generated in the heavy water is detected by 9456 PMTs mounted on a 17.8 m diameter stainless steel frame. SNO can detect energies greater than 5 MeV, and measures ^8B solar neutrinos through the reactions:

$$\nu_e + d \rightarrow p + p + e^- \quad (\text{CC}) \quad (1.37)$$

$$\nu_x + d \rightarrow p + n + \nu_x \quad (\text{NC}) \quad (1.38)$$

$$\nu_x + e^- \rightarrow \nu_x + e^- \quad (\text{ES}). \quad (1.39)$$

The Q-value of the CC reactions is -1.4 MeV and the electron energy has a strong correlation with neutrino energy. The CC reaction is sensitive only to electron type neutrinos, while the NC reaction is equally sensitive to all active neutrino flavors.

The threshold of the NC reaction is 2.2 MeV. The NC reactions are detected by neutron capture on deuterium, which generates a 6.25 MeV γ -ray. In order to enhance the detection

efficiency, 2.5 tons of NaCl was added to the heavy water in the second phase of the SNO experiment. Chlorine (^{35}Cl) has a high absorption cross section for thermal neutrons, resulting in a gamma ray cascade peak at around 8 MeV.

The observed ^8B neutrino flux in the salt phase was [35]

$$\Phi_{^8\text{B}(\text{CC})}^{\text{SNO}} = 1.59_{-0.07}^{+0.08}(\text{stat})_{-0.08}^{+0.06}(\text{syst}) \times 10^6 \text{ cm}^{-2}\text{sec}^{-1} \quad (1.40)$$

$$\Phi_{^8\text{B}(\text{NC})}^{\text{SNO}} = 5.21 \pm 0.27(\text{stat}) \pm 0.38(\text{syst}) \times 10^6 \text{ cm}^{-2}\text{sec}^{-1} \quad (1.41)$$

$$\Phi_{^8\text{B}(\text{ES})}^{\text{SNO}} = 2.21_{-0.26}^{+0.31}(\text{stat}) \pm 0.10(\text{syst}) \times 10^6 \text{ cm}^{-2}\text{sec}^{-1}. \quad (1.42)$$

The ratio of the observed rate to the SSM (BP2000) prediction was as follows,

$$\Phi_{^8\text{B}(\text{CC})}^{\text{SNO}}/\Phi_{^8\text{B}}^{\text{SSM}} = 0.315_{-0.014}^{+0.016}(\text{stat})_{-0.016}^{+0.012}(\text{syst}) \quad (1.43)$$

$$\Phi_{^8\text{B}(\text{NC})}^{\text{SNO}}/\Phi_{^8\text{B}}^{\text{SSM}} = 1.030 \pm 0.053(\text{stat}) \pm 0.075(\text{syst}) \quad (1.44)$$

$$\Phi_{^8\text{B}(\text{ES})}^{\text{SNO}}/\Phi_{^8\text{B}}^{\text{SSM}} = 0.438_{-0.051}^{+0.061}(\text{stat}) \pm 0.020(\text{syst}), \quad (1.45)$$

where the SSM uncertainty is not included. The SNO result provides strong evidence for solar ν_e flavor transformation. The total flux, measured by the NC reaction, is consistent with the SSM prediction. Figure 1.8 shows the ^8B solar neutrino flux other than ν_e vs ν_e deduced from the SNO data. The three flux bands meet at one point giving a high reliability of the experiment.

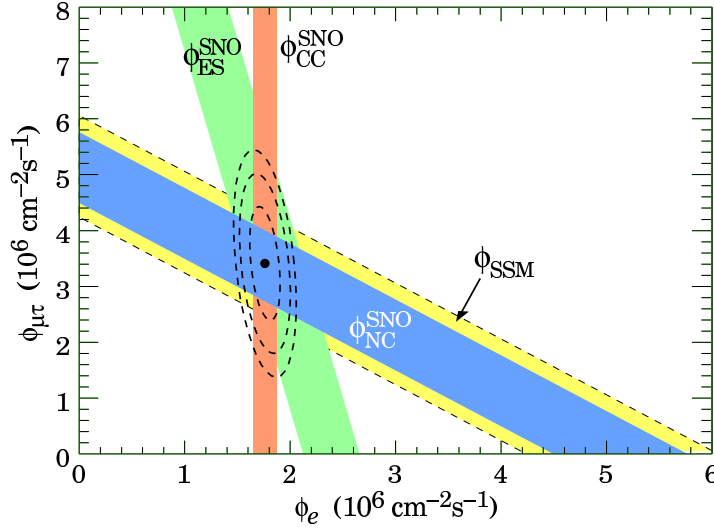


Figure 1.8: Flux of ^8B solar neutrinos from active neutrinos other than ν_e vs that from ν_e deduced from the three neutrino reactions in SNO [5].

1.3.2 Atmospheric Neutrinos

Atmospheric Neutrino Experiments

Atmospheric neutrinos are produced in decays of pions and kaons generated from interaction of primary cosmic rays with the upper atmosphere. The flight length of atmospheric neutrinos is between 15 km for neutrinos produced at the zenith and 13,000 km for the nadir respectively. The energy spectrum is peaked at ~ 1 GeV and extends to hundreds of GeV. The following production reactions predict the ratio of $\nu_\mu + \bar{\nu}_\mu$ flux to $\nu_e + \bar{\nu}_e$ to be about 2:

$$\pi^+(\pi^-) \rightarrow \mu^+(\mu^-) + \nu_\mu(\bar{\nu}_\mu) \quad (1.46)$$

$$\mu^+(\mu^-) \rightarrow e^+(e^-) + \bar{\nu}_\mu(\nu_\mu) + \nu_e(\bar{\nu}_e). \quad (1.47)$$

The ratio $(\nu_\mu + \bar{\nu}_\mu)/(\nu_e + \bar{\nu}_e)$ has been measured by several underground experiments. The detectors are classified broadly into two types, water Cherenkov detectors (Kamiokande [41], IMB [42] and Super-Kamiokande [43]) and iron calorimeter detectors (Fréjus [44], NUSEX [45], and Soudan2 [46]). The results of those experiments are summarized in Table 1.5. Kamiokande, IMB, Super-Kamiokande and Soudan2 reported that the ratio $(\nu_\mu + \bar{\nu}_\mu)/(\nu_e + \bar{\nu}_e)$ was significantly smaller than expected, while Fréjus and NUSEX reported results consistent with expected within errors. An anomaly in the zenith angle dependence was observed by the Kamiokande experiment for the first time, and the Super-Kamiokande experiment confirmed it with much better statistical significance, and reported evidence for oscillations of atmospheric neutrinos in 1998 [6]. Figure 1.9 shows the zenith angle distribution of μ -like events, e -like events and multi-ring events for the sub-GeV and multi-GeV sample, upward stopping muons and upward through-going muons, as observed in Super-Kamiokande. However, it was difficult to distinguish neutrino oscillation from other hypotheses, such as neutrino decay and neutrino decoherence, because of the bad resolution at the dip which is expected from the neutrino oscillation probability.

Recently, the Super-Kamiokande group optimized their analysis of atmospheric neutrinos, i.e. selected the events with good resolution in L/E in order to search for the dip in oscillation probability [48]. Figure 1.10 shows the L/E distribution for the best-fit expectation for neutrino oscillation, decay and decoherence. The χ^2 values for neutrino decay and decoherence are 11.3 (3.4 standard deviations) and 14.5 (3.8 standard deviations) larger than that for neutrino oscillation. Figure 1.11 shows the allowed regions for two flavor $\nu_\mu \leftrightarrow \nu_x$ oscillation. As the e -like appearance data shows no excess, $\nu_\mu \leftrightarrow \nu_e$ oscillations are disfavored relative to $\nu_\mu \leftrightarrow \nu_\tau$.

Table 1.5: Result of the atmospheric neutrino experiments

experiment	measurement/prediction
Cherenkov detector	
Kamiokande [41]	
(sub-GeV)	$0.60^{+0.06}_{-0.05} \pm 0.05$
(multi-GeV)	$0.57^{+0.08}_{-0.07} \pm 0.07$
IMB [42]	$0.54 \pm 0.05 \pm 0.012$
Super-Kamiokande [43]	
(sub-GeV)	$0.638 \pm 0.016 \pm 0.050$
(multi-GeV)	$0.658^{+0.030}_{-0.028} \pm 0.078$
iron calorimeter detector	
Fréjus [44]	$1.00 \pm 0.15 \pm 0.08$
NUSEX [45]	$0.99^{+0.35}_{-0.25}$
Soudan2 [46]	$0.64 \pm 0.11^{+0.06}_{-0.05}$

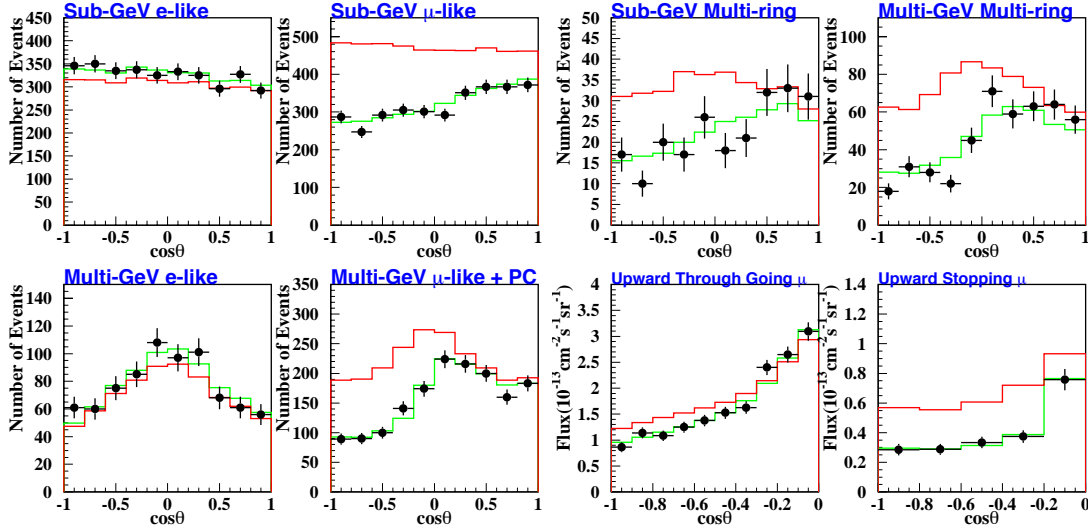


Figure 1.9: Zenith angle distribution of μ -like events, e-like events and multi-ring events for sub-GeV and multi-GeV sample, upward stopping muons and upward through-going muons, observed in Super-Kamiokande [47]. Black dots indicate the data and the red and green lines indicate the MC expectation for no oscillation case and the best fit oscillation case, respectively.

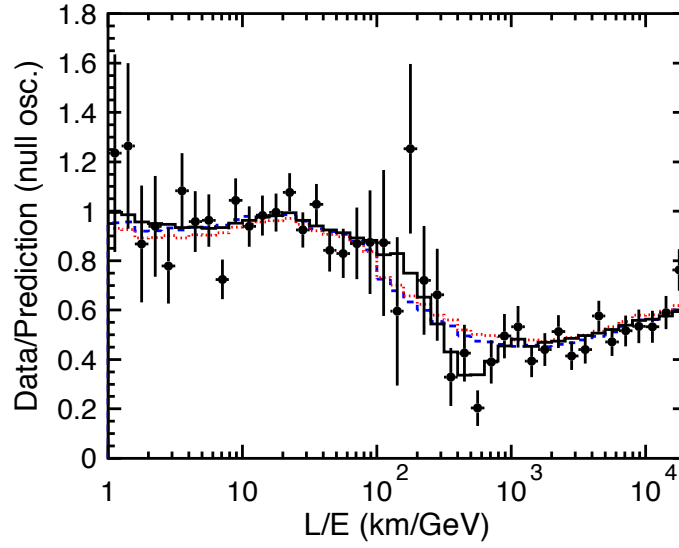


Figure 1.10: Ratio of the data to the MC events without neutrino oscillation (dots) as a function of the reconstructed L/E together with the best fit expectation for the two flavor oscillations (solid line) for atmospheric neutrinos in the Super-Kamiokande experiment [48]. Also shown are the best-fit expectation for neutrino decay (dashed line) and neutrino decoherence (dotted line).

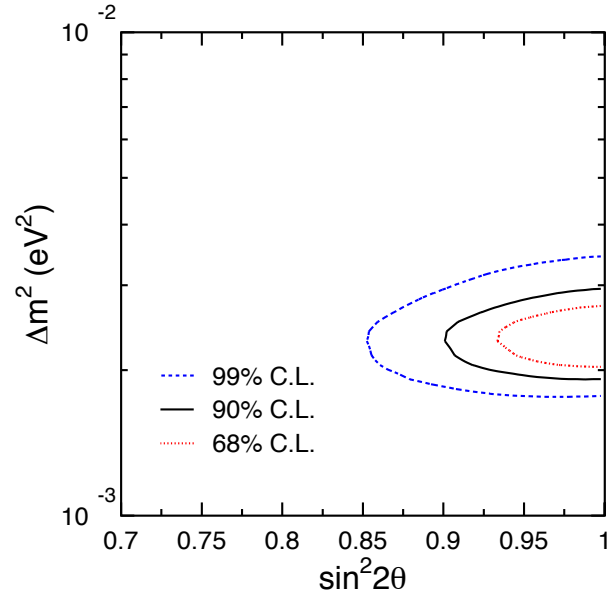


Figure 1.11: Allowed regions for two flavor $\nu_\mu \leftrightarrow \nu_x$ oscillations at 68%, 90% and 99% C.L. from the L/E analysis of atmospheric neutrinos at the Super-Kamiokande experiment [48]. The best fit value of Δm^2 is $2.4 \times 10^{-3} \text{ eV}^2$.

1.3.3 Accelerator Neutrinos

K2K

The KEK to Kamioka long baseline neutrino oscillation experiment (K2K) is an accelerator-based experiment [49]. The primary motivation of the K2K experiment is the confirmation of atmospheric neutrino oscillations using terrestrial neutrinos. The ν_μ are produced by a 12 GeV proton beam from the High Energy Accelerator Research Organization (KEK) in Ibaraki Prefecture, Japan. After the protons hit an aluminum target, π^+ are mainly produced and decay

$$\pi^+ \rightarrow \mu^+ \nu_\mu \quad (1.48)$$

with a mean energy 1.3 GeV. The neutrinos produced in KEK are detected in Super-Kamiokande in the Kamioka mine, at a distance of 250 km. This experimental condition allows the examination of $\nu_\mu \leftrightarrow \nu_\tau$ oscillation for Δm^2 down to $3 \times 10^{-3} \text{ eV}^2$ relevant for atmospheric neutrino oscillation.

The data sample called K2K-I has been taken from June 1999 to July 2001, corresponding to 4.8×10^{19} protons on target. K2K-I observed 56 events, while the expected number of events was estimated to be $80.1^{+6.2}_{-5.4}$. The probability that the observed flux at Super-Kamiokande is explained by statistical fluctuation without neutrino oscillations is less than 1%. K2K-II started in December 2002. Recently, the data of K2K-II, corresponding to 4.1×10^{19} protons on target, have been presented [47]. The combined analysis of K2K-I and K2K-II gives 108 observed events, while $150.9^{+11.6}_{-10.0}$ were expected in the no oscillation case. Figure 1.12 shows the energy spectrum for 1 ring μ -like sample in K2K-I sample. An oscillation analysis was performed assuming two flavor oscillation. Figure 1.13 shows the allowed regions of oscillation parameter using not only 1 ring μ -like events, with $N^{obs} = 56$, but the whole data sample in K2K-I.

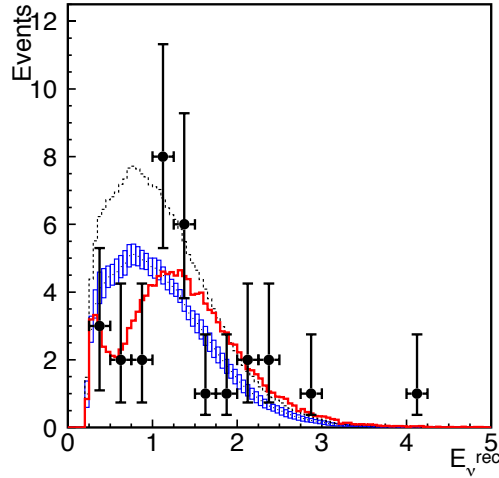


Figure 1.12: Reconstructed neutrino energy distribution for 1 ring μ -like sample at the K2K experiment [49]. The black dots with error bars are data. The black, blue and red line indicate the expectations from the no oscillation case, the no oscillation scaled and the best fit oscillation, respectively.

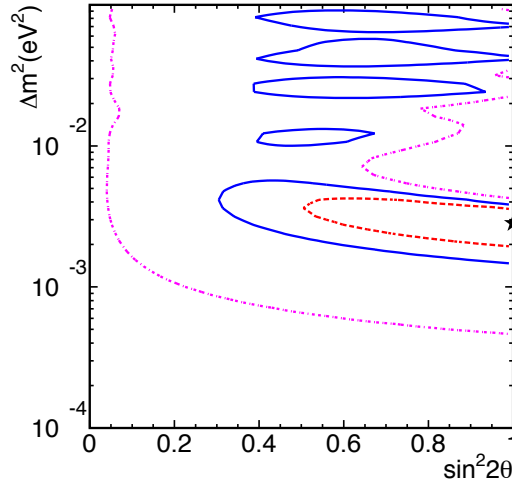


Figure 1.13: Allowed regions of oscillation parameters at the K2K experiment [49]. Dashed, solid and dot-dashed lines are 68.4%, 90% and 99% C.L. contours, respectively. The best fit value of Δm^2 is $2.8 \times 10^{-3} \text{ eV}^2$.

LSND

The Liquid Scintillator Neutrino Detector (LSND) experiment [50] started in 1993 and ended in 1998. The detector is located at the Los Alamos Neutron Science Center. Using a 800 MeV proton beam accelerator, the experiment studied neutrinos coming from the decay of muons $\mu^+ \rightarrow e^+ \nu_e \bar{\nu}_\mu$ at rest (DAR) and from the decay of pions $\pi^+ \rightarrow \mu^+ \nu_\mu$ in flight (DIF). The neutrino energy is up to the 52.8 MeV decay endpoint for DAR, and up to 300 MeV for DIF.

In 2001, LSND showed that a total excess of $87.9 \pm 22.4 \pm 6.0$ events was observed in the $\bar{\nu}_\mu \rightarrow \bar{\nu}_e$ search, corresponding to an oscillation probability of $(0.264 \pm 0.081)\%$. This excess may be interpreted as due to $\bar{\nu}_\mu \rightarrow \bar{\nu}_e$ oscillation, however, that mass-square difference $\Delta m_{\text{LSND}}^2 > 0.1 \text{ eV}^2$ is much higher than those of solar ($\Delta m_{\text{SOL}}^2 \sim 7 \times 10^{-5} \text{ eV}^2$) and atmospheric ($\Delta m_{\text{ATM}}^2 \sim 2 \times 10^{-3} \text{ eV}^2$). Therefore, this result cannot be explained by three neutrinos, which produce only two distinct Δm^2 . It is important to confirm or refute the LSND result.

KARMEN

The KARlsruhe Rutherford Medium Energy Neutrino (KARMEN) experiment [51] at the ISIS facility of the Rutherford Lab can also search for $\bar{\nu}_\mu \rightarrow \bar{\nu}_e$ using $\bar{\nu}_\mu$ from μ^+ decay at rest. The experiment employed a 56 ton segmented liquid scintillator detector located at 18 m distance from the beam target.

The analyzed data recorded with the full experimental setup of KARMEN-2 from February 1997 to March 2001 showed no excess of events, i.e. 15 events were observed while 15.8 ± 0.5 background events were expected. However, KARMEN-2 only had the sensitivity to exclude a portion of the LSND allowed regions.

MiniBooNE

MiniBooNE [52], the Mini Booster Neutrino Experiment at Fermilab refers to the first phase of the BooNE experiment, which searches for a precision measurement of the oscillation parameters allowed by the LSND experiment. If MiniBooNE verifies the LSND signal, then BooNE will proceed with its next stage. The MiniBooNE neutrino beam is produced by a primary beam of 8 GeV protons from Fermilab Booster. The ν_μ beam energy is from 0.5 to 1.5 GeV.

The MiniBooNE experiment can definitively confirm or refute the LSND oscillation signal with 1×10^{21} protons on target., started in 2002, currently in 2004, 30% of this amount has been collected. The conclusion will be reported in 2005.

1.3.4 Reactor Neutrinos

Bugey

A high statistics search for neutrino oscillations at the 2.8 GW Bugey reactor with detectors at 15 m, 40 m and 95 m, was reported by the Bugey group in 1995 [53]. The inverse beta decay reaction

$$\bar{\nu}_e + p \rightarrow e^+ + n \quad (1.49)$$

was used to detect the reactor $\bar{\nu}_e$ in the Bugey experiment as well as other reactor neutrino detectors. The Bugey detector used three identical 600 l segmented detectors, which were filled with ^6Li loaded (0.15%) scintillator. There are two advantages of ^6Li loaded scintillator, the neutron capture time in the scintillator is reduced to 30 μsec , and the α particle can be distinguished using pulse shape discrimination.

The combined result of the three detectors gives no evidence for oscillations, the ratio of the observed to the prediction in the no oscillation case is $0.987 \pm 0.014(\text{syst}) \pm 0.027(\sigma_{V-A})$ [54]. The sensitivity for Δm^2 is down to 10^{-2} eV^2 .

CHOOZ

The CHOOZ experiment [55] measured reactor neutrinos from April 1997 to July 1998. The experiment looked at neutrinos coming from two pressurized-water reactors with a total thermal power of 8.5 GW, in the Chooz power station in northern France, in the Ardennes region. The detector was located in a tunnel protected from cosmic rays by a 300 m water equivalent rock overburden, and at $\sim 1 \text{ km}$ distance from the reactors. Therefore, the sensitivity for Δm^2 was down to 10^{-3} eV^2 , an improvement of one order from the Bugey experiment. The target, 5 ton Gd loaded ($\sim 0.1\%$) liquid scintillator, was contained in an acrylic vessel. Gd loading reduces the capture time owing to its large cross section for neutron capture, and also gives rise to 8 MeV γ cascade, reducing accidental background.

The $\bar{\nu}_e$ rate is consistent with the expectation in the no oscillation case, the ratio is $1.01 \pm 0.028(\text{stat}) \pm 0.027(\text{syst})$. The detail of the oscillation analysis is given in Section 7.1.3.

Palo Verde

The Palo Verde experiment [56] was performed at the Palo Verde Nuclear Generating Station in Arizona. The nuclear power plant consists of three identical pressurized water reactors with a total thermal power of 11.6 GW. The detector was located in an underground cave with 32 m water equivalent overhead, 890 m from two reactors and 750 m from the third. The segmented detector consisted of 66 acrylic cells filled with 11.3 tons of Gd loaded ($\sim 0.1\%$) liquid scintillator similar to the CHOOZ experiment.

From the analysis of the data set between September 1998 and July 2000, the ratio of the observed $\bar{\nu}_e$ interaction rate to the one expected in the no oscillation case is $1.01 \pm 0.024(\text{stat}) \pm 0.053(\text{syst})$, which is consistent with the CHOOZ result.

KamLAND

The KamLAND experiment is a very long baseline reactor experiment, designed to explore $\bar{\nu}_e$ disappearance from reactors, at a flux-weighted average distance of 180 km. The details of the KamLAND detector are described in Chapter 2. Due to the long baseline, in the KamLAND experiment, the sensitivity for Δm^2 goes down to 10^{-5} eV^2 , which includes the Large Mixing Angle solution (LMA) to solar neutrino problem.

In December 2002, the KamLAND experiment reported the first evidence of reactor neutrino disappearance using the data collected between March 2002 and October 2002 [9]. The ratio of the number of observed events to the expected was $0.611 \pm 0.085(\text{stat}) \pm 0.041(\text{syst})$, which is inconsistent with the expected rate for standard $\bar{\nu}_e$ propagation at 99.95% C.L. The ratios of reactor neutrino experiments are summarized in Figure 1.14. The agreement with the solar neutrino solution suggests that the solar neutrino problem is caused by neutrino oscillation with parameters in the LMA.

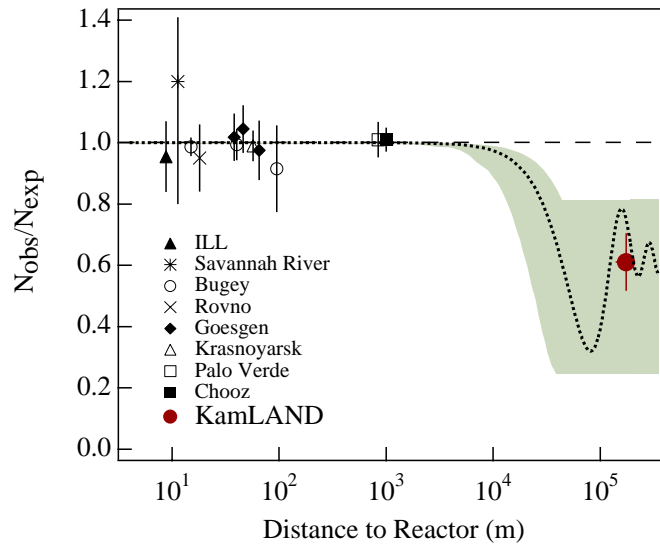


Figure 1.14: Ratio of measured to expected $\bar{\nu}_e$ flux from reactor experiments [9].

1.4 Neutrino Mass Measurement

If the neutrino oscillation scenario is correct, neutrinos are massive particles. Since the Standard Model assumes that neutrinos are massless, the study of neutrino mass gives important information for a more fundamental theory beyond the Standard Model. However, the neutrino oscillation experiments don't test the absolute mass scale. In this section, the experiments which have the potential to teach us about the absolute mass scale are introduced.

1.4.1 Cosmological Data

Massive neutrinos would contribute to the cosmological matter density. In the early universe, copious numbers of neutrinos were produced. The massive neutrinos make cluster on very large scales during matter domination. This effect changes the shape of the matter power spectrum and suppresses the amplitude of fluctuations in the CMB (cosmic microwave background). The contribution of neutrinos to the energy density of the universe depends on the sum of the neutrino masses,

$$\Omega_\nu h^2 = \frac{\sum_i m_i}{94.0 \text{ eV}} \quad (1.50)$$

where Ω_ν is the neutrino mass density relative to the critical density, and h is the Hubble constant (in units of 100 km/s/Mpc). The combined result of WMAP, CBI, ACBAR, 2dFGRS and Lyman α data provides the limit, $\Omega_\nu h^2 < 0.0076$, which corresponds to $m_\nu < 0.23 \text{ eV}$ for three degenerate neutrino species [17]. However, this limit from cosmology is complicated by the large number of correlated parameters that must be measured.

1.4.2 Semileptonic Decay

The direct measurement of neutrino mass can be achieved by the study of the neutrino momentum-energy balance in weak semileptonic decays. If the neutrino has a finite mass, the maximum electron energy gets lowered by the amount of its mass. The most sensitive neutrino mass measurement to date, involving electron type neutrinos, is based on fitting the energy spectrum of the tritium β -decay. From the results of the Troitsk experiment [18], the upper limit (95% C.L.) for effective electron anti-neutrino mass is

$$\langle m_{\nu_e} \rangle < 2.5 \text{ eV} \quad (1.51)$$

where the effective neutrino mass is defined as $\langle m_{\nu_e} \rangle = \sqrt{\sum_i |U_{ei}|^2 m_{\nu_i}^2}$. The experimental uncertainty is mainly caused by the background and energy resolution. The KATRIN experiment is a next generation tritium beta-decay experiment scaling up the size and precision of previous experiments by an order of magnitude to reach a sensitivity to $\langle m_{\nu_e} \rangle$ near 0.2 eV [57].

For the masses of ν_μ and ν_τ , the measurement of the muon momentum in the pion decay $\pi^+ \rightarrow \mu^+ + \nu_\mu$ and the shape of the spectrum of decay products of the τ lepton give the upper limits [19, 20]

$$\langle m_{\nu_\mu} \rangle < 0.17 \text{ MeV} \quad (1.52)$$

$$\langle m_{\nu_\tau} \rangle < 18.2 \text{ MeV}. \quad (1.53)$$

Both limits are much larger than the limits derived from cosmology.

1.4.3 Supernova 1987A

From the neutrino signal of supernova 1987A, the spread of arrival times related to the neutrino mass can be evaluated. Recently, a Bayesian analysis provides the upper limit (95% C.L.) [58] for effective electron anti-neutrino mass

$$\langle m_{\nu_e} \rangle < 5.7 \text{ eV} \quad (1.54)$$

using an improved theoretical model of the supernova.

1.4.4 Double Beta Decay

If neutrinos are Majorana particles ($\nu_i = \bar{\nu}_i$), there is a possibility that the absolute neutrino mass scale is measured by the ‘neutrino-less double beta decay’ ($0\nu\beta\beta$), which is written as

$$A \rightarrow B + \beta + \beta \quad (1.55)$$

and its reaction violates the lepton-number conservation law. In the search for double beta decay, one uses nuclei where the single beta decay is energetically forbidden. The $0\nu\beta\beta$ is dominated by a neutrino exchange mechanism, so its rate is proportional to $\langle m_{\beta\beta} \rangle^2$,

$$[T_{1/2}^{0\nu}]^{-1} = G^{0\nu}(E_0, Z) |M^{0\nu}|^2 \langle m_{\beta\beta} \rangle^2 \quad (1.56)$$

where $G^{0\nu}(E_0, Z)$ is the phase-space factor, $M^{0\nu}$ the nuclear matrix element, $\langle m_{\beta\beta} \rangle$ the effective Majorana mass for $0\nu\beta\beta$. In the case of Majorana particles, the Maki-Nakagawa-Sakata (MNS) matrix (Eq. (1.4)) is written as

$$U = \begin{pmatrix} c_{12}c_{13} & s_{12}c_{13} & s_{13}e^{-i\delta} \\ -s_{12}c_{23} - c_{12}s_{23}s_{13} & c_{12}c_{23} - s_{12}s_{23}s_{13}e^{i\delta} & s_{23}c_{13} \\ s_{12}s_{23} - c_{12}c_{23}s_{13} & -c_{12}s_{23} - s_{12}c_{23}s_{13}e^{i\delta} & c_{23}c_{13} \end{pmatrix} \times \begin{pmatrix} e^{i\alpha_1} & 0 & 0 \\ 0 & e^{i\alpha_2} & 0 \\ 0 & 0 & 1 \end{pmatrix} \quad (1.57)$$

with the other two CP phase α_1 and α_2 . Thus the effective Majorana mass is given by

$$\langle m_{\beta\beta} \rangle = \left| \sum_i U_{ei}^2 m_{\nu_i} \right| \quad (1.58)$$

$$= \left| c_{12}^2 c_{13}^2 m_1 + s_{12}^2 c_{13}^2 m_2 e^{2i\phi_2} + s_{13}^2 m_3 e^{2i\phi_3} \right| \quad (1.59)$$

where $\phi_2 = \alpha_2 - \alpha_1$ and $\phi_3 = -\delta - \alpha_1$.

The determination of the effective Majorana neutrino mass $\langle m_{\beta\beta} \rangle$ can be achieved by the measurement of the lifetime of $0\nu\beta\beta$ nuclei using the calculation of the nuclear matrix element $M^{0\nu}$, expressed as

$$M^{0\nu} = -\frac{M_F^{0\nu}}{g_A^2} + M_{GT}^{0\nu} + M_T^{0\nu} \quad (1.60)$$

where $M_F^{0\nu}$, $M_{GT}^{0\nu}$ and $M_T^{0\nu}$ are given in [59]. The evaluation of the matrix element is difficult, because the nuclear structure is complicated, and its calculation is based on many-body approximation. To evaluate the nuclear matrix element, different groups calculated with different models of the quasiparticle random phase approximation (QRPA) or its extension. The calculation depends on the method and the model space size, so its value has an uncertainty by a factor 2 to 3. However, its calculation precision was recently significantly improved [60]. The new calculations indicate that when the strength of the particle-particle interaction is adjusted so that the $2\nu\beta\beta$ is correctly reproduced, the resulting $M^{0\nu}$ values become essentially independent of the size of the basis, and of the form of different realistic nucleon-nucleon potentials. From this improvement, the uncertainty of the nuclear matrix element for ^{76}Ge , ^{100}Mo , ^{130}Te , and ^{136}Xe is evaluated to be less than 10%. Table 1.6 shows the limits on effective Majorana neutrino mass from $0\nu\beta\beta$ experiments. The best result have been achieved in the Heidelberg-Moscow (HM) ^{76}Ge experiment. Some members of the HM collaboration have claimed evidence for $0\nu\beta\beta$, however several authors claimed a definitely weaker statistical significance. The HM results will be verified in future experiments.

In the context of three neutrinos, the neutrino mass spectrum contains two mass eigenstates separated by Δm_{SOL}^2 which explains the solar and KamLAND data, and Δm_{ATM}^2 which explains the atmospheric and K2K data. Currently, no neutrino experiments tell whether the two eigenstates separated by Δm_{SOL}^2 are at the bottom or the top of the spectrum, usually referred to, respectively, as a normal and an inverted hierarchy (Figure 1.15). Figure 1.16 shows the effective Majorana mass $\langle m_{\beta\beta} \rangle$ for $0\nu\beta\beta$ experiments, when the two possibilities of neutrino mass hierarchy are considered. In the next generation of experiments, the sensitivity to effective neutrino mass will be reach down to the order of $\sqrt{\Delta m_{ATM}^2}$. If a nonzero signal is observed, neutrinos are Majorana particles. If no signal is seen, it can be concluded either that the hierarchy is normal or that neutrinos are Dirac particles ($\nu_i \neq \bar{\nu}_i$).

Table 1.6: Experimental limits on effective neutrino mass contributing to $0\nu\beta\beta$ [61]

isotope	method	effective Majorana mass (eV)	C.L. (%)
^{130}Te	cryogenic calorimeter	$< 1.1 - 2.6$	90
^{116}Cd	$^{116}\text{CdWO}_4$ scintillator	$< 1.5 - 1.7$	90
^{76}Ge	enriched HPGe	$< 0.33 - 1.35$	90
^{136}Xe	liquid Xe scintillator	< 2.9	90
^{76}Ge	enriched HPGe	$0.39^{+0.17}_{-0.28}$	-
^{100}Mo	ELEGANT V	$< 2.1 - 4.8$	90
^{76}Ge	enriched HPGe	< 0.35	90
^{96}Zr	NEMO-2	< 23	90
^{128}Te	geo chemical	$< 1.1 - 1.5$	-
^{82}Se	TPC	< 5	68
^{48}Ca	CaF_2 scintillator	< 8.3	76

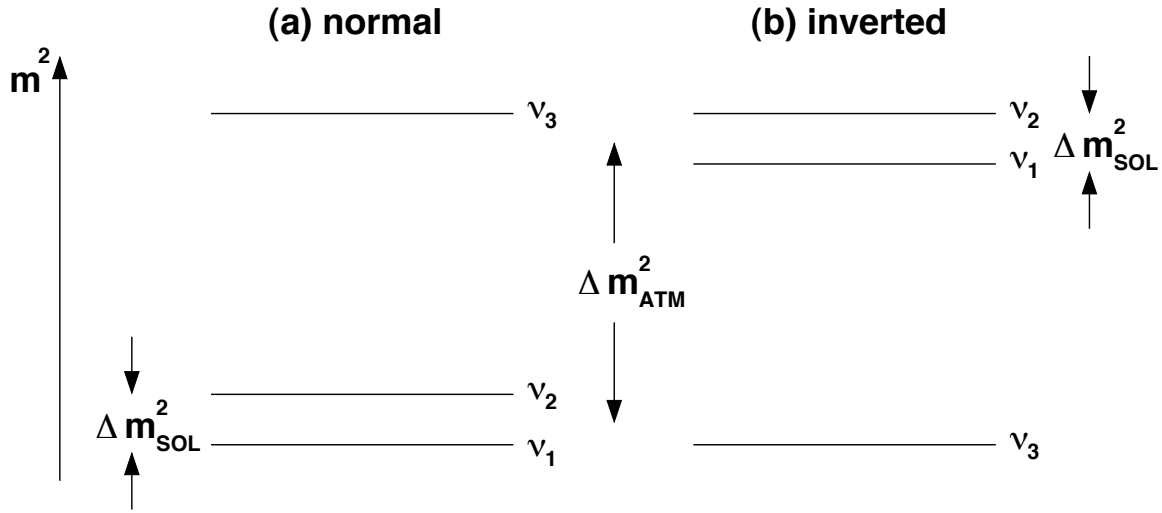


Figure 1.15: Schematic view of the neutrino mass hierarchy for the case of (a) the normal and (b) inverted.

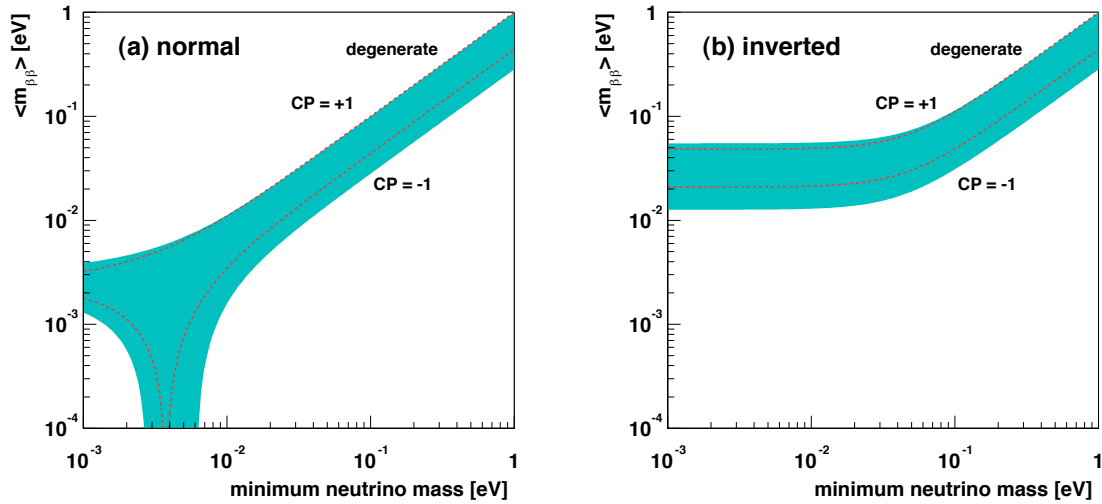


Figure 1.16: Effective Majorana mass $\langle m_{\beta\beta} \rangle^2$ as a function of the lightest neutrino for the case of (a) the normal hierarchy and (b) inverted hierarchy. The dashed lines are based on the best-fit oscillation parameters with the CP-conserving phases, $e^{2i\phi_2} = \pm 1$. In this calculation, $\sin^2 \theta_{13}$ is fixed to zero, and uncertainties for the other oscillation parameters are given in Chapter 7. The 95% C.L. are shown in the shaded regions.

1.5 Motivation

The solar and atmospheric neutrino experiments have reported a deficit of neutrinos. Their results were tested by terrestrial neutrino experiments. Most of the terrestrial experiments gave no evidence of neutrino disappearance. However long baseline experiments, K2K and KamLAND, measured deficits of neutrinos using muon neutrinos from accelerator and electron anti-neutrinos from reactors, respectively.

The solar neutrino measurement by the neutral current (NC) reaction in the SNO experiment is in good agreement with the SSM prediction. This indicates that the solar neutrinos change flavor, during their propagation from the sun to the earth, via the flavor transition process, possibly neutrino oscillation. The KamLAND experiment provides important information about the reason for the solar neutrino problem, because it has a good sensitivity to LMA, a solution of the solar neutrino oscillation. The most important element to confirm the neutrino oscillation is detecting the oscillation shape directly using the neutrino energy information. Solar neutrinos may lose the coherence effect of neutrino oscillation in various scenarios, however, the KamLAND experiment can see the oscillatory shape with high sensitivity.

When neutrino oscillation is confirmed, the next subject is the determination of the neutrino oscillation parameters. Conventionally, neutrino oscillation analysis assumes two flavor oscillation with CPT invariance, grouping neutrinos together with anti-neutrinos. However, the neutrinos actually consist of three generations, therefore, a 3-flavor oscillation analysis is more appropriate. In the KamLAND oscillation analysis, θ_{13} uncertainty contributes to the error for the determination of the oscillation parameter set, θ_{12} and Δm_{21}^2 .

Currently, θ_{13} is an unknown parameter, however, the JHF-Kamioka neutrino experiment [62] can measure the θ_{13} in high sensitivity using the search in the $\nu_\mu \rightarrow \nu_e$ appearance (Figure 1.17). That experiment can also measure the oscillation parameters Δm_{32}^2 and θ_{23} with ν_μ disappearance.

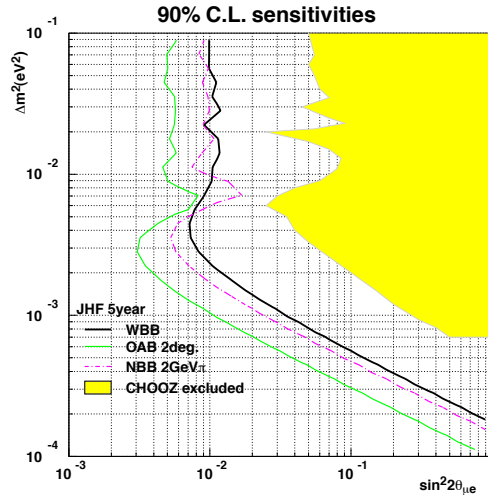


Figure 1.17: Sensitivity of the JHF-Kamioka experiment [62] for 5 years at 90% C.L.

If $\nu_\mu \rightarrow \nu_e$ appearance is observed, that experiment can test CP violation. The CP asymmetry is calculated as

$$A_{CP} = \frac{P(\nu_\mu \rightarrow \nu_e) - P(\bar{\nu}_\mu \rightarrow \bar{\nu}_e)}{P(\nu_\mu \rightarrow \nu_e) + P(\bar{\nu}_\mu \rightarrow \bar{\nu}_e)} \simeq \frac{\Delta m_{21}^2 L}{4E_\nu} \cdot \frac{\sin 2\theta_{12}}{\sin \theta_{13}} \cdot \sin \delta \quad (1.61)$$

where δ is a CP phase. In order to measure the CP violation effect at a high sensitivity, we need to measure θ_{12} and Δm_{21}^2 precisely in three neutrino scheme. Figure 1.18 shows the sensitivity for CP violation.

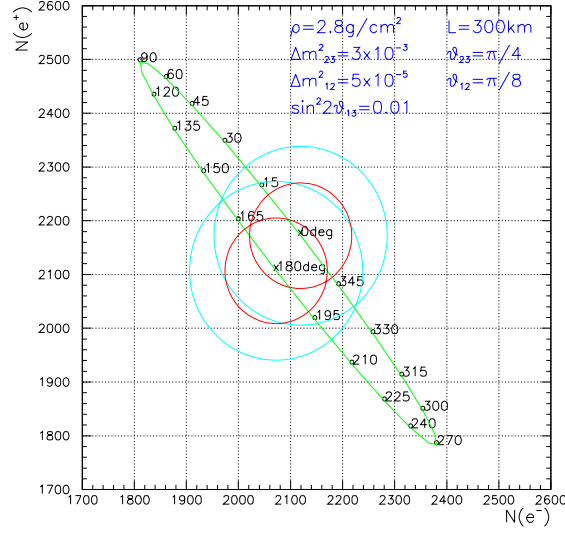


Figure 1.18: Sensitivity for CP violation at the long baseline experiment JHF-Kamioka [62].

This thesis focuses on two subjects,

1. testing the oscillatory shape from the KamLAND data to confirm neutrino oscillation,
2. measuring the neutrino oscillation parameters precisely in three generation analysis.

The deficits of solar and atmospheric neutrinos indicate the existence of two types of neutrino oscillations. The neutrino oscillation should be confirmed by the spectrum coming from the oscillatory probability (Chapter 6). The oscillation parameters, θ_{12} and Δm_{21}^2 , are measured only by the KamLAND experiment and solar neutrino experiments. θ_{13} is unknown, but limited by the global analysis of neutrino oscillation experiments (Chapter 7).

Chapter 2

Detector

The primary goal of the Kamioka Liquid Scintillator Anti-Neutrino Detector (KamLAND) experiment is a search for electron anti-neutrino oscillation [63]. The experiment is located at the site of former Kamiokande [64], and is surrounded by 53 power reactor units in Japan. The long baselines between the reactors and the detector, typically 180 km, enable KamLAND to search for the oscillation solution of solar neutrino problem using reactor anti-neutrinos under laboratory conditions.

The electron anti-neutrinos are detected via the inverse β -decay reaction, $\bar{\nu}_e + p \rightarrow e^+ + n$. The neutron is thermalized in the liquid scintillator through elastic scatterings from protons. Prompt scintillation light from the e^+ gives information on the incident $\bar{\nu}_e$ energy. Neutron capture on hydrogen emits 2.2 MeV γ -ray with ~ 200 μ sec delay and is a powerful tool for reducing background events.

In this chapter, the anti-neutrino detection method and the construction of the detector are described in detail.

2.1 KamLAND Detector

2.1.1 Design

KamLAND is located at the site of the former Kamiokande experiment [64] in Gifu Prefecture, Japan. The detector is in a mine, 1,000 m underground from the top of Mt. Ikenoyama. Figure 2.1 shows the KamLAND detector and experimental site. The average rock overburden of 2,700 meter water equivalent reduces the cosmic-ray muon rate to 0.34 Hz in the inner detector volume. The detector consists of 1,000 ton of ultra-pure liquid scintillator (LS) contained in a transparent nylon-based balloon suspended in non-scintillating oil (Figure 2.2). The balloon is a 13-m-diameter plastic spherical balloon made of 135- μ m-thick transparent nylon/EVOH (Ethylene vinyl alcohol copolymer) composite film and is suspended with Kevlar ropes to keep a spherical shape. The LS is prepared with 80.2% by volume of dodecane, 19.8% pseudocumene (1,2,4-Trimethylbenzene), and 1.52 g/liter of PPO (2,5-Diphenyloxazole) as a fluor. A mixture of dodecane and isoparaffin oils is filled between the balloon and the 18-m-diameter spherical stainless-steel containment vessel to shield the LS from external radiations. External γ -rays coming from radioactive impurities, especially ^{208}Tl and ^{40}K , contained isotopes in detector

materials and surrounding rock. To reduce a load on the balloon, the specific gravity of the buffer oil is adjusted to be 0.04% less than that of the LS.

Radiation energy loss of particles traversing the LS will excite the scintillator, causing it to emit fluorescence (scintillation light). This light is detected by 1,879 photomultiplier tubes (PMTs), mounted on the inner surface of the containment vessel. The PMT array includes 1,325 specially developed fast PMTs with 17-inch-diameter photocathodes and 554 older Kamiokande 20-inch PMTs. In the earlier period of KamLAND, only the 17-inch PMTs corresponding to 22% photo-cathode coverage were used. On February 27, 2003, the detector was upgraded by commissioning the 20-inch PMTs, increasing the photo-cathode coverage from 22% to 34% and improving the energy resolution from $7.3\%/\sqrt{E(\text{MeV})}$ to $6.2\%/\sqrt{E(\text{MeV})}$. This is the inner detector (ID).

The containment vessel is surrounded by a 3.2 kton water-Cherenkov detector with 225 20-inch PMTs. The outer detector (OD) absorbs γ -rays and neutrons from the surrounding rock and acts as a veto counter for cosmic-ray muons. The top region of the detector called ‘chimney’ has several functions, such as supporting the balloon straps, the circulation line from the vessels to the purification system, and entrance of calibration devices into the LS. There are various special veto counters around the chimney to make up for a short of the water shield by the OD. The additional PMTs in the chimney region are 16 8-inch PMTs and 6 5-inch PMTs.

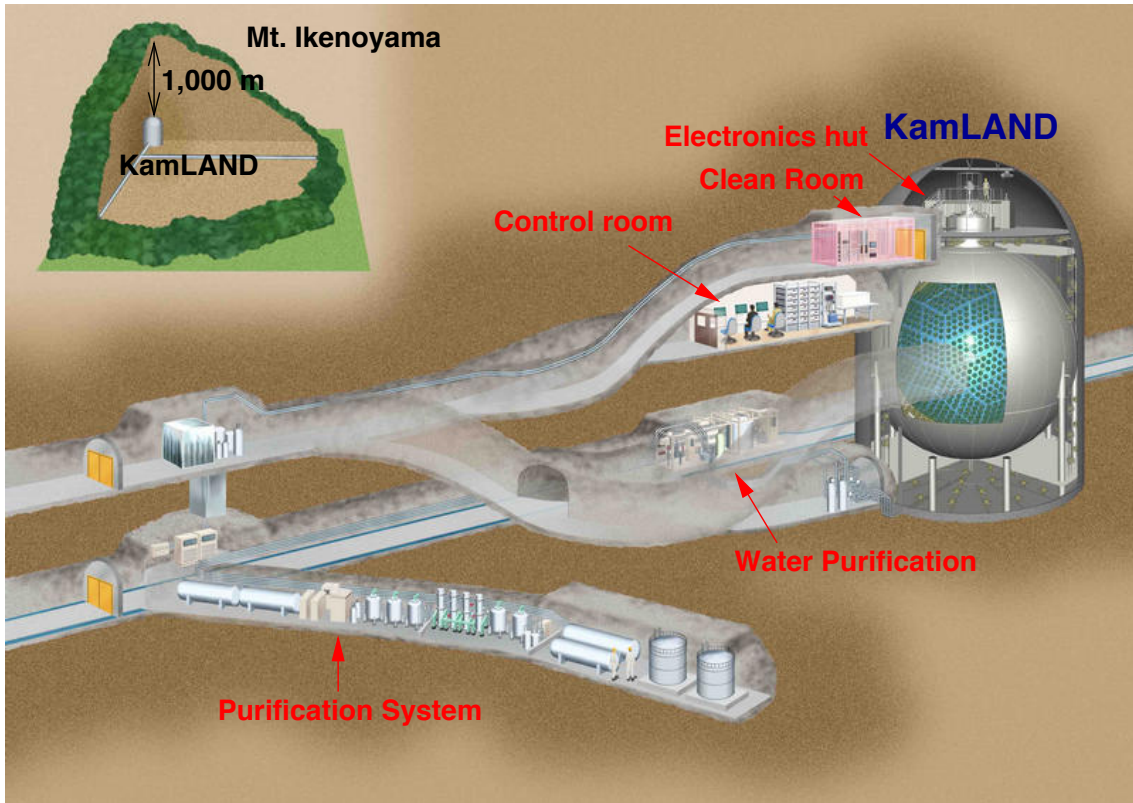


Figure 2.1: The KamLAND detector and experimental site.

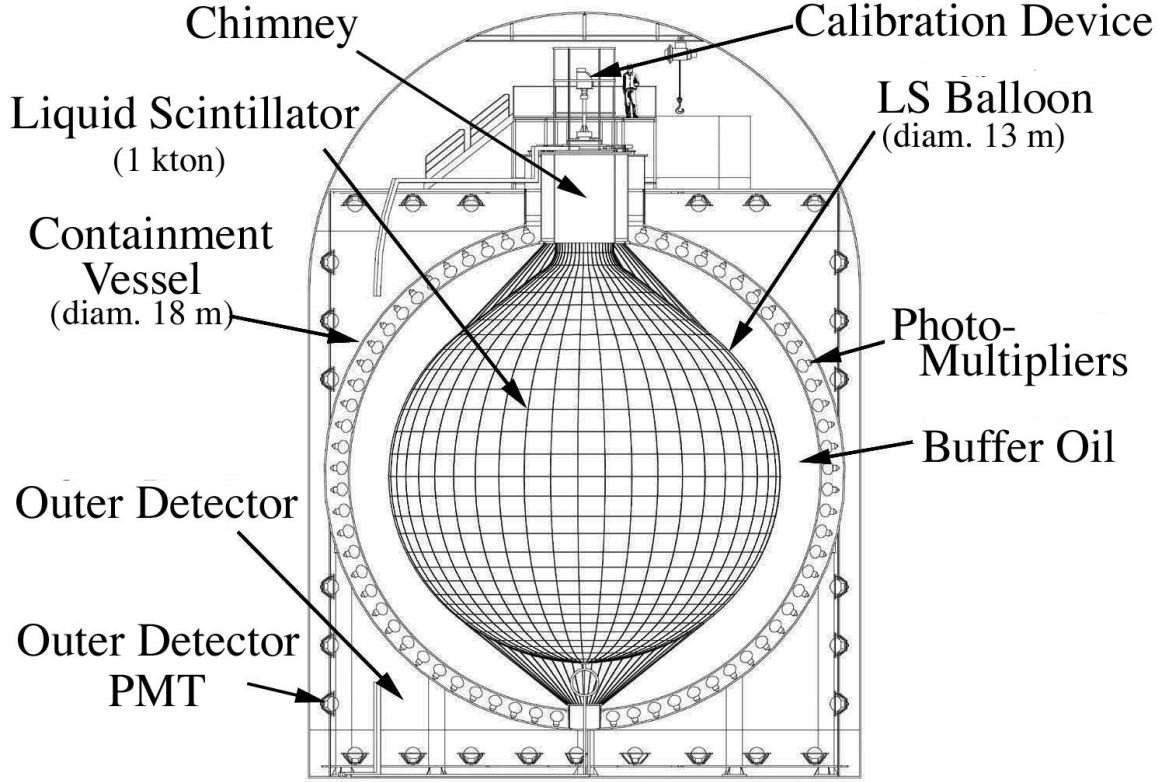


Figure 2.2: Schematic diagram of the KamLAND detector.

2.1.2 Anti-Neutrino Detection

The inverse β -decay reaction,

$$\bar{\nu}_e + p \rightarrow e^+ + n \quad (2.1)$$

is utilized to detect $\bar{\nu}_e$'s with energies above 1.8 MeV. The neutron emitted in the reaction is thermalized in the liquid scintillator through repeated elastic scatterings from protons. After $\sim 200 \mu\text{sec}$, the neutron capture reaction

$$n + p \rightarrow d + \gamma \ (2.22\text{MeV}) \quad (2.2)$$

generate a 2.22 MeV γ -ray.

In the limit where nucleon mass is taken to be infinite, i.e., zeroth order in $1/M$, the positron energy is [65][66]

$$E_e^{(0)} = E_\nu - \Delta, \quad (2.3)$$

where $\Delta = M_n - M_p$. The differential inverse beta decay cross section at this order is

$$\left(\frac{d\sigma}{d\cos\theta} \right)^{(0)} = \frac{\sigma_0}{2} \left[(f^2 + 3g^2) + (f^2 - g^2)v_e^{(0)} \cos\theta \right] E_e^{(0)} p_e^{(0)}, \quad (2.4)$$

where $p_e = \sqrt{E_e^2 - m_e^2}$ is the positron momentum and $v_e = p_e/E_e$ is its velocity, $f = 1.0$ and $g = 1.267$ are the vector coupling constant and the axial-vector coupling constant respectively. The overall factor σ_0 , including the energy-independent inner radiative corrections, is

$$\sigma_0 = \frac{G_F^2 \cos^2 \theta_C}{\pi} (1 + \delta_{inner}^{rad}), \quad (2.5)$$

where $\delta_{inner}^R \simeq 0.024$. This gives the standard result for the total cross section,

$$\sigma_{tot}^{(0)} = \sigma_0 (f^2 + 3g^2) E_e^{(0)} p_e^{(0)} \quad (2.6)$$

$$= 0.0952 \left(\frac{E_e^{(0)} p_e^{(0)}}{1 \text{ MeV}^2} \right) \times 10^{-42} \text{ cm}^2. \quad (2.7)$$

On the other hand the decay rate of neutron is similarly influenced by the energy independent inner radiative corrections. Consequently, the total cross section can also be expressed as

$$\sigma_{tot}^{(0)} = \frac{2\pi/m_e^5}{f_{p.s.}^R \tau_n} E_e^{(0)} p_e^{(0)}, \quad (2.8)$$

where τ_n is the measured neutron lifetime and $f_{p.s.}^R = 1.7152$ is the phase space factor, including Coulomb, weak magnetism, recoil, and outer radiative corrections.

At the first order in $1/M$, the positron energy depends on its scattering angle and is

$$E_e^{(1)} = E_e^{(0)} \left[1 - \frac{E_\nu}{M} (1 - v_e^{(0)} \cos \theta) \right] - y^2/M, \quad (2.9)$$

where $y^2 = (\Delta^2 - m_e^2)/2$, and M is the average nucleon mass. The differential cross section to the first order is:

$$\left(\frac{d\sigma}{d\cos\theta} \right)^{(1)} = \frac{\sigma_0}{2} \left[(f^2 + 3g^2) + (f^2 - g^2) v_e^{(1)} \cos \theta \right] E_e^{(1)} p_e^{(1)} - \frac{\sigma_0}{2} \left[\frac{\Gamma}{M} \right] E_e^{(0)} p_e^{(0)}, \quad (2.10)$$

where

$$\Gamma = 2(f + f_2)g \left[(2E_e^{(0)} + \Delta)(1 - v_e^{(0)} \cos \theta) - \frac{m_e^2}{E_e^{(0)}} \right] \quad (2.11)$$

$$+ (f^2 + g^2) \left[\Delta(1 + v_e^{(0)} \cos \theta) + \frac{m_e^2}{E_e^{(0)}} \right] \quad (2.12)$$

$$+ (f^2 + 3g^2) \left[(E_e^{(0)} + \Delta) \left(1 - \frac{1}{v_e^{(0)}} \cos \theta \right) - \Delta \right] \quad (2.13)$$

$$+ (f^2 - g^2) \left[(E_e^{(0)} + \Delta) \left(1 - \frac{1}{v_e^{(0)}} \cos \theta \right) - \Delta \right] v_e^{(0)} \cos \theta, \quad (2.14)$$

and the anomalous nucleon isovector magnetic moment is defined with $f_2 = \mu_p - \mu_n = 3.706$.

The total cross section of the inverse β -decay reaction $\bar{\nu}_e + p \rightarrow e^+ + n$ to $O(1/M)$ is then given by

$$\sigma(E_{\bar{\nu}_e}) = \left[\int_{-1}^1 \left(\frac{d\sigma(E_{\bar{\nu}_e})}{d\cos\theta} \right)^{(1)} d\cos\theta \right] \cdot (1 + \delta_{outer}^{rad}), \quad (2.15)$$

where δ_{outer}^{rad} are the energy-dependent outer radiative corrections [67]. The energy threshold for this reaction in the laboratory frame is

$$E_{\bar{\nu}_e}^{thr} = \frac{(M_n + m_e)^2 - M_p^2}{2M_p} = 1.806 \text{ MeV}. \quad (2.16)$$

The total cross section as a function of neutrino energy is shown in Figure 2.3.

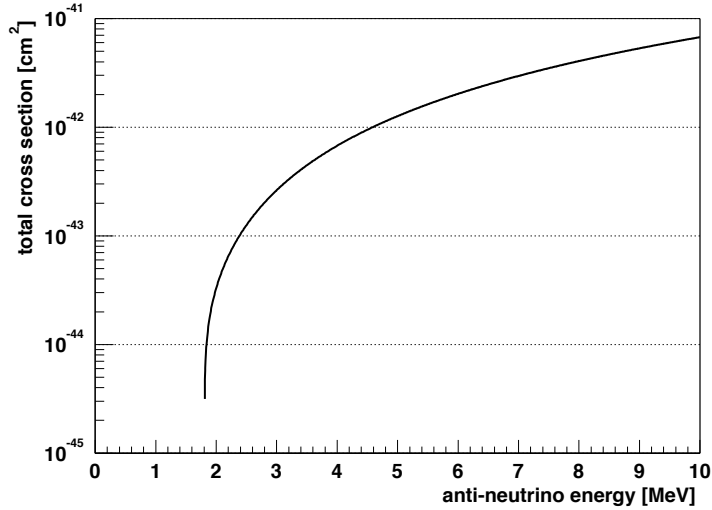


Figure 2.3: Total cross section of the inverse β -decay reaction $\bar{\nu}_e + p \rightarrow e^+ + n$.

2.2 Purification System

The KamLAND detector uses the delayed coincidence technique for anti-neutrino detection. Radioactive impurities may potentially become backgrounds, as accidental coincidence or as correlated events. The typical event rate for reactor anti-neutrinos is ~ 1 event/day. To reduce the background event rates to < 0.1 event/day, concentrations of ^{238}U , ^{232}Th , and ^{40}K should be $< 10^{-14}$ g/g, $< 10^{-14}$ g/g and $< 10^{-15}$ g/g, respectively.

Figure 2.4 shows a schematic view of the purification system. The purification system consists of two main devices, a water extraction tower and a N_2 purge tower. In water extraction, liquid scintillator is mixed with purified water. Metal atoms including radioactive isotopes such as ^{238}U , ^{232}Th , and ^{40}K are removed by water because metal ions are many order of magnitude more soluble in water than in hydrocarbon molecules. The water purified LS is sent to the

N_2 purge tower. The small amount of dissolved water in the LS is removed with N_2 gas. As an added benefit, the N_2 purge tower also removes O_2 dissolved in the LS which quenches scintillation light output. Finally, three filters are used for removing any remaining dust. These water extraction, nitrogen bubbling and filtration methods were used to purify both the LS and buffer oil.

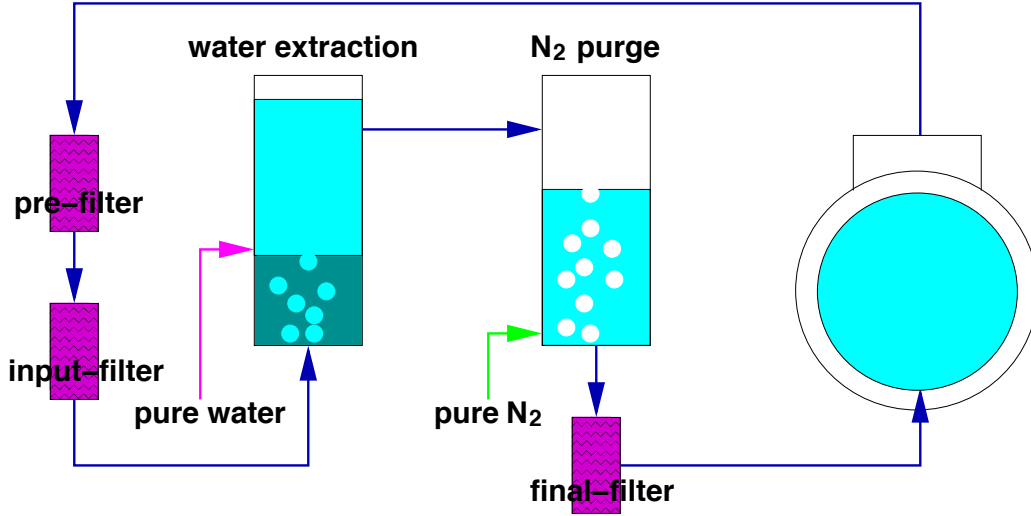


Figure 2.4: Schematic view of the purification system.

2.3 Liquid Scintillator and Buffer Oil

The KamLAND detector has 1,000 ton of ultra-pure liquid scintillator in the center. The large number of target protons makes it possible to test disappearance of reactor anti-neutrinos with high statistics. However, in order to have high sensitivity to Δm^2 , and therefore test neutrino oscillation, high energy resolution is essential. The LS must have high light output, high optical transparency, low radioactive impurity level and long term stability. In KamLAND, hand-made LS was employed for cost reduction. Its composition is 80.2% normalparaffin (Dodecane: $C_{12}H_{26}$), 19.8% pseudocumene (1,2,4-Trimethylbenzene: C_9H_{12}), and 1.52 g/liter of PPO (2,5-Diphenyloxazole: $C_{15}H_{11}NO$).

$$\text{Normalparaffin}(80.2\%) + \text{Pseudocumene}(19.8\%) + \text{PPO}(1.52\text{g/l}) \quad (2.17)$$

Light yield depends on its transparency as well as light output. Mixture ratio of normalparaffin to pseudocumene is adjusted to obtain the maximum light yield for central events [68]. The actual light yield is ~ 300 p.e./MeV (500 p.e./MeV) with 17-inch PMTs(17-inch + 20-inch PMTs) at center. Attenuation length of the LS was measured by using a dye-laser as ~ 10 m at

400 nm wavelength [68]. The light output is 49% anthracene (8,300 photons/MeV). Designed parameters and actual values of LS are shown in Table 2.1.

Table 2.1: Liquid scintillator parameters [69]

parameter	design value	actual value
temperature [$^{\circ}\text{C}$]	~ 12	11.5
specific density [g/cm^3] @ 15°C	0.778	0.77754 ± 0.00010
H/C ratio	1.902	1.969
refractive index @ $\lambda=590\text{nm}$, 14°C	1.44	1.44087 ± 0.00015
light yield [p.e./MeV]		
(i) 17-inch PMTs	~ 250	~ 300 @ center
(ii) 17-inch PMTs + 20-inch PMTs	~ 400	~ 500 @ center
time response parameters $R(t) = a/\tau_a \exp(-t/\tau_a) + b/\tau_b \exp(-t/\tau_b)$		
a	0.86	0.69
b	0.14	0.31
τ_a	6.9	4.0
τ_b	8.8	8.6
neutron capture time [μsec]	~ 212	211.2 ± 2.6
radiation length [cm]	18	—
flash point [$^{\circ}\text{C}$]	64	—
thermal expansion coefficient [$/^{\circ}\text{C}$]	-0.00095	—
kinetic viscosity @ 30°C [cSt]	1.4	—

The buffer oil surrounding the liquid scintillator reduces external γ -ray backgrounds from the radioactive impurities in the detector material like stainless tank and PMTs or in surrounding rock containing ^{208}Tl and ^{40}K . Specific gravity of the buffer oil is adjusted to be 0.04% less than that of the LS so that a load on the balloon is safely acceptable. For this purpose, the buffer oil is a mixture of mineral oils, normalparaffin ($\text{C}_{12}\text{H}_{26}$) and isoparaffin ($\text{C}_n\text{H}_{2n+2}$, $n \sim 14$). The composition ratio of normalparaffin to isoparaffin is 53 : 47.

The index of refraction of liquid scintillator, buffer oil and acrylic boards are shown in Figure 2.5. The speed of light for liquid scintillator and buffer oil are evaluated from this wavelength-dependence.

2.4 PMT

The KamLAND detector has 1,325 specially developed fast photomultipliers (PMTs) with 17-inch-diameter photocathodes and 554 PMTs with 20-inch-diameter photocathodes. The schematic views of the 17-inch PMT and 20-inch PMT are shown in Fig 2.6. The photocathode receives scintillation light and emits photoelectrons. Timing resolution becomes worse in a process of electron amplification and the different path length of photo-electron tracks due

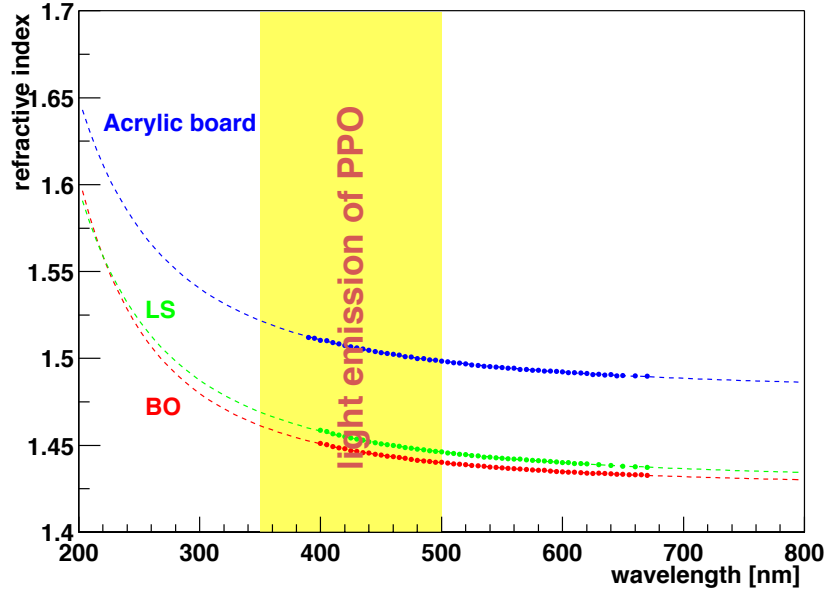


Figure 2.5: Wavelength-dependence of the index of refraction of liquid scintillator, buffer oil and acrylic boards at 14°C. The dots indicate the data, and the dashed lines indicate the extrapolation by fitting. The wavelength of PPO light emission is 350 ~ 500 nm corresponding to an index of refraction 1.44 ~ 1.47 for liquid scintillator. The speed of light is defined by the group velocity, which is the propagation speed of energy. In a dispersive medium, group velocity is slower than the phase velocity. Therefore, the speed of light in liquid scintillator is 19 ~ 20 cm/nsec.

to the large PMT size. By limiting the photon acceptance area to the central 17 inches and replacing the original Venetian-blind dynode with a line-focus type, the transit time spread (TTS) is significantly improved from ~ 5.5 nsec (FWHM) to ~ 3 nsec (FWHM), and the peak-to-valley ratio (P/V ratio) is improved from ~ 1.5 to ~ 3.

A magnetic field affects the electron trajectory and thus the PMT gain. Its effect is less than 20% in a magnetic field below 50 mGauss. In KamLAND, a set of compensating coils was installed in the cavern to cancel the Earth's magnetic field (~ 500 mGauss) to a level well below the limit of 50 mGauss necessary for proper operation of the PMTs. Figure 2.7 shows the quantum efficiency as a function of the wavelength. A typical value of the quantum efficiency is about 22% from approximately 350 nm to 400 nm. The total photo-cathode coverage is 22% for 17 inch PMTs, and it increases to 34% when the 20 inch PMTs are included.

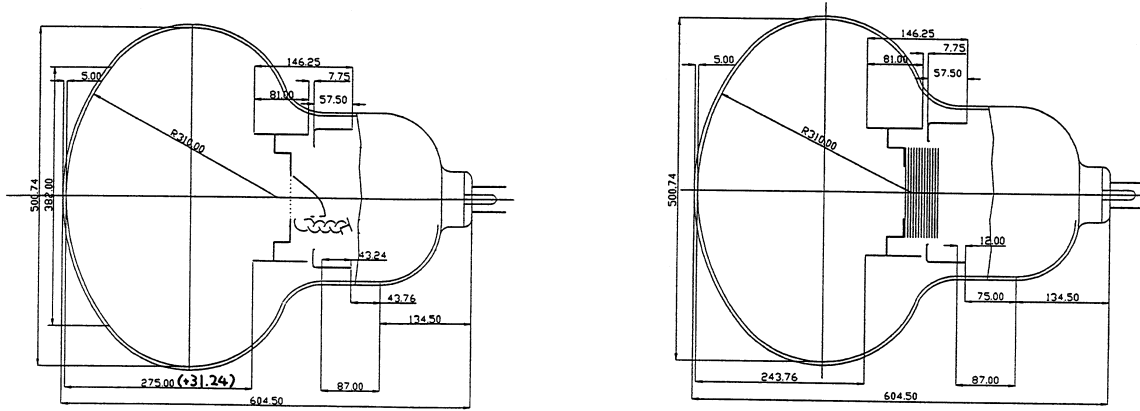


Figure 2.6: Schematic view of the 17-inch and 20-inch PMTs.

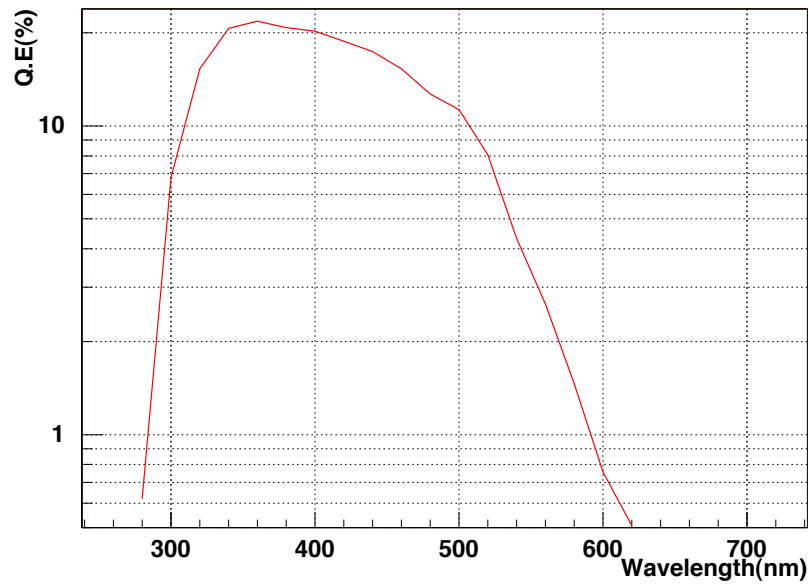


Figure 2.7: Quantum efficiency of the KamLAND PMTs.

2.5 Front-End Electronics

KamLAND has an electronics system called ‘Front-End Electronics’, or FEE (Figure 2.8). The electronics are based on the Analog Transient Waveform Digitizer (ATWD). The ATWD has an array of condensers, and it maintains waveform information in an analog form. When each discriminator is triggered, the waveform is captured for 175 nsec. If global trigger is issued, the waveform is digitized within 25 μ sec. In order to reduce deadtime during the analog-digital conversion (A/D conversion), FEE has two sets of ATWD, A and B, for each PMT channel. Moreover, the PMT signal is divided into three gains, high gain, medium gain, low gain in each ATWD, in order to extend the dynamic range of PMT signals.

- High gain channel
collect 20 times amplified waveforms in order to detect single photo-electron signals.
- Medium gain channel
collect 4 times amplified waveforms.
- Low gain channel
collect 0.5 times amplified waveforms, large signal generated by muons are detected in this gain.

The lower gain channels get enabled when the higher gain channels are saturated. The discriminator threshold is adjusted to about 1/3 p.e. pulse height. The discriminator generates an 125 nsec pulse, and the number of triggered discriminators is called the ‘Nsum’ and is calculated by the trigger-system in real-time. Global triggers are issued based on the ‘Nsum’ information.

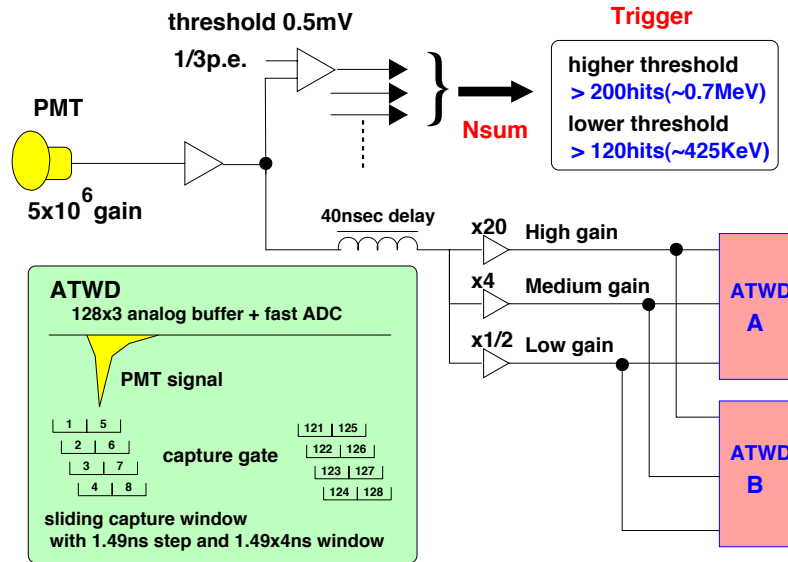


Figure 2.8: Schematic diagram of the Front-End Electronics readout system.

2.6 Trigger System

The trigger decision is based on the hit information (Nsum) from the FEE board. When a global trigger is issued, the waveforms are digitized only for hit channels. Normal data acquisition has two types of global trigger related to the inner detector, called the ID prompt trigger and ID delayed trigger. The prompt trigger threshold is set at 200 hits corresponding to about 0.7 MeV. The delayed trigger threshold is lowered to 120 hits for 1 msec after the prompt trigger. The delayed trigger is mainly used to study of low energy backgrounds such as uranium and thorium. In the outer detector, the number of hit PMTs is counted separately at top, upper side, lower side and bottom regions. Their nsum thresholds are 6, 5, 6 and 7 hits, respectively.

ID Nsum history is recorded while the ID nsum exceeds a particular threshold for every 25 nsec up to a maximum of 200 nsec (8 records). The maximum Nsum in the history is called ‘NsumMax’. This history data doesn’t require waveform digitization and a continuous data acquisition with a very low threshold is possible. Moreover, the trigger system is programmable and computer controllable. Appropriate parameters and thresholds are set run by run. Details of built-in trigger types are described in Appendix A.

In the reactor $\bar{\nu}_e$ analysis, high threshold events ($\text{NsumMax} \geq 200$) are used. The delayed trigger is useful to estimate an efficiency in energy-basis as follows,

$$(\text{trigger efficiency}) = \frac{(\text{number of high threshold events with } \text{NsumMax} \geq 200)}{(\text{number of low threshold events with } \text{NsumMax} \geq 120)} \quad (2.18)$$

and it is energy and position dependent. Around the high trigger threshold, there are a lot of events at various positions in the detector and the position dependence of the trigger efficiency can be studied in detail using background events. These position distribution of background events is almost uniform in 5.5-m-radius fiducial volume and overall efficiency for the uniformly distributing neutrino signal can be obtained by just taking the overall efficiency. The efficiency is 99% at 0.86 MeV in the visible energy scale (Figure 2.9), and at 1.04, 0.84, and 0.95 MeV in the e^+ , e^- and γ energy scale (Section 3.6.5), respectively. Similarly, special low threshold runs allow the evaluation of the delayed trigger efficiency,

$$(\text{trigger efficiency}) = \frac{(\text{number of high threshold events with } \text{NsumMax} \geq 120)}{(\text{number of low threshold events with } \text{NsumMax} \geq 50)}. \quad (2.19)$$

The low threshold run is operated by a ‘prescale’ trigger. Trigger enable and disable are periodically cycled to reduce data flow rate. The delayed trigger efficiency is 99% at 0.46 MeV in the visible energy scale (Figure 2.10), and at 0.46 and 0.55 MeV in the e^- and γ energy scale, respectively.

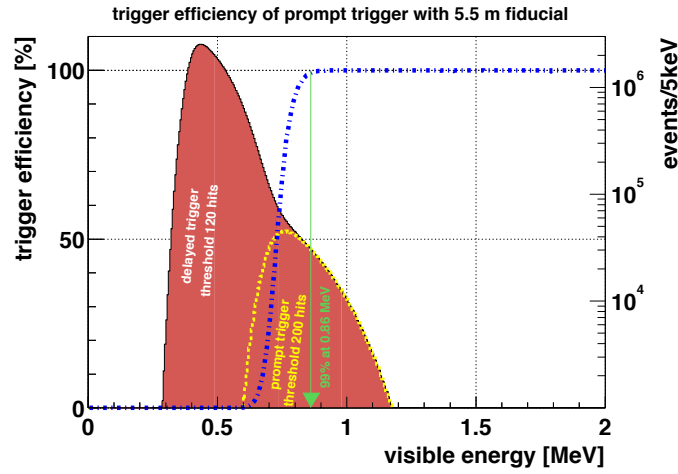


Figure 2.9: The prompt trigger efficiency within 5.5-m-radius fiducial volume (dash-dot line). Energy spectra with 200 and 120 hits trigger threshold are compared and the ratio of them gives the trigger efficiency at a given energy. A 99% efficiency is achieved at 0.86 MeV in the visible energy scale. In the e^+ , e^- and γ energy scale, its energy corresponds to 1.04, 0.84, and 0.95 MeV, respectively, where the positron energy includes the annihilation gamma energy.

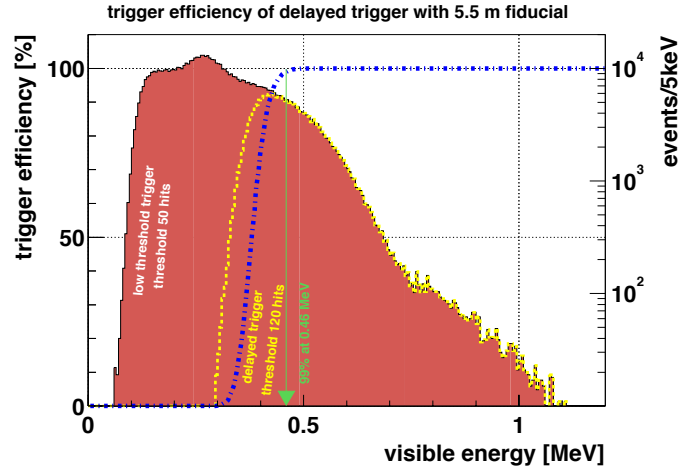


Figure 2.10: The delayed trigger efficiency within 5.5-m-radius fiducial volume (dash-dot line). Energy spectra with 120 and 50 hits trigger threshold are compared and the ratio of them gives the trigger efficiency at a given energy. A 99% efficiency is achieved at 0.46 MeV in the visible energy scale. In the e^- and γ energy scale, its energy corresponds to 0.46 and 0.55 MeV, respectively.

2.7 Calibration System

In KamLAND, various radioactive sources and a light source are deployed to calibrate the detector response. Currently, a z-axis deployment system is utilized for its purpose. A remote controlled motor lowers the source with a cable into the detector, and an electronic readout of a shaft encoder tracks the position of the source. The deployment assembly is encased within a sealed glovebox. The glovebox is purged with nitrogen gas to eliminate Rn contamination before opening the gate valve between the glove box and the detector. The following sources are used to calibrate the detector:

- radioactive source

For a study of the vertex and energy response, five radioactive sources, ^{203}Hg , ^{68}Ge , ^{65}Zn , ^{60}Co and Am-Be, are used. Details of these sources are summarized in Appendix C and D. Each source is encapsulated in stainless steel and lowered with a stainless steel weight (Figure 2.11 and Figure D.1). The MC simulations show that a shadowing effects from the weight are less than 0.2% and the energy loss of γ -rays in the capsule is less than 0.05%, but the Am-Be source with a large moderator has an effect up to 2.6%.

- dye-laser (diffusion ball)

A dye-laser calibration is performed in order to adjust PMT timing. Dye-laser pulses are sent to the center of the detector via a optical fiber, and the photons spread uniformly in a diffusion ball made of MgO-particle-contained acrylic chip and sphere (Figure 2.12). The MgO chip is at the center of the acrylic sphere. The MgO has a high reflectance, and its concentration is 10,000 ppm and 700 ppm for the acrylic chip and sphere, respectively. It allows a simultaneous timing calibration for all PMTs with isotropic light emission. Details of the dye-laser calibration are described in Section 3.2.

These calibration are performed periodically to monitor the detector status. Most of the corrections to vertex and energy reconstruction are based on these calibration data.

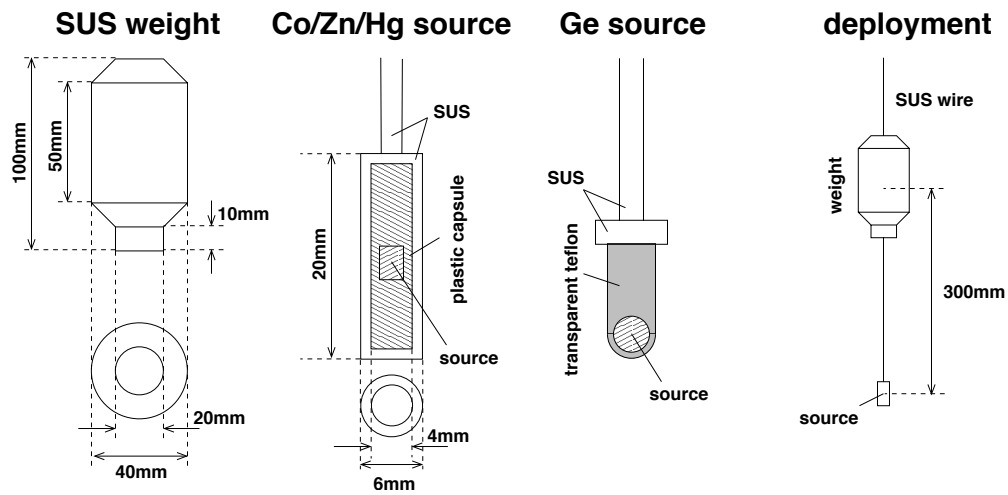


Figure 2.11: Layouts of various calibration sources.

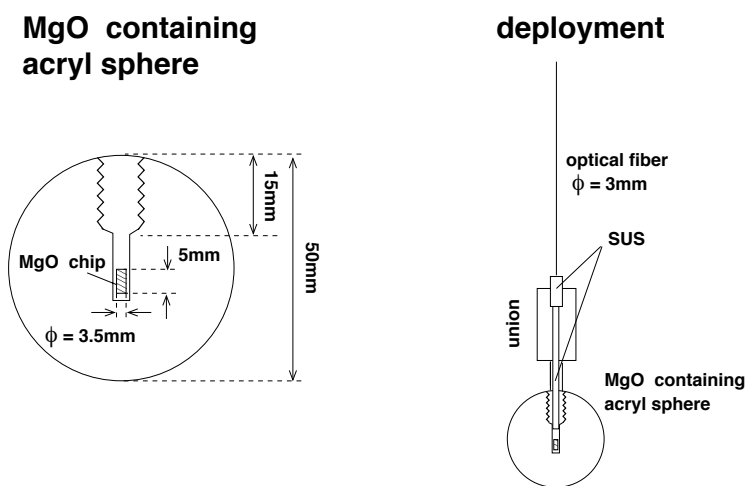


Figure 2.12: Layout of the dye-laser diffusion ball and the deployment system.

Chapter 3

Event Reconstruction and Detector Calibration

KamLAND is a liquid scintillator detector, especially designed for anti-neutrino observations via an inverse β -decay reaction. Fast scintillation emission (~ 10 nsec) makes it possible to detect physics events in real time and to reconstruct their positions and energies. Reconstructed events are classified into two types. The first is ‘point-like’ making light emission at an interaction point. Most of low energy events are classified into this category. Also reactor anti-neutrino events are point-like. Precision of the reconstructed position is related to an uncertainty of the number of target via determination of the fiducial volume. The energy reconstruction is also important for a measurement of neutrino oscillations. The second is ‘track-like’ making light emission along its long track. These events are dominated by cosmic-ray muons (~ 0.3 Hz at KamLAND). Muons cause various backgrounds for the reactor anti-neutrino observation. Therefore, identification of muons and reconstruction precision of their tracks are important.

Raw data from KamLAND contains trigger information and digital waveforms of all hit PMTs, and data flow rate is huge (~ 120 GB/day). Procedure of the event reconstruction consists of six parts,

1. waveform analysis

Digital waveforms are converted to time and charge information. The analysis consists of pedestal subtraction, waveform smoothing, baseline adjustment, and pulse peak finding (Section 3.1).

2. time and charge calibration of PMTs

Time and charge information just after the waveform analysis is not adjusted among PMTs. Transit time of each PMT is calibrated with a pulse dye-laser (Section 3.2). Charge distribution of 17-inch PMTs show one photo-electron (1 p.e.) peak in low light level. The 1 p.e. peak positions are calibrated run by run (Section 3.3). Dead or unstable PMTs (bad channel) are selected here and are masked before vertex and energy reconstructions (Section 3.4).

3. event identification

Reconstructed events are classified into two types. Most of muons penetrating liquid scintillator are identified by a high energy event selection as they cause large light output. Muons which go only through the inner buffer regions emit Cherenkov light, of which intensity is about 1/20 of scintillation light. These muons are tagged by OD hits. The high energy and OD tagged events are classified into ‘track-like’, and are reconstructed in 4.

The others are ‘point-like’ events, and vertices and energies are reconstructed in 5. and 6.

4. muon track reconstruction

Muon tracks are reconstructed using time and charge information simultaneously. This reconstruction applies only to ‘track-like’ events (Section 3.7). Also reconstruction qualities are estimated in a naive way to identify badly reconstructed events, which are mainly caused by muon bundles or stopping muons.

5. vertex reconstruction

The vertices (positions) are also reconstructed using both time and charge information (Section 3.5). This reconstruction applies only to ‘point-like’ events.

6. energy reconstruction

Energy is reconstructed from charge distribution of PMT hits (Section 3.6). The reconstructed vertex information is also necessary, because the charge distribution depends on the event position. This reconstruction applies to ‘point-like’ events. Also their quality are estimated to distinguish miss identification of ‘track-like’ events and unphysical events, such as electronics circuit noise.

Finally, the reconstruction quality is evaluated from the time and charge information of PMTs, and parameterized (Section 3.8). If the quality of a event is bad, the reconstructed vertex and energy is not reliable, and possibly the event may be an unphysical event such as the electronics noise.

3.1 Waveform Analysis

In the waveform analysis, digital waveforms are converted to time and charge information for each PMT. The total sampling time for one channel is about 190 nsec. There are 128 samples with about 1.49 nsec between each sample. Photon signals make clear pulses (Figure 3.1). Time and charge information are extracted from smoothed waveform after pedestal subtraction. Currently, all event reconstruction processes use the time of the first pulses and the charge sum of all pulses for each channel. Accuracy of the pulse timing is determined by the sampling width 1.49 nsec, which is almost comparable with the transit time spread (TTS) of 17 inch PMTs. Charge is digitized by 10 bit ADC channel and its accuracy is enough to see a single photo-electron peak.

3.1.1 Algorithm of Waveform Analysis

Individual analog buffers have particular offsets for each channel and for each sampling bin. This fine structure is subtracted from the waveform. At the beginning of each run, 50 pedestal waveforms are recorded. To estimate the pedestal value, those waveforms are averaged rejecting noise or dark hit pulses. After the pedestal subtraction, waveforms are smoothed to avoid a high frequency noise. Moreover, the baseline is readjusted in order that its baseline is centered at zero, because the baseline can move event by event and channel by channel due to aftereffects of a previous pulse. Peak in the waveform is searched with derivatives, and the ‘leading edges’ are defined as the start time bin of each pulse. In the event reconstruction, the leading edge of the first pulse is used. The ‘charge’ is defined as the total area of all pulses, and it is normalized with the mean area of a single photon pulse, as described in (Section 3.3).

3.1.2 Calibration of Time Bin Width

Clock test pulses are used for a calibration of time bin width. The calibration is performed for each channel at the beginning of each run. The time interval of the clock pulse is 25 nsec. A typical number of sampling is ~ 17 per one clock pulse (Figure 3.2). The time information for each channel is corrected by this calibration.

3.2 Timing Calibration

Transit time of each PMT is calibrated in order to cancel their differences among PMTs. A dye laser pulse (width ~ 1.2 nsec) is sent to the center of the detector via a quartz optical fiber, and illuminates PMTs (Figure 3.3). Wavelength of dye-laser is 500 nm, and absorption edge of the liquid scintillator is less than 400 nsec. That means there is no effect of reemission of the scintillator, possible cause of timing degrade. A variable neutral density filter and spherical diffuser provide uniform and variable light intensities from a single photo-electron level to about 5,000 photo-electron level. The dye laser pulse is monitored by a 2 inch PMT and its time information is used for removing a time jitter of laser flash.

Rise time of each channel is different mainly because gain of PMTs and FEE amplifiers are different each other. Correlations between time and charge are verified channel by channel using the dye laser pulse in various light intensities (Figure 3.4 and Figure 3.5). The slewing effect is fitted by a simple polynomial, and the effect is corrected (TQ-correction). Figure 3.6 and 3.6 show the time distribution in low charge pulse for 17 inch PMT and 20 inch PMT hits, respectively. After the timing calibration, sigma of the distribution was reduced, and is almost consistent with the transit time spread (TTS) of the 17 inch PMTs and 20 inch PMTs.

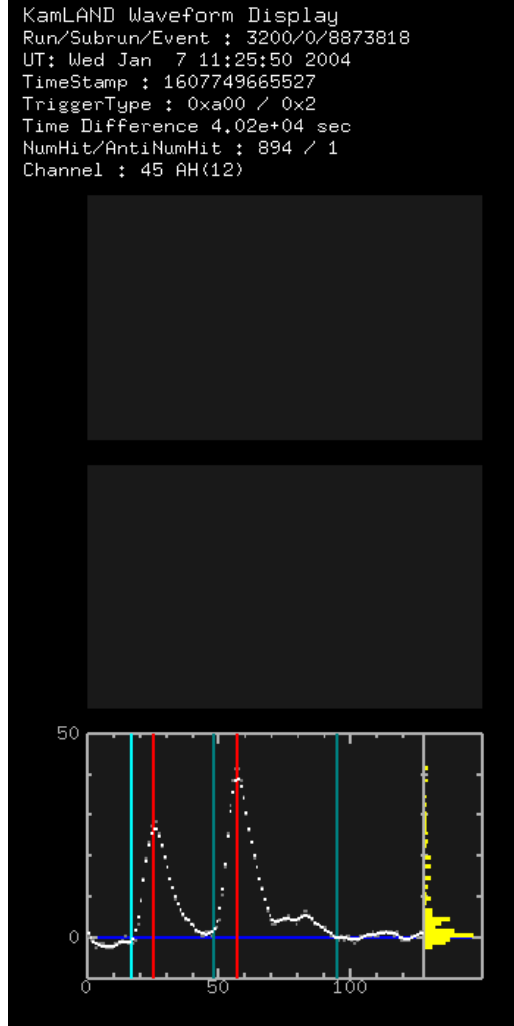


Figure 3.1: Typical waveform of a two-photon signal. The red lines indicate the analyzed peak position of the pulse, and the purple line indicates the baseline of this waveform.

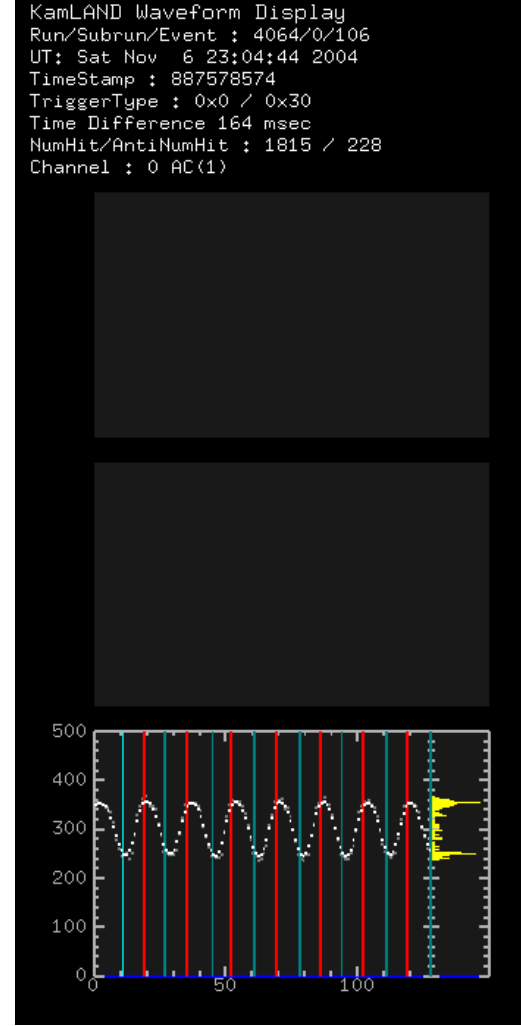


Figure 3.2: Clock test pulse for the calibration of time bin width. The time interval of the clock pulse is 25 nsec. A typical number of sampling is ~ 17 per one clock pulse.

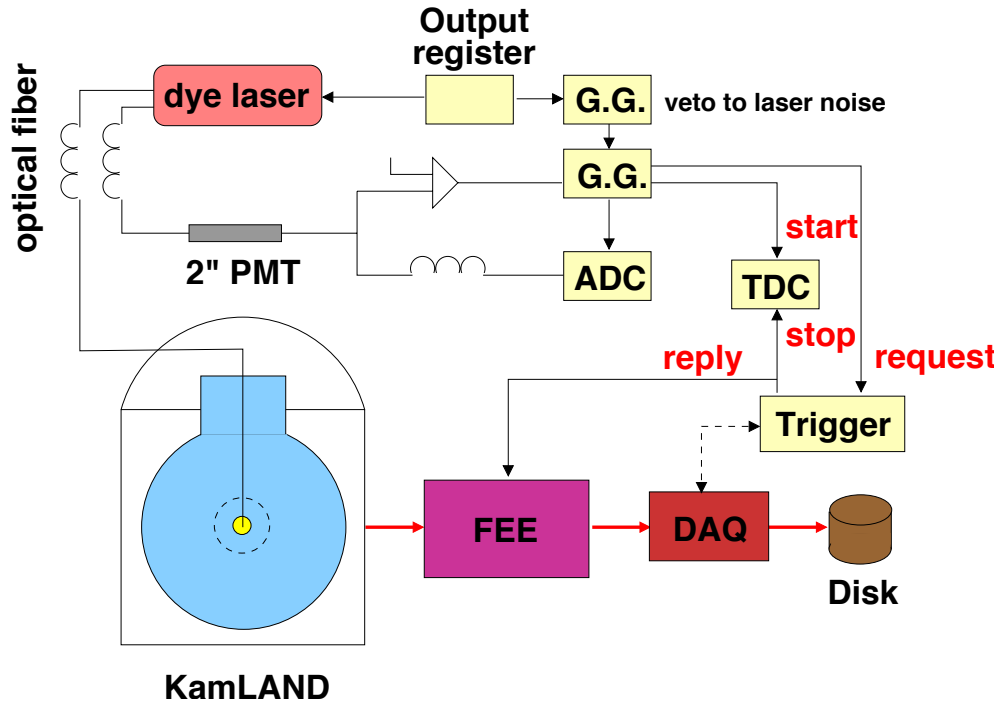


Figure 3.3: Schematic view of the timing calibration system. The dye laser pulse is sent to the detector through a optical fiber, and triggers the FEE at the same time. The wavelength of the dye-laser pulse is 500 nm, while absorption by liquid scintillator happens at less than 400 nsec. Therefore, there is no effect of reemission in the timing calibration.

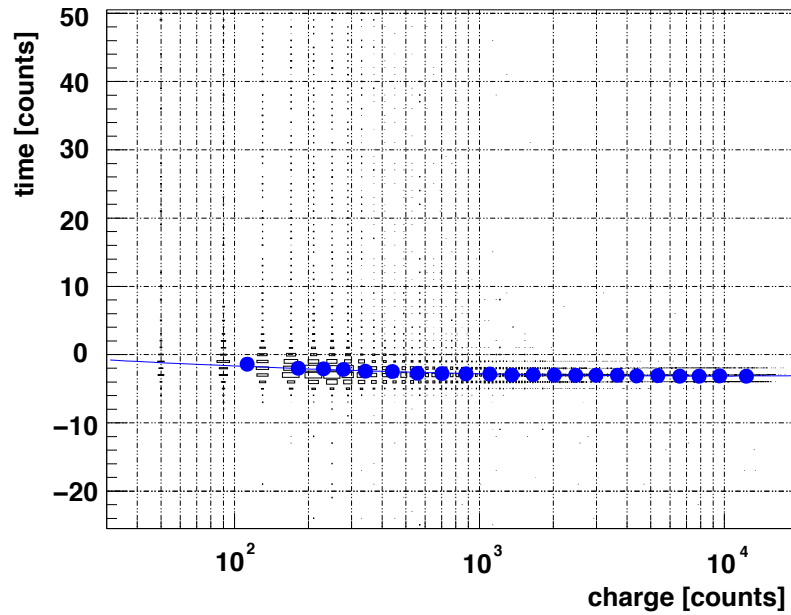


Figure 3.4: Typical correlation between time and charge for a channel of 17 inch PMT in the timing calibration data.

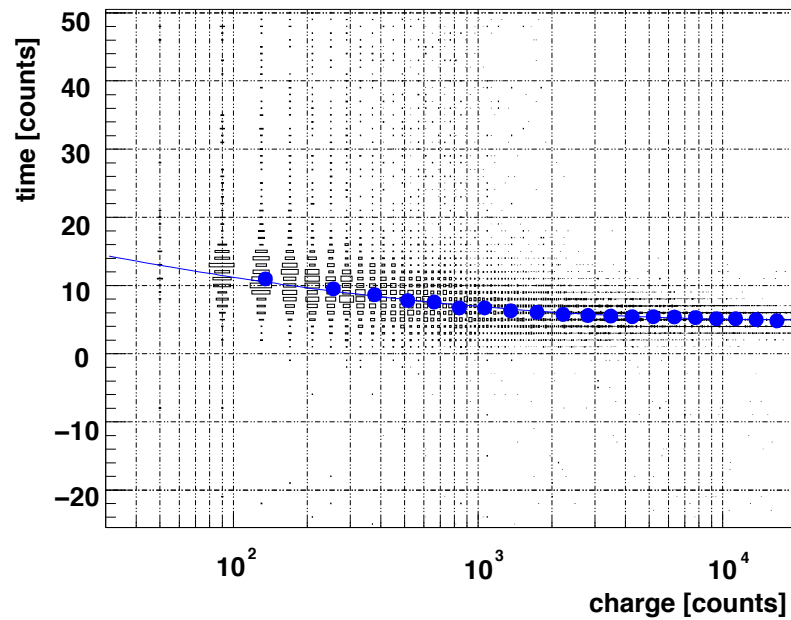


Figure 3.5: Correlation between the time and charge for a typical channel of 20 inch PMT in the timing calibration data.

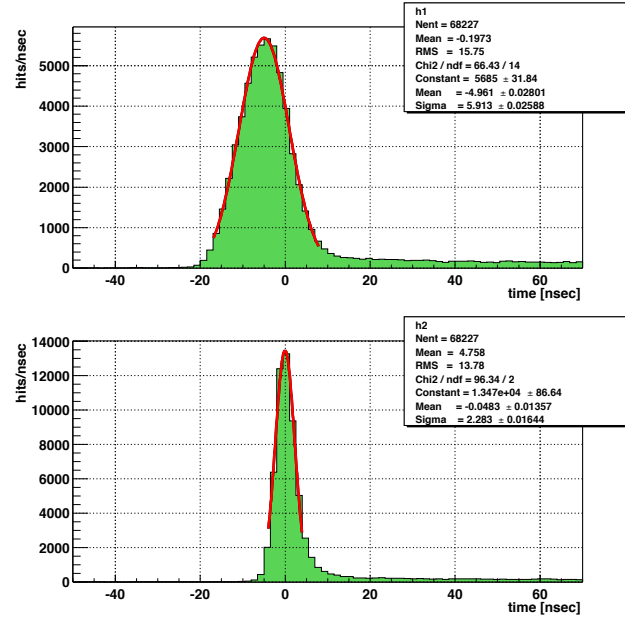


Figure 3.6: Time distribution of 17 inch PMT hits in low charge pulse before and after the timing calibration.

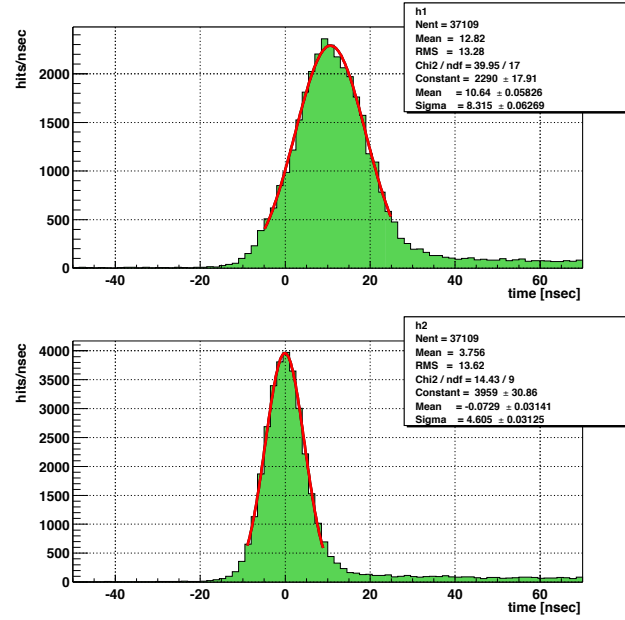


Figure 3.7: Time distribution of 20 inch PMT hits in low charge pulse before and after the timing calibration.

3.3 Gain Calibration

The single photo-electron charge is defined by area of a 1 p.e. pulse in a waveform. The 1 p.e. charge changed gradually over ~ 22 month period. The charge had to be normalized channel by channel and run by run.

The 1 p.e. distribution of the 17 inch PMTs has a clear peak, but that of the 20 inch PMTs doesn't show a peak (Figure 3.8) because of the difference of the dynode type. For gain calibration of 17 inch PMTs, correction using the 1 p.e. peak is possible. The peak is fitted with Gaussian. For gain calibration of 20 inch PMTs, relative charge at high photon level between adjacent 17 inch PMTs and each 20 inch PMT are used. Figure 3.9 shows time variation of the mean 1 p.e. charge for 17 inch PMTs and 20 inch PMTs. The gradual rise and unstable gain are compensated by this correction.

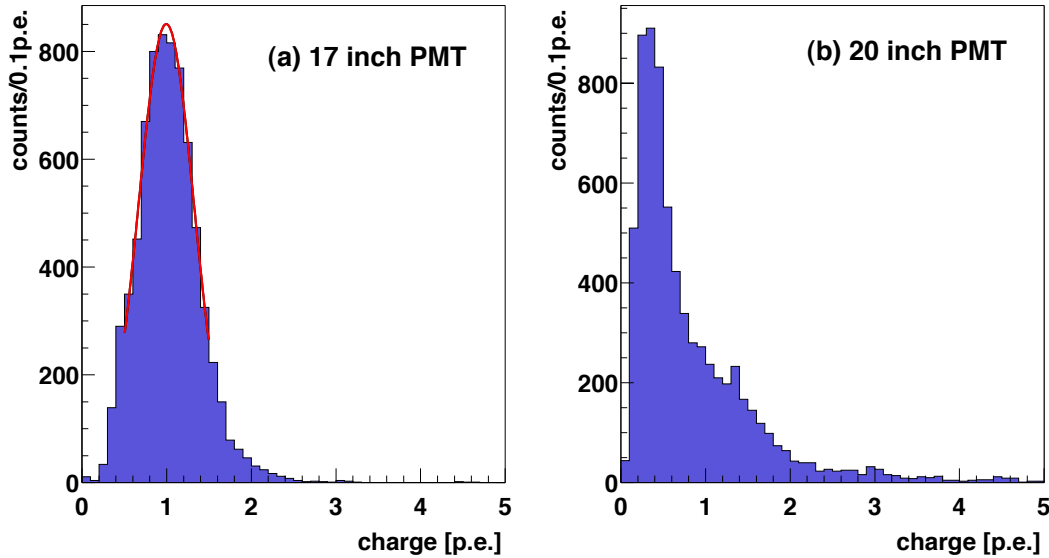


Figure 3.8: Single photo-electron distributions for the typical 17 inch PMT and 20 inch PMT. The distribution of the 17 inch PMTs with improved dynode structure has a clear peak, but that of the 20 inch PMTs doesn't.

3.4 Bad Channel Selection

There are unstable channels, which have too many hits, no hits or strange charge occasionally. These abnormal signals are caused by malfunctioning PMTs or unstable high voltage supplies for each PMT or miss connection of signal cables. There are many bad channels in the outer detector, mainly caused by dead PMTs via a water leak.

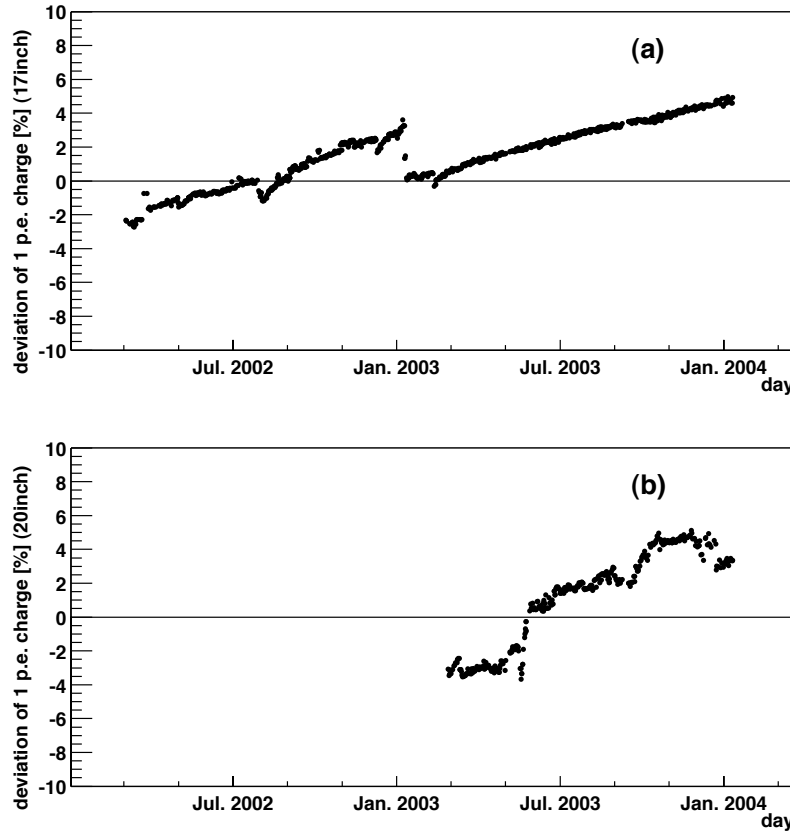


Figure 3.9: Time variation of the mean 1 p.e. charge. (a) and (b) show the 1 p.e. charge deviation of 17 inch PMTs and 20 inch PMTs respectively. The 1 p.e. charge increased gradually over ~ 22 month period for 17 inch PMTs and 20 inch PMTs. (a) The drop in the gain in January 2003 is due to the electronics (FEE) upgrade. (b) The gain rise since May 2003 is due to a gradual increase of the high voltage supplies.

These unstable channels are called as ‘bad channels’, and are masked in event reconstruction to prevent systematic biases. Selection criteria for bad channels of the inner detector are as follows,

1. Hit rate ($< 1,000$ hits / 10,000 events)
Find low response channels due to electronics failures.
2. No-hit rate ($> 1,000$ no-hits / 10,000 events)
Find no response channels due to high voltage problem.
3. Hit rate in high charge muon event (< 80 hits / 100 high-charge-muon)
Find excessively low gain channels.

4. Difference of hit rate between A-ch and B-ch ($> 22\%$ difference in 10,000 events)
Find bad-ch in which ping-pong scheme of the FEE failed.
5. Charge difference in high charge muon event

$$\frac{1}{N_i} \sum_{j=1}^{N_i} \frac{(Q_i - Q_j)^2}{Q_j} > 400 \text{ p.e.} \quad (Q_j > 0, j : \text{neighbor PMT}) \quad (3.1)$$

Find channels with a large gain difference by a comparison of the gain between neighboring channels.

6. ADC counts for 1 p.e. is too low ($< \bar{Q}_{adc} \times 1/4$) or too high ($> \bar{Q}_{adc} \times 4$)

Find very low gain or very high gain channels. The \bar{Q}_{adc} is the mean of ADC counts corresponding to 1 p.e. of all 17 inch channels.

For the outer detector, only criterion 1 applies to.

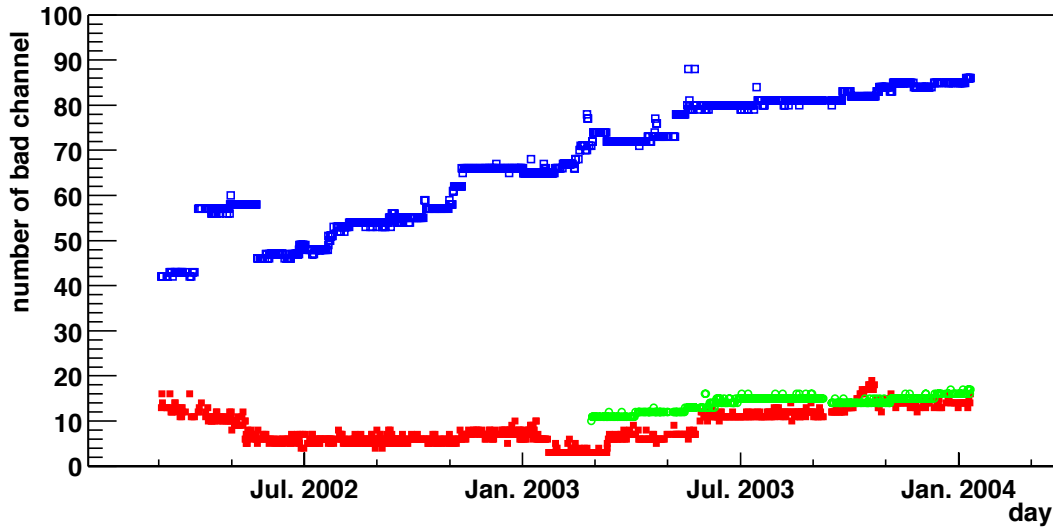


Figure 3.10: Time variation of the number of bad channels. The red marker and green marker indicate the number of bad channels in the inner detector for 17 inch PMTs and 20 inch PMTs respectively. The blue marker indicates the number of bad channels in the outer detector for 20 inch PMTs.

3.5 Vertex Reconstruction

The vertex is a fundamental parameter for ‘point-like’ events. That result is used for the energy reconstruction (Section 3.6) and the evaluation of the event reconstruction quality (Section 3.8). The vertex reconstruction is based on relative timing of PMT hits. Possible reconstruction biases affect a fiducial volume determination. Uncertainty of the fiducial volume is estimated from uniformities of spallation neutron and $^{12}\text{B}/^{12}\text{N}$ distributions.

3.5.1 Algorithm of Vertex Reconstruction

The vertex reconstruction is based on the relative times of the PMT hits. When a vertex point (x, y, z) is assumed, the light emission time is calculable from each PMT hit,

$$t_i(x, y, z) = T_{\text{detected},i} - T_{\text{of},i}(x, y, z) \quad (3.2)$$

where $T_{\text{detected},i}$ is the detected time of the photon, and $T_{\text{of},i}(x, y, z)$ is the time of flight, calculated from path length L_i and speed of light V (Figure 3.11),

$$T_{\text{of},i} = \frac{L_i}{V} \quad (3.3)$$

$$L_i = \sqrt{(x - x_i)^2 + (y - y_i)^2 + (z - z_i)^2} \quad (3.4)$$

$$V = \frac{c}{n_{\text{eff}}} \quad (3.5)$$

where n_{eff} is an effective index of refraction representing both the liquid scintillator and the buffer oil. In reality, T_{detected} depends on charge because of a multi photon effect. That charge dependence is measured by source calibrations at various energies. At an ideal vertex point, there is no correlation between t_i and the space-time correlation coefficient dt_i/dx , expressed as [70]

$$\frac{dt_i}{dx} = -\frac{dT_{\text{of},i}}{dx} \quad (3.6)$$

$$= -\frac{1}{dx} \left(\frac{L_i}{V} \right) \quad (3.7)$$

$$= \frac{x_i - x}{LV}, \quad (3.8)$$

and the covariance between t_i and dt_i/dx is

$$\sigma_{t_i, dt_i/dx} = \sum_i w_i (t_i - \langle t_i \rangle) \left(\frac{dt_i}{dx} - \left\langle \frac{dt_i}{dx} \right\rangle \right) / \sum_i w_i \quad (3.9)$$

$$= \left[\sum_i w_i \left(t_i \frac{dt_i}{dx} \right) / \sum_i w_i \right] - \left[\langle t_i \rangle \left\langle \frac{dt_i}{dx} \right\rangle \right] \quad (3.10)$$

where w_i is the distance dependent weight for each PMT, $\langle t_i \rangle$ and $\langle dt_i/dx \rangle$ indicate their mean value. The first term in Eq (3.10) works as a pull-push balance term for each PMTs with the

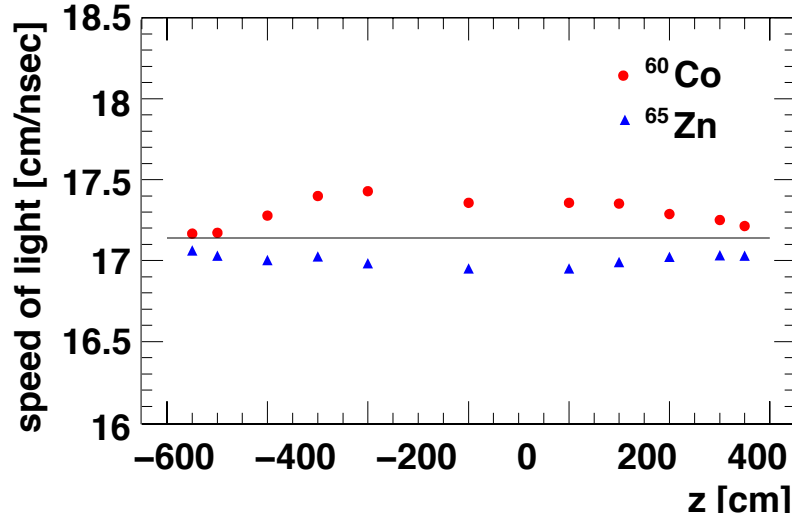


Figure 3.11: Measured speed of light for calibration sources, ^{60}Co and ^{65}Zn , at various z positions. The small energy dependence is due to a multi photon effect.

deviation from the origin of time. The second term is a constant in a event, but it is independent of the pull-push balance term and related to the time profile of scintillation light emission. The vertex position is moved in order that the covariance for x , y , z converges on zero (Figure 3.12).

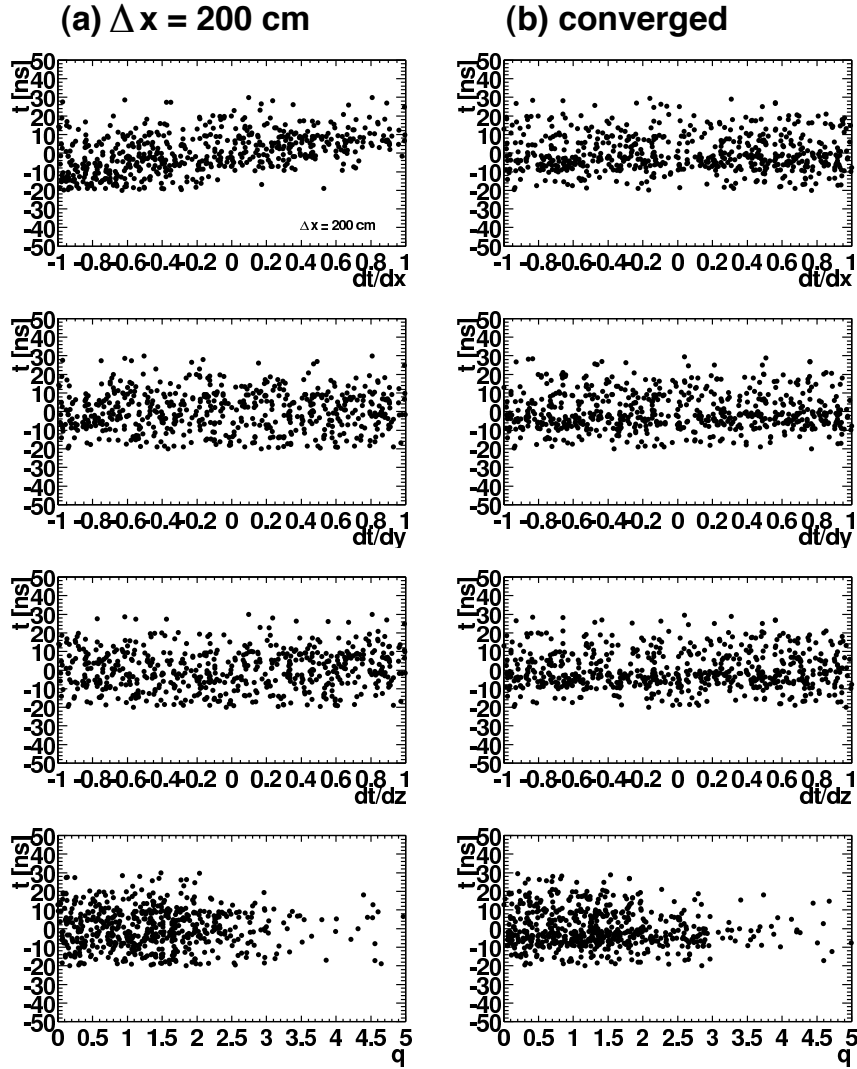


Figure 3.12: Correlation between t and dt/dx , dt/dy , dt/dz , q (charge). (a) At the $\Delta x = 200$ cm (intentionally shifted from the converged point), there is a correlation between t and dt/dx , while no correlation between t and dt/dy , dt/dz . (b) After the convergence, there is no correlation between t and dt/dx . The small correlation between t and q is tuned by a multi photon correction.

3.5.2 Reconstruction Performance

The reconstruction performance is verified with source calibrations. Vertex biases at various energies are less than 5 cm within 5.5 m fiducial radius along z-axis (Figure 3.13). The vertex resolution for the ^{60}Co source is about 20 cm. The resolution after commissioning the 20 inch PMTs is about 19 cm, slightly better than only 17 inch PMTs. Energy dependence of the resolution is estimated to be $\sim 30 \text{ cm}/\sqrt{E(\text{MeV})}$ from various energy sources. Miss fitting probability is less than 0.1% (Figure 3.14).

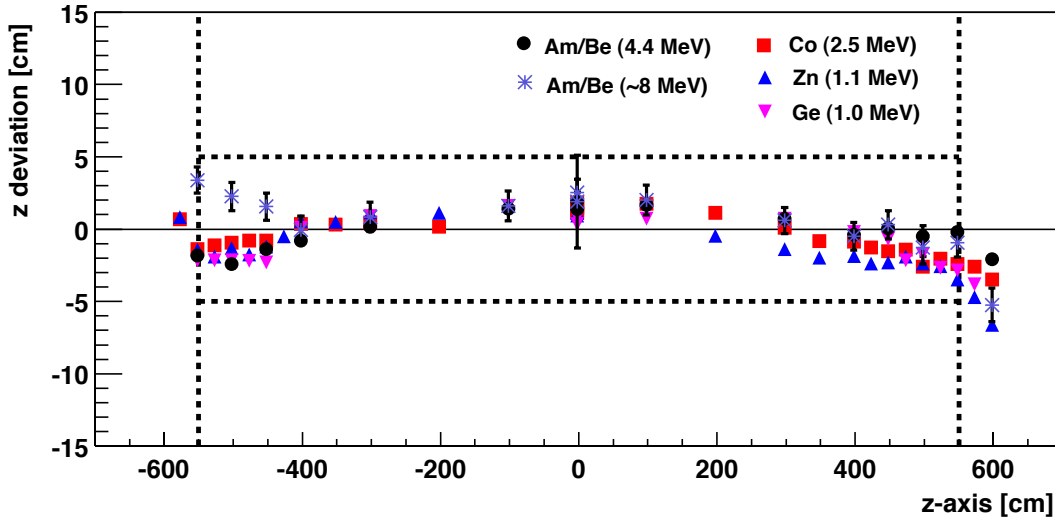


Figure 3.13: Deviations of reconstructed vertex along z-axis for various radioactivities, ^{68}Ge (2γ , $0.511 \times 2 \text{ MeV}$), ^{65}Zn (1γ , 1.1152 MeV), ^{60}Co (2γ , 1.173 + 1.333 MeV) and Am-Be (1γ , 4.438 MeV and 1γ , $\sim 8 \text{ MeV}$ by neutron capture on Ni or Fe). Their biases for various energies are less than 5 cm within 5.5 m fiducial radius.

3.5.3 Fiducial Volume Uncertainty

The total volume of the liquid scintillator is $1171 \pm 25 \text{ m}^3$, as measured by flow meters during the detector filling (Figure 3.15). The nominal 5.5-m-radius fiducial volume corresponds to 0.595 ± 0.013 of the total scintillator volume, and its ratio is compared with the reconstructed number of events in the fiducial volume to that in the total volume using uniformly distributing events, such as the 2.2 MeV neutron capture γ events and $^{12}\text{B}/^{12}\text{N}$ events. The ratio difference is included in the systematic uncertainty on the fiducial volume.

The neutron events are produced after muons. But there are many ‘bad events’ (events incorrectly reconstructed to bad vertices) in these events, because the ringing problem in FEE makes many busy channels. When time difference from muon is shorter, bad events ratio are

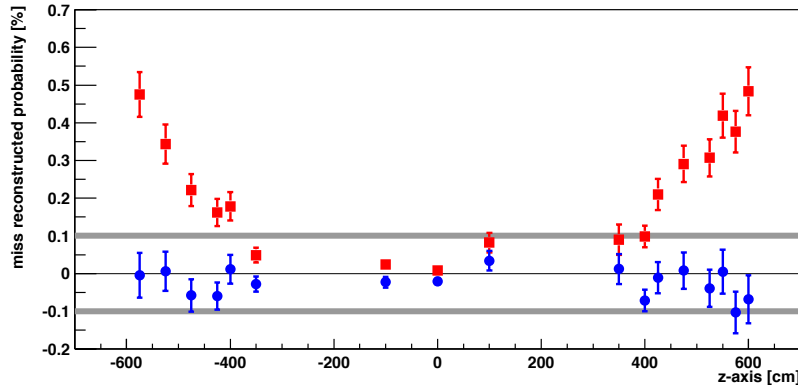


Figure 3.14: Miss reconstructed probability of the ^{60}Co events which has the vertex position larger than 150 cm from the source position. The square and circle marker indicate before and after the background subtraction using a background run. The miss reconstructed probability is estimated to be less than 0.1%.

larger (Figure 4.6) because the ATWD channels become busy due to multiple neutron events induced by energetic muons. In order to avoid unknown effects from the missing waveform events, neutron events with the time difference larger than 1200 μsec are used. Figure 3.16 (a) shows R^3 distribution of 2.2 MeV neutron capture γ 's made by an energy cut $1.8 < E < 2.6$ MeV and off-timing background subtraction. The reconstructed fiducial ratio is

$$N_{5.5\text{m}}/N_{\text{total}} = 0.587 \pm 0.013(\text{stat}) \pm 0.012(\text{syst-bad}) \pm 0.003(\text{syst-edge}) \quad (3.11)$$

where the residual bad events ratio in the on-time window is conservatively assigned as the systematic error 2.0%, and the contribution of events near the balloon surface that deposit a fraction of their energy (edge effect) is corrected by 2.7%, and the correction error is 0.5%.

The $^{12}\text{B}/^{12}\text{N}$ distribution is made by an energy cut $E > 4$ MeV and off-timing background subtraction. Its fiducial ratio is

$$N_{5.5\text{m}}/N_{\text{total}} = 0.607 \pm 0.006(\text{stat}) \pm 0.006(\text{syst-edge}) \quad (3.12)$$

where the systematic error of the edge effect is 1.0%. The neutron and $^{12}\text{B}/^{12}\text{N}$ fiducial ratios are consistent with the expectation as shown in Figure 3.15, and their small difference constrains the energy dependence of the fiducial volume. Moreover, it was verified by comparing the prompt and delayed event positions of the $^8\text{He}/^9\text{Li}$ (neutron emitter) coincidence events. The high energy prompt events ($E > 4$ MeV) are β -decays, and the low energy events are 2.2 MeV neutron capture γ 's, and the position bias at the 5.5 m radius is less than 5 cm, which corresponds to 2.7% volume error. Therefore, the overall uncertainty estimated from the scintillator volume measurement, $^{12}\text{B}/^{12}\text{N}$ and $^8\text{He}/^9\text{Li}$ coincidence is given by

$$\begin{aligned} N_{5.5\text{m}}/N_{\text{total}} - V_{5.5\text{m}}/V_{\text{total}} &= 0.012 \pm 0.006(\text{stat}) \pm 0.016(\text{syst-He/Li}) \\ &\quad \pm 0.006(\text{syst-edge}) \pm 0.013(\text{syst-volume}) \end{aligned} \quad (3.13)$$

then,

$$\begin{aligned} |N_{5.5\text{m}}/N_{\text{total}} - V_{5.5\text{m}}/V_{\text{total}}| &= 0.018(\text{deviation}) \pm 0.016(\text{syst-He/Li}) \\ &\quad \pm 0.006(\text{syst-edge}) \pm 0.013(\text{syst-volume}) \end{aligned} \quad (3.14)$$

$$\begin{aligned} (\text{total scintillator mass error}) &= 0.018 \oplus 0.016 \oplus 0.006 \oplus 0.013 \\ &= 0.028 \end{aligned} \quad (3.15)$$

which corresponds to a 4.7% fiducial uncertainty.

Radial stability of the vertex reconstruction is verified by radioactivities (Figure 3.17) at various energies near the balloon surface. The time variation of the fitted balloon edge is less than 1.5 cm, which corresponds to 0.7% volume error, and it gives a negligible contribution to the fiducial volume uncertainty.

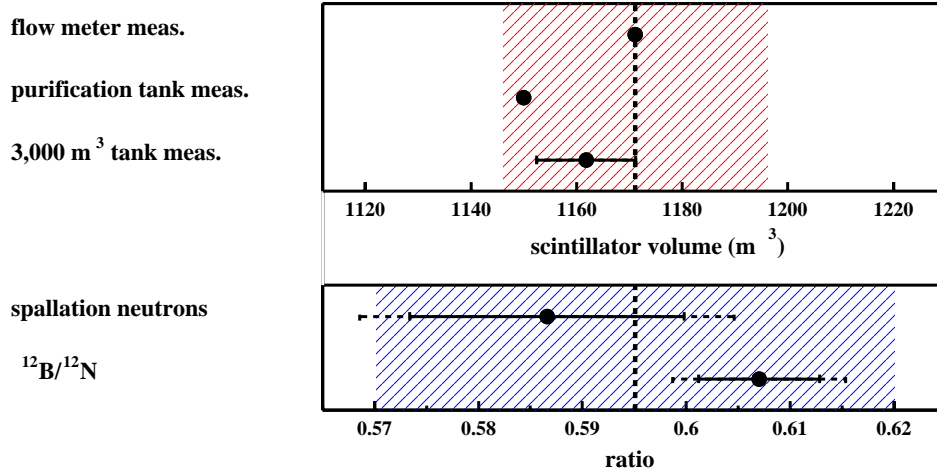


Figure 3.15: Fiducial volume error for the 5.5-m radius, estimated from the difference between the nominal 5.5 m radius fiducial ratio, as measured by flow meters during the detector filling, and the reconstructed ratio with the uniformly distributing events. The total volume of the liquid scintillator is $V_{\text{total}} = 1171 \pm 25 \text{ m}^3$, so the nominal 5.5-m-radius fiducial ratio is $V_{5.5\text{m}}/V_{\text{total}} = 0.595 \pm 0.013$. From the spallation neutron counting, the reconstructed fiducial ratio is $N_{5.5\text{m}}/N_{\text{total}} = 0.587 \pm 0.013(\text{stat}) \pm 0.012(\text{syst-bad}) \pm 0.003(\text{syst-edge})$ including the correction of the event loss 2.7% by the balloon edge effect, and in the $^{12}\text{B}/^{12}\text{N}$ event case, its ratio is $N_{5.5\text{m}}/N_{\text{total}} = 0.607 \pm 0.006(\text{stat}) \pm 0.006(\text{syst-edge})$, where the statistical uncertainties are expressed in the solid lines, and the contribution of the systematic uncertainties are in the dashed lines. The shaded regions mean the total uncertainties.

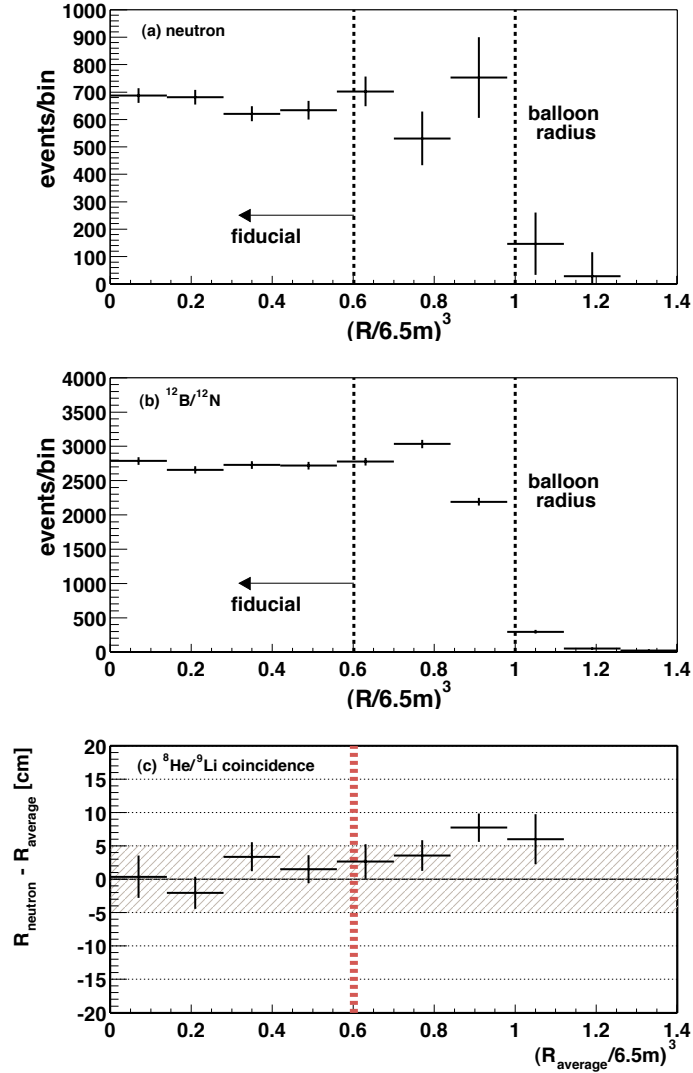


Figure 3.16: R^3 distribution of (a) 2.2 MeV neutron capture γ 's and (b) β -decay events from $^{12}\text{B}/^{12}\text{N}$ (>4 MeV) spallation products. Vertex reconstruction performance is verified by reproducing this uniform distribution. (c) Energy dependent vertex bias at the 5.5 m radius is estimated to be less than 5 cm from the $^8\text{He}/^9\text{Li}$ coincidence events. It corresponds to 2.7% volume error. Moreover, the expectation has the uncertainties coming from the scintillator volume measurement and the balloon edge effect. The overall uncertainty on the fiducial volume is estimated to be 4.7%.

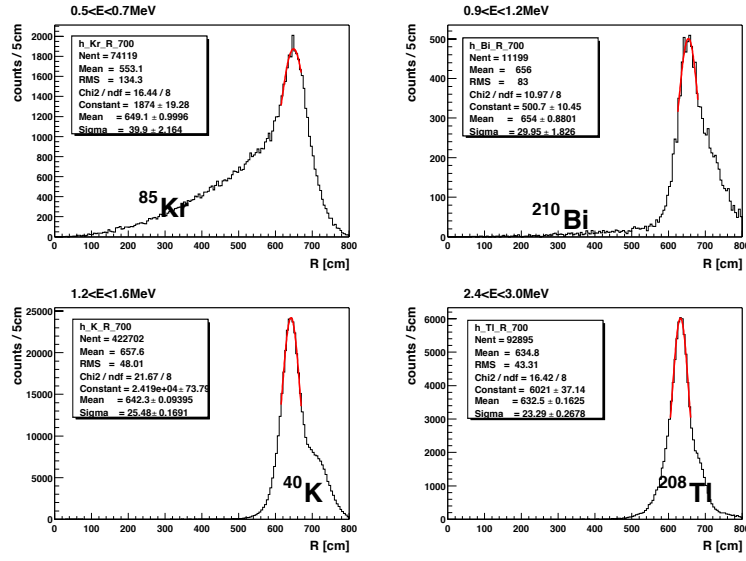


Figure 3.17: R distribution for various radioactivities.

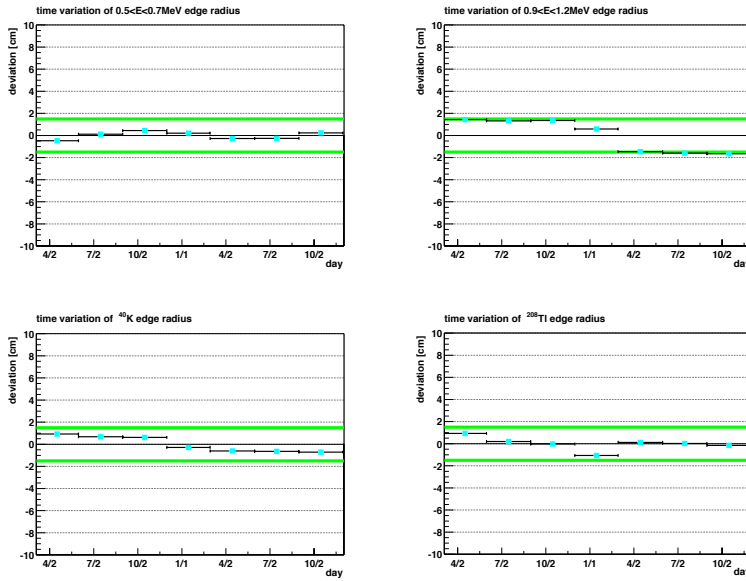


Figure 3.18: Time variation of the balloon edge R using various radioactivities.

3.6 Energy Reconstruction

The energy is defined by the deposited energy in the detector. Most of the ‘point-like’ events deposit all of their energies in the detector. The deposited energy is calculated using the visible energy corresponds to the scintillation light emission. There is a nonlinear relation between them because of the dark hit charge, single photo-electron detection efficiency, the quenching effect, and Cherenkov light. These nonlinear sources generate uncertainties of energy scale.

The visible energy is reconstructed from charge distribution of PMT hits. To account for position dependence and time variation caused by the detector status, various corrections are applied for each PMT charge and the total charge sum. The position dependence is calibrated with ^{68}Ge , ^{65}Zn , ^{60}Co γ -ray sources along z-axis, and γ -rays from neutron capture on protons. Time variation is corrected by time evolutions of single photo-electron charge and dark hit rate for each PMT in advance, and after the energy reconstruction, the residual time variation is corrected again using the ^{40}K γ -rays from the balloon. The systematic uncertainty of the visible energy reconstruction consists of the position dependence error and the time variation error. In KamLAND, the inner detector has 1325 17 inch PMTs and 554 20 inch PMTs. These PMTs have different characteristics in the sensitive area, time resolution and charge resolution. Actually, there is a clear 1 p.e. peak in the 17 inch PMT while the peak is not observed in the 20 inch PMT. Therefore, the primary energy calibration is only performed using the 17 inch PMTs, and after that, the energy reconstruction with the 20 inch PMTs are tuned by the energy with the 17 inch PMTs. Finally, the energies of 17 inch PMTs and 20 inch PMTs are combined as follows,

$$\begin{aligned} (\text{visible energy}) &= (1 - \alpha) \times (\text{energy : 17 inch PMTs}) \\ &\quad + \alpha \times (\text{energy : 20 inch PMTs}) \end{aligned} \quad (3.16)$$

where α is a weight factor, determined so as to get the best energy resolution. The uncertainty from commissioning the 20 inch PMTs is added to the uncertainty of the visible energy reconstruction.

3.6.1 Algorithm for Position Dependence Correction

The energy reconstruction is based on the total charge sum of PMT hits, however, it depends on the vertex point. The correction is not so simple due to the asymmetric geometry of the KamLAND detector. For example, the events which has the vertex in the top region are affected by the missing PMTs around the chimney. The photon yield for each PMT depends on solid angle, transparencies of the liquid scintillator and buffer oil, shadowing by suspension ropes, dark hit of PMTs, and one photoelectron threshold effect. Those effects are naively parameterized for inputs of the energy estimation.

The expected photon yield (overall efficiency) is expressed by various correction parameters, and the visible energy is calculated from the overall efficiency,

$$E = \frac{\sum_i Q_i^{\text{observed}}}{\sum_i Q_i^{\text{expected}}} \times (\text{const}) \quad (3.17)$$

$$Q_i^{\text{expected}} = \frac{\eta_i e^{-L_i/\lambda} \cos \theta_i}{L_i^2} \cdot \xi_i \quad (3.18)$$

where

$Q_i^{observed}$: observed PMT charge (p.e.)
$Q_i^{expected}$: expected PMT charge (arbitrary)
η_i	: light loss by balloon shadow
θ_i	: angle of incidence
L_i	: distance to light generation point
λ	: light attenuation length
ξ_i	: single photo electron threshold effect.

The light generation point refers to the reconstructed vertex. The dark hit contribution are subtracted from the total observed charge. The light attenuation length, light loss by balloon shadow and the dark hits are estimated in following sections.

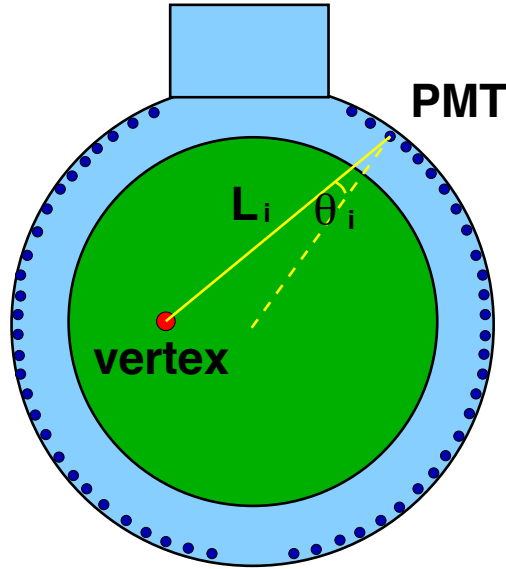


Figure 3.19: Definition of variables used in the energy reconstruction.

3.6.2 Basic Corrections

In order to reduce time variation of energy scale, various fundamental corrections are applied for each PMT charge in advance.

- Gain calibration

There are small differences of the single photo-electron charge among PMTs, even after

all the high voltage supplies were adjusted. Each PMT charge is normalized channel by channel and run by run, using the 1 p.e. peak (Section 3.3).

- **Bad channel selection**
The bad channels, which have too many hits, no hits or strange charge are selected and are masked in the energy estimation (Section 3.4). The charge from bad channels doesn't contribute to both charge sum, $\sum_i Q_i^{observed}$ and $\sum_i Q_i^{expected}$, therefore, an effect from the bad channels cancels out (Eq. (3.17)).
- **Software discriminator threshold**
The PMT noise causes the accidental dark hit. In order to reduce its contribution, the software discrimination is applied at a 0.3 p.e. threshold for each PMT charge. Hardware thresholds are set below 0.3 p.e. and the software threshold eliminates small nonuniformity of the hardware threshold.
- **Dark hit subtraction**
The accidental dark hits influence the energy estimation. It can be estimated from an off-time window of the timing distribution run by run, and its contribution is subtracted from the charge sum ($\sum_i Q_i^{observed}$) event by event.

3.6.3 Dark Hit Subtraction

Timing distribution of scintillation are reconstructed event by event using the information of reconstructed vertex points. The time of flight is calculated for each PMT, and subtracted from the time of PMT hits. In order to reduce the dark hit contributions, maximum number of hits in the 150 nsec sliding time window is used (Figure 3.20). The dark hit contribution is estimated from hits in the off-time window (width = 50 nsec). The time variation of the dark hit charge sum (17 inch PMTs) scaled to the 150 nsec width are shown in Figure 3.21 (a). The contribution of dark hit charge (10~15 p.e.) is about 3~5% for 1 MeV event. In order to reduce the non-linear bias for the visible energy, the dark hit charge are subtracted from the on-time window event by event.

The time variation of the temperature of the outer buffer oil at various positions, upper, equator, lower and bottom, are shown in Figure 3.21 (b), which illustrates a correlation between the dark hit charge and the temperature, especially for the upper region. The decrease of the temperature in December 2003 is caused by increased flow rate of the purified water in the outer detector.

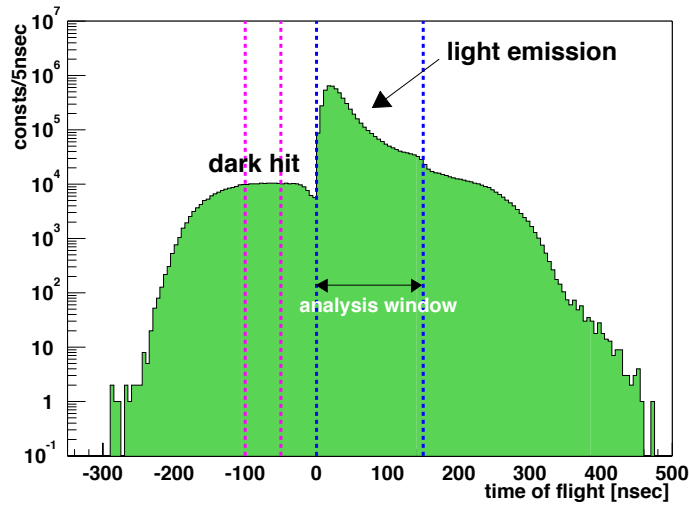


Figure 3.20: Timing distribution of PMTs hits after the correction for time of flight.

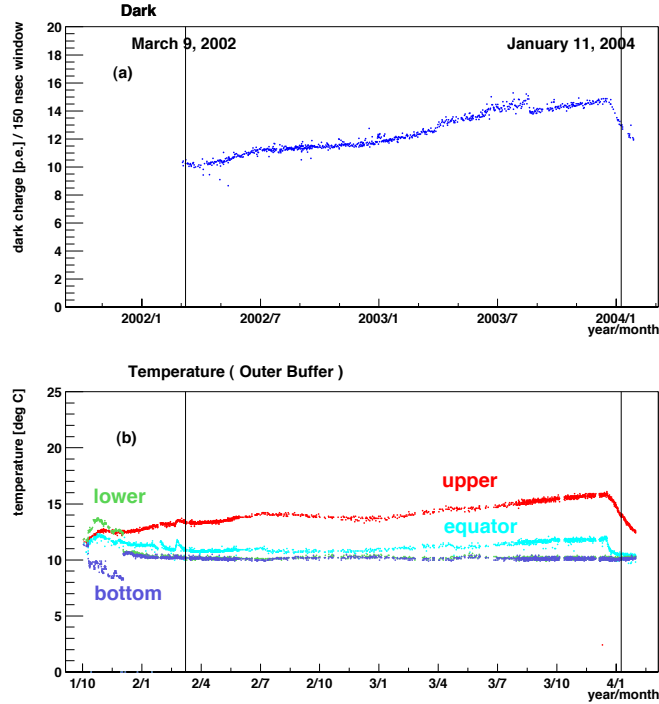


Figure 3.21: Time variation of (a) the dark charge for 17 inch PMTs and (b) temperature of the outer buffer oil for various positions, upper, equator, lower and bottom. There is correlation between the dark charge and the temperature, especially for the upper region.

3.6.4 Photon Yield Efficiencies

Shadow Effect

The photon yield for each PMT depends on the shadow effect by the balloon and its suspension ropes. The light loss by the ropes is calculated from the geometrical information of the ropes. The shadow effect was calibrated with the ^{60}Co source at the center of the detector so that the photon yields of the PMTs become symmetric. Figure 3.22 shows the position dependence of the charge for each PMT, before and after the shadow correction. At the top and bottom of the balloon, the vertical suspension ropes are dense, and the shadow effect becomes larger. The PMT charge distribution becomes uniform after the shadow correction.

The shadow effect has a slight time dependence. The time dependent effect is corrected by the periodical ^{60}Co source calibration once a week.

Attenuation Length

The attenuation length is an important parameter to the calibration of the position dependence. The light yield depends heavily on this parameter. In KamLAND, the liquid scintillator is contained in the 6.5-m-radius balloon, surrounded by a high light transparency buffer oil. Primary photons are emitted at the vertex point in the balloon. During a passage in the liquid scintillator and the buffer oil, the light intensity weakens due to an absorption mainly in the liquid scintillator. A portion of the absorbed photons excites the fluor, and produces reemission photons, which increase the light yield. Another effect increasing the photon yield is the slight reflection on the transparent acrylic sphere segmenting the buffer oil. The ‘effective attenuation length’ includes those effects, and it can be measured by the source calibration in the actual equipment, the KamLAND detector.

Figure 3.23 shows the effective charge variation after the shadow correction, the angle of incidence and the solid angle corrections, as a function of the distance from the PMT to the ^{65}Zn source position ($z = -5.5 \text{ m} \sim +5.5 \text{ m}$). It is naively fitted with one exponential curve, and the obtained attenuation length is 22 m. The attenuation length is the tuning parameter so as to reproduce the uniform position dependence.

Single Photo-electron Efficiency

The inefficiency of 1 p.e. detection due to the 0.3 p.e. threshold causes the non-linear bias to the visible energy [70]. The mean number of photo-electrons μ is at first calculated using the preliminary estimation of the expected charge for each PMT,

$$\mu \equiv (\text{mean number of p.e. in } j\text{-th PMT}) = \sum_i Q_i^{\text{observed}} \times \frac{Q_j^{\text{expected-no-threshold}}}{\sum_i Q_i^{\text{expected-no-threshold}}}. \quad (3.19)$$

Using a detection efficiency (ϵ) of 1 p.e. and the mean number of p.e., the probability of 0 p.e. and 1 p.e. and N p.e. ($N \geq 2$) detection efficiencies are given with Poisson statistics

$$P(0) = e^{-\mu} + (1 - \epsilon)\mu e^{-\mu} \quad (3.20)$$

$$= e^{-\mu}[1 + (1 - \epsilon)\mu] \quad (3.21)$$

$$P(1) = \epsilon\mu e^{-\mu} \quad (3.22)$$

$$P(N) = \frac{\mu^N}{N!} e^{-\mu} \quad (N \geq 2). \quad (3.23)$$

The expected charge is calculated by adding up charges,

$$Q_i^{expected} = q(1) \times P(1) + \sum_{N \geq 2} [q(N) \times P(N)]. \quad (3.24)$$

here, normalization constant is omitted because it doesn't matter to energy nonlinearity. If there is no threshold effect,

$$\sum_{N \geq 1} [q(N) \times P(N)] = \mu q_1 \equiv Q_i^{expected-no-threshold} \quad (3.25)$$

where q_1 is the mean charge of 1 p.e. distribution with no threshold effect. Then, considering that only 1 p.e. events are affected by the threshold effect, Eq (3.24) is converted to

$$Q_i^{expected} = \mu q_1 - \mu e^{-\mu} q_1 + q(1)\epsilon\mu e^{-\mu} \quad (3.26)$$

$$= \mu q_1 \left[1 - e^{-\mu} + \frac{q(1)}{q_1} \epsilon e^{-\mu} \right] \quad (3.27)$$

$$= Q_i^{expected-no-threshold} \left[1 - e^{-\mu} \left(1 - \frac{q(1)}{q_1} \epsilon \right) \right], \quad (3.28)$$

here, the $q(1)$ is determined from the following relation.

$$q_1 = q(1)\epsilon + q_{loss}(1 - \epsilon), \quad (3.29)$$

where q_{loss} is the mean charge of the events under threshold, then, it should be less than 1/3 p.e. From Eq. (3.28) and Eq. (3.29),

$$Q_i^{expected} = Q_i^{expected-no-threshold} (1 - e^{-\mu} \delta) \quad (3.30)$$

$$\delta \equiv \frac{q_{loss}}{q_1} (1 - \epsilon). \quad (3.31)$$

The parameter δ are determined using the real data. For the radioactive source ^{60}Co (2γ , 1.173 + 1.333 MeV) and ^{65}Zn (1γ , 1.11552 MeV), individual gamma-ray energies are similar, so the effects of quenching and Cherenkov light work similarly. Therefore, it is useful to separate the threshold effect and the quenching and Cherenkov light effects. The residual energy non-linearity can be caused by the single photo electron threshold effect, and the δ is measured to be 0.03.

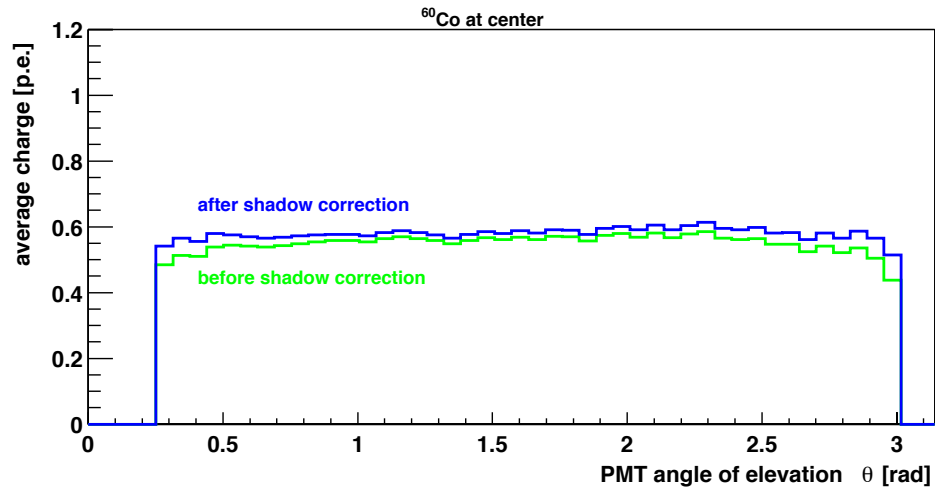


Figure 3.22: Correction of shadow effect from the balloon and its rope.

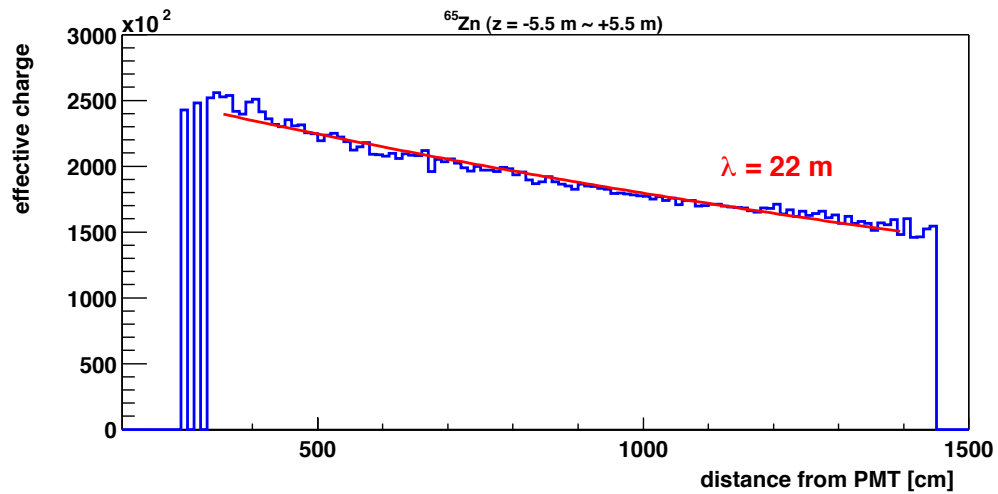


Figure 3.23: Effective light attenuation length in the liquid scintillator and the buffer oil.

3.6.5 Uncertainty of Energy Scale

In KamLAND, $\bar{\nu}_e$ energy is calibrated using radioactive sources and muon-induced spallation events. The visible energy deviation is caused by the position dependence, time variation and combining error of 20 inch PMTs. The visible energy uncertainty are estimated for each position and period, conservatively. In addition, there are uncertainties related to the conversion from the visible energy to the deposited energy, and they contribute to the energy non-linearity.

The source calibration are performed along the vertical axis periodically, using various radioactive gamma-ray sources. The spallation neutron capture gamma-rays on protons and ^{12}C provide the energy information for entire detector volume and period. Table 3.1 shows the correlation between the deposited energy (real energy) and the visible energy using only 17 inch PMTs. The energy non-linearity calibration is based on this correlation, except ^{203}Hg to avoid the larger dark hit uncertainty. The combined analysis of the Cherenkov light effect and quenching effect gives the conversion functions for each particle, gamma, electron and positron. In the reactor $\bar{\nu}_e$ event, the conversion to the positron energy is applied. The conversion error contributes to the energy distortion, so its contribution is included in the oscillation analysis.

Table 3.1: Reconstructed visible energies for various gamma sources

sources	gamma energy (MeV)	visible energy (MeV)	resolution $\sigma/\sqrt{E_{vis}}(\text{MeV})$ (%)
^{203}Hg	0.279197	0.197	8.2
^{68}Ge	0.511×2	0.846	7.9
^{65}Zn	1.11552	1.021	7.2
^{60}Co	$1.173 + 1.333$	2.346	7.3
$np \rightarrow d\gamma$	2.22457	2.211	-
$n^{12}\text{C} \rightarrow ^{13}\text{C}\gamma$	4.9468	5.061	-

The uncertainties of the energy scale are summarized as follows,

- Position Dependence

The uncertainty of the position dependence is estimated from the neutron capture gamma events and source calibrations along z-axis. The deviation with the radius dependence from the neutron events is less than 0.3% (Figure 3.24 (a)), while the deviation with the z-dependence from the source calibration is less than 0.8% (Figure 3.25). For conservative error estimation, the local deviation 0.92% (Figure 3.24 (b)) near the top and bottom is assigned to the systematic error.

- Time Variation

After the fundamental corrections, time variation still remains in the visible energy. Its

variation is verified with the 1.46 MeV ^{40}K gamma peak (Figure 3.27). The peak value is used for the relative time dependent correction. The visible energies in Table 3.1 include this correction. After the correction, the uncertainty of the time variation is estimated from the neutron capture gamma events and source calibrations along z-axis. The reconstructed energy variation is less than 1.3% during the livetime (Figure 3.28 and Figure 3.29). The variation of the energy resolution is shown in Figure 3.30.

- Non-linearity for 20 inch PMTs

In the 20 inch PMT, there is no 1 p.e. peak because of the bad charge resolution. Moreover, the charge dependence on the energy is different between the 17 inch PMTs and 20 inch PMTs. Thus, the reconstructed energy with the 20 inch PMTs are tuned by the energy with the 17 inch PMTs, and their energies are combined by Eq. (3.16). The combining factor α is 0.3, tuned to get the best resolution (Figure 3.31). The uncertainty from commissioning the 20 inch PMTs is less than 0.8% estimated from the linearity between the combined energy and the energy with the 17 inch PMTs using various radioactivities (Figure 3.32).

- Contribution of Cherenkov light

The Cherenkov photons are emitted from the charged particle, and the number of photons depends on its energy. Cherenkov light can not be seen directly because the dominant wavelength is below the absorption wavelength of the scintillator. However, the scintillator reemits absorbed Cherenkov photons and the reemission photons contribute to the reconstructed energy. This contribution give rise to the energy nonlinearity, and is globally treated by altering the contribution of the quenching effect.

- Quenching Effect

In the first order, the number of scintillation photons is proportional to the deposited energy, but its small dependence on the ionization density is not negligible. Such dependence causes the specific energy non-linearity for each particle [71]. This effect is so called ‘quenching effect’. In the heavy slow particle case, the quenching effect becomes very large due to its high ionization density. In order to estimate the contribution of the quenching effect, the most common way is using Birk’s formula,

$$\frac{dL}{dX} \propto \frac{dE/dX}{1 + k_B(dE/dX)} \quad (3.32)$$

where the dL/dX is the emitted light intensity per unit length and k_B is Birk’s constant. Using the 5 gamma ray data (^{68}Ge , ^{65}Zn , ^{60}Co , np , $n^{12}\text{C}$) and 1 electron data ($^{12}\text{B}/^{12}\text{N}$), the contributions from the quenching and Cherenkov light are tuned. The 2 γ ’s of ^{68}Ge and ^{60}Co are treated as 1 γ whose energy is the effective mean of them. In the γ -ray case, the recoil energies of electron are calculated with a MC simulation. The uncertainty in the parameters, the Birk’s constant, the Cherenkov intensity and an absolute normalization factor (Figure 3.33) is assigned to the energy non-linearity error.

Thus, the energy scale uncertainty at 2.6 MeV, which is the threshold of the reactor $\bar{\nu}_e$ analysis, is the combination of the uncertainties for Cherenkov/Birk’s 1.0%, time dependence

1.3%, position dependence 0.92%, non-linearity for 20 inch PMTs 0.8%,

(Energy Scale Error at 2.6 MeV : only 17 inch PMTs) = 1.88%

(Energy Scale Error at 2.6 MeV : including 20 inch PMTs) = 2.04%

and those error is considered in the reactor $\bar{\nu}_e$ analysis at 2.6 MeV threshold. The uncertainty becomes slightly larger when 20 inch PMTs are used. On the other hand the energy resolution is improved by commissioning the 20 inch PMTs,

(Energy Resolution : only 17 inch PMTs) = $7.3\%/\sqrt{E(\text{MeV})}$

(Energy Resolution : including 20 inch PMTs) = $6.2\%/\sqrt{E(\text{MeV})}$

because of increasing the photo-cathode coverage.

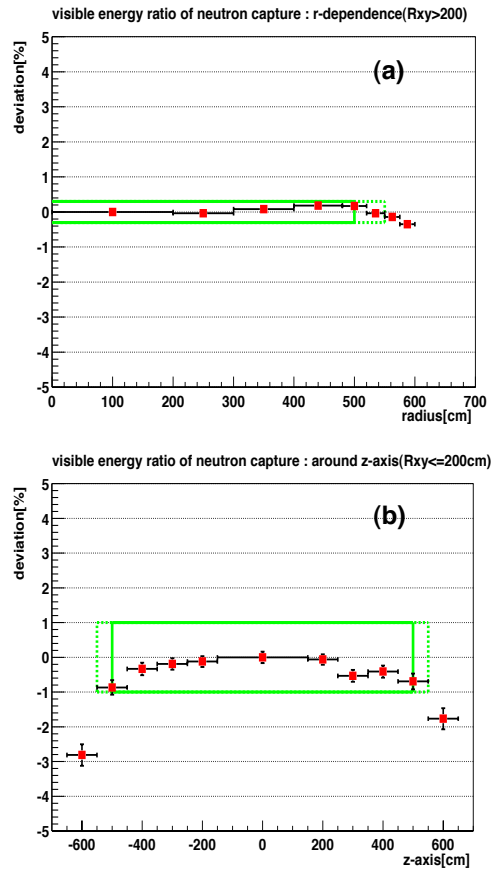


Figure 3.24: Position dependence of visible energy for neutron capture gamma events (2.22457 MeV). (a) The reconstructed energy varies less than 0.3% with the radius within 5.5 m radius. (b) The local variation near the top and bottom region is less than 0.92%.

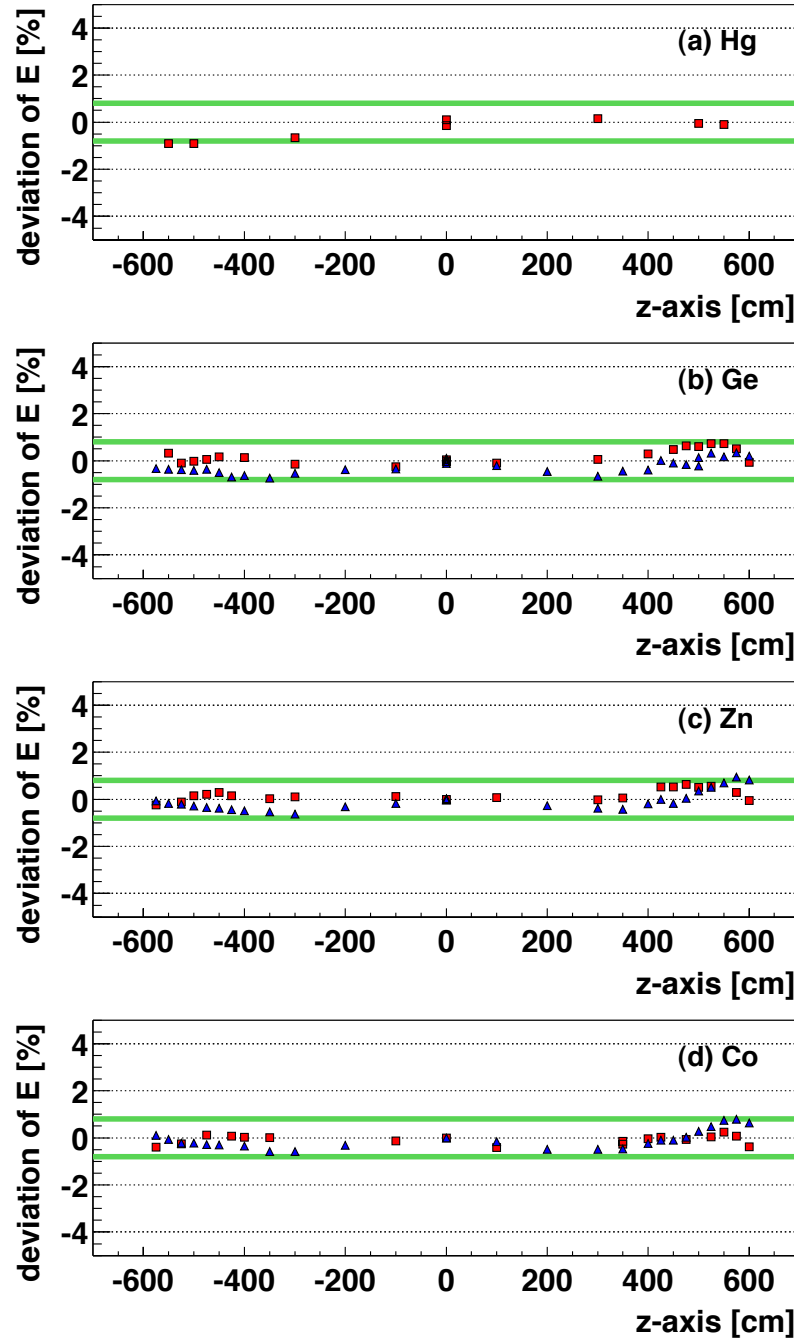


Figure 3.25: Deviation of reconstructed energy at various positions on z-axis for various sources, (a) ^{203}Hg (1γ , 0.279197 MeV), (b) ^{68}Ge (2γ , 0.511×2 MeV), (c) ^{65}Zn (1γ , 1.11552 MeV) and (d) ^{60}Co (2γ , 1.173 + 1.333 MeV). To see the position dependence, the energy is normalized with the mean energy of the central calibrations for each source. The deviation means the difference from the mean energy for each source. The square and triangle markers indicate the data with the 17 inch PMTs and 17 inch + 20 inch PMTs, respectively.

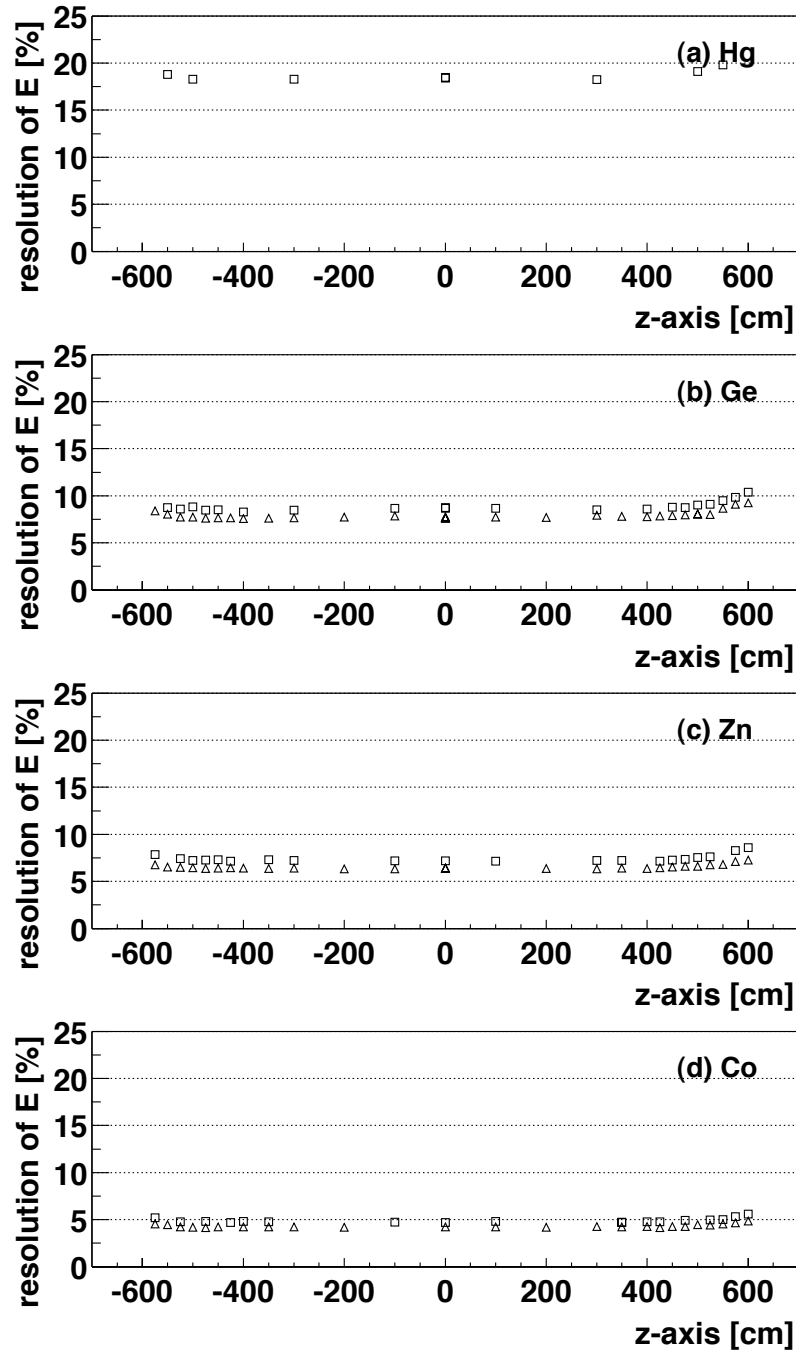


Figure 3.26: Correlation of the resolution σ/E at various positions on z-axis for various sources, (a) ^{203}Hg (1 γ , 0.279197 MeV), (b) ^{68}Ge (2 γ , 0.511×2 MeV), (c) ^{65}Zn (1 γ , 1.11552 MeV) and (d) ^{60}Co (2 γ , 1.173 + 1.333 MeV). The square and triangle markers indicate the data with the 17 inch PMTs and 17 inch + 20 inch PMTs, respectively.

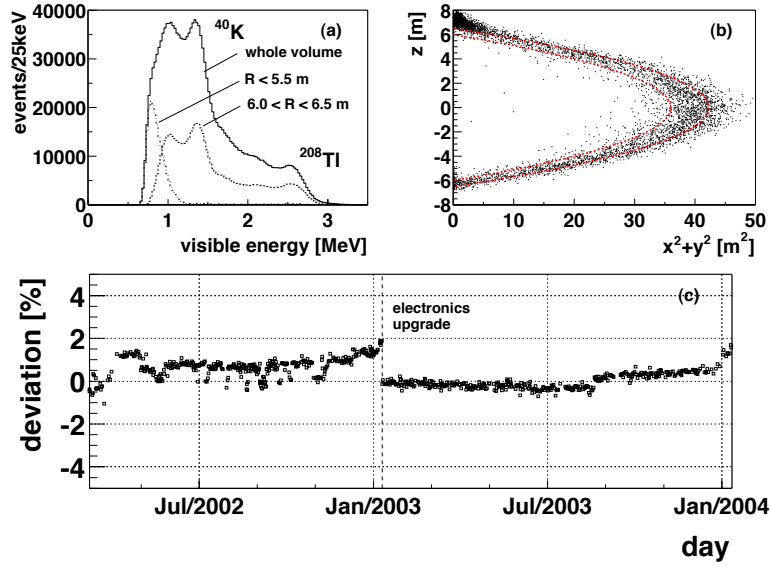


Figure 3.27: (a) Visible energy spectra for the whole volume (solid line), $R < 5.5$ m (dash-dot line) and $6.0 < R < 6.5$ m (dash line). The ^{40}K γ peak position becomes clear after the volume cut, $6.0 < R < 6.5$ m. (b) The ^{40}K event is intensive near the balloon. (c) Time variation of the ^{40}K γ peak, and its factor is used for the time dependent energy correction run by run.

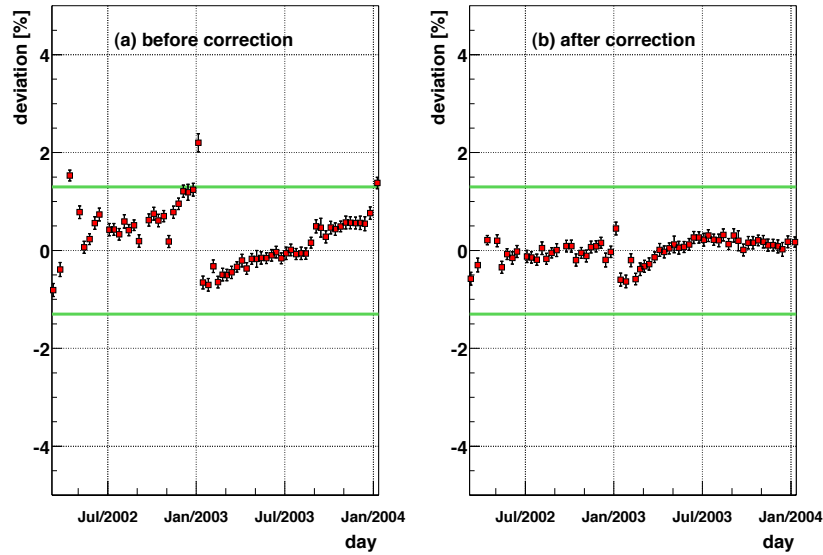


Figure 3.28: Time variation of spallation neutrons which were captured on protons (1 γ , 2.22457 MeV) (a) before and (b) after the time dependent correction based on the ^{40}K energy variation.

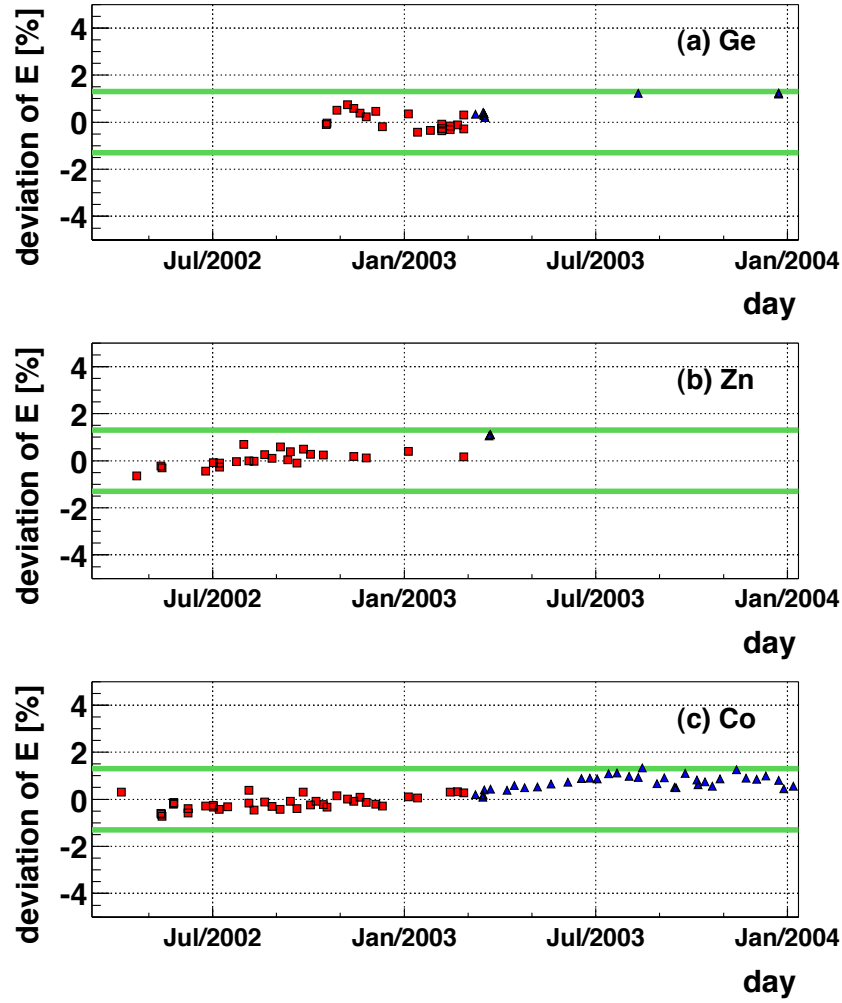


Figure 3.29: Deviation of reconstructed energy at the center of the detector for various sources, (a) ^{68}Ge (2γ , 0.511×2 MeV), (b) ^{65}Zn (1γ , 1.11552 MeV) and (c) ^{60}Co (2γ , 1.173 + 1.333 MeV). The square and triangle markers indicate the data with the 17 inch PMTs and 17 inch + 20 inch PMTs, respectively. The 20 inch PMT data was included on February 27, 2003.

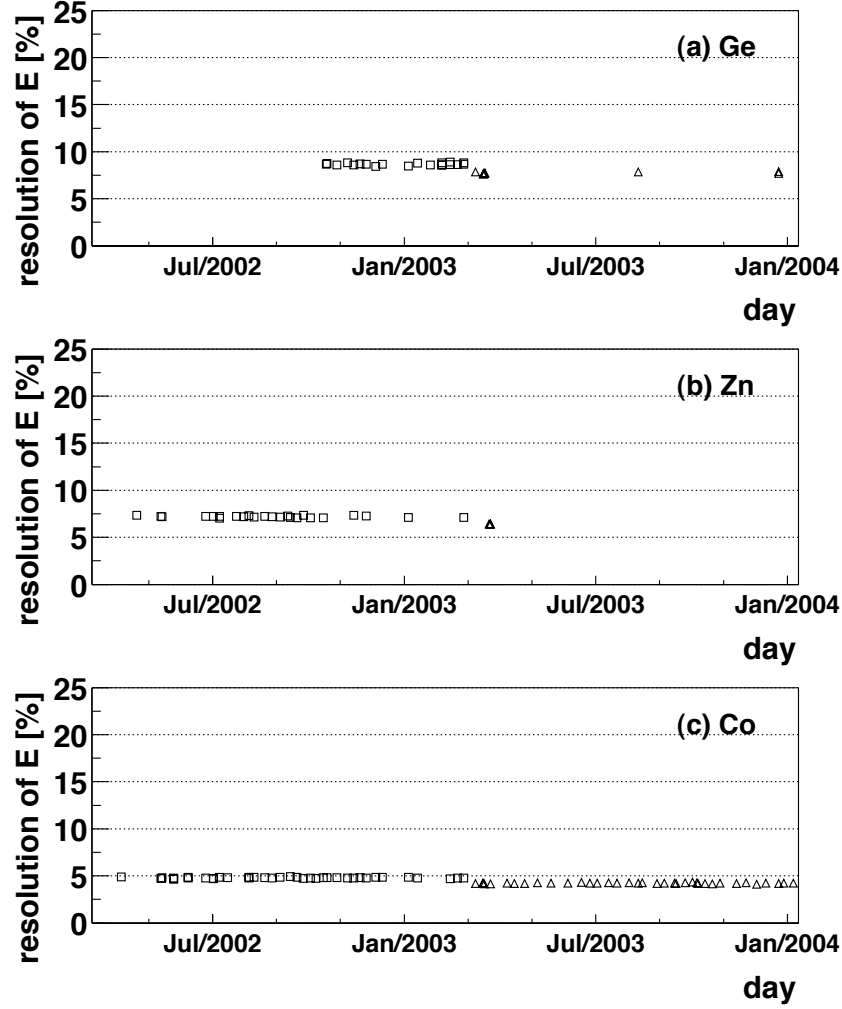


Figure 3.30: Time variation of the resolution σ/E at the center of the detector for various sources, (a) ^{68}Ge (2γ , 0.511×2 MeV), (b) ^{65}Zn (1γ , 1.11552 MeV) and (c) ^{60}Co (2γ , 1.173 + 1.333 MeV). The square and triangle markers indicate the data with the 17 inch PMTs and 17 inch + 20 inch PMTs, respectively.

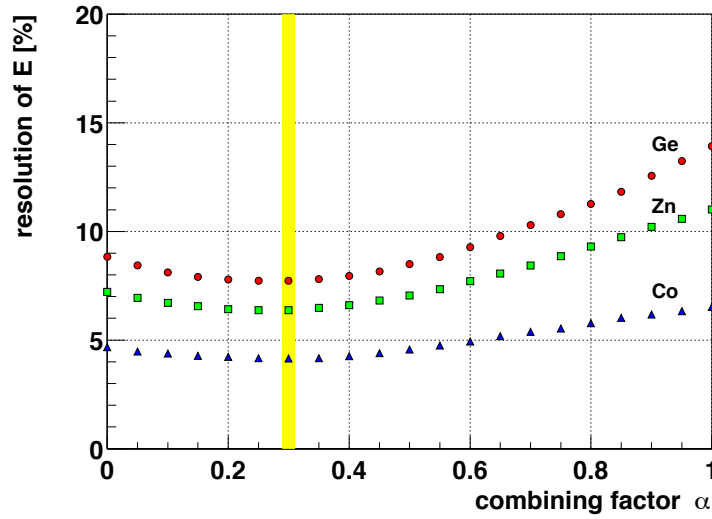


Figure 3.31: Variation of the energy resolution (17 inch PMTs + 20 inch PMTs) as a function of the combining factor α . The vertical yellow line indicates the best parameter ($\alpha = 0.3$) for various source calibrations.

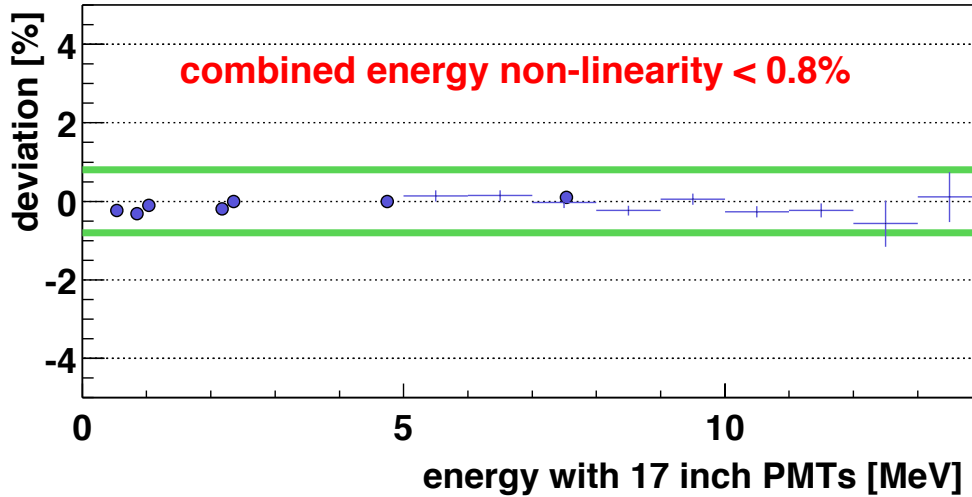


Figure 3.32: Combined energy (17 inch PMTs + 20 inch PMTs) linearity as a function of the energy with only 17 inch PMTs. The linearity of the combined energy is verified by the radioactive isotopes, ^{214}Po , ^{68}Ge , ^{65}Zn , Am-Be (2.22457 MeV, 4.438 MeV and ~ 8 MeV) and ^{60}Co . The high energy region up to 14 MeV is supported by the spallation products. The uncertainty on the combined energy non-linearity is less than 0.8%.

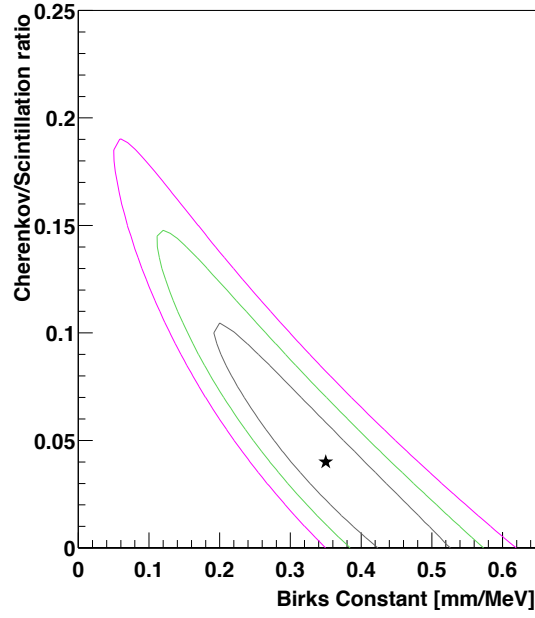


Figure 3.33: Uncertainty in the parameters for the nonlinearity calibration. The star marker indicates the best fit parameters from various source calibrations. The contour lines mean 1σ , 2σ and 3σ C.L.

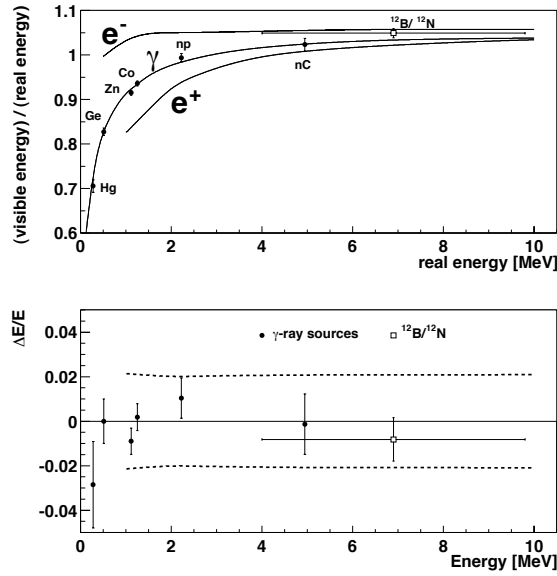


Figure 3.34: Non-linearity correction (upper) and uncertainty in the energy (lower).

3.7 Muon Track Reconstruction

The KamLAND detector is located at an average rock overburden of 2,700 m.w.e. resulting in 0.34 Hz of cosmic ray muons which go through the inner detector. The cosmic ray muons occasionally produce radioactive isotopes by the interaction with nuclei in the detector. Most of the isotopes β -decay with various energies less than 20 MeV. Some of the nuclei emit neutrons and mimic the $\bar{\nu}_e$ signal. They can be the correlated backgrounds for the delayed coincidence signal around muon tracks (Section 4.3.2). Therefore, it is important for the $\bar{\nu}_e$ selection to identify muon tracks and to reject the correlated backgrounds. In this section, the selection criteria for muons, the tracking algorithm and its performance are described.

3.7.1 Selection Criteria

Selection criteria for muon events are as follows,

- $Q_{\text{ID}} \geq 10,000$ p.e.
Total charge sum of the 17 inch PMTs in the inner detector is greater than 10,000 p.e.
The event rate with this selection criteria is $0.31 \sim 0.32$ Hz.
- $Q_{\text{ID}} \geq 500$ p.e. and $N_{\text{OD}} \geq 5$ hits
Total charge sum of the 17 inch PMTs in the inner detector is greater than 500 p.e. and the number of hits in the outer detector is greater than 5 hits. When a muon go through only the buffer oil region, the muon emits only Cherenkov photons resulting in the lower charge sum. The ‘Cherenkov muon’ selection is covered by the OD tagging using the PMT hit information. The event rate with this selection criteria is $0.027 \sim 0.028$ Hz.

The selected events are shown in Figure 3.35. The muon rate is estimated to be about 0.34 Hz. There are two clear peaks in the charge distribution, which correspond to ‘through going muons’ (scintillation light + Cherenkov light) and ‘clipping muons’ (Cherenkov light), respectively. The discrimination of these two types of muons is verified by the muon track information as described in the following sections.

3.7.2 Algorithm for Muon Track Reconstruction

The muon track reconstruction is based on the timing information of PMT hits. A muon event generates the Cherenkov photons and scintillation photons along its track in the detector. The Cherenkov photons are emitted to the constant angle θ related to the index of refraction (Figure 3.36 (a)) when the later reemission photons are ignored. In the scintillation photon case, the PMTs detect photons in all directions. Using the notation of Figure 3.36 (b), the time when a muon entered to the detector t_0 and the index of refraction n , the observed time at the PMT is expressed as a function of l [70],

$$t = t_0 + \frac{l}{c} + \frac{z-l}{\cos \theta} \cdot \frac{n}{c} \quad (3.33)$$

$$= t_0 + \frac{l}{c} + \sqrt{(z-l)^2 + \rho^2} \cdot \frac{n}{c} \quad (3.34)$$

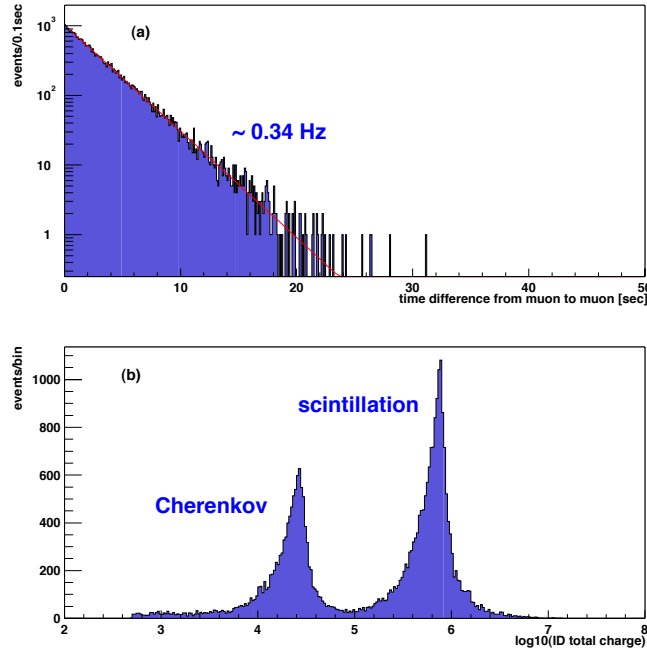


Figure 3.35: (a) Time difference from muon to muon, and the muon rate is estimated to be about 0.34 Hz. (b) Charge distribution of muons. It has two clear peaks, ‘through going muons’ (scintillation light + Cherenkov light) and ‘clipping muons’ (Cherenkov light).

where the velocity of the muon was approximated to be the speed of light. Thus, the minimum of t calculated by the equation $dt/dl = 0$,

$$\cos \theta = \frac{1}{n}. \quad (3.35)$$

This angle indicates the angle from which the earliest photons come, and it is exactly same as the Cherenkov angle when the velocity of the muon is the same as the speed of light. It allows the simplification of the optical system using only earliest photons. The muon track is reconstructed to get the most balanced track which reproduce the time of PMT hits. In order to avoid the complicated time information, the PMTs out of the range of the Cherenkov angle are not used for the reconstruction. The index of refraction of the liquid scintillator and the buffer oil is measured to be $1.44 \sim 1.47$ in the various wavelength relevant to the scintillation light (Figure 2.5). In order to consider the difference of the pass length in the scintillator and buffer oil for each track, that parameter is tuned within the measured value. When the stopping muon or multi muon events are reconstructed, the above algorithm is not appropriate. The muon which has too small charge sum for the reconstructed track length is classified into the ‘miss-reconstructed muon’. The miss-reconstructed ‘through going muon’ rate is about 0.2% for all muons. The muon which has too large charge sum for the track length is classified into the ‘showering muon’, and its fraction is about 1.5% of all muons.

3.7.3 Tracking Performance

Correlations between the total charge in the inner detector and the muon track length, in the liquid scintillator and in the buffer oil, are shown in Figure 3.37 without miss-reconstructed muons. These two parameters have a linear correlation as expected. Figure 3.38 shows the distribution of normalized charge by reconstructed muon track length in the buffer oil and in the scintillator. It is so called dQ/dX , defined as follows,

$$\left(\frac{dQ}{dX}\right)_{Cherenkov} = \frac{Q_{ID}}{L_{ID}} \quad (\text{clipping muon}) \quad (3.36)$$

$$\left(\frac{dQ}{dX}\right)_{Scintillation} = \frac{Q_{ID} - L_{ID}(dQ/dX)_{Cherenkov}}{L_{Scintillation}} \quad (\text{through going muon}) \quad (3.37)$$

where Q_{ID} , L_{ID} and $L_{Scintillation}$ are the total charge sum of the inner detector, the reconstructed track length for the inner detector and the scintillator region. The ideal light emission per length is approximated by the mean of a Gaussian fit with a lower edge,

$$\left(\frac{dQ}{dX}\right)_{Cherenkov}^{ideal} = 31.45 \quad \text{p.e./cm} \quad (3.38)$$

$$\left(\frac{dQ}{dX}\right)_{Scintillation}^{ideal} = 629.4 \quad \text{p.e./cm.} \quad (3.39)$$

The $(dQ/dX)_{Scintillation}$ is about 20 times higher than the $(dQ/dX)_{Cherenkov}$. In this thesis, the parameter of the residual charge (ΔQ) is often used in order to reject the spallation backgrounds. The definition of the residual charge is

$$\Delta Q = Q_{ID} - L_{ID} \left(\frac{dQ}{dX}\right)_{Cherenkov}^{ideal} - L_{Scintillation} \left(\frac{dQ}{dX}\right)_{Scintillation}^{ideal}. \quad (3.40)$$

The correlation of the track length and the total charge sum is important information for the understanding of events. Figure 3.39 (a) shows the correlation between the total charge in the inner detector and the distance from the center to muon track (impact parameter). The high charge events concentrate at the smaller distance, i.e. the larger track length, and there is a step which separates the ‘through going muons’ and ‘clipping muons’, at around 650 cm, the balloon radius. Moreover, the muon track reconstruction reproduces the linear distribution of the track length in the scintillator as shown in Figure 3.39 (b).

The tracking performance is also verified by the correlation between spallation neutrons and reconstructed muon tracks. The efficiency within 2 m and 3 m from the muon track is evaluated to be 90.7% and 93.8% respectively. The reconstructed track information is used for the background estimation and reduction (spallation cut) as described in Section 4.3.2 and 5.4.2.

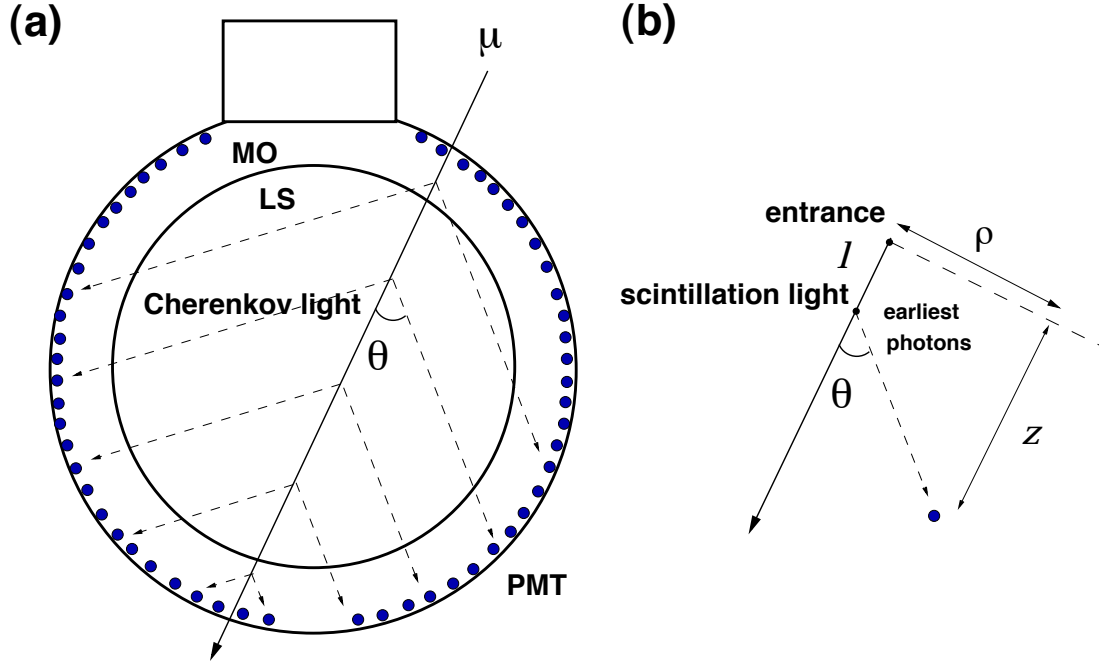


Figure 3.36: (a) Cherenkov photons are emitted from the constant θ (Cherenkov angle) related to the index of refraction. (b) In the scintillation photon case, the PMTs detect photons in all directions, however, the earliest photons come from the θ which corresponds to the Cherenkov angle.

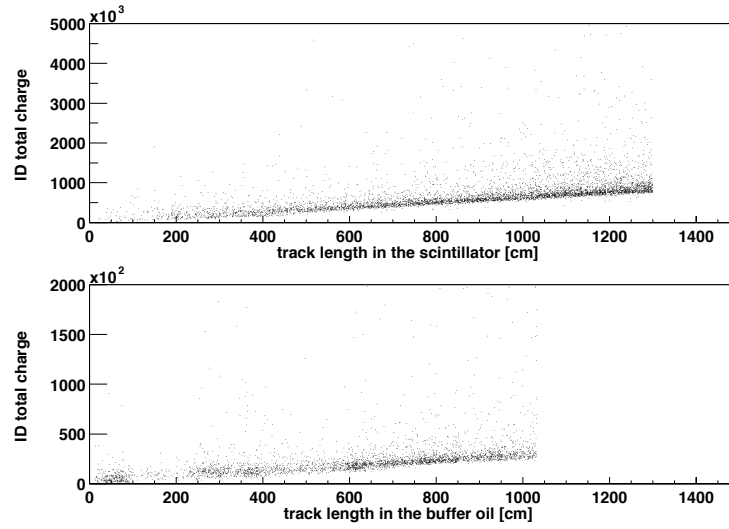


Figure 3.37: Correlations between the total charge in the inner detector and the muon track length, in the liquid scintillator (upper) and in the buffer oil (lower).

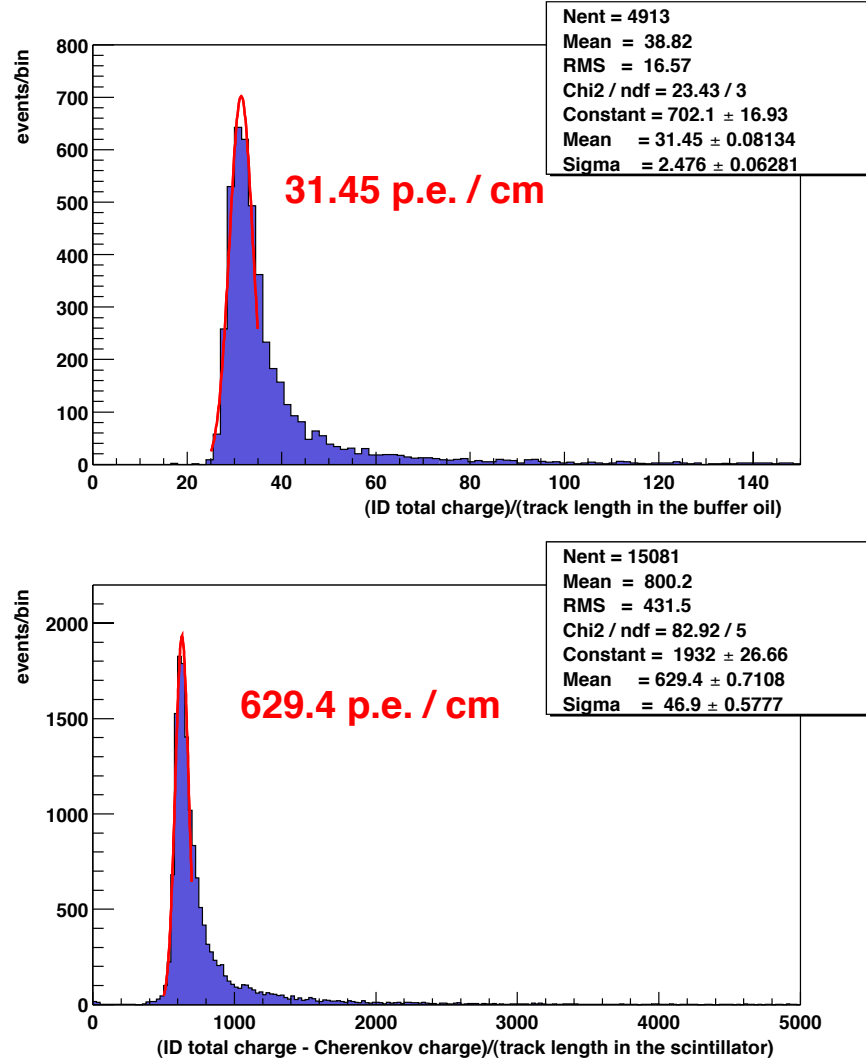


Figure 3.38: Normalized charge by reconstructed muon track length (dQ/dX). The ideal light emission per length is approximated by the mean of a Gaussian fit with a lower edge. Upper figure is for clipping muons and lower is for through going muons.

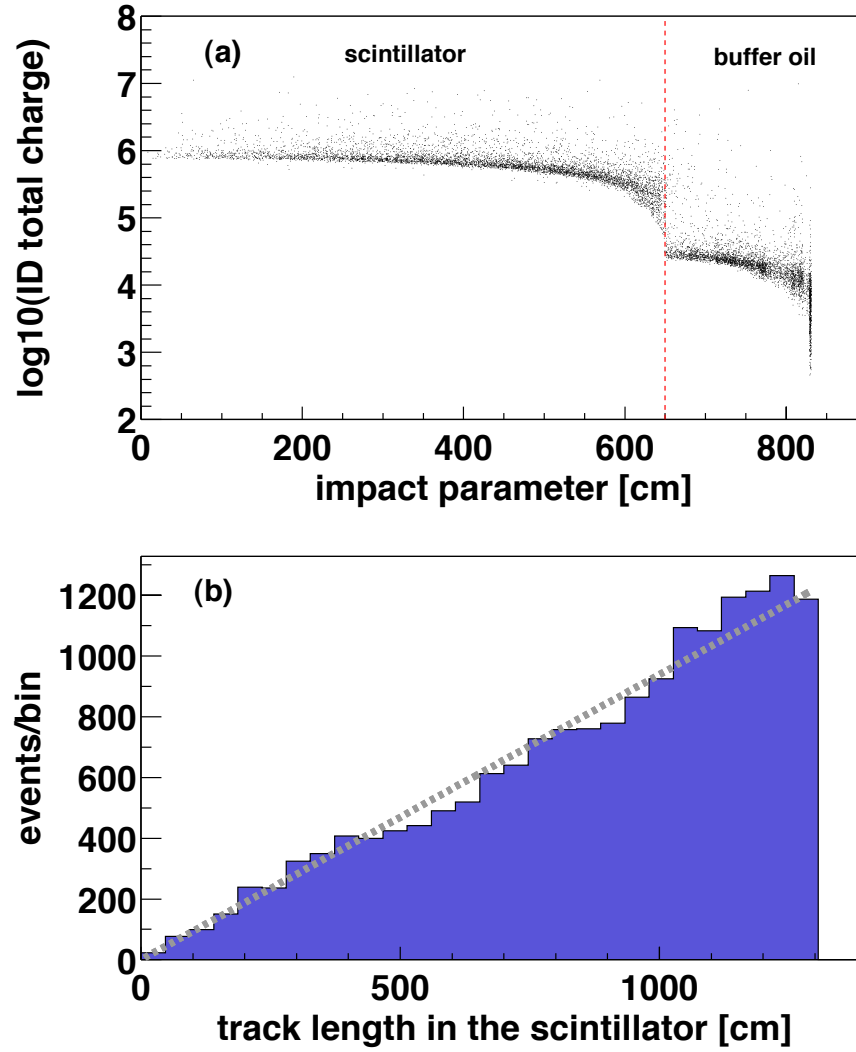


Figure 3.39: (a) Correlation between the total charge in the inner detector and the distance from the center to muon track (impact parameter). The lower edge in the scintillator region indicates the minimum ionization of muons. (b) Muon track reconstruction reproduces the linear distribution of the track length in the scintillator.

3.8 Reconstruction Quality

In real physics events, there are a good correlation among the reconstructed vertex, PMT position, time and charge if the event reconstruction succeeds. The badness of the reconstruction quality is parameterized, and it is used for the quality check of neutrino candidates. The bad quality event such as the noise event and flasher event are eliminated in advance.

3.8.1 Noise Event Selection

The ‘noise event’ is defined as the event which has no timing cluster in PMT hits. It is easily selected (Figure 3.41) using a following criterion,

$$n100 \leq (nhit + 50)/2 \quad (3.41)$$

where the ‘nhit’ means the number of PMT hits in a event and ‘n100’ means the number of the maximum PMT hits within a 100 nsec time window in a event. Most of noise events are created by unstable conditions of the data taking, the ringing problem of the electronics after muons or the data transfer problem during unexpectedly high trigger rate.

The accidental noise rate is calculated using the trigger rate (~ 250 Hz) of the low threshold special run, in which threshold is a 100 trigger hit, i.e. a half level of the normal run,

$$(\text{accidental noise rate}) = 250 \text{ Hz} \times 250 \text{ Hz} \times 100 \text{ nsec} \sim 6 \times 10^{-3} \text{ Hz} \quad (3.42)$$

and its rate is almost consistent with the actual noise rate $\sim 5 \times 10^{-3}$ Hz. The inefficiency for the normal run due to the noise selection cut is calculated using its trigger rate ~ 21 Hz,

$$(\text{inefficiency by noise cut}) = 21 \text{ Hz} \times 100 \text{ nsec} \sim 2 \times 10^{-4} \% \quad (3.43)$$

and assigned as the systematic uncertainty.

3.8.2 Flasher Event Selection

The ‘flasher event’ is caused by light emission from the PMT presumably due to discharge in dynodes. The surrounding PMTs detect the light from the flasher PMT (Figure 3.45). The flasher signal mimics the high energy event up to ~ 20 MeV, however, they are easy to select using the maximum of the PMT charge. The selection criteria are,

- Total charge in the inner detector ≥ 2500 p.e.
- Ratio of the maximum of the PMT charge to the total charge sum ≥ 0.6

as shown in Figure 3.45. The flasher event rate is 3×10^{-3} Hz, which corresponds to $\sim 0.01\%$ of total low energy events. Therefore, the inefficiency of the flasher cut is estimated to be less than 0.01%.

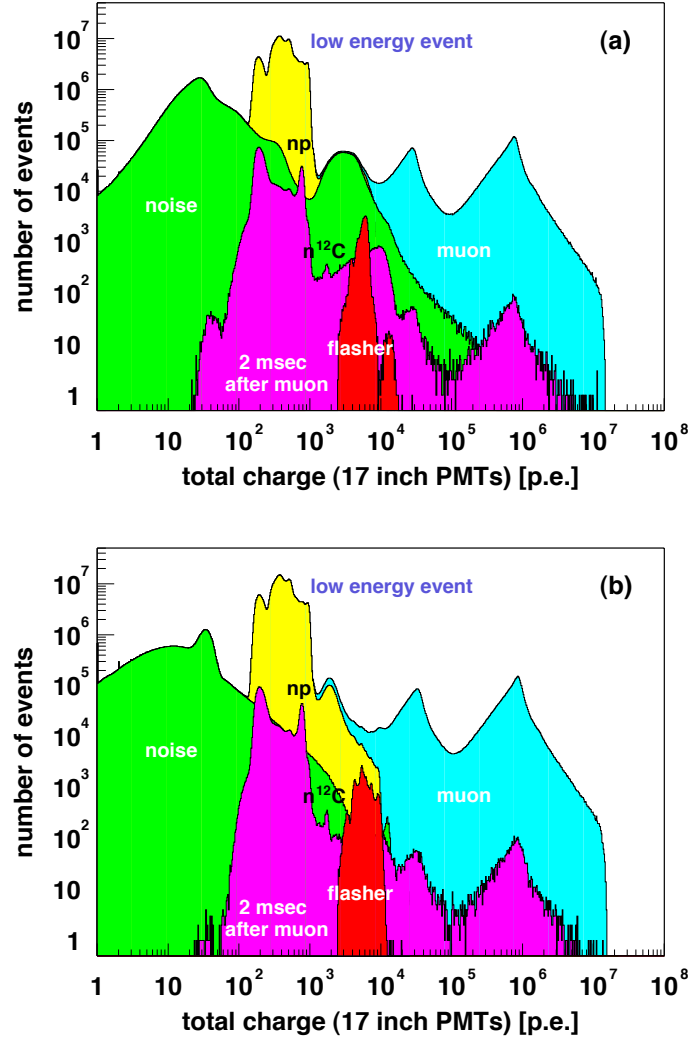


Figure 3.40: Distribution of various classified events with the total charge sum (17 inch PMTs) for (a) ‘before’ and (b) ‘after’ the electronics upgrade. The remarkable difference between ‘before’ and ‘after’ is the shape of the noise distribution. After the electronics upgrade, events at ~ 2000 p.e. is not selected by the noise selection criteria, $n_{100} \leq (n_{hit} + 50)/2$, but strongly suppressed by the short muon veto $\Delta T_{muon} < 1\mu\text{sec}$ because those events are caused by the ringing problem of the electronics after muons.

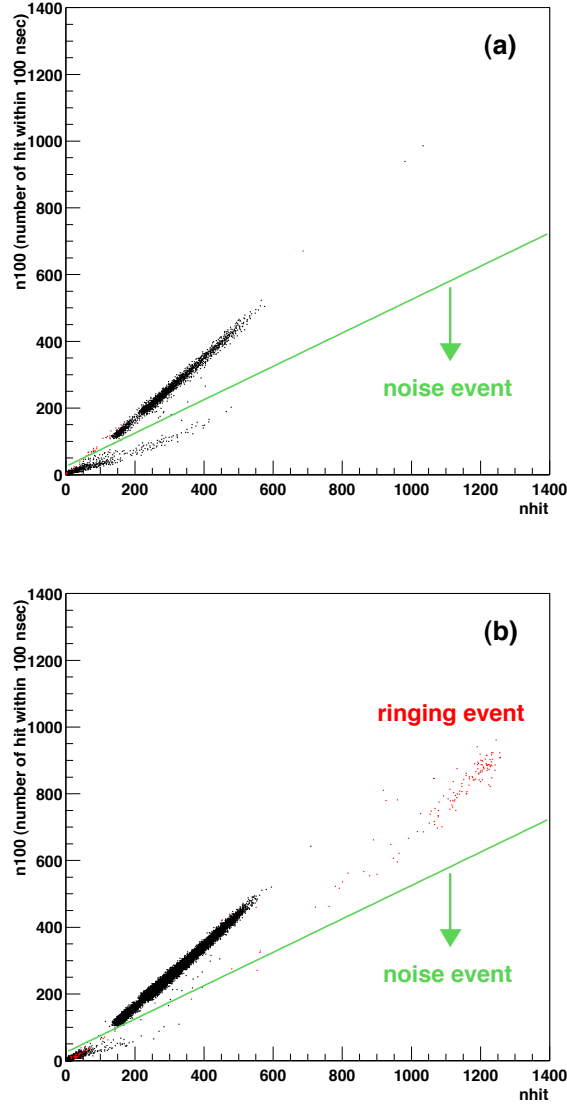


Figure 3.41: Noise event selection criteria with the low energy event. The ‘ $nhit$ ’ means the number of PMT hits in a event and ‘ $n100$ ’ means the number of the maximum PMT hits within a 100 nsec time window in a event. The solid line shows the noise selection criteria, $n100 \leq (nhit + 50)/2$. After the electronics upgrade, the ringing events appeared at the larger ‘ $nhit$ ’ region, selected by the $\Delta T_{muon} < 1\mu\text{sec}$ (red marker).

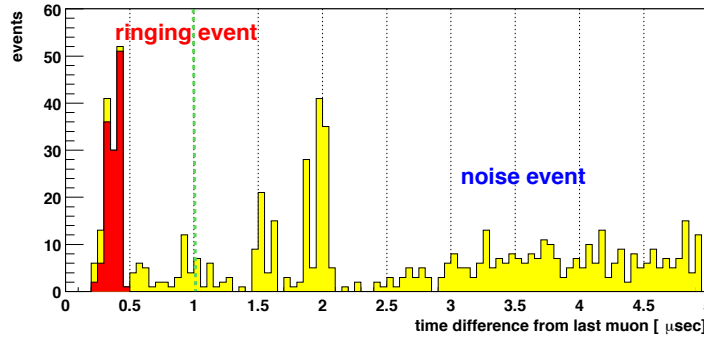


Figure 3.42: Ringing events selected by the $\text{nhit} > 600$ with the low energy event. Those events, which caused by the ringing problem of the electronics, are strongly suppressed by the muon veto $\Delta T_{\text{muon}} < 1\mu\text{sec}$.

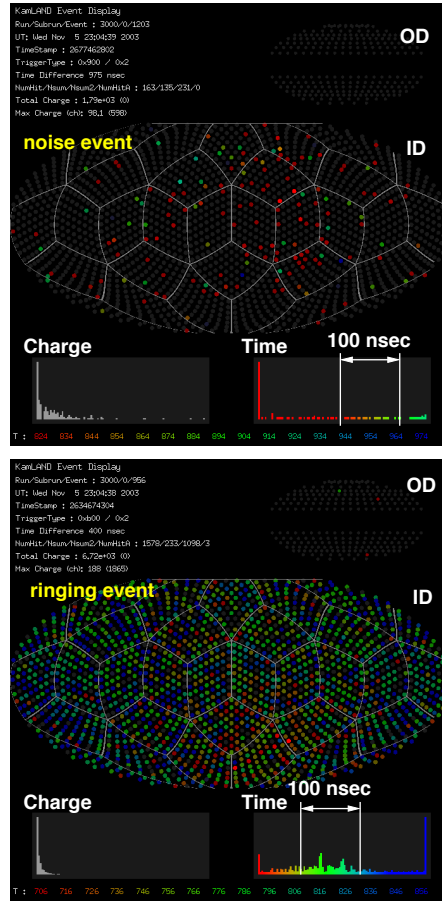


Figure 3.43: Event display of a typical noise event (upper) and ringing event (lower).

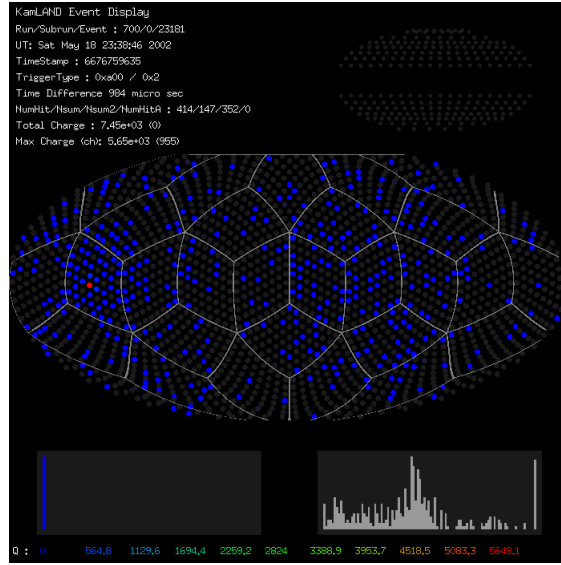


Figure 3.44: Event display of a typical flasher event.

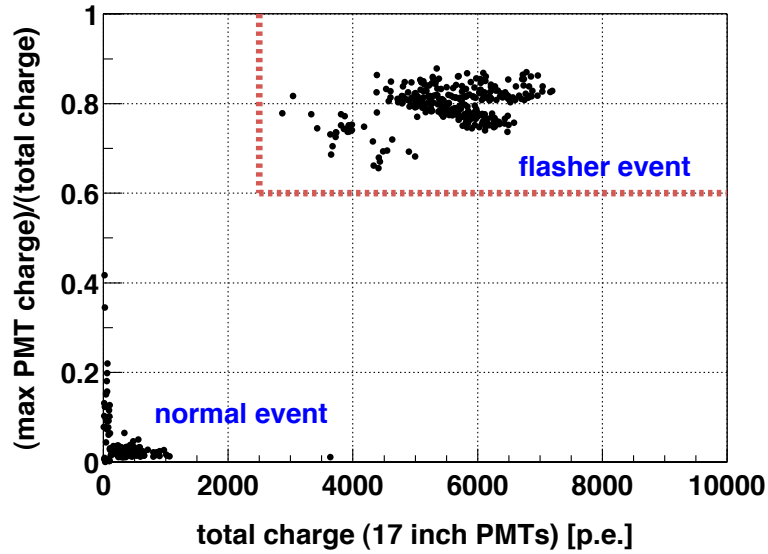


Figure 3.45: Flasher event selection criteria. The ‘max PMT charge’ means the maximum of the PMT charge of the inner detector in a event. The selection criteria require that the ratio of the ‘max PMT charge’ to the total charge be larger than 0.6 and the total charge be larger than 2500 p.e.

3.8.3 Estimation of Reconstruction Quality

For the reactor $\bar{\nu}_e$ events, the important parameters are the reconstructed vertex and energy. The reconstruction is based on the time and charge information of PMTs assuming its vertex is ‘point-like’. If the vertex is not point-like or is inconsistent with the expectation in the time or charge distribution, there is a possibility that it is an unphysical event related to the detector noise, accidentally reconstructed. However, those events have much worse reconstruction quality than the real ‘point-like’ events, so it is easy to discriminate.

The basic information for a event quality is the correlation between the reconstructed vertex, PMT position, time and charge (hit). The reconstruction quality of events within 1 m from the source position is verified with the time and charge distribution for various sources and positions, ^{60}Co (Figure 3.46, 3.47), ^{65}Zn (Figure 3.48, 3.49), ^{68}Ge (Figure 3.50, 3.51) and ^{203}Hg (Figure 3.52, 3.53). In the delayed coincidence detection, the time and charge are independent between prompt and delayed events except for the similar vertex. On the contrary the unphysical coincidence events due to the electronics ringing have the correlation between prompt and delayed events. It correlation is parameterized to see the quality of coincidence events. The parameters for estimation of the reconstruction quality are as follows [70],

- Reduced χ^2 for time-distance relation (χ_T^2)
There is a linear correlation between the time of PMT hits and the distance from the vertex to the PMT position as shown in Figure 3.54 (a). The slope corresponds to the inverse of a speed of light in the detector. The reduced χ^2 is evaluated for each event. For the typical low energy event (1 ~ 15 MeV), the χ_T^2 is less than 2. The much worse χ_T^2 means that the event was not a point-like event or the vertex reconstruction didn’t work correctly.
- Sigma and hight of time spectrum after the subtraction of the time of flight (σ_T , H_T)
The time distribution of PMT hits after the subtraction of the time of flight reproduces the time spectrum of the scintillation light emission, which including the transit time spread (TTS) of PMTs and the resolution of the vertex reconstruction. Its spectrum is shown in Figure 3.54 (b). The width of the spectrum σ_T is parameterized by the r.m.s. in 48 nsec. The peak hight H_T (maximum number in 4 nsec / 4 nsec / total number in 48 nsec) is also shown. For the typical low energy event, the σ_T is 8 ~ 11 nsec. The much larger σ_T means that the event was not a point-like event or the vertex reconstruction didn’t work correctly.
- Reduced χ^2 for charge-distance relation (χ_Q^2)
The correlation between the charge and the distance from the vertex to the PMT position is shown in Figure 3.54 (c). The expectation is calculated from the expected charge used in the energy estimation (Section 3.6). The reduced χ^2 is evaluated for each event. For the typical low energy event, the χ_Q^2 is less than 2. If the χ_Q^2 is much worse, the energy estimation is not reliable.
- Reduced χ^2 for occupancy-distance relation (χ_P^2), and ratio of number of total hits to its expectation (R_P)
The number of hit information can be substituted for the charge information. In the

low energy event, the ratio of the hit number to the total number of PMTs (occupancy) is a good parameter for the estimation of expected number of photo-electrons (expected charge). The occupancy can be also a parameter of the reconstruction quality. The correlation between the occupancy and the distance from the vertex to the PMTs is shown in Figure 3.54 (d). The occupancy is calculated for each bin, and its expected is given by

$$(\text{expected occupancy with Poisson probability}) = 1 - e^{-\mu} \quad (3.44)$$

where μ is the expected photo-electrons calculated as follows,

$$\mu = (\text{total expected charge in the bin}) / (\text{total number of PMTs in the bin}). \quad (3.45)$$

The reduced χ^2 is calculated from the scaled expectation with Poisson probability (χ_P^2). The ratio of the number of total hit to the integrated expected occupancy (R_P), which corresponds to the overall deviation of number of hits, is also shown.

- Sigma of distribution of charge divided by expected (σ_Q), hit ratio (R_{N150} , R_{N48})
The parameter is similar to the χ_Q^2 , but the parameter distance is degenerated. The distribution of charge divided by the expected charge is shown in Figure 3.54 (e). The width of the distribution is parameterized by the r.m.s. If the σ_Q is much larger, the energy estimation is not reliable. The ratio of the number of hit within 150 nsec to the NsumMax (R_{N150}), and number of hit within 48 nsec to within 150 nsec (R_{N48}) are evaluated.
- Correlation coefficients between prompt and delayed events
In the coincidence detection, there is a possibility that the electronics ringing events become backgrounds. In order to check the ringing effect, the correlation coefficients between prompt and delayed events for the hit channel, the timing after the subtraction of the time of flight and charge are parameterized as shown in Figure 3.54 (f). The space and time correlation between prompt and delayed events are also shown. The larger correlation coefficients means the unphysical coincidence event possibly due to the ringing of electric circuit.

The overall badness is estimated from above 9 parameters related to the event quality. The badness is calculated for each event, on the other hand, the correlation coefficients between prompt and delayed events are calculated for each coincidence event. Reconstruction quality of a typical neutrino coincidence event is checked using those parameters (Figure 3.55). All neutrino candidates are checked with those parameters to confirm that the candidates were physical events. The Am-Be source coincidence event is very similar to neutrino candidate events (Figure 3.56). On the contrary the unphysical noise event has very bad time and charge distribution (Figure 3.55). The noise event is selected by the cut $n100 \leq (n\text{hit} + 50)/2$ described in Section 3.8.1. The ringing event also has bad distribution (Figure 3.58). There are correlations in time and charge between successive events, and that strongly indicates the ringing of electric circuit. The flasher event has a little good time and charge distribution. However, its χ^2 is very bad because the light emission is not isotropic. The flasher event is selected by the cuts described in Section 3.8.2.

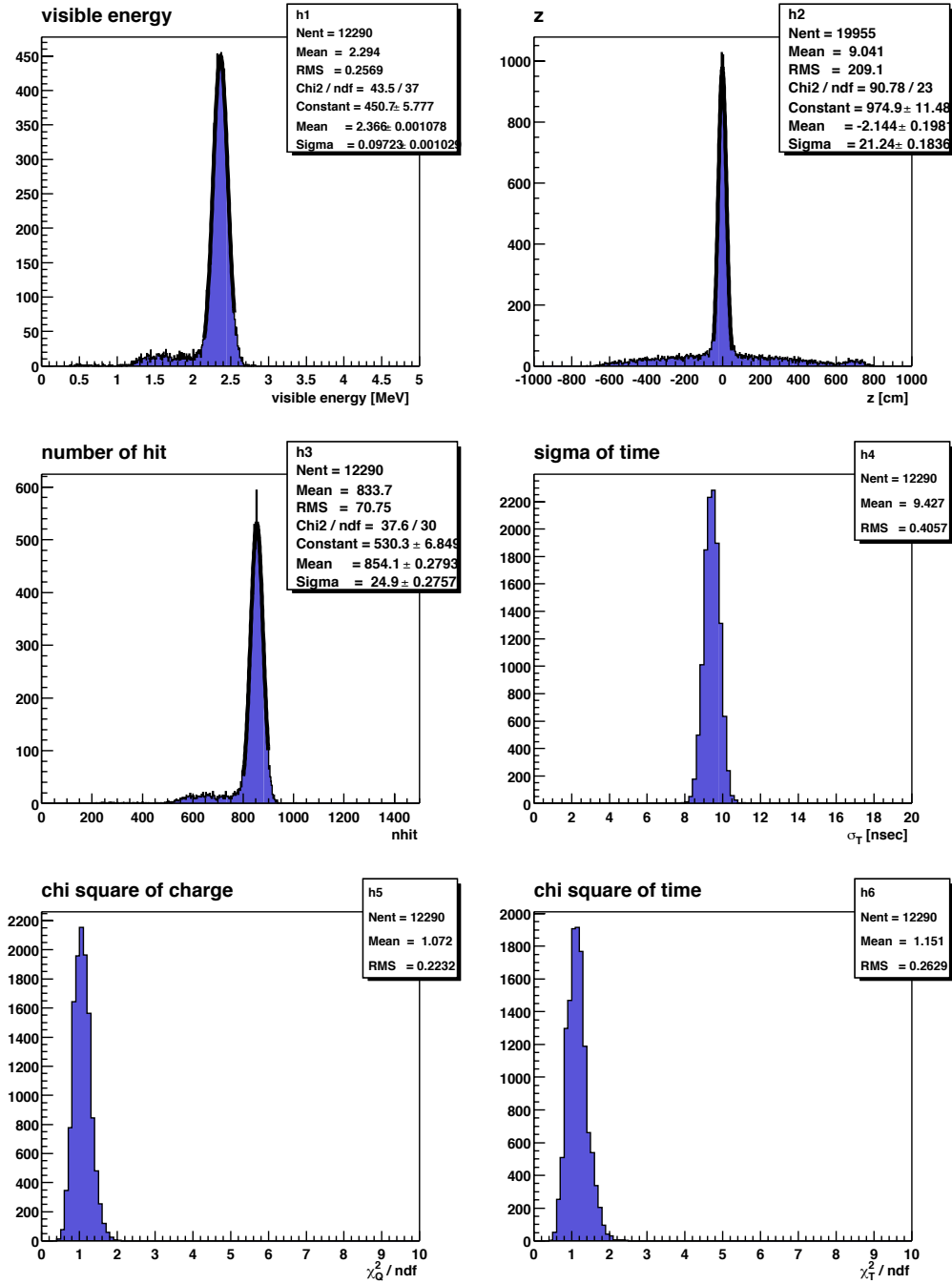
Co at center

Figure 3.46: ^{60}Co (2γ , $1.173 + 1.333$ MeV) at the center position : visible energy, reconstructed z position, number of PMT hits, sigma of time, reduced χ^2 of charge, reduced χ^2 of time.

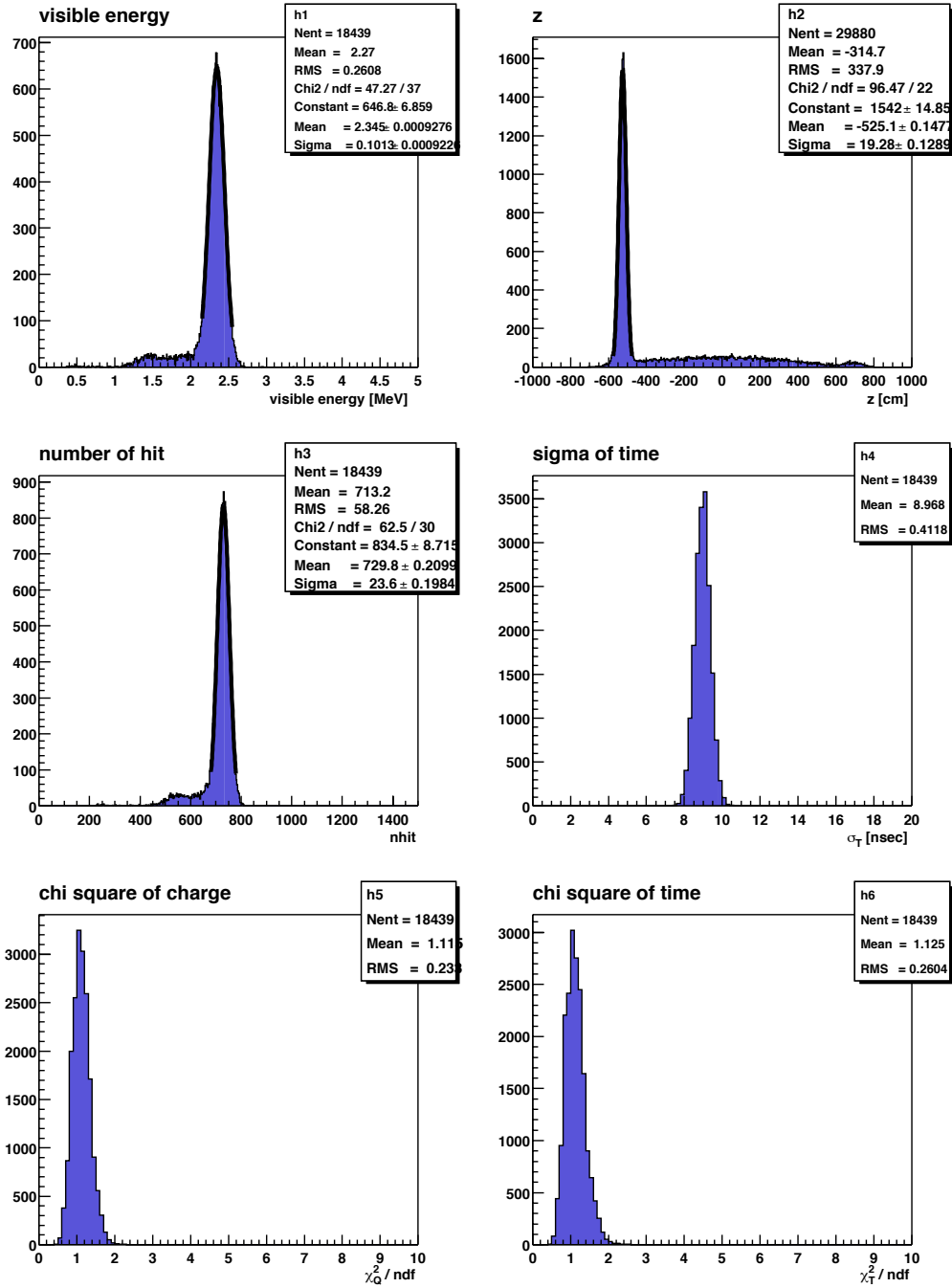
Co at $z = -5.25$ m

Figure 3.47: ^{60}Co (2γ , $1.173 + 1.333$ MeV) at $z = -5.25$ m : visible energy, reconstructed z position, number of PMT hits, sigma of time, reduced χ^2 of charge, reduced χ^2 of time.

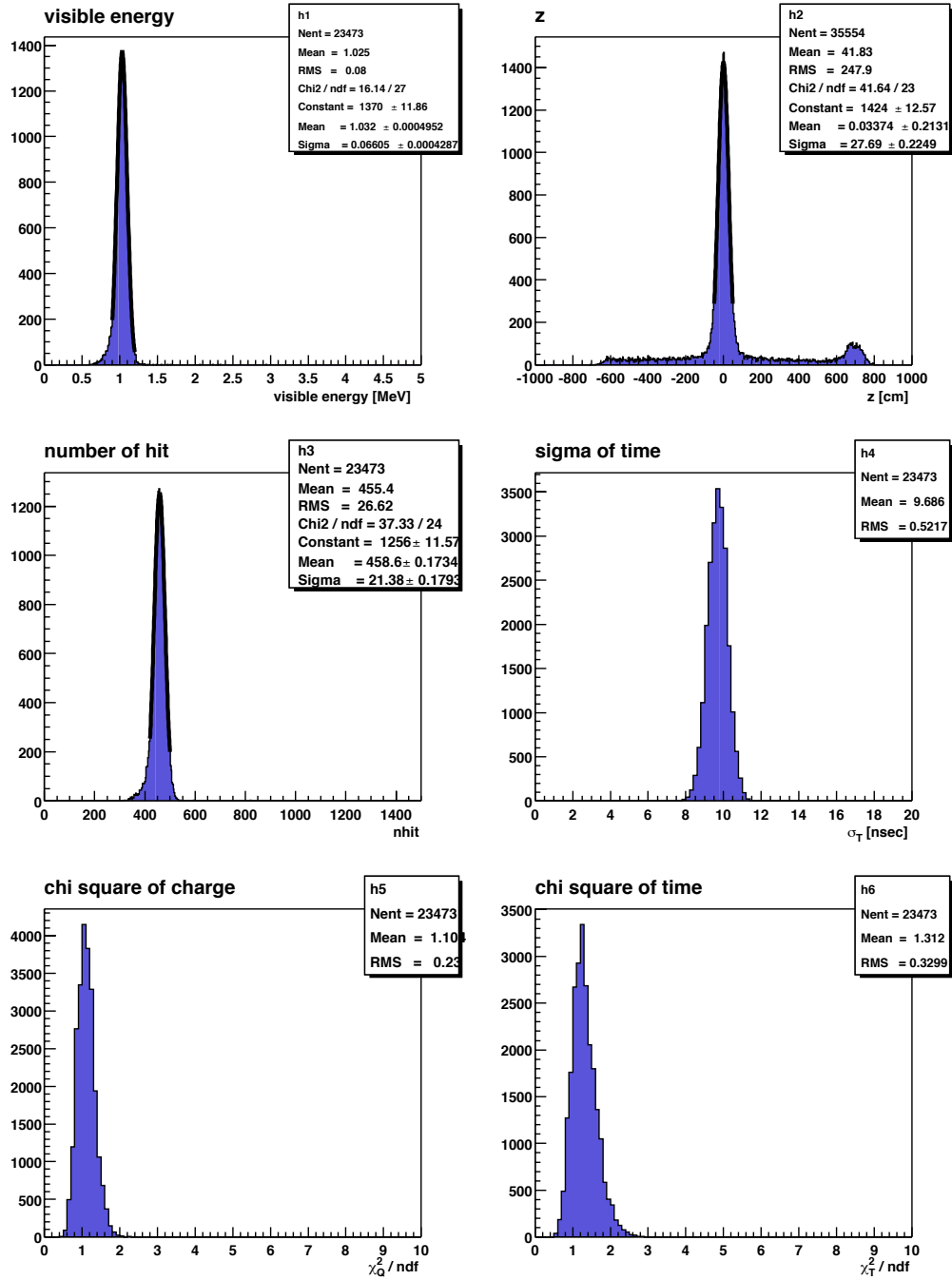
Zn at center

Figure 3.48: ^{65}Zn (1γ , 1.11552 MeV) at the center position : visible energy, reconstructed z position, number of PMT hits, sigma of time, reduced χ^2 of charge, reduced χ^2 of time.

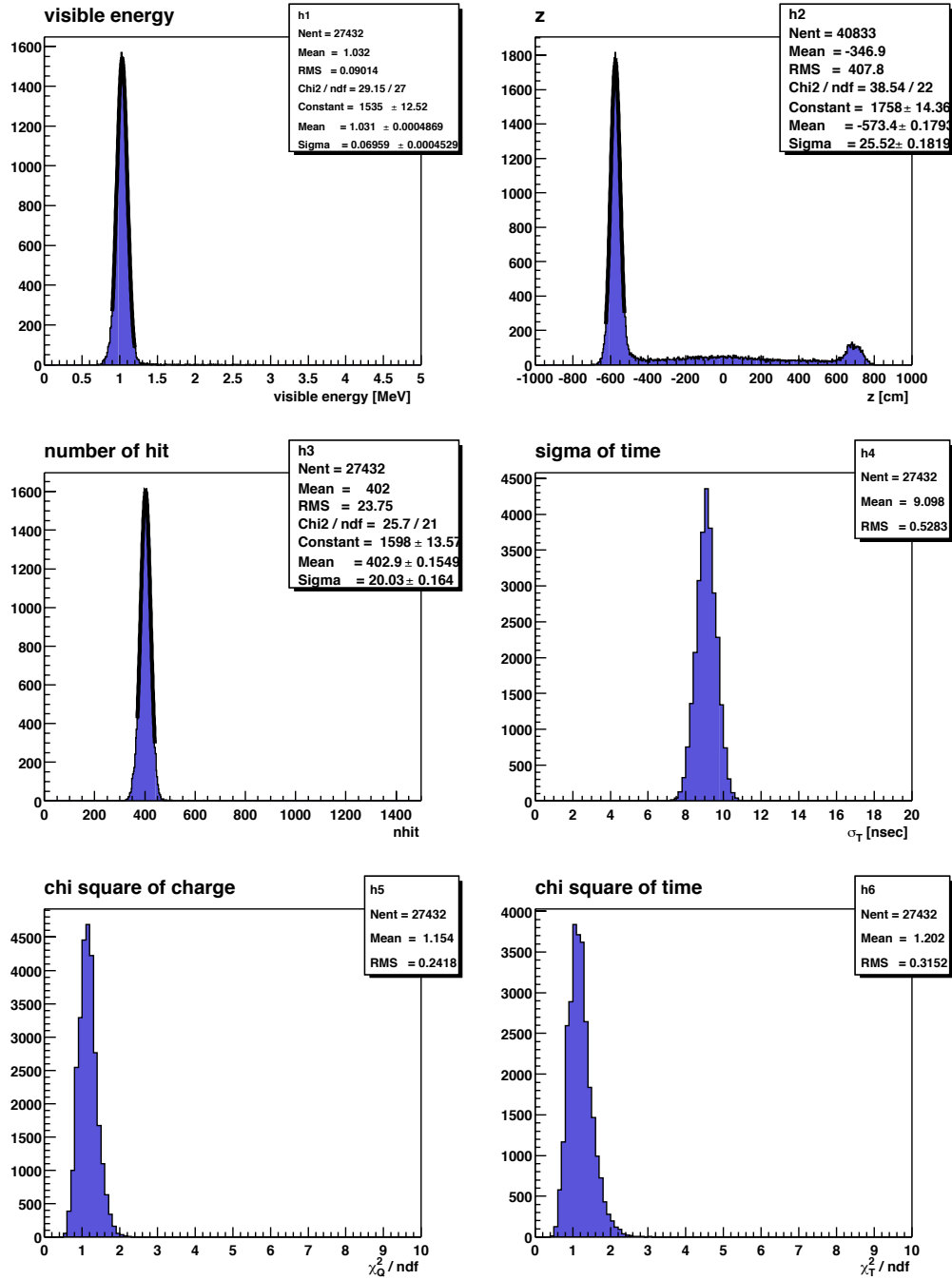
Zn at $z = -5.75$ m

Figure 3.49: ^{65}Zn (1γ , 1.11552 MeV) at $z = -5.75$ m : visible energy, reconstructed z position, number of PMT hits, sigma of time, reduced χ^2 of charge, reduced χ^2 of time.

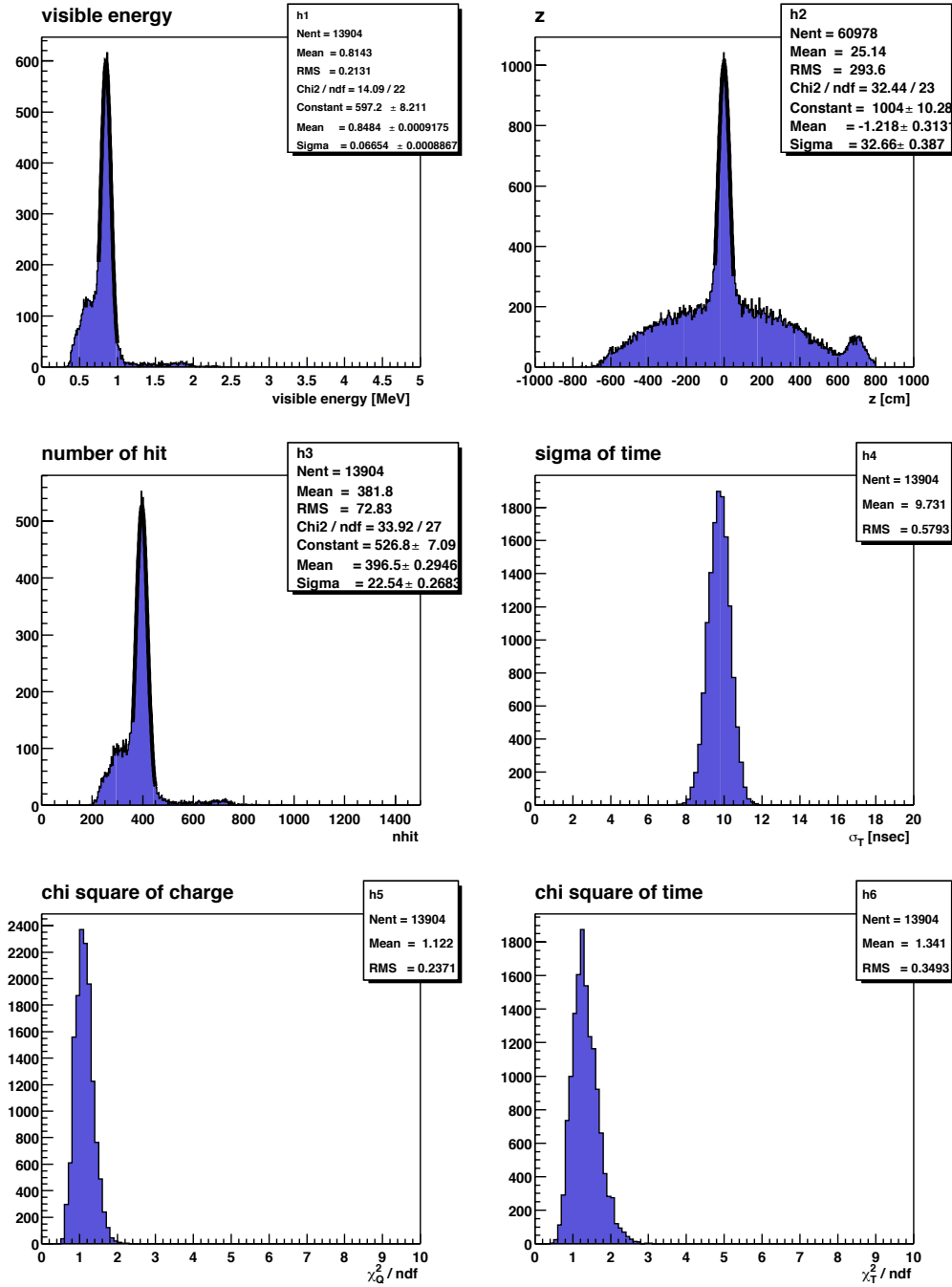
Ge at center

Figure 3.50: ^{68}Ge (2γ , 0.511×2 MeV) at the center position : visible energy, reconstructed z position, number of PMT hits, sigma of time, reduced χ^2 of charge, reduced χ^2 of time.

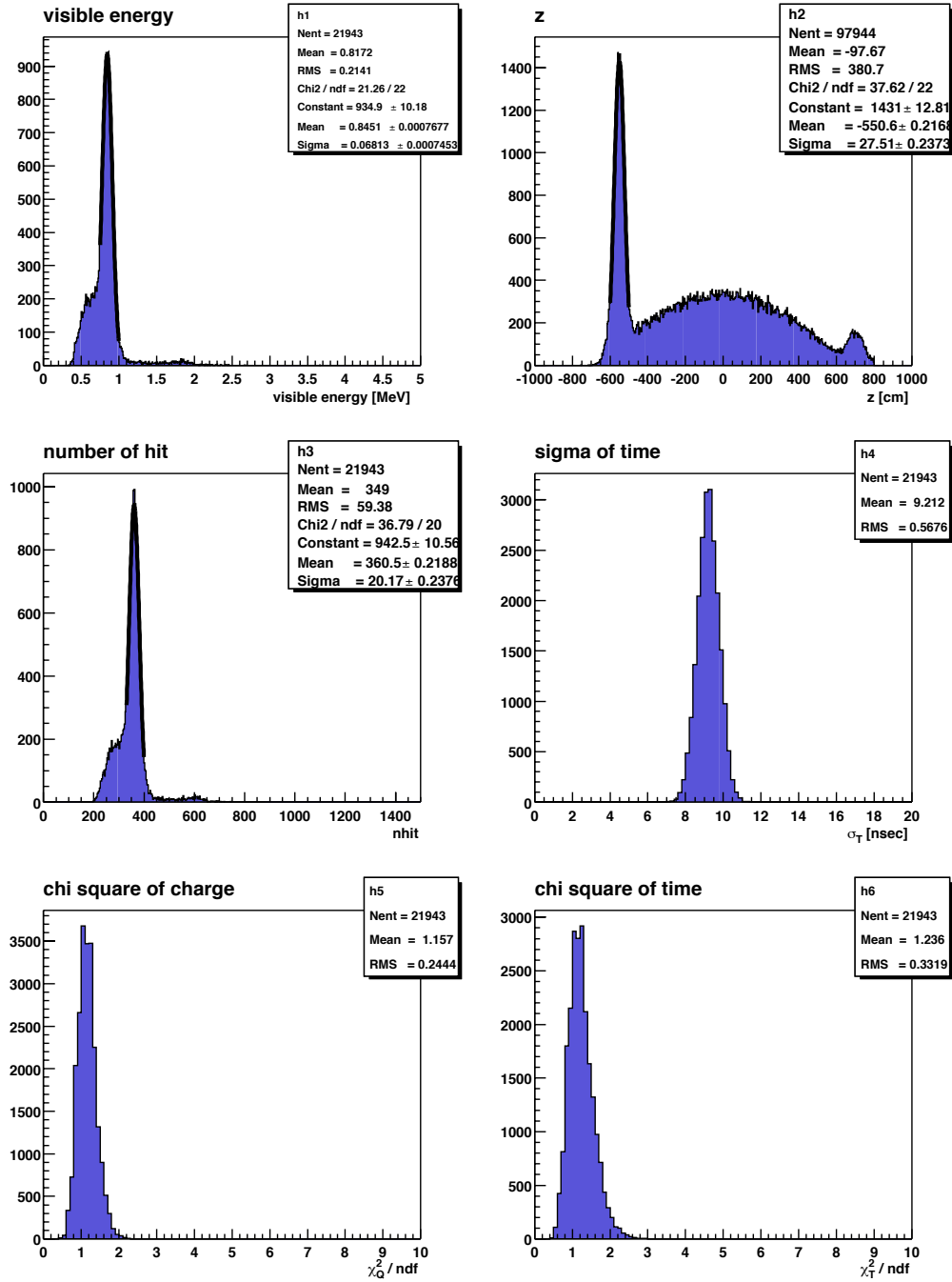
Ge at $z = -5.5$ m

Figure 3.51: ^{68}Ge (2γ , 0.511×2 MeV) at $z = -5.5$ m : visible energy, reconstructed z position, number of PMT hits, sigma of time, reduced χ^2 of charge, reduced χ^2 of time.

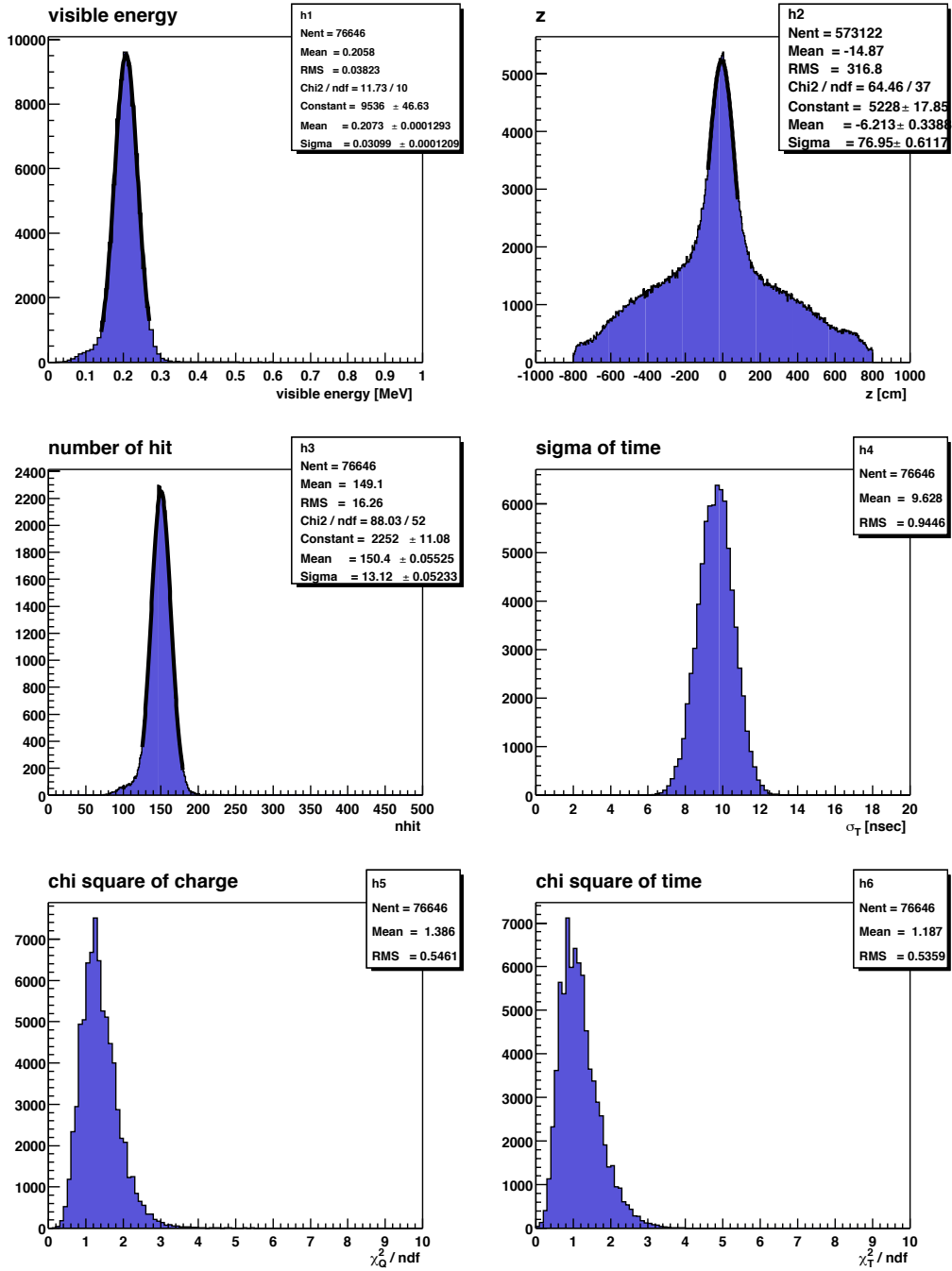
Hg at center

Figure 3.52: ^{203}Hg (1γ , 0.279197 MeV) at the center position : visible energy, reconstructed z position, number of PMT hits, sigma of time, reduced χ^2 of charge, reduced χ^2 of time.

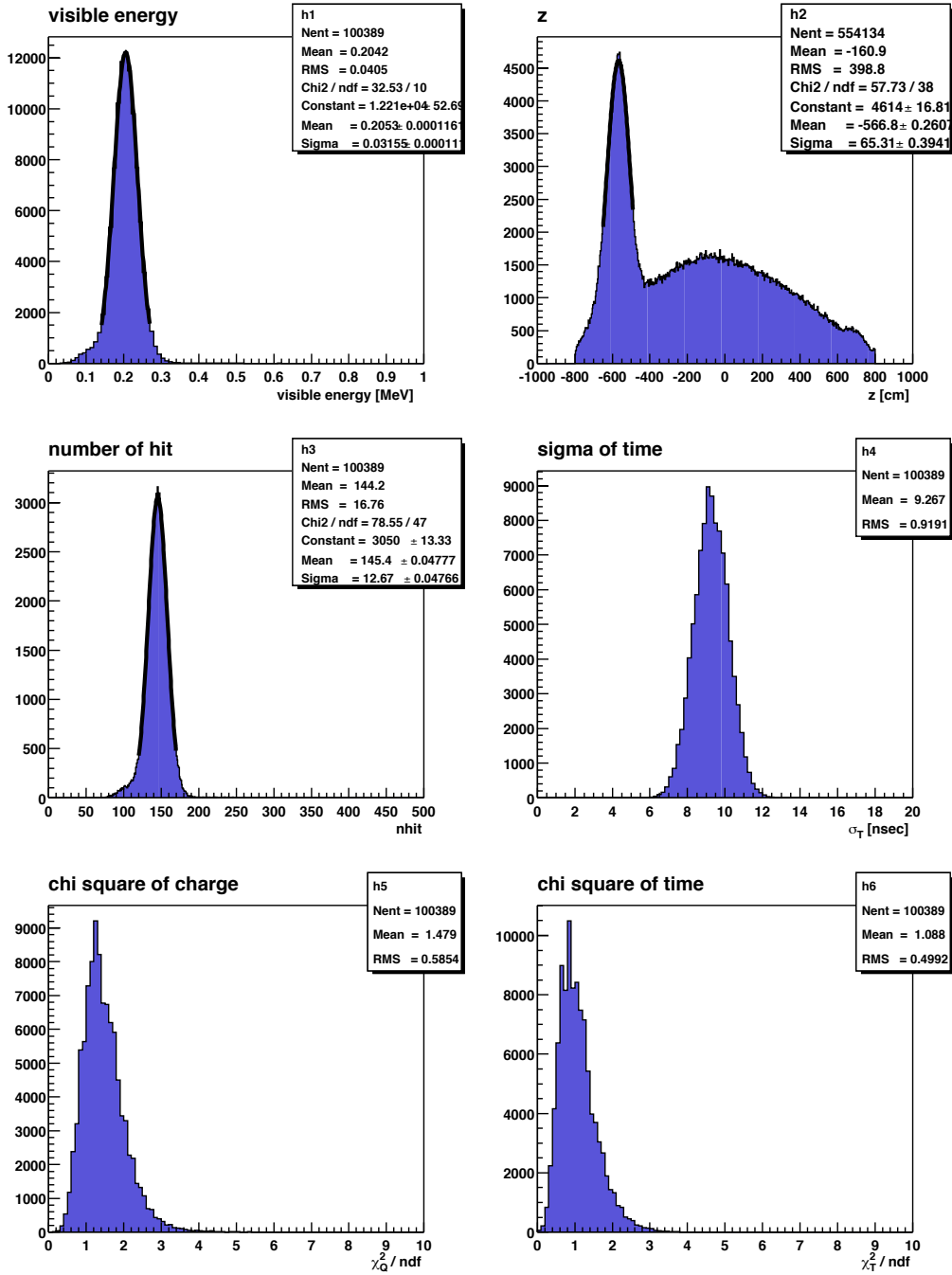
Hg at $z = -5.5$ m

Figure 3.53: ^{203}Hg (1γ , 0.279197 MeV) at $z = -5.5$ m : visible energy, reconstructed z position, number of PMT hits, sigma of time, reduced χ^2 of charge, reduced χ^2 of time.

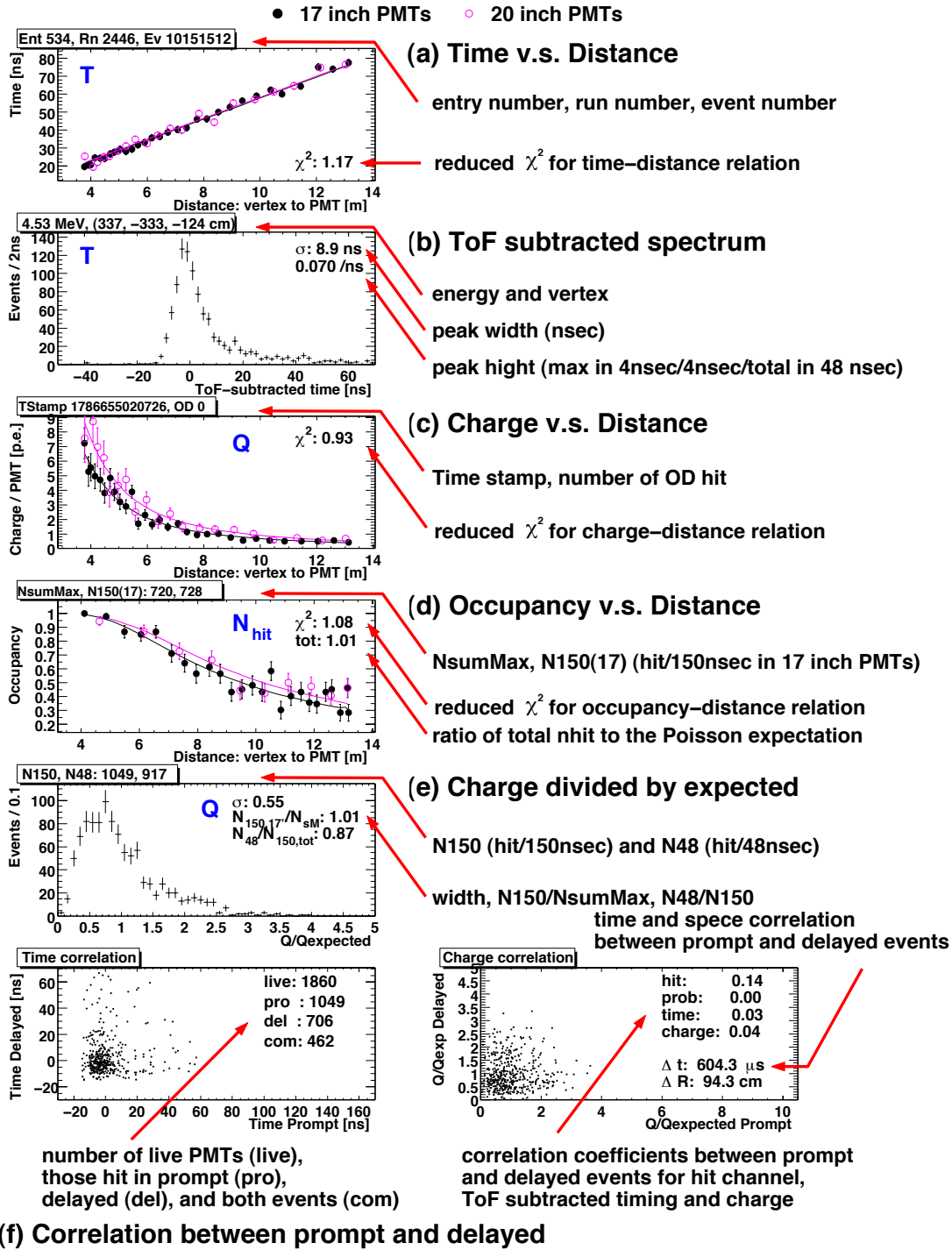


Figure 3.54: Explanation of criteria of the reconstruction quality check. All reactor $\bar{\nu}_e$ candidates are checked with those criteria in order to confirm that the candidates were physical events.

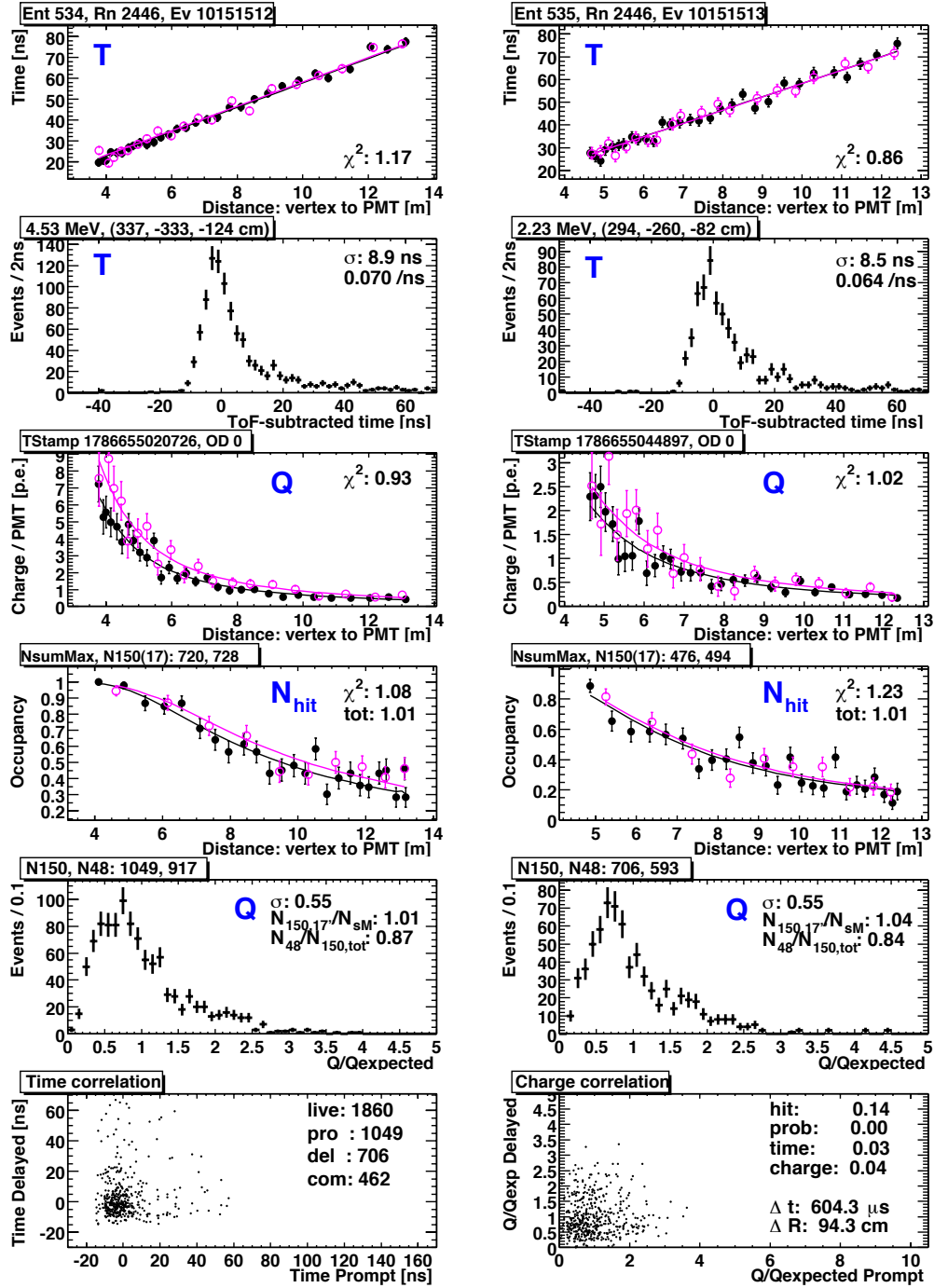


Figure 3.55: Reconstruction quality of a typical neutrino coincidence event.

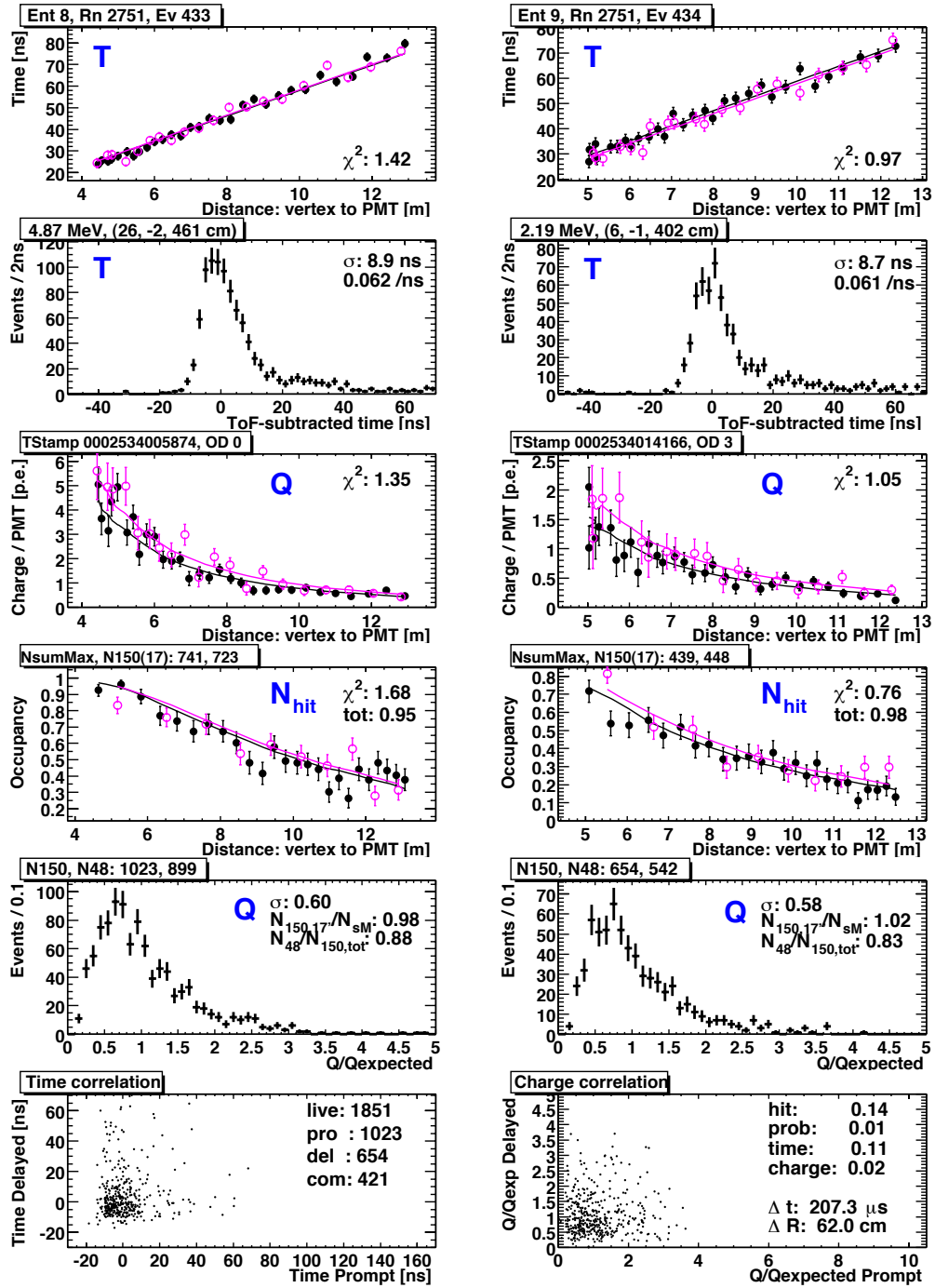


Figure 3.56: Reconstruction quality of a typical Am-Be source coincidence event.

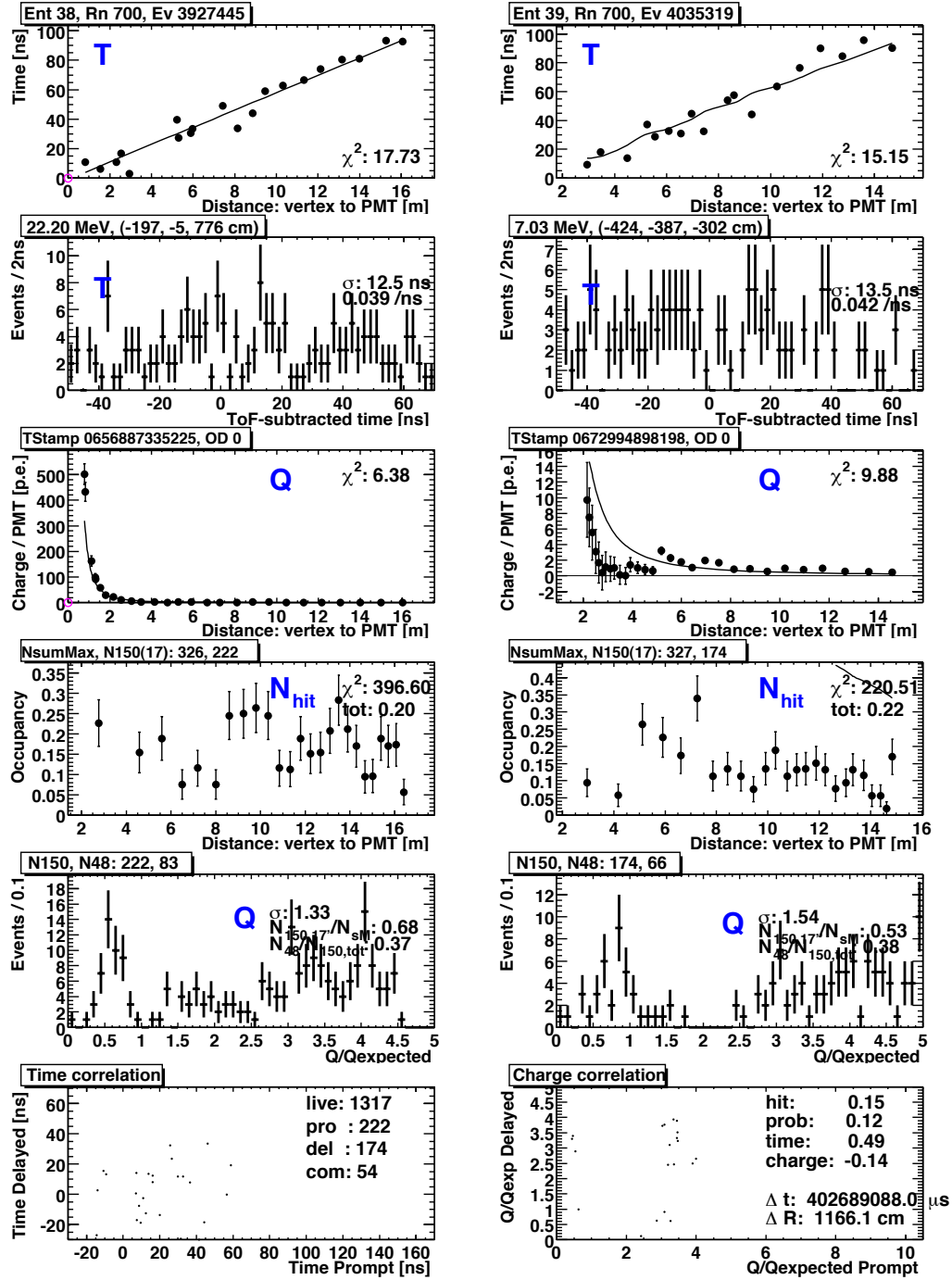


Figure 3.57: Reconstruction quality of a typical noise coincidence event.

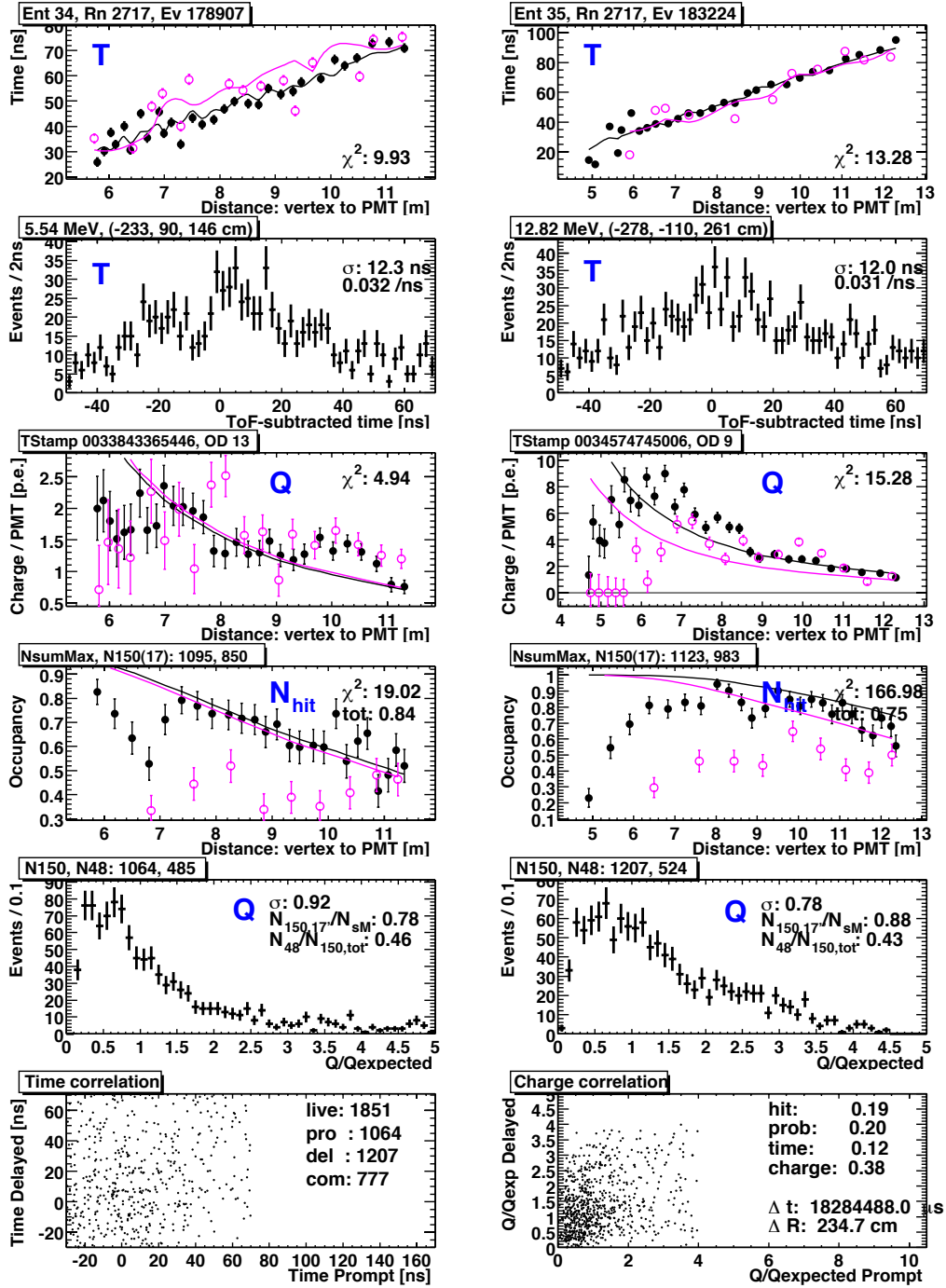


Figure 3.58: Reconstruction quality of a typical ringing coincidence event.

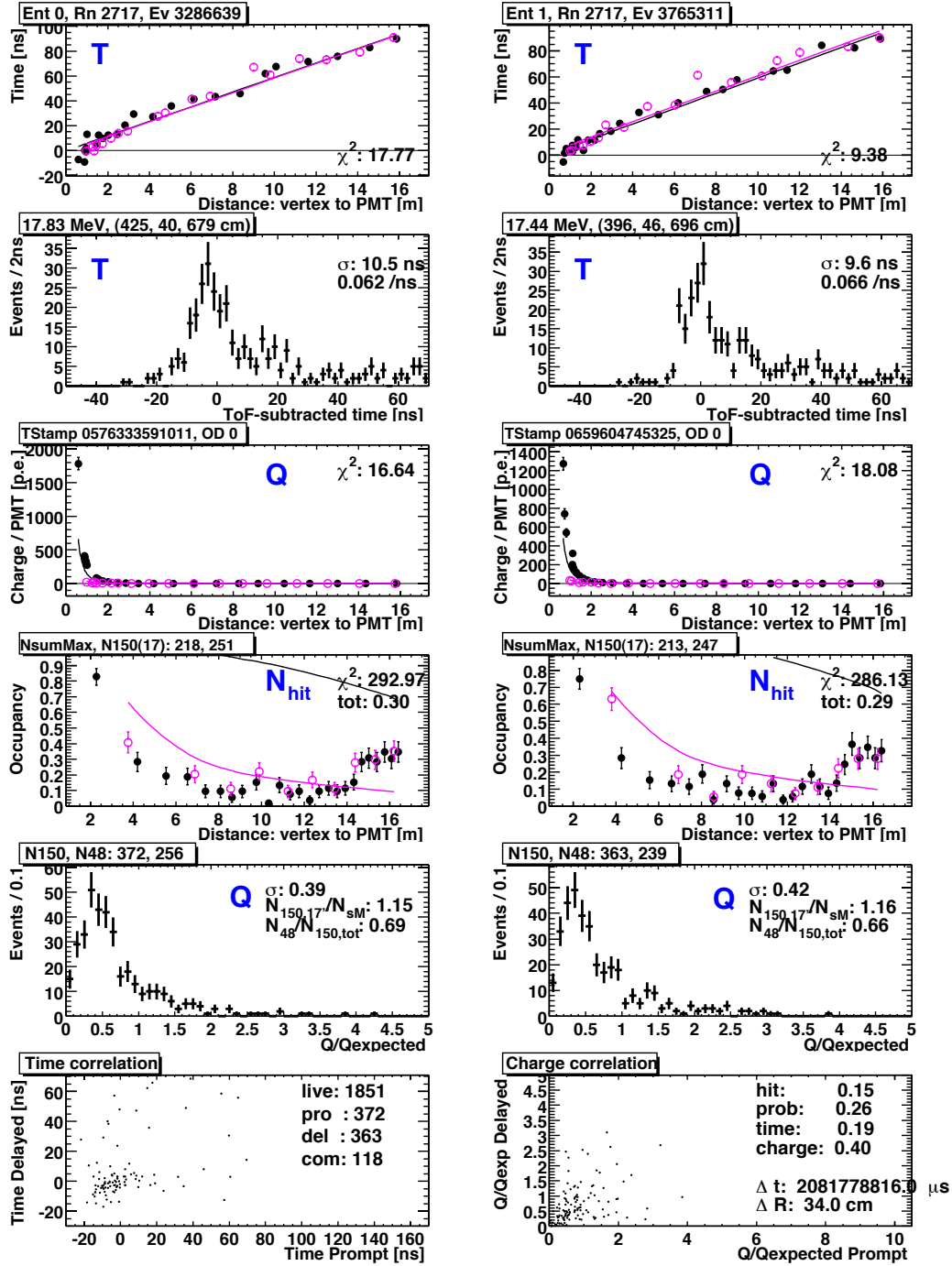


Figure 3.59: Reconstruction quality of a typical flasher coincidence event.

Chapter 4

Background Estimation

The electron anti-neutrinos are identified by the delayed coincidence using the prompt scintillation light from the e^+ and the delayed 2.2MeV γ -ray from neutron capture on hydrogen. There are various radioactivities in the detector. Main radioactive impurities are ^{238}U , ^{232}Th , ^{40}K , and ^{85}Kr in the scintillator, γ -ray of ^{40}K and ^{208}Tl from the balloon or outside of the detector. Cosmic-ray muons create various spallation products, neutrons and β -decay nuclei and neutron emitters (^8He and ^9Li). Some spallation neutrons are produced in the rock or the outer detector and come into the inner detector.

For the reactor $\bar{\nu}_e$ detection, the background events can be classified into two types. The first is correlated events related to neutrons produced by muons or α -rays, spallation products with neutron emitters, short life nuclei, spontaneous fission of nuclei and other $\bar{\nu}_e$ sources. The second is uncorrelated events (accidental events). Fiducial cut criteria are decided by the accidental background.

The backgrounds for reactor $\bar{\nu}_e$ detection is summarized in Table 4.1. The backgrounds are categorized,

- Accidental

There are various radioactivities, which make accidental coincidence. The events around the balloon and the center of the detector are dominant, because of the 2.6 MeV γ (^{208}Tl) from the outer and radiation from a thermometer at the center.

- $^8\text{He}/^9\text{Li}$

The muon rate is ~ 0.34 Hz, and the spallation production rate is estimated by a muon bombing experiment [72]. ^8He and ^9Li are neutron emitters with mean life time of 171.7 msec and 257.2 msec. These events are selected using the delayed coincidence and time correlation to parent muons.

- Fast neutron

The fast neutron events are selectable as delayed coincidence events with outer detector muon tag. The fast neutron strongly recoils proton, and makes a prompt signal. The outer detector has small inefficiency, so the miss-tagging events are possible backgrounds

for $\bar{\nu}_e$. The contribution from a muon passing only the surrounding rock are considered separately.

- (α, n)

The main (α, n) reaction is $^{13}\text{C}(\alpha, n)^{16}\text{O}$. The dominant alpha source is ^{210}Po . The number of target ^{13}C is calculated from the composition of liquid scintillator and the natural abundance of ^{13}C , 1.1%. The prompt signal is made by the recoil proton and the γ -rays from the excited states of ^{16}O and the inelastic reaction of $^{12}\text{C}(n, n\gamma)^{12}\text{C}$.

- (γ, n)

The photodisintegration of nuclei is estimated. The reaction $^2\text{H}(\gamma, n)\text{p}$ is dominant because its energy threshold (2.22 MeV) is small. The prompt events can be generated by the proton and neutron, whose total kinetic energies are $(E_\gamma - 2.22)$ MeV.

- Spontaneous fission

The spontaneous fission of ^{238}U can be a background source. The upper limit of ^{238}U decay rate is estimated from the ^{234}Pa decay rate, assuming the radiation equilibrium of the ^{238}U chain down to ^{234}Pa . Most of those events are identified as the triple coincidence, because the fission reaction is observed as the multiple neutron events. In the reactor $\bar{\nu}_e$ analysis, the multiple neutron events are vetoed (Section 5.7.1), so only the single neutron events contribute to backgrounds.

- Atmospheric $\bar{\nu}_e$

The $\bar{\nu}_e$ events from the atmospheric neutrinos at the low energy regions should be estimated. The conservative background rates of the atmospheric neutrinos are estimated by a typical flux calculation model.

- Geo $\bar{\nu}_e$

The $\bar{\nu}_e$ emitted by ^{238}U and ^{232}Th decays in the crust and mantle of the earth, called ‘geo-neutrinos’, contribute to low energy events less than 2.6 MeV prompt energy. Observation of the geo-neutrino is important for understanding the earth energetics, and this is one of the purposes of our experiment. The evaluation of the geo-neutrino contribution is based on the amount of the radioactivities from geo-chemical estimation. However, that estimation has very large uncertainty. Therefore, in this thesis, the data above 2.6 MeV prompt energy are analyzed.

- Neutral current (NC) reaction of atmospheric neutrinos and solar neutrinos

Neutrino-disintegration of nuclei with NC reaction produces neutrons and makes backgrounds. The largest contribution comes from high energy neutrinos, such as atmospheric neutrinos. Those reaction rate are estimated to be ~ 20 events/year, however most of the events are very high energy. Solar neutrinos give low energy NC reaction. The deuteron disintegration rate is evaluated to be 0.76 events from the SSM flux, but those visible energies are very small. Thus these backgrounds are negligible.

The detail of the reactor $\bar{\nu}_e$ background estimation is in Section 4.3.

Table 4.1: Summary of Backgrounds for $\bar{\nu}_e$ (events / data-set)

Background	0.9 MeV analysis threshold (LAT)	2.6 MeV analysis threshold (HAT)
Accidental	134.82 ± 0.05	2.69 ± 0.02
$^8\text{He}/^9\text{Li}$	5.61 ± 1.07	4.82 ± 0.92
Fast neutron	< 0.89	< 0.89
(α , n)	-	10.31 ± 7.14
(γ , n)	< 0.039	< 0.039
Spontaneous fission	< 0.4	< 0.4
Atmospheric $\bar{\nu}_e$	2.6×10^{-4}	2.6×10^{-4}
Geo $\bar{\nu}_e$		
(i) 0 TW	0	0
(ii) 16 TW	42.8	0.18
(iii) 30 TW	80.3	0.34
total		
w/o Geo $\bar{\nu}_e$	-	17.82 ± 7.26

4.1 Backgrounds for Single Events

The backgrounds for single events are mainly caused by the radioactivities in the liquid scintillator and the spallation products related to muons. The understanding of the single events is important to grasp the background status in KamLAND. Figure 4.1 shows the energy spectrum for various fiducial volume, where the events within 2 msec following muons are vetoed to remove spallation neutron events or bad quality events during the electronics dead time. The fiducial radius cut is effective to suppress external radiations. There are two peaks, possibly corresponding to the γ -rays from ^{208}Tl (2.62 MeV) and ^{40}K (1.46 MeV). The most of ^{208}Tl γ -rays are emitted from the outside of the detector, because there is a huge amount of radioactive isotopes of ^{232}Th , which has the daughter isotope of the ^{208}Tl in the surrounding rock. On the other hand, the most of ^{40}K γ -rays are emitted from the balloon, especially its ropes. Their concentration are given in Table 4.2 measured by the ICP-MASS. The measured rates for ^{40}K γ -rays and ^{208}Tl γ -rays ($2 < E < 3$ MeV) from the outside are about 0.86 Hz and 2.8 Hz, respectively. Both external γ -rays are strongly suppressed by the fiducial radius cut as shown in Figure 4.1. The ^{40}K may contribute to backgrounds for the reactor $\bar{\nu}_e$ around 1.46 MeV in the prompt energy, however the ^{208}Tl is background for both prompt energy and delayed energy 1.8 \sim 2.6 MeV. Figure 4.2 shows the vertex distributions of various energy events. In the energy region of ^{208}Tl and ^{40}K γ -rays, the attenuation of external γ -rays can be seen. The central cylinder region is intensive because of thermometers and its cable, which are deployed at the center, $z = +5.5$ m and $z = -5.5$ m. The events in 1.5 \sim 4 MeV vanish after cylinder cut and thus are caused by the thermometers as shown in Figure 4.1. The high energy region is dominated by the long-lived spallation products produced by cosmic ray muons. The detail

of the spallation study is described in Section 4.2. Below 1 MeV, the distribution of events is uniform as in Figure 4.2 (f). In this energy region, the background is dominated by the radioactive isotopes ^{85}Kr and ^{210}Bi in the liquid scintillator, and they disturb the detection of solar neutrinos below 1 MeV (Section 4.2.3).

Figure 4.3 shows the single spectrum with the 5 m fiducial radius, and the expectation of the spallation products and radioactivities. The high energy region is well explained by the spallation products, and the low energy is by the radioactivities. The concentration of ^{40}K , ^{238}U and ^{232}Th are summarized in Table 4.3.

Table 4.2: Concentration of radioactivities in the balloon and suspending rope

	^{40}K	^{238}U	^{232}Th
- balloon -			
contamination	0.27 ppb	0.018 ppb	0.014 ppb
radio-activity	7.2 Bq	0.02 Bq	0.006 Bq
- balloon rope (~ 100 kg) -			
contamination	1.2 ppb	0.08 ppb	0.8 ppb
radio-activity	31 Bq	0.1 Bq	0.33 Bq

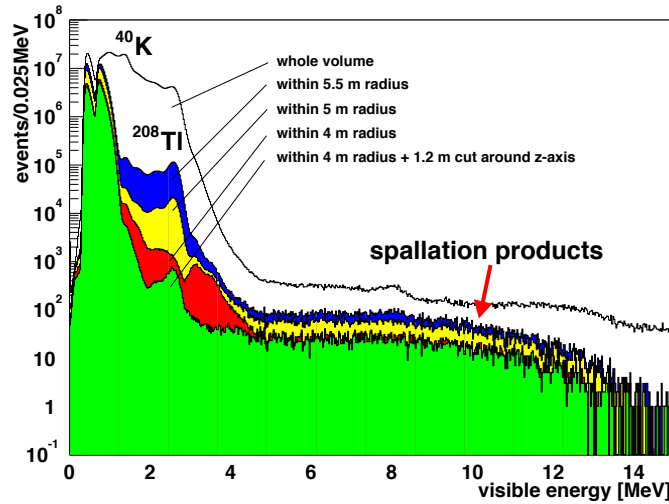


Figure 4.1: Correlation of the energy spectrum with fiducial radius. The fiducial radius cut is effective to suppress external radiations, γ -rays from ^{208}Tl (2.62 MeV) and ^{40}K (1.46 MeV). The central cylinder region has radioactivities in the thermometers and their cables. The energy resolution is $\sim 7.3\%/\sqrt{E(\text{MeV})}$ using only 17 inch PMTs. The two peaks in the low energy means the prompt and delayed trigger threshold. The high energy region is dominated by the spallation products.

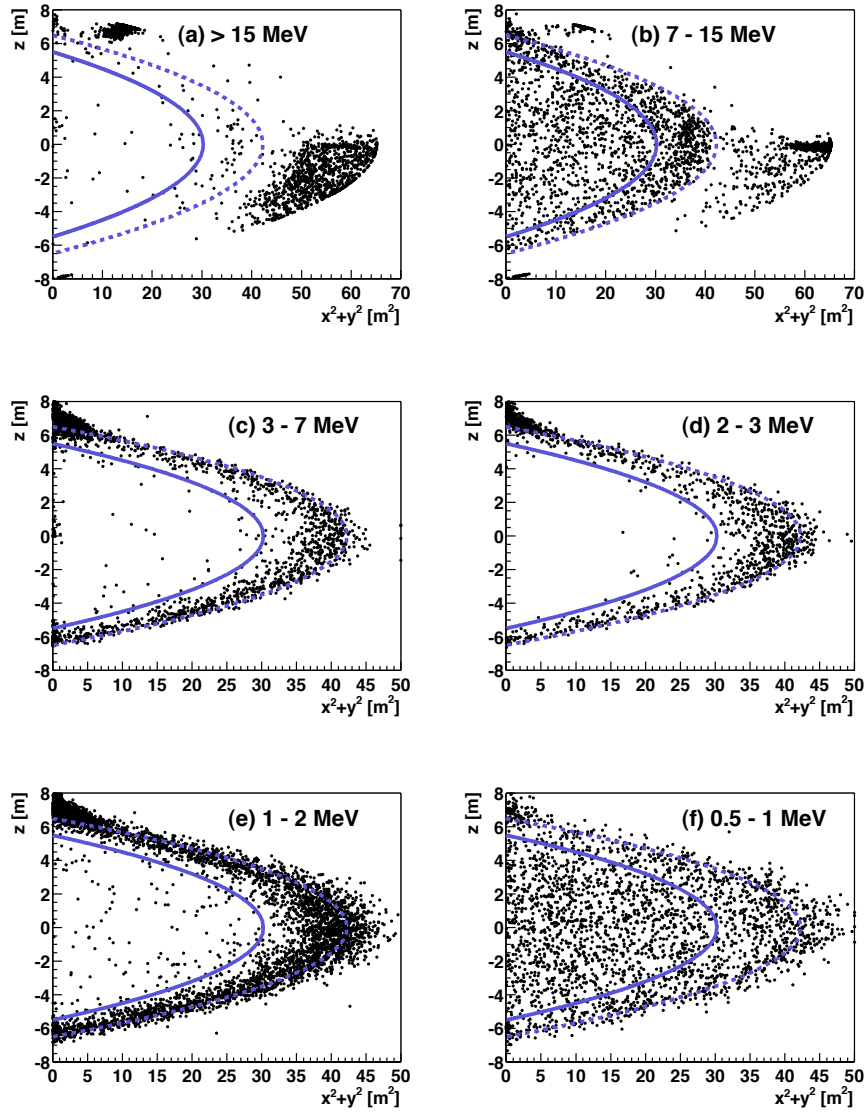


Figure 4.2: Vertex distributions of various energy events in the whole volume. There are intensive regions around the equator and outside of the balloon at the higher energy, possibly due to stop or clipping muons because there is no PMT in the outer detector around equator and the water buffer is thin. External radiations from ^{208}Tl and ^{40}K are clear at MeV order energy region. Below 1 MeV, the distribution of events is uniform because of the radioactive isotopes ^{85}Kr and ^{210}Bi in the liquid scintillator

Table 4.3: Concentration of radioactivities in the liquid scintillator

	^{40}K	^{238}U	^{232}Th
- liquid scintillator -			
contamination	$< 2.7 \times 10^{-16} \text{ g/g}$	$3.4 \times 10^{-18} \text{ g/g}$	$8.7 \times 10^{-17} \text{ g/g}$
radio-activity	$< 5.5 \times 10^{-5} \text{ Bq/m}^3$	$3.3 \times 10^{-8} \text{ Bq/m}^3$	$2.8 \times 10^{-7} \text{ Bq/m}^3$

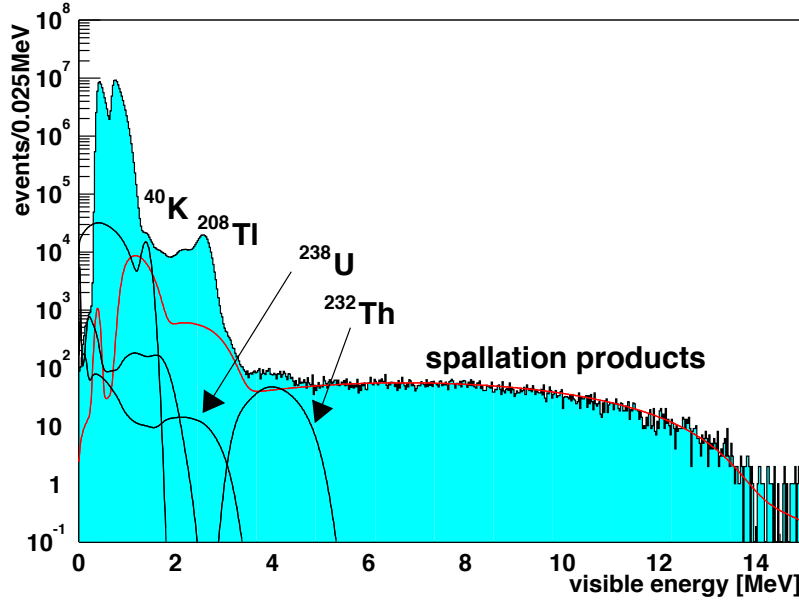


Figure 4.3: Single spectrum with the 5 m fiducial radius. The high energy spallation products, ^{12}B (57.9 events/day/kton), ^{12}N (< 0.6 events/day/kton), ^9C (3.1 events/day/kton), ^8Li (26.8 events/day/kton) and ^8B (< 9.2 events/day/kton) which have the high endpoint above 10 MeV, are estimated from the time correlation from muons and the energy spectrum (Section 4.2.2). The low energy spallation products are uncertain due to the intensive low energy radioactivities, so their expectation, ^6He (19 events/day/kton), ^{10}C (139 events/day/kton), ^{11}C (1039 events/day/kton) and ^7Be (231 events/day/kton) from [72] are adopted. In addition, the contribution of the neutron emitter ^8He and ^9Li (2.4 events/day/kton) is included. The concentration of ^{238}U and ^{232}Th is evaluated to be $3.4 \times 10^{-18} \text{ g/g}$ and $8.7 \times 10^{-17} \text{ g/g}$, respectively, using the tagging with the sequential decay of Bi-Po (Section 4.2.3). From the single spectrum, the upper limit of the ^{40}K decay rate is estimated to be $2.7 \times 10^{-16} \text{ g/g}$.

4.2 Spallation Study

The radioactive isotopes can be produced in the liquid scintillator by muons. The study of the spallation products is essential for the detection of low energy neutrinos, such as the reactor neutrinos and solar neutrinos. The production cross section of those isotopes was investigated experimentally using the SPS muon beam at CERN [72], especially for ^{12}C which is the most relevant target in the liquid scintillator. Using two muon energies, 100 and 190 GeV, the energy dependence of the cross section was measured. Based on the measured cross section, the production rates in KamLAND were calculated.

In the KamLAND, the remarkable spallation events comes from neutrons, which are generated by the direct interaction with muons via virtual photons, electromagnetic or hadronic showers. The spallation neutrons, which can be observed with capture reaction on protons or ^{12}C , have the time correlation with muons, because of the capture time. Similarly, the spallation products have the time correlation related to those lifetime. That is useful to evaluate the production rate of those isotopes in KamLAND.

4.2.1 Spallation Neutron

The neutrons produced by muons are captured on protons or ^{12}C within several hundred μsec . Their cross section for thermal neutron (2200 m/sec) are 0.332 barn and 0.0034 barn, and the number of target atoms are $8.470 \times 10^{22}/\text{g}$ and $4.254 \times 10^{22}/\text{g}$, respectively. They are observable by the simple selection criteria using NsumMax (the number of hits when trigger was issued) and time difference from muons. Figure 4.4 shows the NsumMax distribution of neutron capture events on protons or ^{12}C . The ratio of proton captured events to ^{12}C captured events agrees with the expected ratio 99.45%/0.55%. Figure 4.5 shows visible energy spectra after muons with the cuts $150 < \Delta T_{\text{muon}} < 1000 \mu\text{sec}$. In order to reduce the effect of missing waveforms, the good event selection cut

$$\text{Nhit (number of waveforms, i.e. PMT hits)} > \text{NsumMax}$$

is useful. The clear energy peaks from the thermal neutron capture on protons and ^{12}C are used for the spallation study, and they are good energy calibration sources.

The neutron production rate in the KamLAND is evaluated by time correlation from last muons to spallation neutron capture events (Figure 4.6). The waveform information for PMTs are lost in shorter time difference. That is caused by the multiple neutron events induced by the energetic muons, because the ATWD channels become busy due to the high rate events. Unfortunately, a part of neutron events can be lost in such a condition, so only larger time events ($\Delta T_{\text{muon}} > 1.1 \text{ msec}$) are used to reduce the unknown effect.

The mean capture time from fitting is $3001 \pm 74 \text{ events/day/kton}$ with the constant neutron capture time $211.2 \mu\text{sec}$ (Section 5.5.2). However, the fitting result is very sensitive to the parameter of the neutron capture time. The additional error is assigned by the capture time for the conservative evaluation using the difference between $211.2 \mu\text{sec}$ and $206.7 \mu\text{sec}$ capture time

obtained with the spallation neutron and Am-Be source calibration (Section 5.5.1).

$$\begin{aligned}
 \text{conservative neutron capture time error} &= |211.2 - 206.7| \\
 &= 4.5 \text{ } \mu\text{sec}.
 \end{aligned}
 \tag{4.1}$$

The fitting result using the changed capture time is

$$\begin{aligned}
 211.2 - 4.5 \text{ } \mu\text{sec} &: 3315 \pm 82 \text{ events/day/kton} \\
 211.2 + 4.5 \text{ } \mu\text{sec} &: 2729 \pm 68 \text{ events/day/kton}
 \end{aligned}$$

Thus, the production rate is evaluated to be 3001 ± 396 events/day/kton. The production rate of spallation neutron depends on a component of the liquid scintillator and muon energies which are generally related to depth of the detector. Figure 4.7 shows the neutron production rate in the KamLAND liquid scintillator as a function of deposit energy per length by muon. The production rate increases exponentially with the deposit energy. The production rate becomes minimum around the minimum ionization $\sim 2.4 \text{ MeV}/(\text{g cm}^{-2})$.

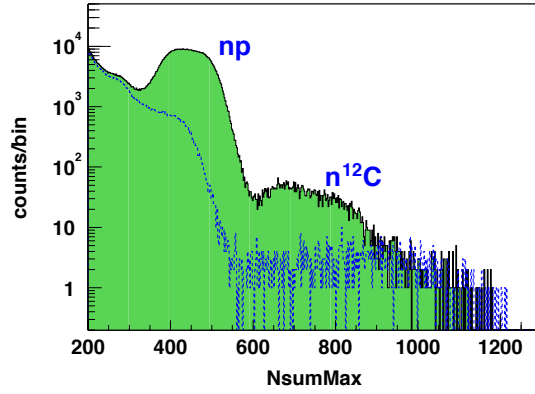


Figure 4.4: NsumMax distribution of neutron capture events on protons or ^{12}C with cuts for the time difference from muons. The shaded histogram corresponds to the on-timing window $150 < \Delta T_{\mu\text{on}} < 1000 \mu\text{sec}$, which contains neutron signals. The events in the first $150 \mu\text{sec}$ were rejected because of the deadtime of electronics noise. The dashed line corresponds to the off-timing window $2150 < \Delta T_{\mu\text{on}} < 3000 \mu\text{sec}$. It is easy to select neutron capture events on protons with a simple cut $350 < \text{NsumMax} < 550$.

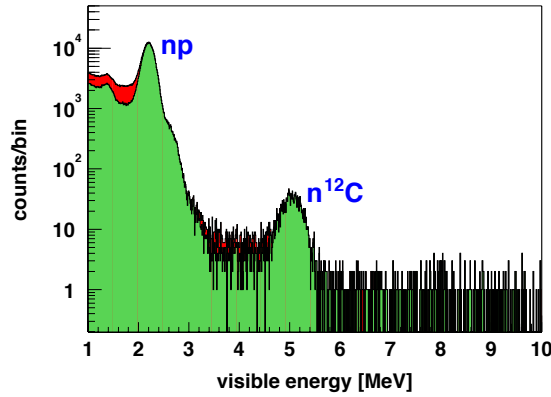


Figure 4.5: Visible energy spectra after muons with the cuts $150 < \Delta T_{\mu\text{on}} < 1000 \mu\text{sec}$. In order to reduce the effect of missing waveforms, the good event selection cut (number of waveforms, i.e. PMT hits, should be larger than NsumMax) is applied for the green shaded histogram (not applied for the red shaded one). The clear energy peaks from the thermal neutron capture on protons (γ , 2.22 MeV) and ^{12}C (γ , 4.95 MeV) can be seen in the visible energy scale, and those events are used for the spallation study and various calibrations.

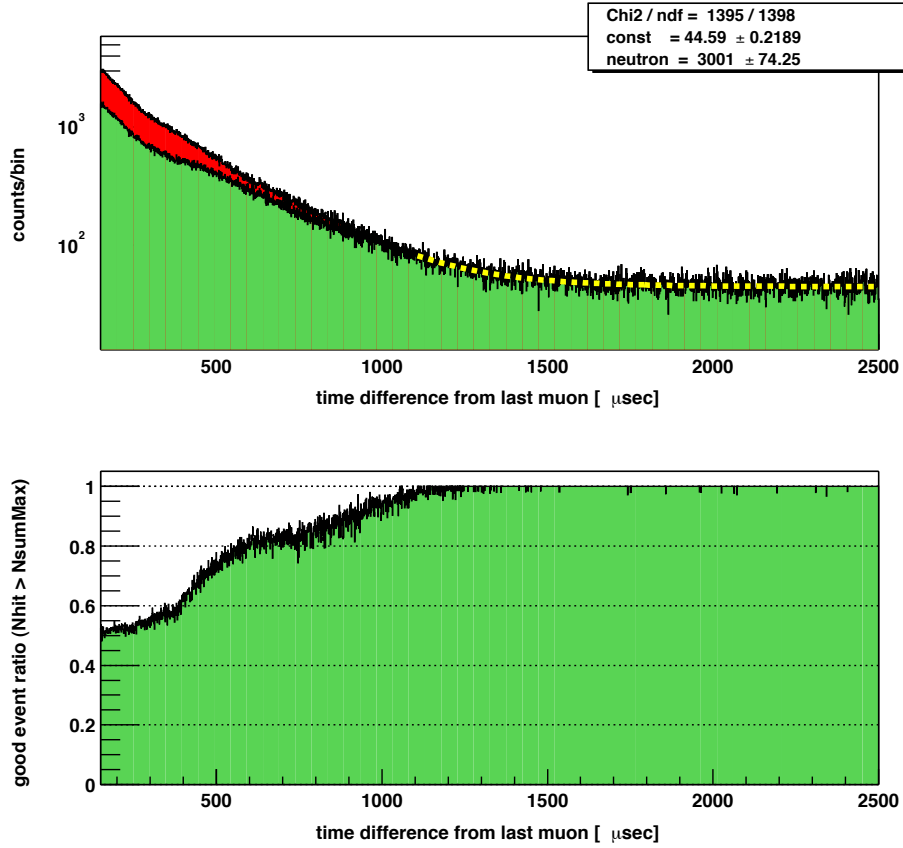


Figure 4.6: Time correlation from last muons to spallation neutron capture events with a simple cut $350 < N_{\text{sumMax}} < 550$ (upper figure). The good event selection cut is applied for the green shaded histogram (not applied for the red shaded one). The lower figure shows the good event ratio defined as the ratio of the green shaded histogram to the red shaded histogram. The waveform information for PMTs are lost within ~ 1.1 msec. The production rate of spallation neutrons is estimated from the time correlation plot, but only larger time events ($\Delta T_{\text{muon}} > 1.1$ msec) are used to reduce the unknown effect. The fitted result gives 3001 ± 74 events/day/kton with the neutron capture time $211.2 \mu\text{sec}$, evaluated in Section 5.5.2. However, the fitting result is very sensitive to the parameter of the neutron capture time. Conservatively, the additional error is assigned by the capture time error $\pm 4.1 \mu\text{sec}$ which is the difference between $211.2 \mu\text{sec}$ and $206.7 \mu\text{sec}$ capture time evaluated by the spallation neutron and Am-Be source calibration (Section 5.5.1). Therefore, the production rate is 3001 ± 366 events/day/kton.

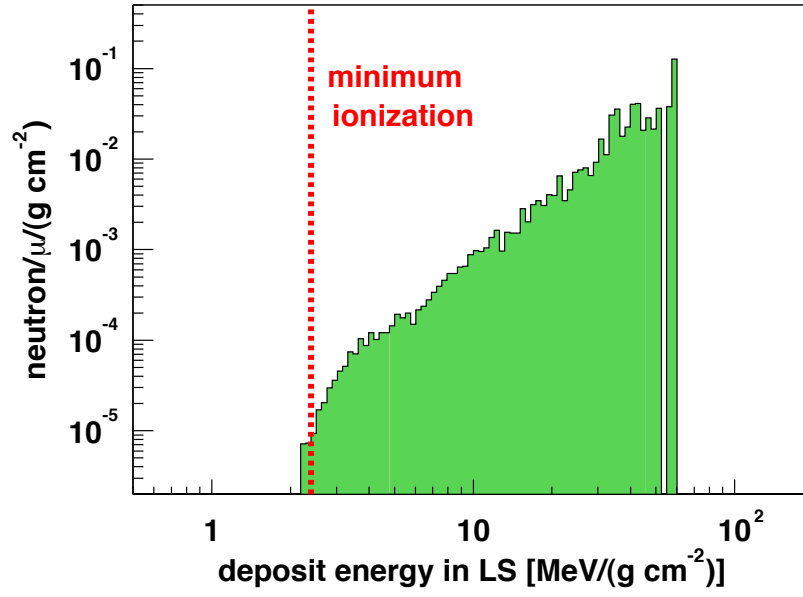


Figure 4.7: Neutron production rate in the KamLAND liquid scintillator as a function of deposit energy per length by muons. The neutrons are selected by $350 \leq \text{NsumMax} \leq 550$, $150 \leq \Delta T_{\mu\text{on}} \leq 2,000 \mu\text{sec}$, and the backgrounds estimated from $10,150 \leq \Delta T_{\mu\text{on}} \leq 12,000 \mu\text{sec}$ are subtracted. The production rate become small around the minimum ionization $\sim 2.4 \text{ MeV}/(\text{g cm}^{-2})$.

4.2.2 Spallation Products

The production rates of spallation isotopes generated by cosmic ray muons were estimated experimentally using accelerator-based muon beam [72]. Based on the measured cross section, the production rates in KamLAND were calculated using the relevant muon energies. Short-lived spallation products can be measured using the time correlation with muons (Figure 4.8 and Figure 4.9). The energy spectra can be reproduced by the background subtraction with the off-timing window, and show that ^{12}B and ^8Li production dominate in 2-60 msec and 0.2-4.0 sec time window, respectively. The contribution of ^{12}N and ^8B are estimated from the time spectrum and energy spectrum (Figure 4.10 and Figure 4.11). In the study for the low energy spallation products, the vertex information of spallation neutrons is useful to reduce the accidental backgrounds (Figure 4.12 and Figure 4.13), and show that ^{10}C and ^{11}C production dominate in 5-90 sec and 5-90 min time window, respectively. However, the contribution from the hadronic interaction, such as $^{12}\text{C}(\pi^+, \pi^0 + p)^{11}\text{C}$ and $^{12}\text{C}(p, d)^{11}\text{C}$, are not measured in this selection, and are estimated to be $\sim 5\%$ of the total production rate [73]. The ^{11}C tagging is very important for the *pep* solar neutrino detection (Figure 4.18). The production rates of spallation isotopes are summarized in Table 4.4. The spallation products which emit neutrons are discussed in Section 4.3.2.

Table 4.4: Summary of the spallation products (not neutron emitter)

isotope	mean life time	Q value	measurement	Hagner et al. [72] (events/day/kton)
high energy spallation products				
^{12}N	15.9 msec	17.3 MeV (β^+)	< 0.6	-
^{12}B	29.1 msec	13.4 MeV (β^-)	57.9 ± 1.8	-
^9C	182.5 msec	16.5 MeV (β^+)	3.1 ± 0.8	5.5
^8B	1.11 sec	18.0 MeV (β^+)	< 9.2	8
^8Li	1.21 sec	16.0 MeV (β^-)	26.8 ± 9.2	5
low energy spallation products				
^6He	1.16 sec	3.51 MeV (β^-)	-	19
^{10}C	27.8 sec	3.65 MeV (β^+)	16.6 ± 1.4 *	139
^{11}C	29.4 min	1.98 MeV (β^+)	818 ± 59 *	1039
^7Be	76.9 day	0.478MeV (EC, γ 10.5%)	-	231
^{14}C	8267 year	0.156MeV (β^-)	-	-

* : tagged by spallation neutrons

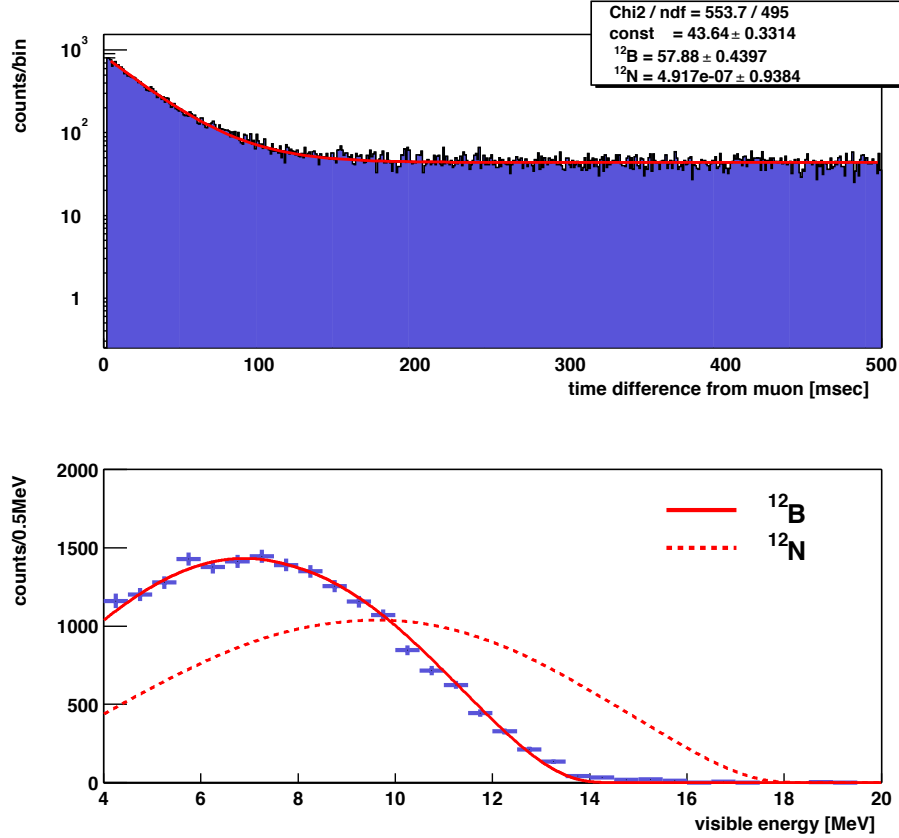


Figure 4.8: Time correlation of spallation products within 500 msec (upper figure), and background subtracted energy spectrum using 2-60 msec and 502-560 msec time window (lower figure). The production rates of ^{12}B ($\tau = 29.1$ msec, $Q = 13.4$ MeV) and ^{12}N ($\tau = 15.9$ msec, $Q = 17.3$ MeV) are fitted to be 57.9 ± 0.4 events/day/kton and 0.0 ± 0.9 events/day/kton, respectively. The uncertainties from the contribution of ^9C , the LS mass and the energy cut efficiency are estimated to be 2.3%, 2.0% and 0.7%, and they are included in the production rate uncertainties. The production ratio uncertainty ($^{12}\text{N}/(^{12}\text{B}+^{12}\text{N}) < 0.011$ at 95% C.L.) estimated from the time spectrum and energy spectrum (Figure 4.10) should be considered as well, thus, the production rate of ^{12}N are evaluated to < 0.6 events/day/kton.

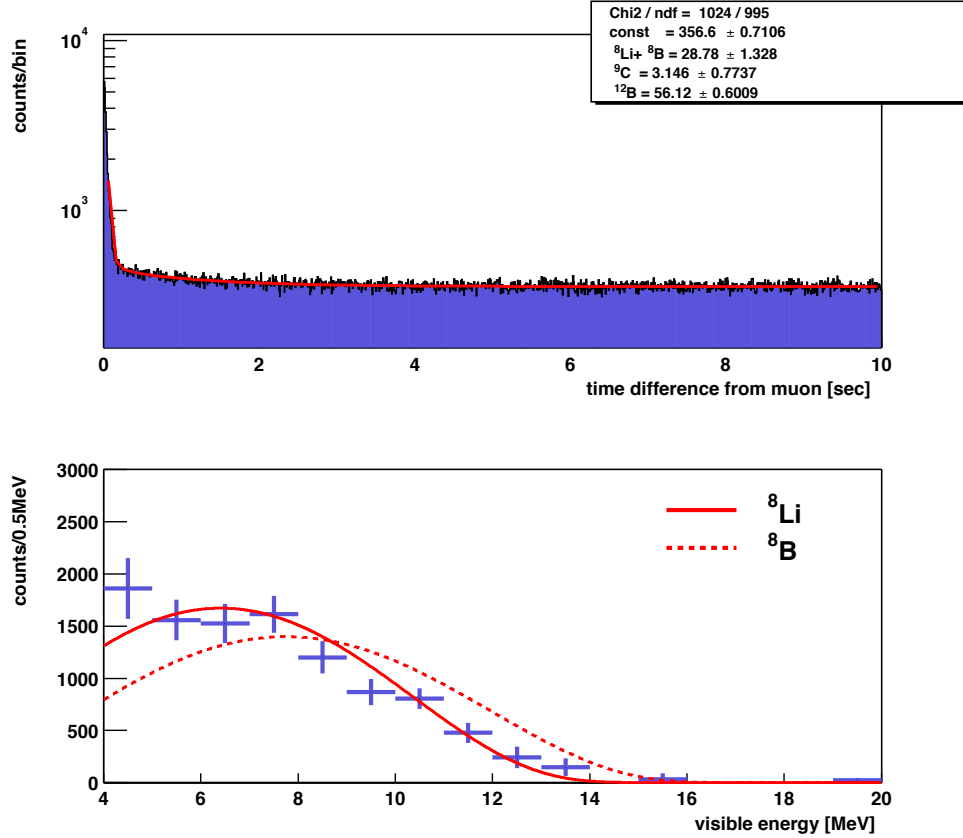


Figure 4.9: Time correlation of spallation products within 10 sec (upper figure), and background subtracted energy spectrum using 0.2-4.0 sec and 10.2-14.0 sec time window (lower figure). The production rates of ${}^8\text{Li}$ ($\tau = 1.21$ sec, $Q = 16.0$ MeV) + ${}^8\text{B}$ ($\tau = 1.11$ msec, $Q = 18.0$ MeV), ${}^9\text{C}$ ($\tau = 182.5$ msec, $Q = 16.5$ MeV) and ${}^{12}\text{B}$ are fitted to be 28.8 ± 1.3 events/day/kton, 3.1 ± 0.8 events/day/kton and 56.1 ± 0.6 events/day/kton, respectively. The production ratio of ${}^8\text{B}$ to ${}^8\text{Li} + {}^8\text{B}$ is fixed to 0.071, which is the best fit ratio estimated from energy spectrum (Figure 4.11). Conservatively, the ratio uncertainly (${}^8\text{B}/({}^8\text{Li} + {}^8\text{B}) < 0.32$ at 95% C.L.) is assigned to the production rate uncertainties, thus, the production rates of ${}^8\text{Li}$ and ${}^8\text{B}$ are evaluated to 26.8 ± 9.2 events/day/kton and < 9.2 events/day/kton, respectively.

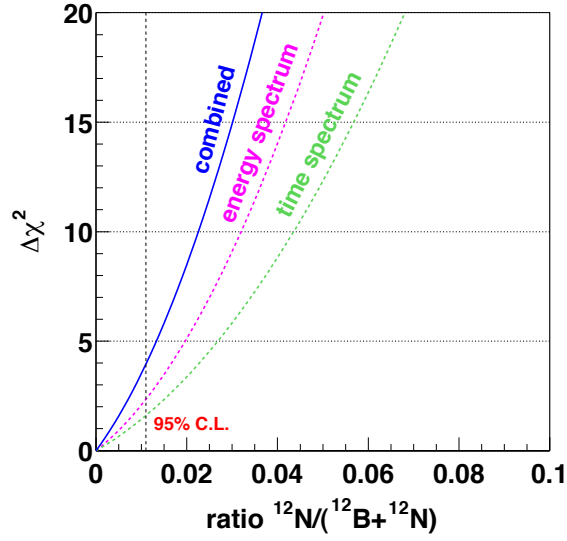


Figure 4.10: $\Delta\chi^2$ profiles projected onto the production ratio of ^{12}N to $^{12}\text{B} + ^{12}\text{N}$. The green and pink dashed lines indicate the results from the time spectrum and energy spectrum (Figure 4.8). The blue line indicates the combined result from the time spectrum and energy spectrum, and it gives the production ratio limit, $^{12}\text{N}/(^{12}\text{B}+^{12}\text{N}) < 0.011$ at 95% C.L.

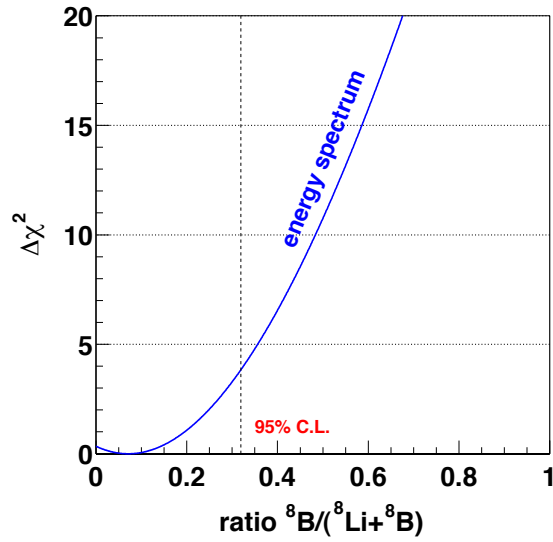


Figure 4.11: $\Delta\chi^2$ profile projected onto the production ratio of ^8B to $^8\text{Li} + ^8\text{B}$. The blue line indicates the result from the energy spectrum (Figure 4.9), and it gives the production ratio limit, $^8\text{B}/(^8\text{Li}+^8\text{B}) < 0.32$ at 95% C.L., and the best fit is 0.071.

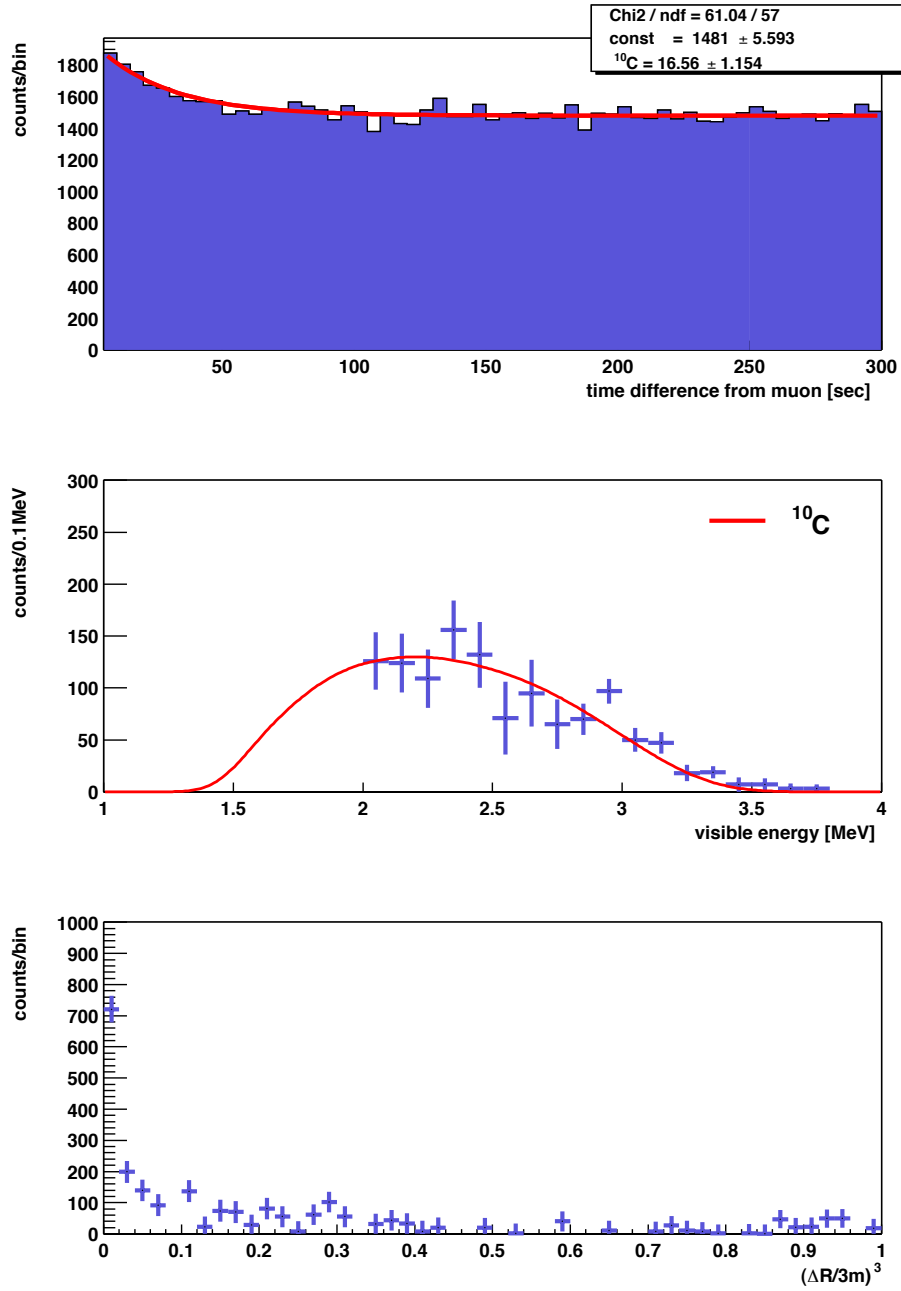


Figure 4.12: Time correlation of spallation products within 300 sec (upper figure), background subtracted energy spectrum for $\Delta R < 1.5$ m (middle figure) and space correlation (lower figure) from the average vertex for clusters of spallation neutrons using 5-90 sec and 185-270 sec time window within 5 m fiducial radius. The production rate of ^{10}C ($\tau = 27.8$ sec, $Q = 3.65$ MeV) which is accompanied by spallation neutrons is fitted to be 16.6 ± 1.2 events/day/kton. The uncertainty from the fiducial volume is included in the production rate uncertainties.

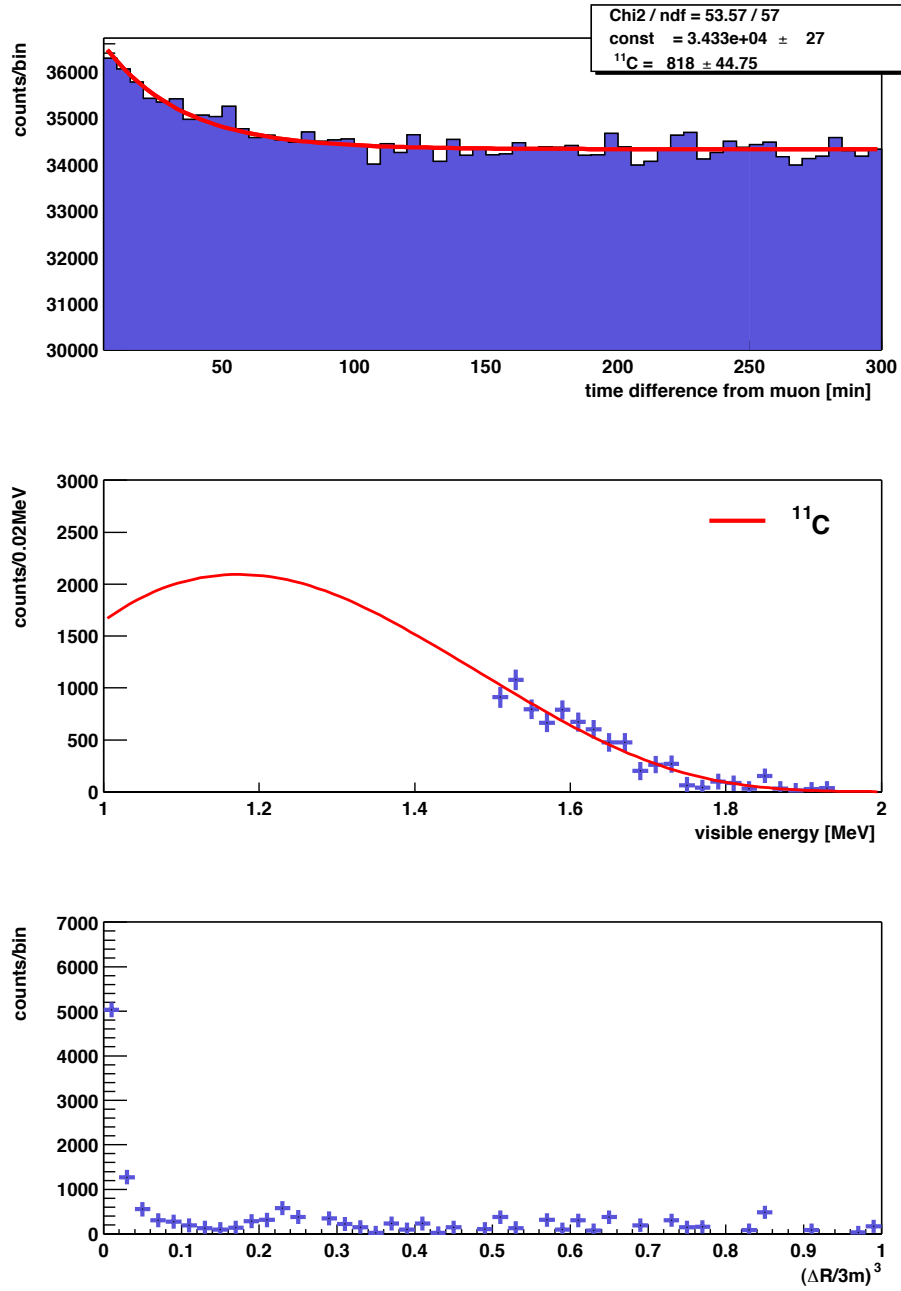
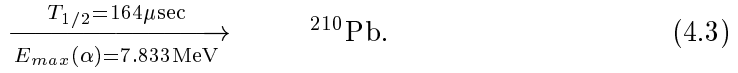
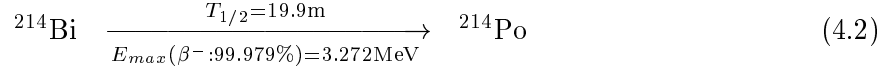


Figure 4.13: Time correlation of spallation products within 300 min (upper figure), background subtracted energy spectrum for $\Delta R < 1.5$ m (middle figure) and space correlation (lower figure) from the average vertex for clusters of spallation neutrons using 5-90 min and 185-270 min time window within 5 m fiducial radius. The production rate of ^{11}C ($\tau = 29.4$ min, $Q = 1.98$ MeV) which is accompanied by spallation neutrons is fitted to be 818 ± 45 events/day/kton. The uncertainty from the fiducial volume is included in the production rate uncertainties.

4.2.3 Radioactivity in Liquid Scintillator

^{238}U

The sequential decays of ^{214}Bi - ^{214}Po in the ^{238}U chain, can be detected by the delayed coincidence,



The mean lifetime of ^{214}Po is 237 μsec . Time window of the delayed trigger is set at 1,000 μsec , so the width of the analysis window is limited by the trigger. In order to avoid the ^{212}Bi - ^{212}Po ($\tau = 431$ nsec) coincidence, the lower time window cut (> 5 μsec) is also applied. The selection criteria, efficiency and systematic uncertainty are summarized in Table 4.5 and Table 4.6.

Table 4.5: Summary of detection efficiency of ^{214}Bi - ^{214}Po coincidence

prompt energy ($E_{\text{prompt}} > 1.3$ MeV, branching ratio 99.979%)	89.4%
delayed energy ($0.3 < E_{\text{delayed}} < 1.0$ MeV)	99.7%
time correlation ($5 < \Delta T < 1000$ μsec)	96.4%
space correlation ($\Delta R < 1$ m)	84.0%
total	71.9%

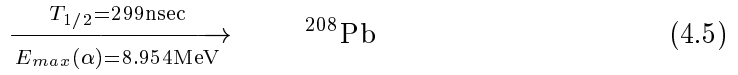
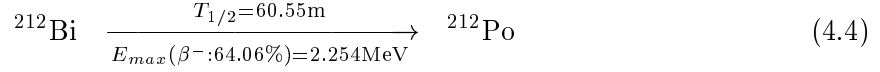
Table 4.6: Summary of systematic uncertainty of ^{214}Bi - ^{214}Po selection

- efficiencies -		
prompt energy ($E_{\text{prompt}} > 1.3$ MeV)	3.4%	(3.0%/89.4%)
delayed energy ($0.3 < E_{\text{delayed}} < 1.0$ MeV)	-	
time correlation ($5 < \Delta T < 1000$ μsec)	0.3%	(0.3%/96.4%)
space correlation ($\Delta R < 1$ m)	8.3%	(7.0%/84.0%)
fiducial cut	4.7%	
total	10.1%	

Figure 4.14 shows the ^{214}Bi - ^{214}Po coincidence events. In the estimation of the event rate, the volume in 4 m radius without 2 m central cylinder is used to avoid the accidental coincidence. The time correlation is fitted to 228 ± 6 nsec, and it agrees with the mean lifetime of ^{214}Po (237 nsec). The center cylindrical region is intensive due to the z-axis calibration. Its rate is sometimes grown up during calibration runs. The measured rate of the ^{214}Bi - ^{214}Po coincidence is $(3.3 \pm 0.4) \times 10^{-8}$ Bq/m³, which corresponds to the ^{238}U concentration $(3.4 \pm 0.4) \times 10^{-18}$ g/g. Its uncertainty 12.7% is dominated by the systematic error 10.1%. The time variation of the ^{212}Bi - ^{212}Po rate is shown in Figure 4.16 (a) and Figure 4.17.

²³²Th

The sequential decays of ²¹²Bi-²¹²Po in the ²³²Th chain, can be detected by the delayed coincidence,



The mean lifetime of ²¹²Po is 431 nsec. In order to avoid the ²¹⁴Bi-²¹⁴Po ($\tau = 237$ nsec) coincidence, the upper time window cut (< 1 μsec) is applied. There are deadtime within 300 nsec from previous events, therefore, the lower cut (> 0.4 μsec) is also applied. The selection criteria, efficiency and systematic uncertainty are summarized in Table 4.7 and Table 4.8.

Table 4.7: Summary of detection efficiency of ²¹²Bi-²¹²Po coincidence

prompt energy ($E_{\text{prompt}} > 1.0$ MeV, branching ratio 64.06%)	44.2%
delayed energy ($0.3 < E_{\text{delayed}} < 1.0$ MeV)	99.9%
time correlation ($0.4 < \Delta T < 1.0$ μsec)	29.7%
space correlation ($\Delta R < 1$ m)	84.0%
total	11.0%

Table 4.8: Summary of systematic uncertainty of ²¹²Bi-²¹²Po selection

- efficiencies -		
prompt energy ($E_{\text{prompt}} > 1.0$ MeV)	2.3%	(1.0%/44.2%)
delayed energy ($0.3 < E_{\text{delayed}} < 1.0$ MeV)	-	
time correlation ($0.4 < \Delta T < 1.0$ μsec)	2.4%	(0.7%/29.7%)
space correlation ($\Delta R < 1$ m)	8.3%	(7.0%/84.0%)
fiducial cut	4.7%	
total	10.1%	

Figure 4.15 shows the ²¹²Bi-²¹²Po coincidence events. The volume in 5 m radius without 2 m central cylinder is used to avoid the accidental coincidence. The efficiency of the space correlation is estimated from ΔR distribution (Figure 4.15 (d)). The regions in the top, bottom and balloon surface are intensive (Figure 4.15 (e),(f)). The time correlation is fitted to 468 ± 26 nsec, and it agrees with the mean lifetime of ²¹²Po (431 nsec). The observed rate of the ²¹²Bi-²¹²Po coincidence is $(1.8 \pm 0.3) \times 10^{-7}$ Bq/m³. It corresponds to the ²³²Th concentration $(8.7 \pm 1.0) \times 10^{-17}$ g/g, and its uncertainty 11.5% is dominated by the systematic error 10.1%. The time variation of the ²¹²Bi-²¹²Po rate is shown in Figure 4.16 (b), and it has no time dependence as well as the ²¹⁴Bi-²¹⁴Po rate (Figure 4.16 (a)).

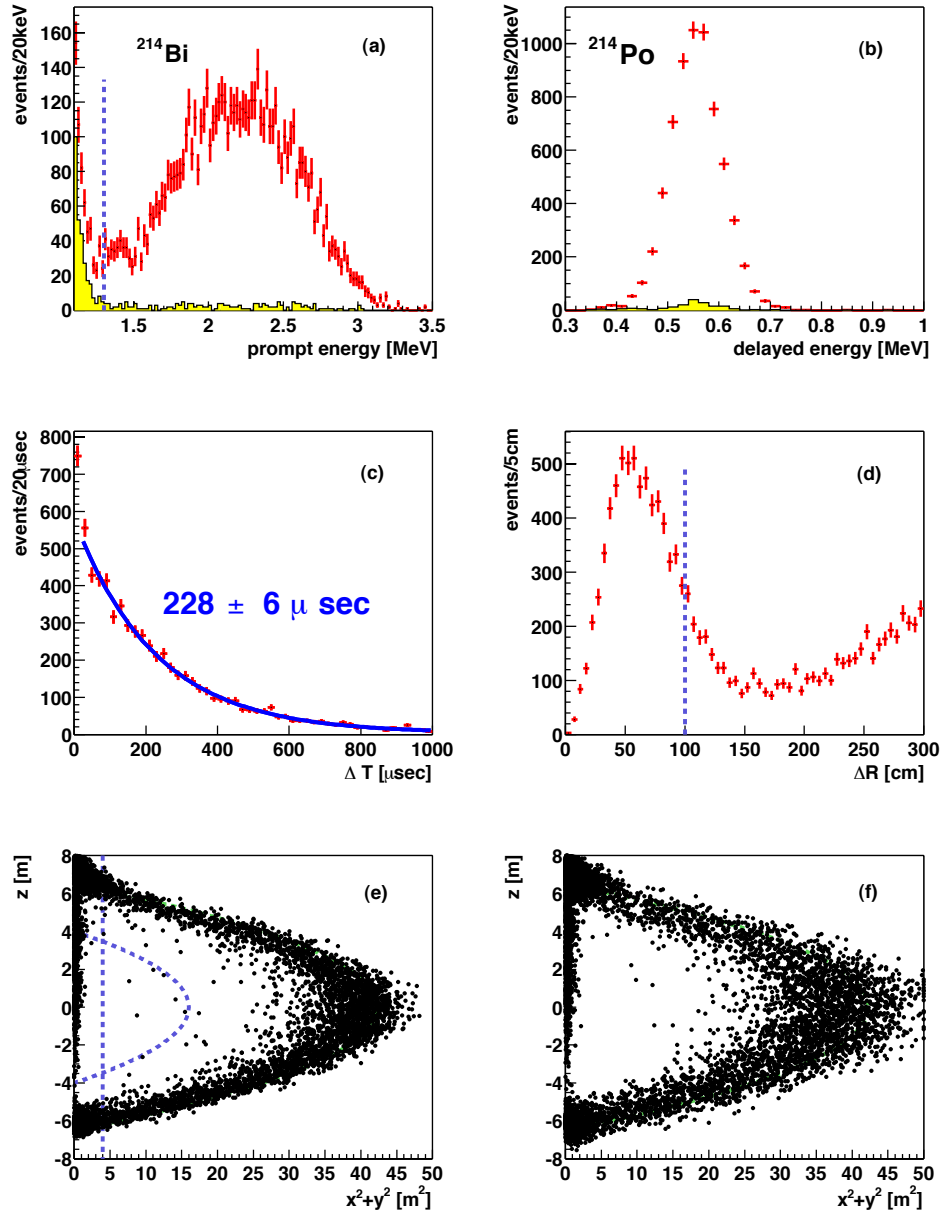


Figure 4.14: ^{214}Bi - ^{214}Po coincidence events. The shaded histogram indicates the events without the 2 m cylindrical region along z-axis. The fiducial volume in 4 m radius without 2 m central cylinder is determined to reduce the accidental coincidence.

- (a) prompt energy spectrum (visible energy)
- (b) delayed energy spectrum (visible energy)
- (c) time correlation between the prompt and delayed events
- (d) space correlation between the prompt and delayed events
- (e) vertex distribution of prompt events
- (f) vertex distribution of prompt events

^{222}Rn concentration in the center cylindrical region is sometimes grown up during calibration runs.

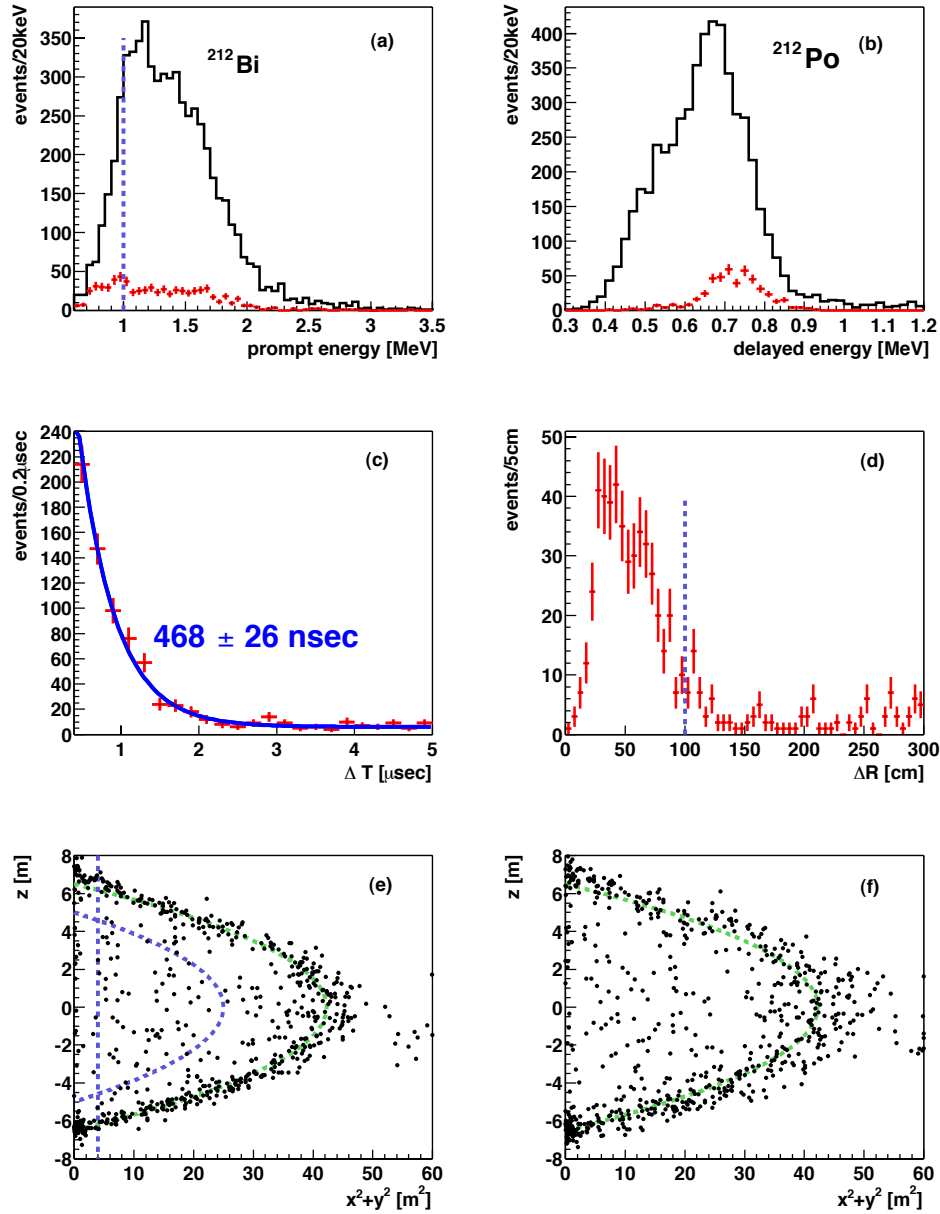


Figure 4.15: ^{212}Bi - ^{212}Po coincidence events. The black line histogram indicates the events in all volume. The fiducial volume in 5 m radius without 2 m central cylinder is determined to reduce the accidental coincidence.

- (a) prompt energy spectrum (visible energy)
- (b) delayed energy spectrum (visible energy)
- (c) time correlation between the prompt and delayed events
- (d) space correlation between the prompt and delayed events
- (e) vertex distribution of prompt events
- (f) vertex distribution of prompt events

The regions in the top, bottom and balloon surface have higher thorium contents.

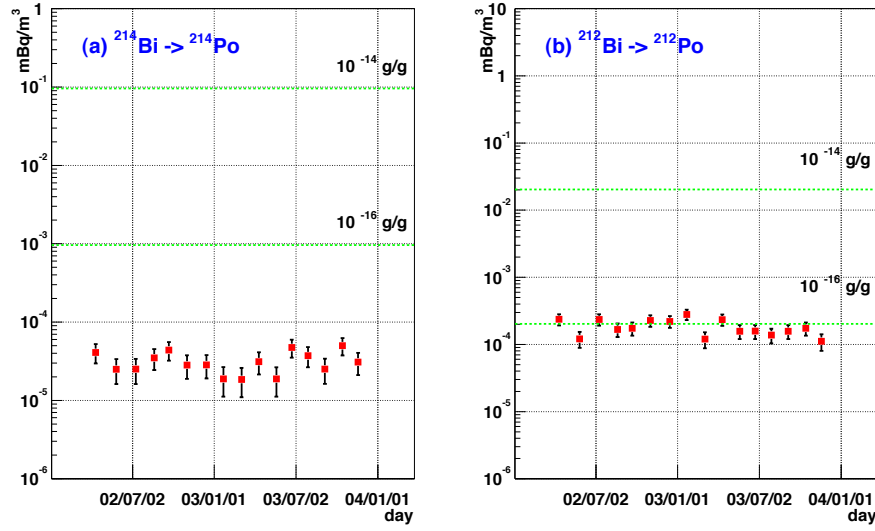


Figure 4.16: Time variation of the event rate of (a) ^{214}Bi - ^{214}Po and (b) ^{212}Bi - ^{212}Po coincidence in the liquid scintillator. The overall concentration of ^{238}U and ^{232}Th is calculated to be 3.4×10^{-18} g/g and 8.7×10^{-17} g/g, respectively.

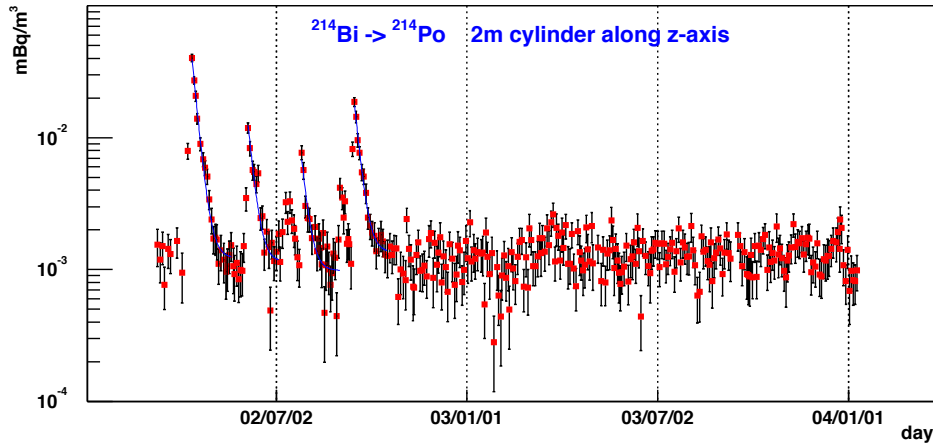


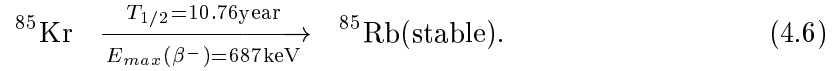
Figure 4.17: Time variation of the event rate of ^{214}Bi - ^{214}Po in the center cylindrical region with radius 2 m. There are the decay curves with the exponential fit using the lifetime of ^{222}Rn before October 2002. That indicates that there was the slight injection of ^{222}Rn during the z-axis calibration.

Low Energy Backgrounds below 1 MeV

Low energy backgrounds are dominated by the radioactive noble gases, ^{85}Kr , ^{222}Rn (daughter nuclei : ^{210}Bi and ^{210}Po) and ^{39}Ar .

- ^{85}Kr

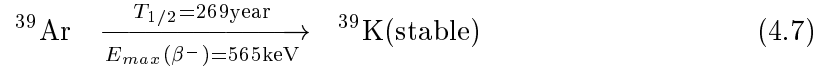
The long-lived krypton, ^{85}Kr was found among the products of uranium fission. It was published by H. Zeldes *et al.* in 1950 [74]. It β -decays with a 99.56% branch to the ground state of ^{85}Rb and a weak 0.43% branch to an excited state with 514 keV γ -ray radiation. The half-life of ^{85}Kr is 10.76 ± 0.02 year [75],



Although It is produced naturally, the production rate is dominated by the fission of uranium and plutonium in nuclear reactors and released into the atmosphere due to reprocessing of spent nuclear fuel rods. Currently, the atmospheric ^{85}Kr activity is ~ 1 Bq/m³ air, which corresponds to an atmospheric ratio of $^{85}\text{Kr}/\text{Kr} \sim 2 \times 10^{-11}$ [76]. The increase of ^{85}Kr concentration has been well measured and it is a useful tracer of circulation and mixing in the atmosphere.

- ^{39}Ar

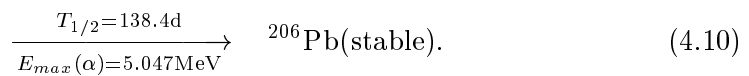
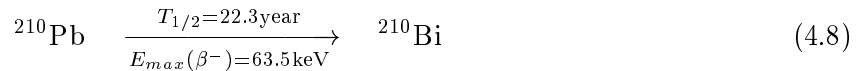
The ^{39}Ar was discovered by Brosi *et al.* in irradiated potassium salts [77]. It β -decays to the ground state of ^{39}K . In nature, ^{39}Ar is mainly produced by cosmic-ray induced $^{40}\text{Ar}(n, 2n)^{39}\text{Ar}$ reactions in the atmosphere [78]. The half-life of ^{39}Ar is (269 ± 3) year [79],



and its half-life lies in between the half-lives of two popular dating isotopes ^3H (12 year) and ^{14}C (5730 year). This favorable half-life makes ^{39}Ar a desirable isotope for dating underground and ocean water sample in the age range of 50-1000 years. In tropospheric argon sample, the activity of ^{39}Ar was measured to be 0.107 ± 0.004 dpm per liter of Ar [80], which corresponds to an atmospheric ratio of $^{39}\text{Ar}/\text{Ar} = (8.1 \pm 0.3) \times 10^{-16}$.

- ^{222}Rn

The ^{222}Rn nuclei are emanated from the solid rock, and its rate is 2000 - 3000 Bq/m³ in the mine tunnel [81]. The ^{222}Rn contamination in the detector are measured by the ^{214}Bi - Po delayed coincidence (Section 4.2.3), but ^{222}Rn nuclei were almost exhausted. The half-life of ^{222}Rn is only 3.8 day, so the radiation equilibrium is established by the daughter nuclei of ^{210}Pb which has long half-life 22.3 y (Appendix B.1),



In the KamLAND, the low threshold runs were performed for the background study in the low energy below 1 MeV. The measured rates of ^{85}Kr , ^{39}Ar , ^{210}Bi and ^{210}Po are summarized in Table 4.9. Figure 4.18 shows the visible energy spectrum in the low threshold data with the expected spectrum from radioactive impurities, ^{85}Kr , ^{210}Bi and ^{210}Po . The existence of the ^{85}Kr is supported by the delayed coincidence tagging of the small branch (0.434%) of the gamma emission (Figure 4.19), however its rate is difficult to estimate because of the uncertain trigger threshold effect.

Table 4.9: Summary of the low energy backgrounds below 1 MeV

isotope	measurement (mBq/m ³)
^{85}Kr	456 ± 96
^{39}Ar	< 207
^{210}Bi	53.2 ± 4.0
^{210}Po	47.4 ± 6.6

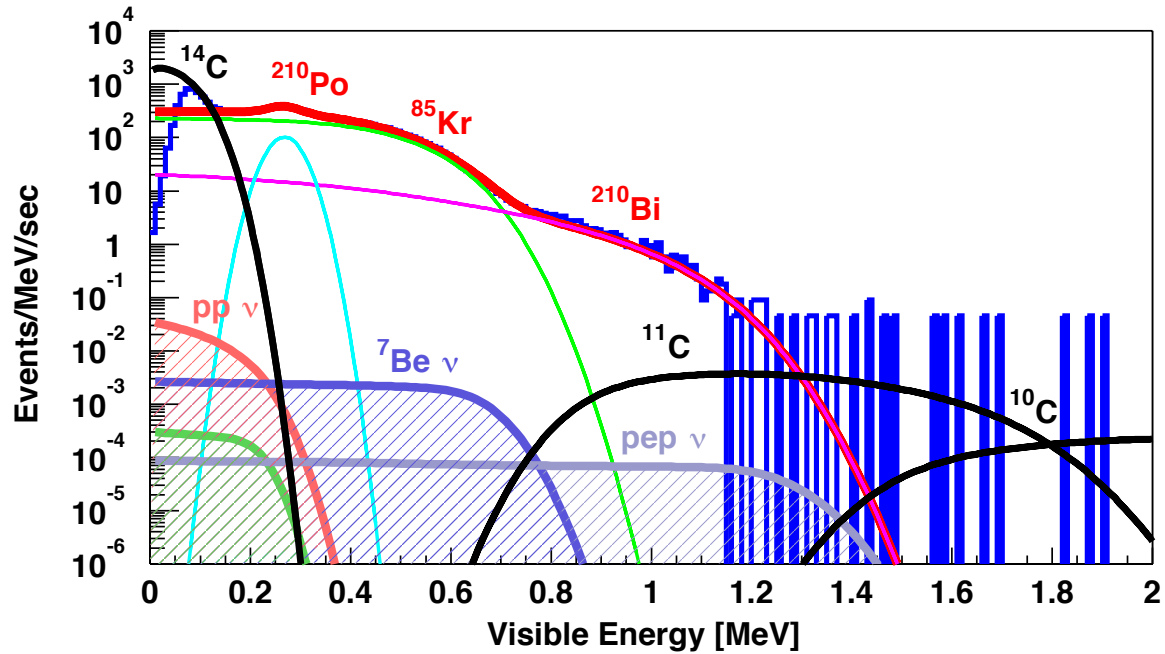


Figure 4.18: Visible energy spectrum of the low energy backgrounds with the expected spectrum from radioactive impurities (red line). The decay rate of the radioactive nuclei, ^{85}Kr , ^{210}Bi and ^{210}Po are estimated to be . The contribution from the spallation products ^{11}C , ^{10}C [72] and ^{14}C (upper limit) and the solar neutrinos are also shown. In order to observe the solar neutrinos, the necessary reduction factors with the radioactive impurities are about 10^{-6} and 10^{-4} for ^{7}Be and pep neutrinos, respectively. The pp neutrinos are difficult to observe, because of ^{14}C .

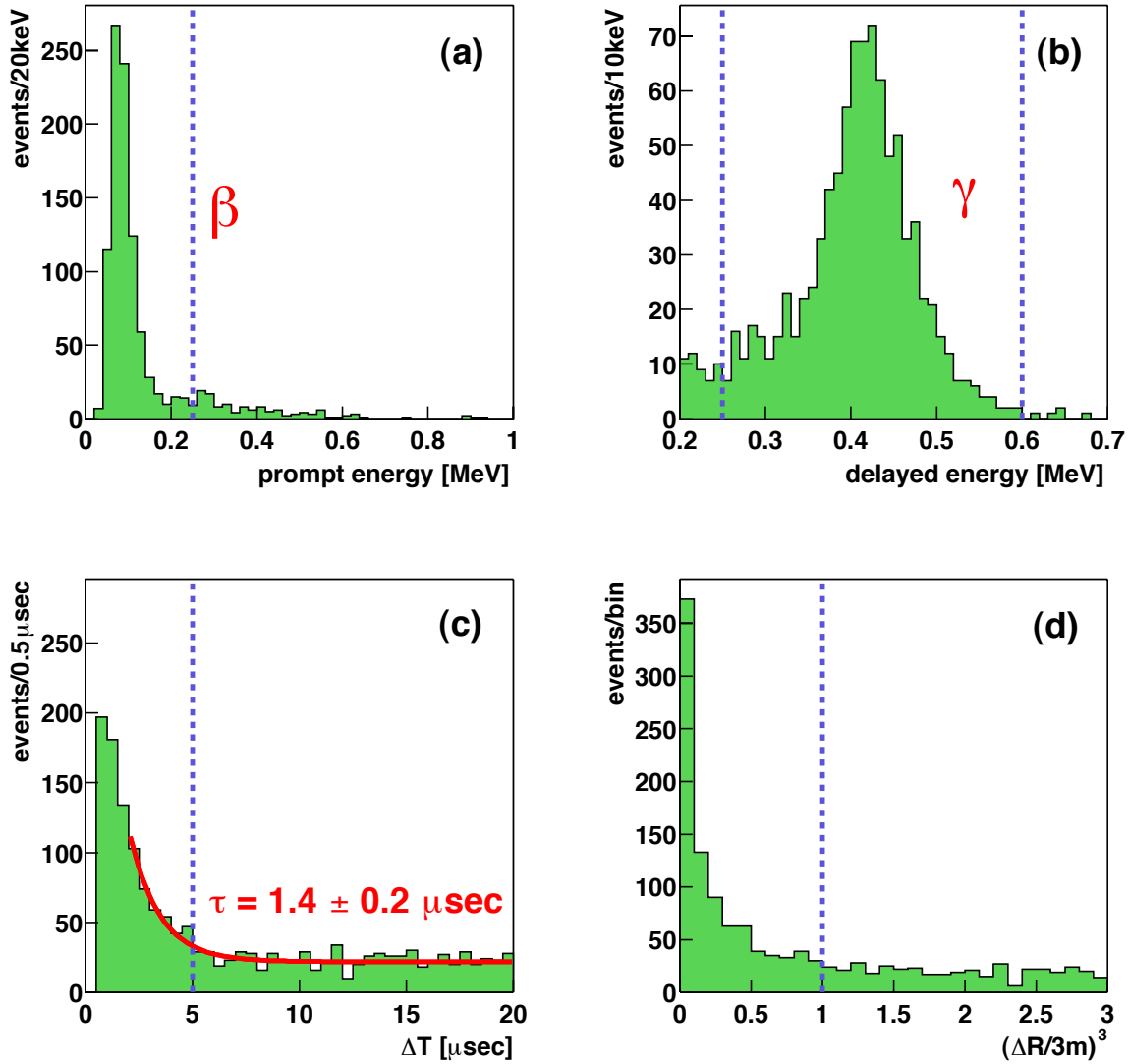


Figure 4.19: Delayed coincidence events of the ^{85}Kr β -decay using the small branch (0.434%) of the gamma emission. The selection cuts for undisplayed parameters are applied. (a) Prompt energy spectrum in visible energy scale. The end point of the ^{85}Kr β -decay in the small branch is 0.1730 MeV. The trigger threshold is ~ 0.1 MeV ($\text{NsumMax} = 30$), so its efficiency become very small. (b) Delayed energy spectrum in visible energy scale. The peak is the γ -ray emission (0.514083 MeV) from the excited state of ^{85}Rb . (c) Time correlation with the exponential fit ($\tau = 1.4 \pm 0.2 \mu\text{sec}$), which is almost consistent with the lifetime of the excited state of ^{85}Rb (1.015 μsec). (d) Space correlation. The distance between the prompt and delayed events becomes greater due to the worse resolution of the reconstructed vertex in the prompt energy region.

4.3 Backgrounds for Electron Anti-Neutrino

4.3.1 Accidental Coincidence

For the accidental background, there is no time correlation between the prompt signal and the delayed signal. The accidental background is estimated by the same cut as the $\bar{\nu}_e$ selection criteria except for the different time window. The time window for delayed events is between 10 msec to 20 sec after prompt events. The time window is decided by the neutron capture time $\sim 200 \mu\text{sec}$ to remove the correlated events.

- Time correlation, $10 \text{ msec} < \Delta T < 20 \text{ sec}$
- Space correlation, $\Delta R < 2 \text{ m}$
- Prompt energy window, $E_{\text{prompt}} > 0.9 \text{ MeV}$ or $E_{\text{prompt}} > 2.6 \text{ MeV}$
- Delayed energy window, $1.8 \text{ MeV} < E_{\text{delayed}} < 2.6 \text{ MeV}$
- Fiducial radius, $R < 5.5 \text{ m}$
- Spallation cut

Figure 4.20 shows the time and energy spectrum of the accidental events for 5.5 m fiducial volume. Time spectrum is flat in the whole time window of 10 msec and 20 sec as expected for random coincidence. This rate is extrapolated into the $\bar{\nu}_e$ selection time window of $0.5 \mu\text{sec}$ and $1000 \mu\text{sec}$. The events around 1 MeV caused by ^{210}Bi β decays in the LS, there are no contribution in 2.6 MeV threshold analysis. The events around 2.6 MeV are caused by ^{208}Tl γ generated in the rock. Fiducial cut criteria are decided by the ^{208}Tl γ background rate.

The total accidental events are estimated to be 134.82 ± 0.05 and 2.69 ± 0.02 at 0.9 MeV threshold and 2.6 MeV threshold respectively. This means that the rate of the accidental background is 0.0052 events / day at 2.6 MeV threshold. This accidental background rate is small enough compared with the reactor $\bar{\nu}_e$ rate (~ 0.7 events / day) in no oscillation case.

4.3.2 $^8\text{He}/^9\text{Li}$

There are several nuclei produced by interaction with cosmic ray muons which emit neutron after β decays. The main reactions are dominated by the spallation of ^{12}C as shown in Table 4.10.

The isotopes with long lifetime are more critical for delayed coincidence analysis, because backgrounds from the shorter-lived isotopes are easily removed by the spallation cut. The selection criteria for these isotopes are same one as that of $\bar{\nu}_e$ without the spallation cut.

- Time correlation, $0.5 \mu\text{sec} < \Delta T < 1000 \mu\text{sec}$
- Space correlation, $\Delta R < 2 \text{ m}$
- Prompt energy window, $E_{\text{prompt}} > 0.9 \text{ MeV}$ or $E_{\text{prompt}} > 2.6 \text{ MeV}$

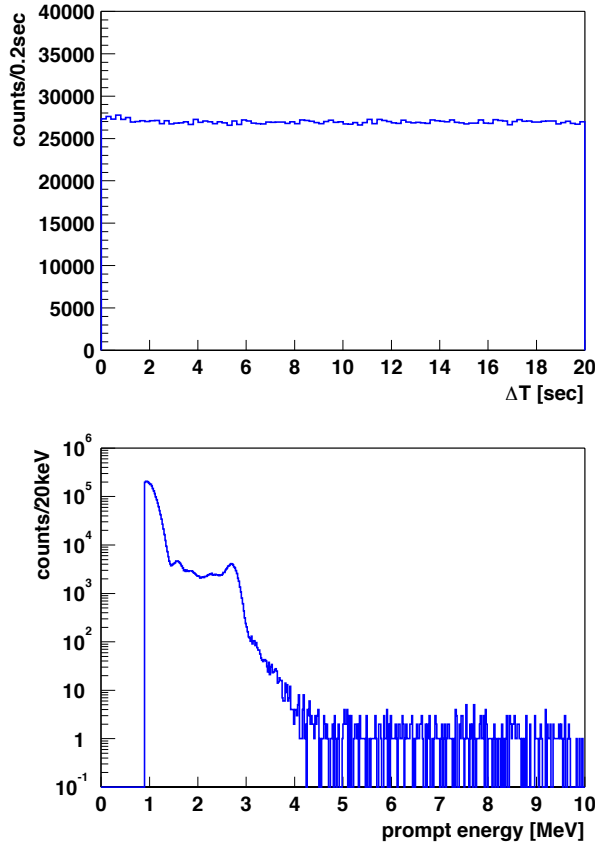


Figure 4.20: Accidental time and energy spectrum for 5.5 m fiducial volume. Time spectrum is flat in the whole time window of 10 msec and 20 sec. The events around 1 MeV are caused by ^{210}Bi β decays in the LS and the events around 2.6 MeV are caused by ^{208}Tl γ generated in the rock.

- Delayed energy window, $1.8 \text{ MeV} < E_{\text{delayed}} < 2.6 \text{ MeV}$
- Fiducial radius, $R < 5.5 \text{ m}$

Time correlation between these delayed coincidence events and muons are shown in Figure 4.21, some events are overlapping to cancel out the time structure of the muon rate. The number of the correlated events are estimated from fitting by exponential function plus constant background. Figure 4.22 shows the allowed region from extended likelihood analysis for the number of ^8He and ^9Li events vs the ratio of ^9Li . The decay time of ^8He and ^9Li are fixed to the each lifetime, 171.7 msec and 257.2 msec respectively. The production ratio of ^8He to ^9Li is free parameter. Total events from showering muons are estimated to be 350 ± 30 , and those from non-showering muons are 86 ± 17 within 3 m from the muon track.

Figure 4.23 shows the track correlation of spallation neutron events for non-showering muons.

Table 4.10: Summary of the nuclei which emit neutron after β decays

isotope	production reaction	lifetime (msec)	decay mode	energy (MeV)	fraction of decays
^8He	$^{12}\text{C}(\gamma, 4\text{p}), ^{12}\text{C}(\pi^-, \text{n}3\text{p})$	171.7	β^-	10.7	0.84
^9Li	$^{12}\text{C}(\gamma, 3\text{p}), ^{12}\text{C}(\pi^-, \text{n}2\text{p})$	257.2	$\beta^- + \text{n}$	13.6	0.16
^{11}Li	$^{12}\text{C}(\gamma, 2\pi^+\text{p}), ^{12}\text{C}(\pi^-, \pi^+\text{p})$	12.3	β^-	20.6	0.52
^{12}Be	$^{12}\text{C}(\gamma, 2\pi^+), ^{12}\text{C}(\pi^-, \pi^+)$	16.4	$\beta^- + \text{n}$	11.7	0.48
			β^-		0.07
			$\beta^- + \text{xn}$		0.92
			β^-		-
			$\beta^- + \text{n}$		-

For non-showering muons, 3 m cylindrical cut along the muon track are applied for 2 sec. The efficiency of the muon tracking within 3 m is estimated to be 93.8%. This means 6.2% of total spallation events remains after spallation cut. For showering muons, all volume veto are applied for 2 sec. The remained background after the spallation cut is estimated to be 4.82 ± 0.92 events at 2.6 MeV energy threshold. The spallation cut efficiency for ^8He and ^9Li is 98.7%.

Prompt energy spectrum of ^8He and ^9Li events within 500 msec following showering muons are shown in Figure 4.24 with those expected spectra. ^9Li is dominant according to the energy spectrum. From fits to the decay time and the prompt energy spectrum, the contribution of ^8He relative to ^9Li is less than 15% at 90% C.L.

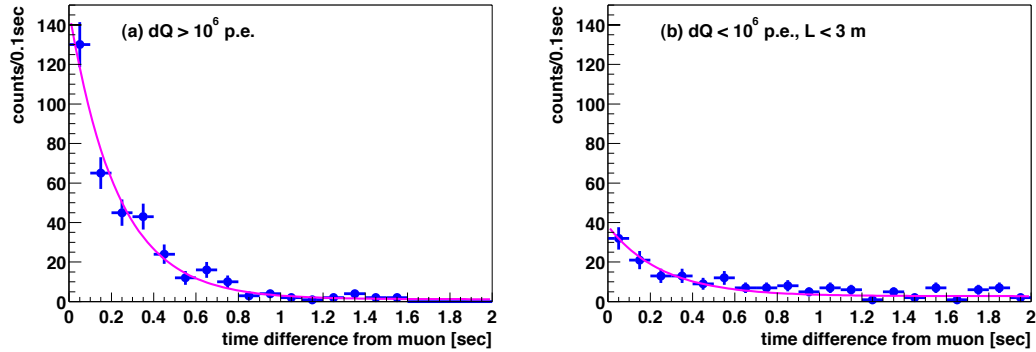


Figure 4.21: Time correlation between these delayed coincidence events and muons, some events are overlapping to cancel out the time structure of the muon rate. (a) indicates time correlation for showering muons and (b) indicates that for non-showering muons with the distance within 3 m from the muon track. The fitting results by exponential function plus constant background are also shown.

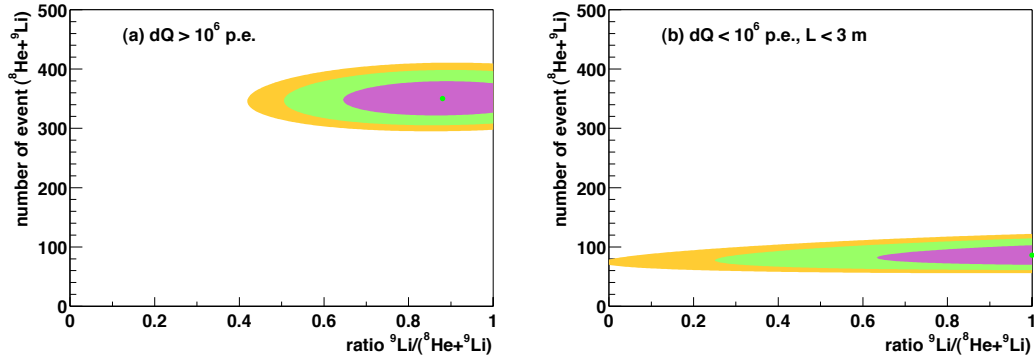


Figure 4.22: Allowed region from extended likelihood analysis for the number of ${}^8\text{He}$ and ${}^9\text{Li}$ events vs the ratio of ${}^9\text{Li}$, the shaded region regions show 68%, 95% and 99% C.L. allowed region. (a) indicates allowed region for showering muons and (b) indicates that for non-showering muons with the distance within 3 m from the muon track. The decay time of ${}^8\text{He}$ and ${}^9\text{Li}$ are fixed to the each lifetime. The production ratio of ${}^8\text{He}$ to ${}^9\text{Li}$ is free parameter. Total events from showering muons are estimated to be 350 ± 30 , and those from non-showering muons are 86 ± 17 within 3 m from the muon track.

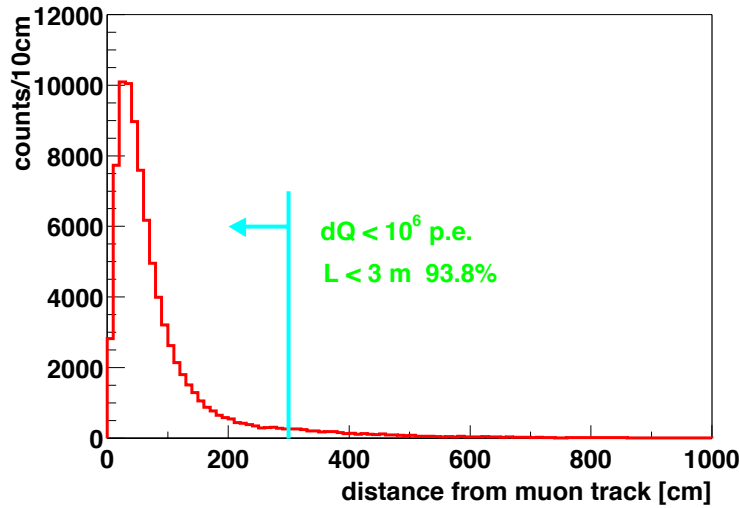


Figure 4.23: Track correlation of spallation neutron events for non-showering muons. For non-showering muons, 3 m cylindrical cut along the muon track are applied for 2 sec. The efficiency of the muon tracking within 3 m is estimated to be 93.8%. This means 6.2% of total spallation events remains after spallation cut.

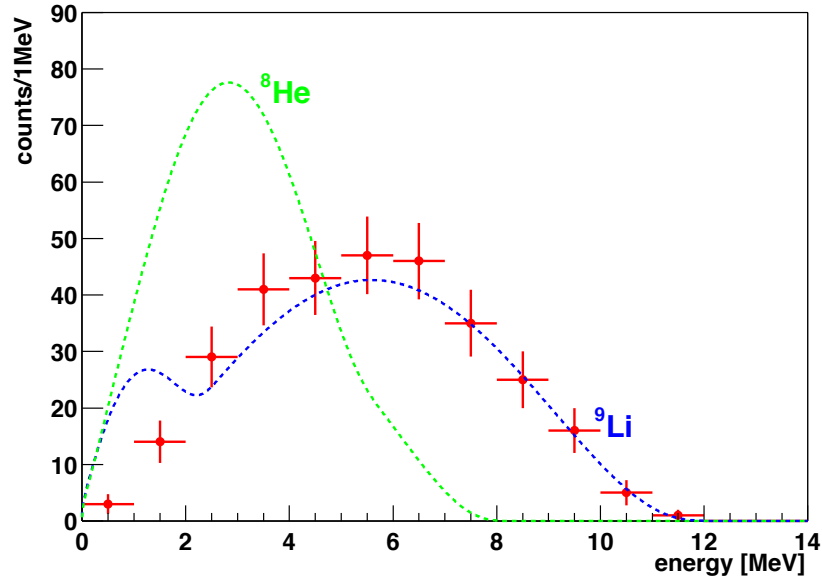


Figure 4.24: Prompt energy spectrum of ^8He and ^9Li events within 500 msec following showering muons. Expected spectra of ^8He and ^9Li are shown in green and blue dashed lines. ^9Li is dominant according to the energy spectrum. From fits to the decay time and the prompt energy spectrum, the contribution of ^8He relative to ^9Li is less than 15% at 90% C.L.

4.3.3 Fast Neutron

Fast neutrons mimic delayed coincidence because it interacts proton and the recoiled proton emits scintillation light and the neutron are finally captured by proton and emits 2.22 MeV γ -rays. These events are selected by the triple coincidence, which is delayed coincidence of the inner detector plus outer detector hits. Decay electron (Michel electron following muon) is also selected by the triple coincidence, and it can be removed with the time interval cut less than 10 μsec .

- Time correlation, $10 \mu\text{sec} < \Delta T < 1000 \mu\text{sec}$
- Space correlation, $\Delta R < 2 \text{ m}$
- Prompt energy window, $0.9 \text{ MeV} < E_{\text{prompt}} < 14 \text{ MeV}$ or $2.6 \text{ MeV} < E_{\text{prompt}} < 14 \text{ MeV}$
- Delayed energy window, $1.8 \text{ MeV} < E_{\text{delayed}} < 2.6 \text{ MeV}$
- Fiducial radius, $R < 5.5 \text{ m}$
- Spallation cut
- Tagging by OD muon, OD hits ≥ 5

Figure 4.25 shows the characteristics of the fast neutron events. The observed mean capture time is $214.9 \pm 23.7 \mu\text{sec}$, which is consistent with the estimation from spallation neutrons by muons.

The attenuation length of neutron from outside to inside are estimated from the radius distribution. The fitting result of the attenuation length is $29.7 \pm 3.4 \text{ cm}$. For the conservative attitude, the worst case of this fit (33.1 cm) are used for the estimation of the fast neutron contamination in the fiducial volume. The number of events is estimated less than 4.3 events. On the other hand, the outer detector has small inefficiency, so the miss-tagging events become backgrounds for $\bar{\nu}_e$. As the outer detector efficiency is larger than 92%, the miss tagging events is less than 0.37. The radius distribution has the second peak around 800 cm, out of the balloon. These events are the clipping muons (Cherenkov light only) which passed only in the buffer oil. The prompt energy spectrum which comes from the recoiled proton is consistent with the flat distribution in the low energy.

The fast neutron contribution from rock outside the detector are calculated by simple simulation, and the total ratio of neutron contribution is 0.11, so the contribution from rock is less than 0.52 events. So the upper limit of background events for the reactor $\bar{\nu}_e$ detection is estimated to be less than 0.89. The cross section of neutron versus proton is about 300 mb at 30 MeV which corresponds to the attenuation length 7cm in the LS. That cross section corresponds to the $\sim 10 \text{ MeV}$ prompt energy because the energy of the recoiled proton by neutron become smaller by quenching effect. So the fitting result 29.7 cm is conservative estimation, and it is affected by the bias of the detector resolution and the background events from clipping muons.

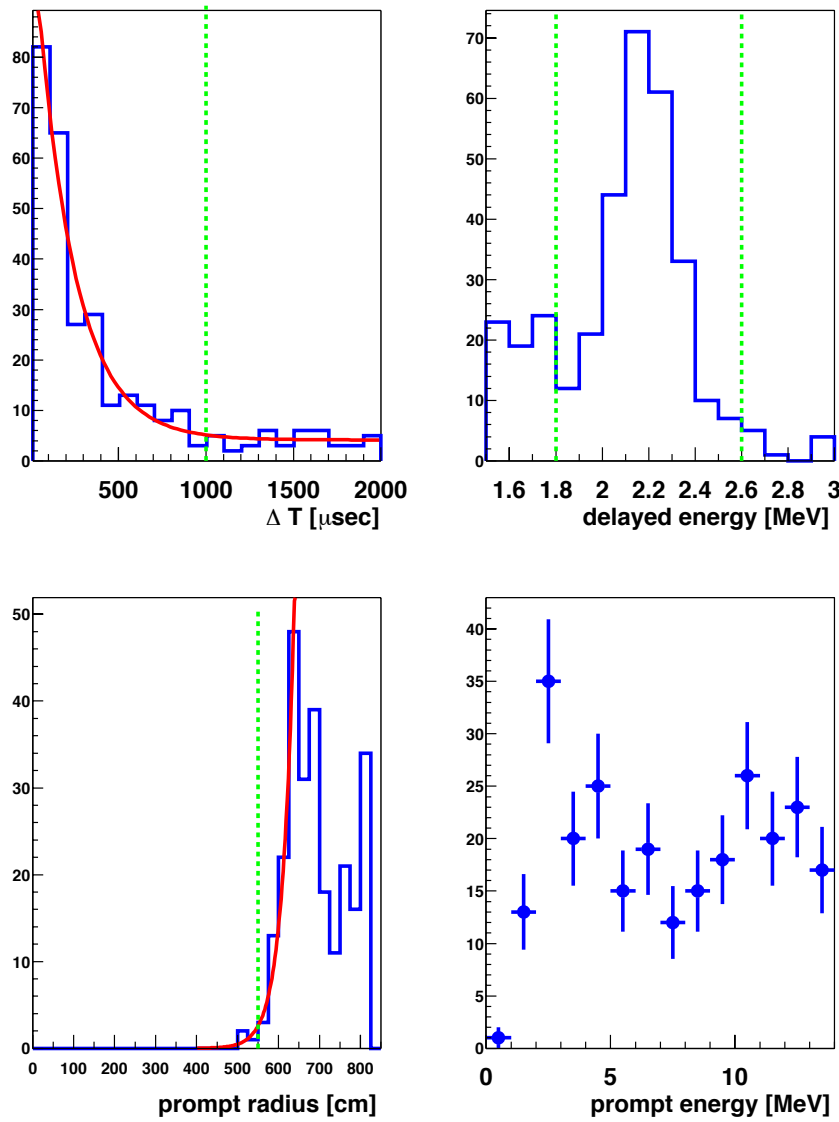


Figure 4.25: Fast neutron events selected by the triple coincidence, which is delayed coincidence of the inner detector plus outer detector hits. The observed mean capture time is $214.9 \pm 23.7 \mu\text{sec}$, which is consistent with the estimation from spallation neutrons ($211.2 \pm 2.6 \mu\text{sec}$). Delayed energy spectrum has 2.22 MeV peak which comes from the neutron capture on proton. From the radius distribution, the attenuation length of neutron from outside are estimated. The fitting result of the attenuation length is $29.7 \pm 3.4 \text{ cm}$, and the worst case of this fit are used for the estimation of the fast neutron contamination in the fiducial volume. The prompt energy spectrum which comes from the recoiled proton is consistent with the flat distribution.

4.3.4 (α , n)

There are various radioactivities which emit α particle in the detector. From background study, α decays are dominated by the ^{210}Po , that rate is ~ 33 Bq in 5.5 m radius fiducial volume (Section 4.2.3). The source of ^{210}Po is ^{222}Rn , which decayed before the data taking of KamLAND experiment, and the daughter nuclei ^{210}Pb accumulated. The radiation equilibrium is established by ^{210}Pb , because of the long half-life 22.3 y (Appendix B.1).

The target nuclei of (α , n) reaction are listed in Table 4.11. The target which has large energy threshold or small natural abundance is negligible. Figure 4.26 shows the total cross sections of (α , n) reactions for various target nuclei, and their cross sections are normalized with the number of target, which is calculated from the composition of liquid scintillator and the natural abundance. The α energy emitted from ^{210}Po is 5.304 MeV, so the dominant reaction is $^{13}\text{C}(\alpha, n)^{16}\text{O}$.

Table 4.11: Target nuclei of (α , n) reaction [82, 83]

target nuclei	Q value (MeV)	threshold (MeV)	natural abundance
^1H	-23.68	115.4	99.985%
^2H	-4.19	12.50	0.015%
^3H	-4.78	11.12	-
^{12}C	-8.50	11.34	98.90%
^{13}C	2.22	0	1.10% ¹
^{14}C	-1.82	2.34	-
^{14}N	-4.73	6.09	99.634%
^{15}N	-6.42	8.13	0.366%
^{16}N	1.52	0	-
^{16}O	-12.13	15.17	99.762%
^{17}O	0.59	0	0.038%
^{18}O	-0.70	0.85	0.200%
^{19}O	5.71	0	-

The $^{13}\text{C}(\alpha, n)^{16}\text{O}$ reaction may populate states in ^{16}O at 6.05, 6.13, 6.92 and 7.12 MeV, with spins and parities 0^+ , 3^- , 2^+ and 1^- respectively; the 6.05 MeV state decays by pair emission (internal pair creation) and the other three states by gamma emission. The Q value of $^{13}\text{C}(\alpha, n)^{16}\text{O}$ reaction is 2.216 MeV, so 5.304 MeV α particle may produce the 6.05, 6.13 MeV states and the ground state of ^{16}O . Figure 4.29 (a) shows the cross section of $^{13}\text{C}(\alpha, n)^{16}\text{O}$ with a function of the α energy in the laboratory system. The number of $^{13}\text{C}(\alpha, n)^{16}\text{O}$ reaction is calculated as follows,

¹The measured abundance of ^{13}C in the KamLAND liquid scintillator is $(^{13}\text{C}/^{12}\text{C}) = 0.0109293 \pm 0.0000011$. It is consistent with the natural abundance of ^{13}C , 1.10%.

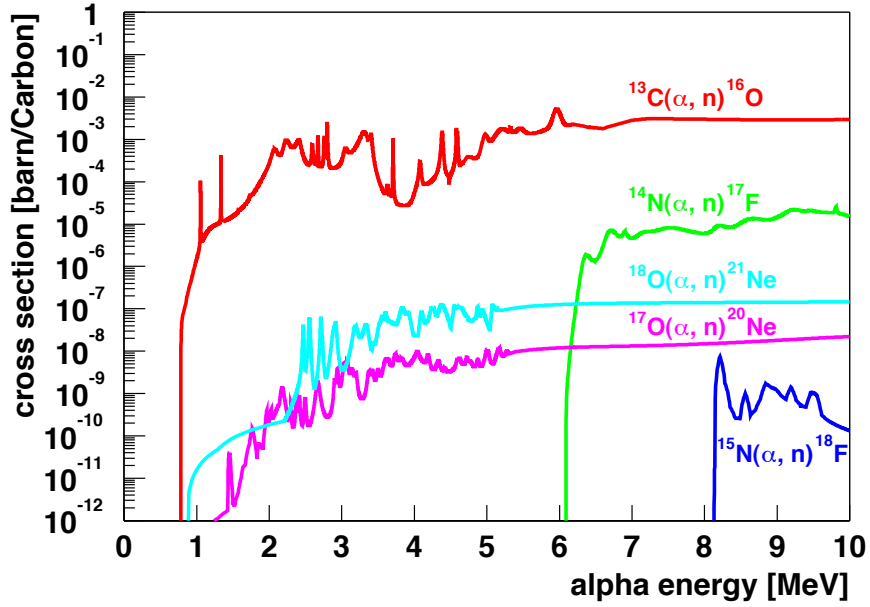


Figure 4.26: Total cross sections of (α, n) reactions for various target nuclei, ^{13}C ($Q = 2.22$ MeV, $N_{abundance} = 1.10\%$), ^{14}N ($Q = -4.73$ MeV, $N_{abundance} = 99.634\%$), ^{15}N ($Q = -6.42$ MeV, $N_{abundance} = 0.366\%$), ^{17}O ($Q = 0.59$ MeV, $N_{abundance} = 0.038\%$) and ^{18}O ($Q = -0.70$ MeV, $N_{abundance} = 0.200\%$). The cross sections are normalized with the number of target, which is calculated from the composition of liquid scintillator and the natural abundance. The dominant reaction is $^{13}\text{C}(\alpha, n)^{16}\text{O}$ at the α energy 5.304 MeV, emitted from ^{210}Po .

$$N = \int_{E_0}^0 dE_\alpha \left(-\frac{dN}{dE_\alpha} \right) \quad (4.11)$$

$$-\frac{dN}{dE_\alpha} = n_{target} I_{source} \sigma(E_\alpha) \left(-\frac{dX}{dE_\alpha} \right) \quad (4.12)$$

$$(4.13)$$

where

E_α : α energy
 E_0 : incident α energy
 n_{target} : number of target
 I_{source} : source intensity
 $\sigma(E_\alpha)$: (α, n) cross section
 $\frac{dX}{dE_\alpha}$: stopping power.

The neutron energy depends on the scattering angle, because the recoiled ^{16}O carry away

a portion of the reaction energy. Figure 4.27 shows the neutron energy vs alpha energy in forward(0°), right(90°), backward(180°) scattering angles. The width of the neutron energy at 5.304 MeV α is 2.65 MeV. The angular distribution of neutron can be expressed by a Legendre-polynomial [84, 85]. The neutron energy spectrum is calculated as follows,

$$n(E_n) = \int_{E_0}^0 dE_\alpha \int d\Omega \delta(\Omega, E_\alpha, E_n) n_{target} I_{source} \frac{d\sigma}{d\Omega} \left(-\frac{dX}{dE_\alpha} \right) \quad (4.14)$$

$$\frac{d\sigma}{d\Omega} = \sum_\nu A_\nu P_\nu(\cos \theta) \quad (4.15)$$

where

E_n : neutron energy
 Ω : scattering solid angle
 $\delta(\Omega, E_\alpha, E_n)$: 1 (conservation of momentum) or 0
 A_ν : coefficients of Legendre-polynomial
 $P_\nu(\cos \theta)$: Legendre-polynomial.

The neutron energy distribution are shown in Figure 4.29 (c). The recoil of protons can be simulated with the MC. The quenching factor of proton is calculated from the Birk's constant, which is estimated by the energy of ^{210}Po , ^{214}Po and ^{212}Po . Figure 4.29 (d) shows the energy distribution of $^{13}\text{C}(\alpha, n)^{16}\text{O}$ in positron scale. The 6.049 MeV e^+e^- by internal pair creation and 6.130 MeV γ are observed at 2.6 MeV energy threshold as well as the 4.438 MeV γ by $^{12}\text{C}(n, n\gamma)^{12}\text{C}$.

The characteristic of the (α, n) background is summarized in Table 4.12. The conservative error for the (α, n) background each energy is assigned.

- low energy : 32% scale error
 (^{210}Po rate, cross section of g.s., neutron angular)
 + 10% quenching error
- ~ 4.4 MeV : 32% scale error
 (^{210}Po rate, cross section of g.s., neutron angular, $(n, n\gamma)$ cross section)
- ~ 6 MeV : 100% scale error (^{210}Po rate, cross section of 1st and 2nd e.s.)

The total number of expected events is 10.31 ± 7.14 at 2.6 MeV energy threshold.

Table 4.12: Summary of (α , n) Backgrounds (events / data-set)

prompt energy	reaction	source	events / data-set
low energy	$^{13}\text{C}(\alpha, n)^{16}\text{O}$ (grand state)	n	67.30
~ 4.4 MeV	$^{13}\text{C}(\alpha, n)^{16}\text{O}$ (grand state) $\rightarrow ^{12}\text{C}(n, n\gamma)^{12}\text{C}$	n $\gamma + n$	1.71
~ 6 MeV	$^{13}\text{C}(\alpha, n)^{16}\text{O}^*$ (first excited state : 6.049 MeV)	$e^+e^- + n$	6.18
	$^{13}\text{C}(\alpha, n)^{16}\text{O}^*$ (second excited state : 6.130 MeV)	$\gamma + n$	0.92

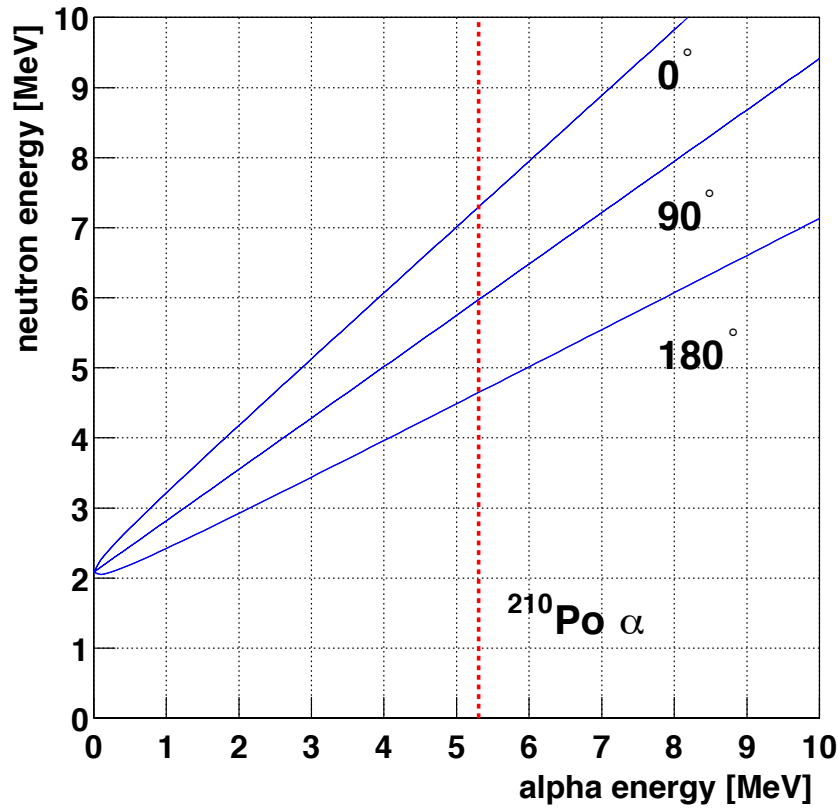


Figure 4.27: Neutron energy vs alpha energy in forward(0°), right(90°), backward(180°) scattering angles in the $^{13}\text{C}(\alpha, n)^{16}\text{O}$ reaction. The dashed line indicates the incident alpha energy of ^{210}Po .

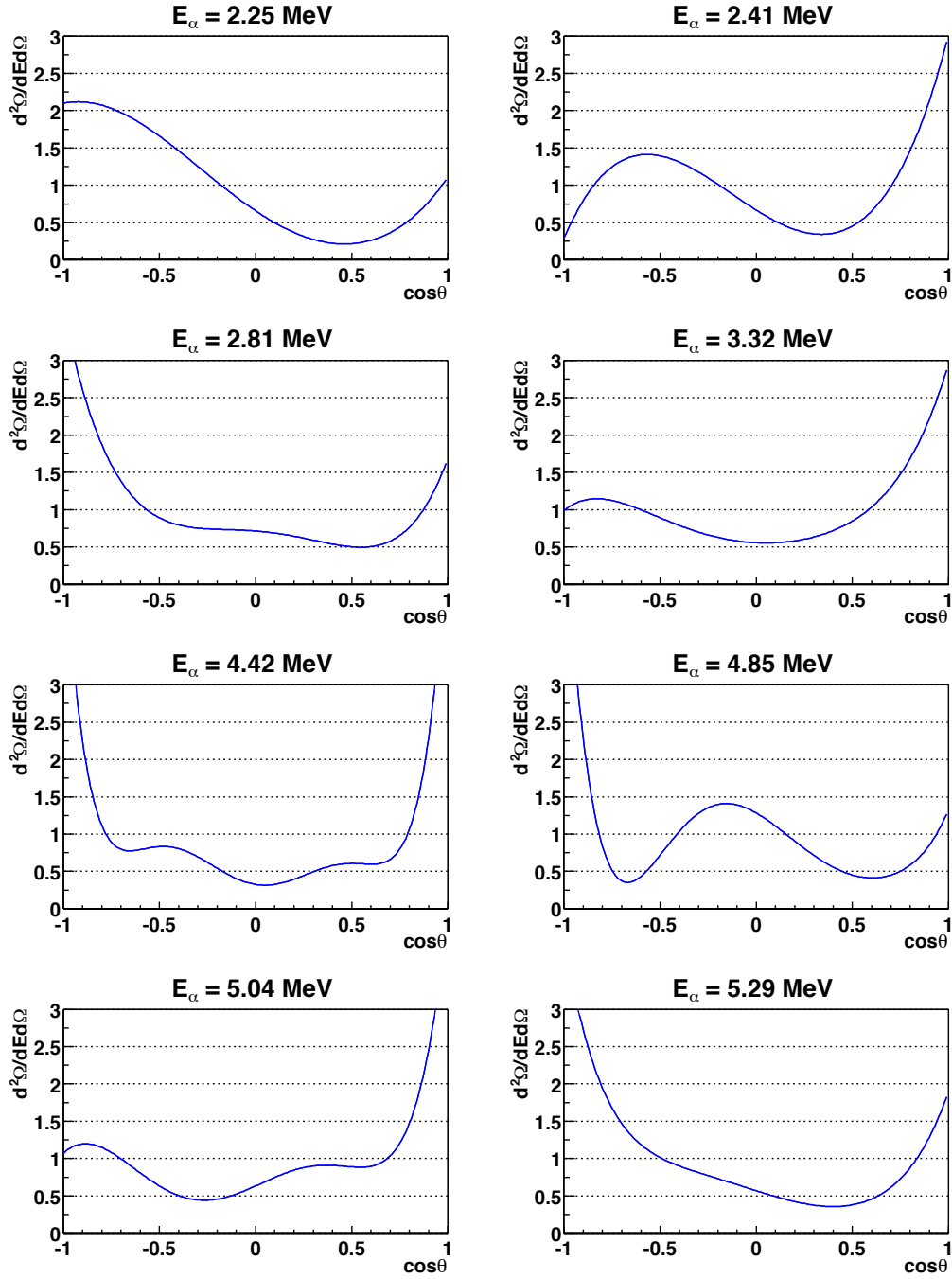


Figure 4.28: Angular distribution of neutron expressed by a Legendre-polynomial [84][85] for each energy.

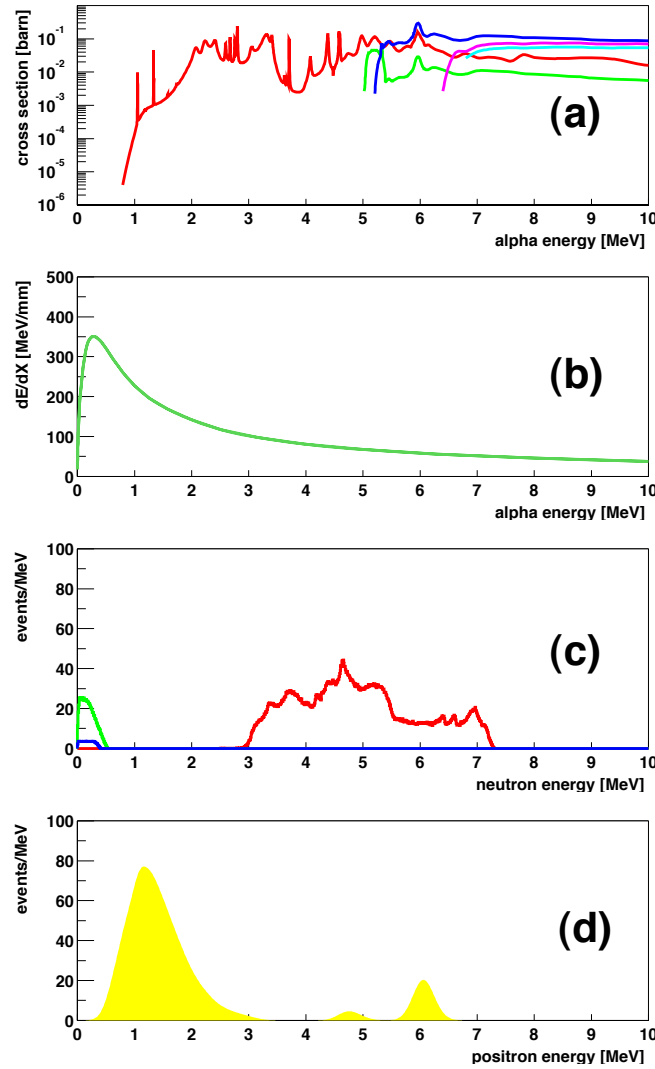


Figure 4.29: (a) Cross section of $^{13}\text{C}(\alpha, n)^{16}\text{O}$ with a function of the α energy in the laboratory system. The red, green, blue, pink and sky blue lines are cross section for grand, first excited, second excited, third excited, forth excited state of ^{16}O respectively. (b) Stopping power of the liquid scintillator in KamLAND. (c) Neutron energy distribution of $^{13}\text{C}(\alpha, n)^{16}\text{O}$ calculated from (a), (b) and the angular distribution of neutron, which is expressed using a Legendre-polynomial. (d) Energy distribution of $^{13}\text{C}(\alpha, n)^{16}\text{O}$ in positron scale. The recoil of protons can be simulated with the MC. The quenching factor of proton is calculated from the Birk's constant, which is estimated by the energy of ^{210}Po , ^{214}Po and ^{212}Po . The 6.049 MeV e^+e^- by internal pair creation and 6.130 MeV γ are observed at 2.6 MeV energy threshold as well as the 4.438 MeV γ by $^{12}\text{C}(n, n\gamma)^{12}\text{C}$.

4.3.5 (γ, n)

The photodisintegration of nuclei may generate neutrons, and its contribution should be considered. The target nuclei of (γ, n) reaction are listed in Table 4.13. The dominant reaction is $^2\text{H}(\gamma, n)\text{p}$ due to its low energy threshold. The prompt events can be generated by the proton and neutron, whose total kinetic energies are $(E_\gamma - 2.22)$ MeV. The upper limit of the $^2\text{H}(\gamma, n)\text{p}$ reaction is estimated from number of events above 3 MeV, conservatively. Using the deuteron photodisintegration cross section [86] related to the neutron capture cross section, the number of (γ, n) events are less than 0.039 events.

Table 4.13: Target nuclei of (γ, n) reaction

target nuclei	threshold (MeV)	natural abundance
^1H	-	99.985%
^2H	2.22	0.015%
^3H	6.26	-
^{12}C	18.7	98.90%
^{13}C	4.95	1.10%
^{14}C	8.18	-
^{14}N	10.6	99.634%
^{15}N	10.8	0.366%
^{16}N	2.49	-
^{16}O	15.7	99.762%
^{17}O	4.14	0.038%
^{18}O	8.04	0.200%
^{19}O	3.96	-

4.3.6 Spontaneous Fission

There are several spontaneously fissile nuclei and neutron emitters in the U/Th/Ac/Np series. Spontaneous fission can make backgrounds for the reactor $\bar{\nu}_e$ analysis, because the fission reaction generates gamma-rays (total energy ~ 6 MeV) and several neutrons. In the reactor $\bar{\nu}_e$ analysis, the multiple neutron events are not selected, so only single neutron events contribute to backgrounds. On the other hand neutron emitters are observed as single neutron events. Those backgrounds are summarized in Table 4.14.

The U and Th series are estimated from Bi-Po coincidence. However, there are long life nuclei in U series, such as ^{234}U , thus the upper limit of ^{238}U decay rate is estimated from the ^{234}Pa decay rate, assuming the radiation equilibrium of the ^{238}U chain down to ^{234}Pa . The Ac and Np series are negligible.

Spontaneous fission of ^{238}U becomes backgrounds due to the high branching ratio, and its upper limit is < 1.8 event. The single neutron detection efficiency is estimated from the average

Table 4.14: Spontaneous fission nuclei and neutron emitters in the U/Th/Ac/Np series

target nuclei	mode	branching ratio	events / data-set
U-series			
^{238}U	SF	$5.45 \times 10^{-5}\%$	1.8
^{234}U	SF	$1.64 \times 10^{-9}\%$	5.5×10^{-5}
^{234}U	$^{234}\text{U} \rightarrow \text{Ne} + \text{X}$	$9 \times 10^{-12}\%$	3.1×10^{-7}
^{234}U	$^{234}\text{U} \rightarrow \text{Mg} + \text{X}$	$1.4 \times 10^{-11}\%$	4.7×10^{-7}
^{230}Th	SF	$< 3.8 \times 10^{-12}\%$	$< 1.3 \times 10^{-7}$
^{210}Tl	$^{210}\text{Tl} \rightarrow ^{209}\text{Pb} + n$	$7 \times 10^{-3}\%$	2.3×10^{-6}
Th-series			
^{232}Th	SF	$< 1.8 \times 10^{-9}\%$	$< 7.7 \times 10^{-8}$
^{228}Th	$^{228}\text{Th} \rightarrow ^{20}\text{O} + n + \dots$	$1.13 \times 10^{-11}\%$	4.8×10^{-10}
^{224}Ra	$^{224}\text{Ra} \rightarrow ^{14}\text{C} + \text{X}$	$< 4.3 \times 10^{-9}\%$	$< 1.9 \times 10^{-7}$
Ac-series			
^{235}U	SF	$7.0 \times 10^{-9}\%$	-
^{235}U	$^{235}\text{U} \rightarrow ^{20}\text{N} + \text{X}$	$8 \times 10^{-10}\%$	-
^{231}Pa	SF	$< 1.6 \times 10^{-11}\%$	-
^{223}Ra	$^{223}\text{Ra} \rightarrow ^{14}\text{C} + ^{209}\text{Pb}$	$6.4 \times 10^{-8}\%$	-
Np-series			
^{237}Np	SF	$< 2.1 \times 10^{-10}\%$	-
^{233}U	SF	$< 6 \times 10^{-11}\%$	-
^{233}U	$^{233}\text{U} \rightarrow ^{24}\text{Ne} + \text{X}$	$< 9.5 \times 10^{-11}\%$	-
^{225}Ac	$^{225}\text{Ac} \rightarrow ^{14}\text{C} + \text{X}$	$6.0 \times 10^{-10}\%$	-
^{221}Fr	$^{211}\text{Fr} \rightarrow \text{C} + \text{X}$	$8.8 \times 10^{-11}\%$	-

number of neutrons emitted per fission event,

$$(\text{Number of Neutron}) = 1.98 \pm 0.89 / \text{fission}, \quad (4.16)$$

therefore a simple gaussian approximation gives ‘1 neutron probability’ $\sim 24.5\%$. Prompt events are gamma-rays from spontaneous fission,

$$(\text{Average Number}) = 6.36 \pm 0.47 \quad (4.17)$$

$$(\text{Average Gamma Energy}) = 0.95 \pm 0.07 \text{ MeV}, \quad (4.18)$$

thus the energy threshold effect is negligible. Considering the single neutron efficiency, the number of spontaneous fission backgrounds are less than 0.4 events.

4.3.7 Atmospheric Neutrino

The atmospheric neutrinos consist of electron and muon neutrinos and their anti-neutrinos, and the ratio of ν_μ to ν_e is expected to be 2. In the reactor $\bar{\nu}_e$ analysis, the atmospheric neutrino is a background at the low energy regions. The base model for the estimation is BGS [87] as shown in Figure 4.30. This model is a calculation at the energy range from 2 MeV to 3 GeV. From the BGS flux model, the number of the atmospheric $\bar{\nu}_e$ events is 2.6×10^{-4} events, so its contribution is negligible.

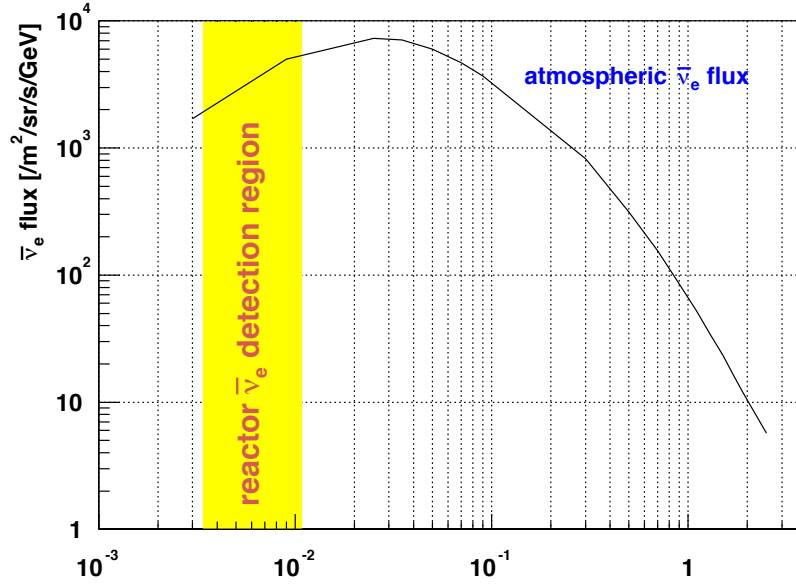


Figure 4.30: Atmospheric anti-neutrino fluxes with the BGS model [87].

4.3.8 Geo Neutrino

The $\bar{\nu}_e$ emitted by radioactivities in the crust and mantle of the earth, is called ‘geo-neutrinos’. It contributes to low energy events. The observation of the geo-neutrino events is important for understanding the earth energetics, however, the geo-neutrino event is a background for the reactor $\bar{\nu}_e$ analysis. Figure 4.31 shows the expected geo-neutrino energy spectrum for 16 TW intensity. The ratio of ^{238}U and ^{232}Th contribution is adopted to 4. Actually, the geo-neutrino flux has large uncertainties, which come from the abundances of U/Th and its ratio due to the uncertainty of the geo-chemical estimation. Therefore, the data above 2.6 MeV prompt energy is analyzed in order to avoid the geo-neutrino background.

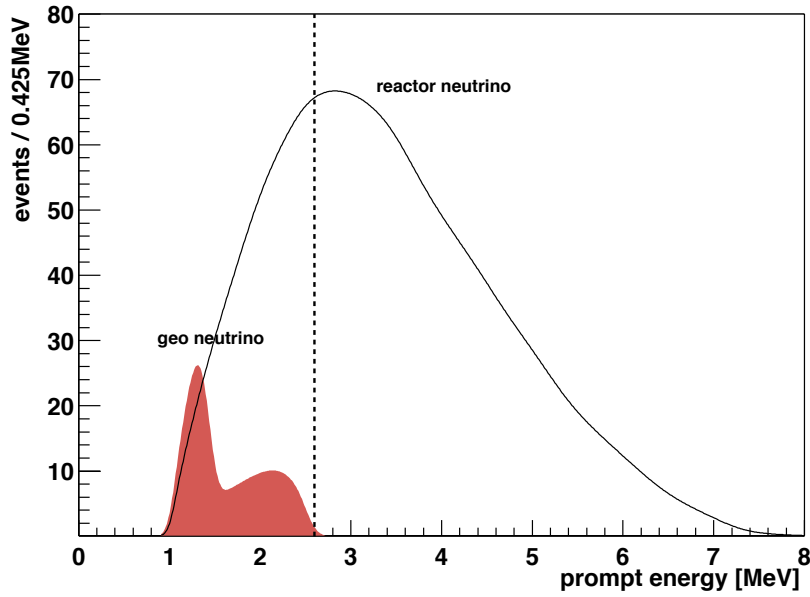


Figure 4.31: Expected geo-neutrino energy spectrum for 16 TW intensity.

Chapter 5

Reactor Anti-Neutrino Estimation

KamLAND observes electron anti-neutrinos from distant reactors. The reactor anti-neutrino event rate is estimated from the thermal power for each reactor and those distances, approximately proportional to $P_{th}/4\pi L^2$, where P_{th} is the thermal power. Uncertainty of the distance is less than 70 m. The anti-neutrino flux at the KamLAND detector is from many nuclear reactors at a range of distances, however, the flux is dominated by reactors at an average distance of ~ 180 km (Figure 5.1). More than 79% of the computed flux arises from 26 reactors within the distance range 138-214 km. One reactor at 88 km contributes an additional 6.7% to the flux and the other reactors are more than 295 km away. This relatively narrow band of distances implies that, for some oscillation parameters, KamLAND can observe a distortion of the $\bar{\nu}_e$ energy spectrum.

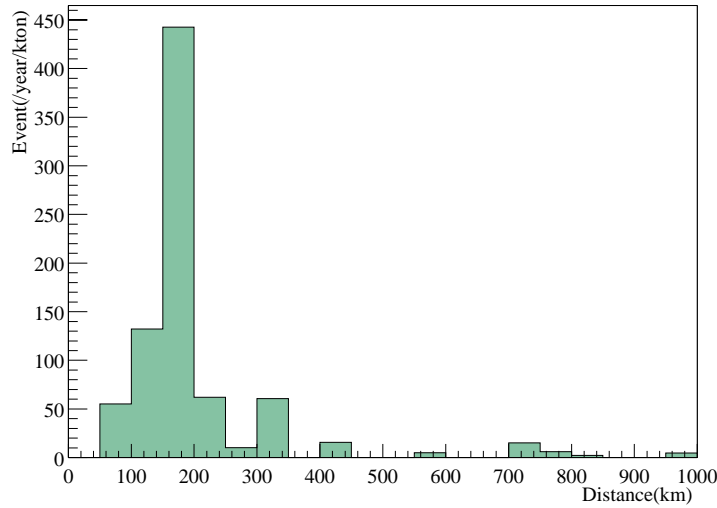


Figure 5.1: Contribution to the expected $\bar{\nu}_e$ events from distant reactors.

5.1 Reactor Anti-Neutrino Flux

There are 53 nuclear power reactors in Japan. Those reactors are supplying about one third of the total electric power in the country. The KamLAND experiment detects $\bar{\nu}_e$ coming from reactors, of which the average distance is about 180 km away (Figure 5.2). Reactors in Japan and Korea are summarized in Table 5.2 and 5.3. The reactors are classified according to power generation procedure, they are mainly Boiling Water Reactor (BWR) or Pressurized Water Reactor (PWR), and two extra types for the study of Plutonium rich reactor, Advanced Thermal Reactor (ATR) and Fast Breeder Reactor (FBR).

^{235}U in the reactor core absorbs a thermal neutron and breaks up into several pieces (nuclear fission). The unstable fission fragments emit anti-neutrinos ($\bar{\nu}_e$) via the β -decays,

$$^{235}\text{U} + n \rightarrow A + B + 6.1\beta^- + 6.1\bar{\nu}_e + 202\text{MeV} + xn. \quad (5.1)$$

^{238}U go into fission with a fast neutron

$$^{238}\text{U} + n(> 1\text{MeV}) \rightarrow C + D + 5 \sim 7\beta^- + 5 \sim 7\bar{\nu}_e + 205\text{MeV} + yn \quad (5.2)$$

or produces the ^{239}Pu via two β -decays after capturing a thermal neutron,

$$n + ^{238}\text{U} \rightarrow ^{239}\text{U} \quad (5.3)$$

$$\rightarrow ^{239}\text{Np} \quad (5.4)$$

$$\rightarrow ^{239}\text{Pu} (T_{1/2} = 24, 100 \text{ year}). \quad (5.5)$$

^{239}Pu go to fission with a thermal neutron

$$^{239}\text{Pu} + n \rightarrow E + F + 5.6\beta^- + 5.6\bar{\nu}_e + 210\text{MeV} + zn \quad (5.6)$$

or produces the ^{241}Pu by absorbing two thermal neutrons

$$n + ^{239}\text{Pu} \rightarrow ^{240}\text{Pu} \quad (5.7)$$

$$n + ^{240}\text{Pu} \rightarrow ^{241}\text{Pu} (T_{1/2} = 14.4 \text{ year}). \quad (5.8)$$

^{241}Pu breaks with a thermal neutron

$$^{241}\text{Pu} + n \rightarrow G + H + 6.4\beta^- + 6.4\bar{\nu}_e + 212\text{MeV} + wn. \quad (5.9)$$

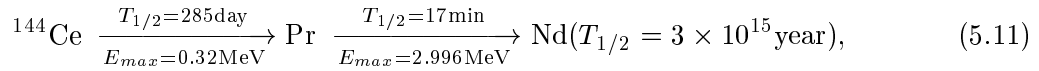
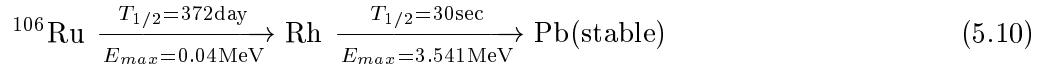
The $\bar{\nu}_e$ flux is calculated with the fission rate of each isotope and each fission (Figure 5.3). Spectrum uncertainty for each isotope is shown in Figure 5.4. These spectra and uncertainties are given in [88, 89, 90], and the overall spectrum has been checked by previous short baseline experiment within 1.4% accuracy [54, 91]. The spectrum uncertainty is assigned to the systematic uncertainty of $\bar{\nu}_e$ detection, in the no oscillation case, 2.29% for LAT (0.9 MeV analysis threshold) and 2.54% for HAT (2.6 MeV analysis threshold).

The fuel composition of each reactor evolves with time, i.e. Uranium is depleted and Plutonium is bred, called as ‘burn-up effect’. The total fission rates of each isotope in the core can be calculated from the thermal power and the burn-up data of each reactor, which are provided

by the Japanese electric power companies. Using a simple and practical modeling of the reactor core to compute the fuel composition, developed by Tokyo Electric Power Company (TEPCO), the fission rate for each isotope at each reactor are calculated. The uncertainty for $\bar{\nu}_e$ flux is estimated to be 1% compared with detailed simulation by TEPCO. The thermal power data is needed to normalize the fission rate which is monitored at each reactor and controlled within 2% error. Figure 5.5 shows an example of the fuel burn-up at a Japanese reactor, and the time variation of $\bar{\nu}_e$ flux from reactors is shown in Figure 5.6. Averaged over the present livetime period, the relative fission yields are $^{235}\text{U} : ^{238}\text{U} : ^{239}\text{Pu} : ^{241}\text{Pu} = 0.563 : 0.079 : 0.301 : 0.057$.

The systematic error for the thermal power is conservatively assigned as 2% from the control precision in the reactor operation. The contribution from Korean reactors is estimated to be $(3.41 \pm 0.34)\%$ based on reported electric power generation. The 0.34% error comes from the 10% uncertainty in procedure of the conversion from electric power to thermal power. The contribution from other countries including the Japanese research reactors is $(1.04 \pm 0.52)\%$ which is estimated using reactor specifications from the International Nuclear Safety Center [92]. This systematic error is addressed as a half of it.

Typically, the fission rate reaches equilibrium within a day above ~ 2 MeV in neutrino energy. Therefore, the 0.01% error of time-lag effect is assigned to the $\bar{\nu}_e$ flux, estimated from the difference of the total $\bar{\nu}_e$ yield associated with shifting the run time by one day. However, there are several long-lived nuclei, such as ^{106}Ru and ^{144}Ce ,



and those nuclei contribute to the $\bar{\nu}_e$ flux, and it is calculated to be only $(0.04 \pm 0.02)\%$ for the HAT (2.6 MeV analysis threshold), where systematic error is addressed as a half of it for the equilibrium uncertainty. The neutrino energy spectra of ^{106}Ru and ^{144}Ce are shown in Figure 5.7. The summary of the $\bar{\nu}_e$ contributions from reactors other than Japan and long-lived nuclei is given in Table 5.1.

Table 5.1: Contributions from world reactors and long-lived nuclei at the HAT (2.6 MeV analysis threshold)

$\bar{\nu}_e$ sources	contributions [%]
Korean reactors	3.41 ± 0.34
other countries and Japanese research reactors	1.04 ± 0.52
long-lived nuclei	0.04 ± 0.02

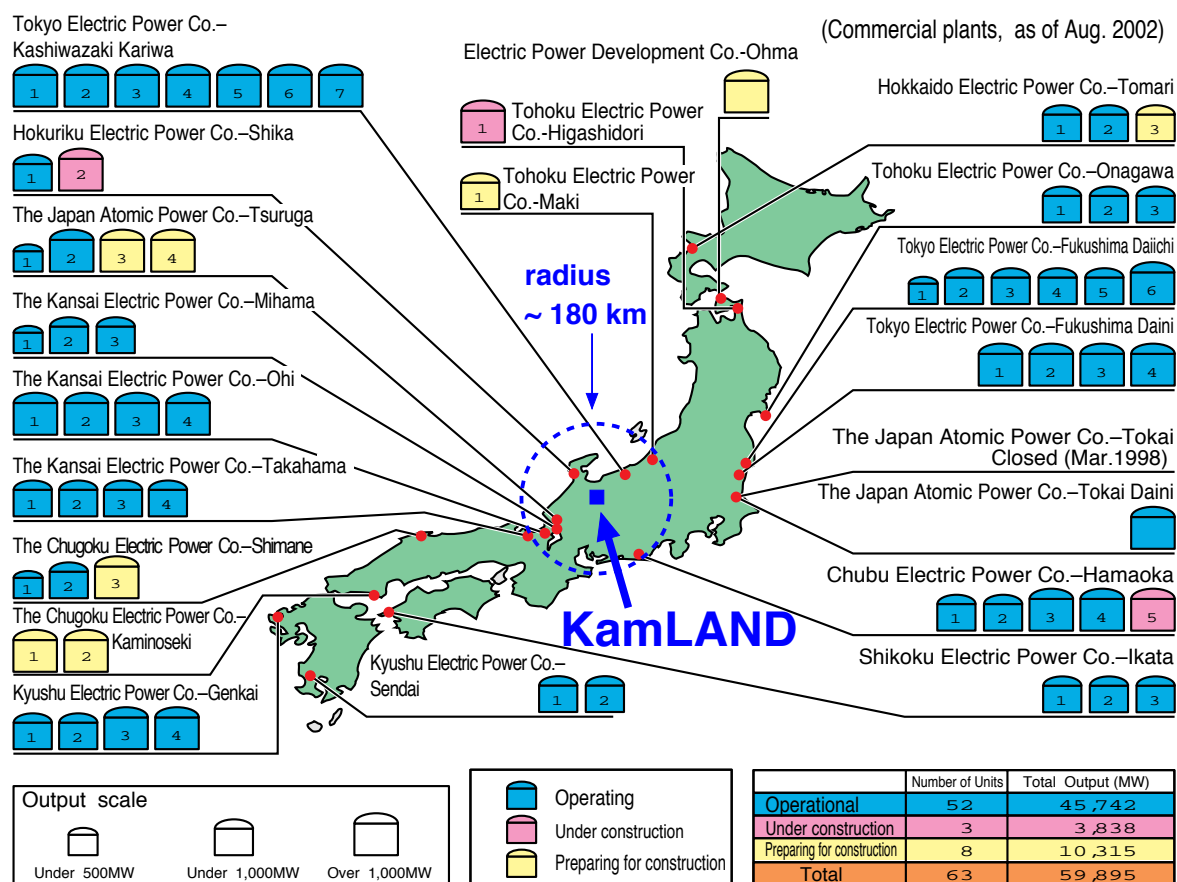


Figure 5.2: The locations of Japanese nuclear reactors and KamLAND. The dashed line shows 180 km radius from KamLAND.

Table 5.2: Japanese and Korean reactors - part 1 -

company	reactor name	distance [km]	type	thermal power [MW]	electrical power [MW]
Chubu	Hamaoka-1	213.72	BWR	1593	540
	Hamaoka-2	213.80	BWR	2436	840
	Hamaoka-3	214.01	BWR	3293	1100
	Hamaoka-4	214.15	BWR	3293	1137
	Hamaoka-5*	-	BWR	3926	1380
Chugoku	Shimane-1	401.07	BWR	1380	460
	Shimane-2	401.22	BWR	2436	820
Genden	Tokai2	295.37	BWR	3293	1100
	Tsuruga-1	138.47	BWR	1064	357
	Tsuruga-2	138.48	PWR	3423	1160
Hokkaido	Tomari-1	783.04	PWR	1650	579
	Tomari-2	782.92	PWR	1650	579
Hokuriku	Shika-1	87.67	BWR	1593	540
	Shika-2*	-	BWR	3926	1358
JapanNuclearCycle	Fugen	138.51	ATR	557	165
	Monju	141.51	FBR	714	280
Kansai	Mihama-1	145.72	PWR	1031	340
	Mihama-2	145.77	PWR	1456	500
	Mihama-3	145.83	PWR	2440	826
	Ohi-1	178.75	PWR	3423	1175
	Ohi-2	178.83	PWR	3423	1175
	Ohi-3	179.04	PWR	3423	1180
	Ohi-4	179.16	PWR	3423	1180
	Takahama-1	191.24	PWR	2440	826
	Takahama-2	191.27	PWR	2440	826
	Takahama-3	191.68	PWR	2660	870
	Takahama-4	191.71	PWR	2660	870
Kyusyu	Genkai-1	754.40	PWR	1650	559
	Genkai-2	754.51	PWR	1650	559
	Genkai-3	754.63	PWR	3423	1180
	Genkai-4	754.74	PWR	3423	1180
	Sendai-1	830.38	PWR	2660	890
	Sendai-2	830.30	PWR	2660	890
Shikoku	Ikata-1	560.79	PWR	1650	566
	Ikata-2	560.85	PWR	1650	566
	Ikata-3	560.70	PWR	2660	890
Tohoku	Onagawa-1	430.48	BWR	1593	524
	Onagawa-2	430.60	BWR	2436	825
	Onagawa-3	430.51	BWR	2436	825
	Higashidori-1*	-	BWR	3293	1100

Table 5.3: Japanese and Korean reactors - part 2 -

company	reactor name	distance [km]	type	thermal power [MW]	electrical power [MW]
Tokyo	Fukushima1-1	349.43	BWR	1380	460
	Fukushima1-2	349.37	BWR	2381	784
	Fukushima1-3	349.34	BWR	2381	784
	Fukushima1-4	349.30	BWR	2381	784
	Fukushima1-5	349.55	BWR	2381	784
	Fukushima1-6	349.59	BWR	3293	1100
	Fukushima2-1	345.34	BWR	3293	1100
	Fukushima2-2	345.40	BWR	3293	1100
	Fukushima2-3	345.44	BWR	3293	1100
	Fukushima2-4	345.47	BWR	3293	1100
	KashiwazakiKariwa-1	159.10	BWR	3293	1100
	KashiwazakiKariwa-2	159.23	BWR	3293	1100
	KashiwazakiKariwa-3	159.34	BWR	3293	1100
	KashiwazakiKariwa-4	159.54	BWR	3293	1100
	KashiwazakiKariwa-5	160.62	BWR	3293	1100
	KashiwazakiKariwa-6	160.52	BWR	3926	1356
	KashiwazakiKariwa-7	160.40	BWR	3926	1356
KHNP	Kori-1	734.52	PWR	1727	587
	Kori-2	734.52	PWR	1913	650
	Kori-3	734.52	PWR	2796	950
	Kori-4	734.52	PWR	2796	950
	Ulchin-1	711.81	PWR	2796	950
	Ulchin-2	711.81	PWR	2796	950
	Ulchin-3	711.81	PWR	2943	1000
	Ulchin-4	711.81	PWR	2943	1000
	Ulchin-5*	711.81	PWR	2943	1000
	Ulchin-6*	711.81	PWR	2943	1000
	Wolsong-1	708.58	PWR	1995	678
	Wolsong-2	708.58	PWR	2060	700
	Wolsong-3	708.58	PWR	2060	700
	Wolsong-4	708.58	PWR	2060	700
	Yonggwang-1	986.41	PWR	2796	950
	Yonggwang-2	986.41	PWR	2796	950
	Yonggwang-3	986.41	PWR	2943	1000
	Yonggwang-4	986.41	PWR	2943	1000
	Yonggwang-5	986.41	PWR	2943	1000
	Yonggwang-6	986.41	PWR	2943	1000

* : under construction

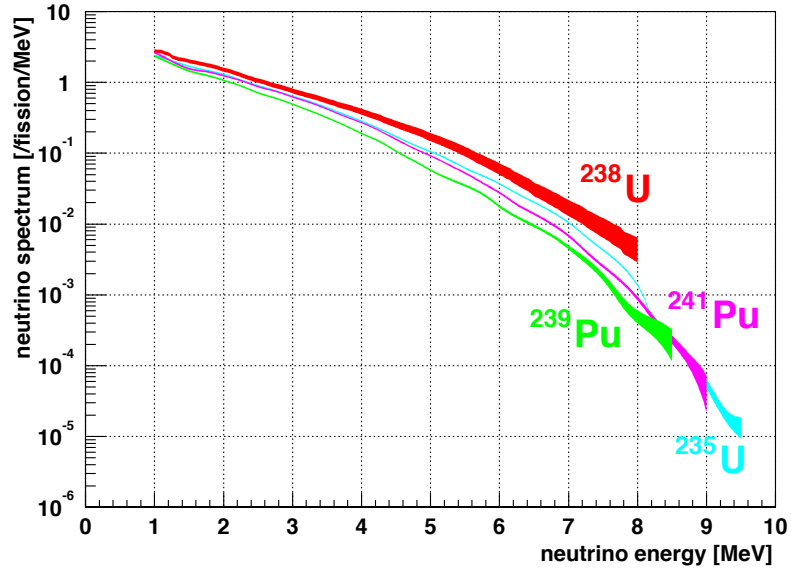


Figure 5.3: Energy spectra of $\bar{\nu}_e$ flux from nuclear fissions, ^{235}U , ^{238}U , ^{239}Pu and ^{241}Pu [88, 89, 90]. Overall spectrum is checked within 1.4% accuracy [54, 91].

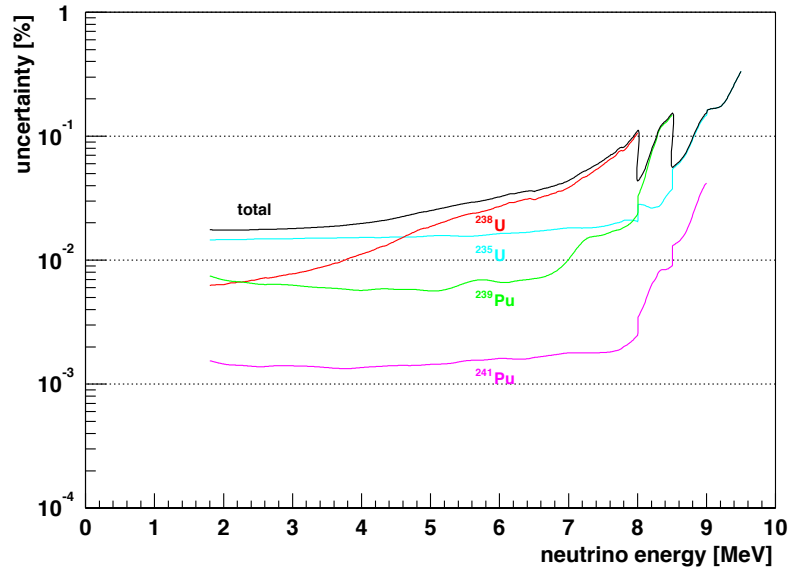


Figure 5.4: Uncertainties of neutrino spectra from four isotopes.

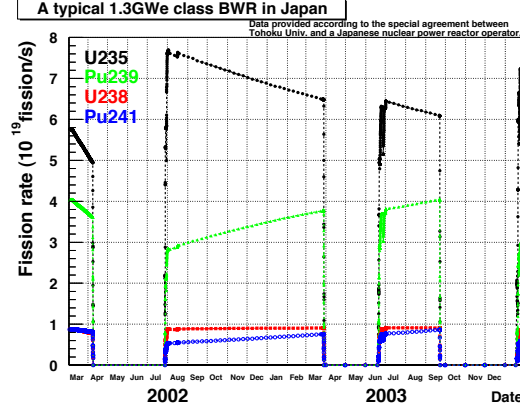


Figure 5.5: Fission rate of each isotopes, ^{235}U , ^{238}U , ^{239}Pu and ^{241}Pu .

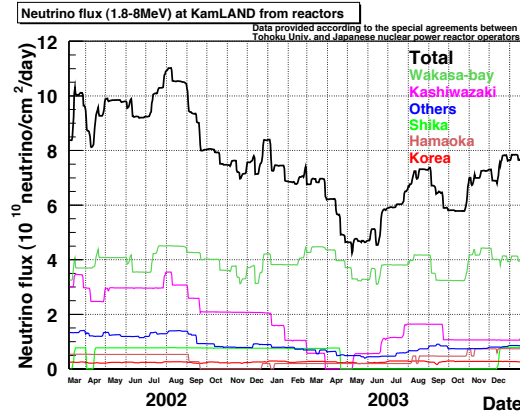


Figure 5.6: Time variation of $\bar{\nu}_e$ flux from reactors.

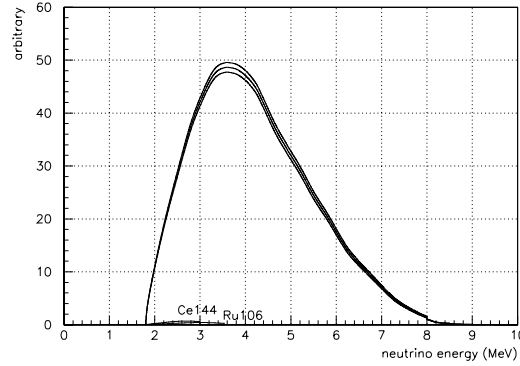


Figure 5.7: $\bar{\nu}_e$ energy spectra from long-lived nuclei (^{106}Ru , ^{144}Ce) and general reactor $\bar{\nu}_e$ spectrum in the no oscillation case. The band means uncertainty of spectrum in the no oscillation case.

5.2 Number of Targets

The calculation of the number of targets is based on the composition of the liquid scintillator materials and density measurement. Chemical composition of the liquid scintillator in KamLAND is as follows,

- normalparaffin (Dodecane: $C_{12}H_{26}$) 80.2% (0.7526 g/cm³ @ 15°C)
- pseudocumene (1,2,4-Trimethylbenzene: C_9H_{12}) 19.8% (0.8796 g/cm³ @ 15°C)
- PPO (2,5-Diphenyloxazole: $C_{15}H_{11}NO$) 1.52 g/liter.

The measured density of the liquid scintillator is 0.77754 ± 0.00010 g/cm³ @ 15°C, and the temperature coefficient of density expansion is measured to be 7.41×10^{-4} g/cm³/K. As the temperature of the KamLAND liquid scintillator is $\sim 11.5^\circ\text{C}$, the actual density is calculated to be 0.78013 g/cm³. The ratios of H/C, H/N and H/O are calculated using those information, and the number of proton is given by

$$\begin{aligned} \text{Number of H} &= \frac{N_A}{1.00794 + 12.011/(H/C) + 14.00674/(H/N) + 15.9994/(H/O)} \\ &= 8.470 \times 10^{22}/g \end{aligned}$$

The fiducial volume is 696.91 m³ in 5.5 m fiducial radius, therefore, the number of the target nuclei ^1H is calculated using the natural abundance 0.99985,

$$\begin{aligned} \text{Number of } ^1\text{H} &= 8.470 \times 10^{22}/g \times (696.91 \times 10^6)\text{cm}^3 \times 0.78013 \text{ g/cm}^3 \times 0.99985 \\ &= 4.604 \times 10^{31} \end{aligned}$$

The water contamination into the liquid scintillator gives a negligible contribution. The systematic uncertainty of the number of target is estimated from the temperature uncertainty $\sim 1.5^\circ\text{C}$. That corresponds to be less than 0.1% error.

5.3 Cross-Section

The cross section of the inverse β -decay reaction $\bar{\nu}_e + p \rightarrow e^+ + n$ is given in Section 2.1.2. The uncertainty of the calculation is directly controlled by the the neutron lifetime, which is measured to be 885.7 ± 0.8 sec, now. The systematic error of the cross section is estimated to be 0.2% [93].

5.4 Live Time Calculation

Livetime is defined as the sensitive time, i.e. the detector is sensitive for $\bar{\nu}_e$ detection. The livetime is calculated for each run with

- **runtime**

Time of the data taking period, defined as

(time of the last event in the run) – (time of the first event in the run).

- **deadtime**

Time of no data taking period or bad (incorrect) data taking period.

- **vetotime**

Time of veto period for the background rejection.

The uncertainty of the runtime is estimated to be ~ 5 msec, which comes from the event rate ~ 200 Hz in the history trigger. It corresponds to $6 \times 10^{-6}\%$ for the typical 24 hours runtime.

5.4.1 Deadtime

The dead time is classified to four types

- **bad run**

The data quality is very poor, for example, the number of bad-channels in the ID 17 inch PMTs is many or bad channel distribution has a cluster ¹ because of the HV supply or electronics problem, the trigger rate or muon rate is strange. And entire run is vetoed.

- **bad period (half-badrun)**

Only a part of run satisfy the conditions of bad run. Typically, its period is within an hour before and after some trouble.

- **trigger dead period**

The trigger module is busy and disable itself to fire. When the trigger module is busy, the disable flag is recorded in data files. The period of the trigger disable is the dead time. Another possible deadtime comes from the broken data packet by network problems. That is tagged by the large time intervals (>100 msec) between each history event.

- **noisy period and missing waveform (missing muon)**

The multiple noise events are usually coming within $150 \mu\text{sec}$ after muons because of the ringing on FEE. If there are no muons before a cluster of noise events, there is a possibility that muons are missed by indistinct deadtime. The missing muon is tagged by plural noise events within 1 msec without any muon, and that period is considered as the deadtime, conservatively. Another method to tag missing muon is to look for missing waveform, $N_{\text{hit}}(\text{i.e. number of waveform}) < N_{\text{sumMax}}$.

There is a possibility muons (possibly energetic muons) come into the detector while the dead-time, therefore, whole volume of the detector should be vetoed for 2 sec, conservatively. Only for the missing waveform case, the trigger hit information (N_{sumMax}) is used in order to decide the veto time width,

$$\begin{aligned} \text{low energy muon } (200 \leq N_{\text{sumMax}} < 1200) & : 2 \text{ msec veto} \\ \text{high energy muon } (N_{\text{sumMax}} \geq 1200) & : 2 \text{ sec veto.} \end{aligned}$$

¹In the case of the ID 20 inch PMTs, that run is treated as a good run using only 17 inch PMTs as before the 20 inch PMTs installation on February 27, 2003.

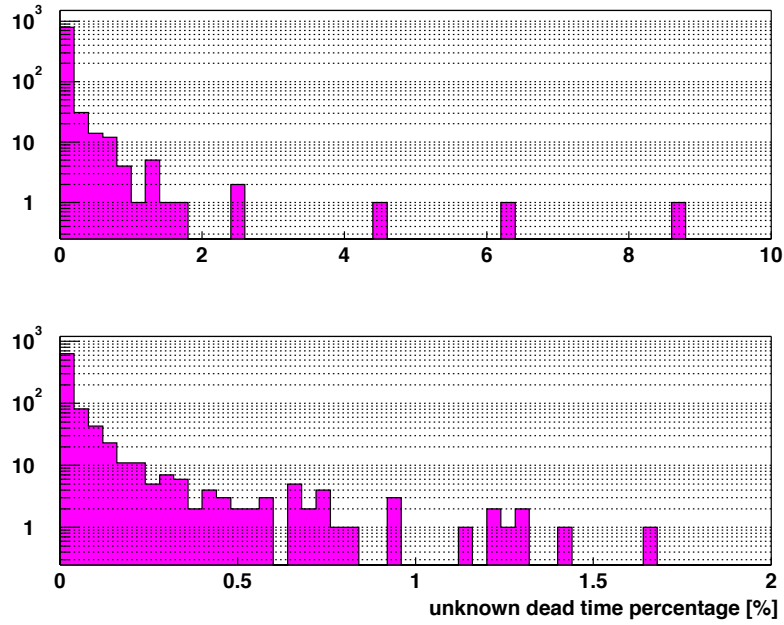


Figure 5.8: Ratio of indistinct deadtime in percentage. It is much less than 2% for almost all run, but it is more than 2% in sometimes. Anyway, percentage of indistinct deadtime is less than 2% and average of it is 0.06%.

5.4.2 Vetotime

The muon is classified to four grades and three types of veto are applied for each muon.

- Low Charge Muon ($Q \leq 40,000$ p.e.)
Whole volume of the detector is vetoed for 2 msec
- Energetic Muon ($Q > 40,000$ p.e. and $\Delta Q \geq 10^6$ p.e.)
Whole volume of the detector is vetoed for 2 sec
- Miss Reconstructed Muon ($Q > 40,000$ p.e. and badness ≥ 100)
Whole volume of the detector is vetoed for 2 sec
- Well Reconstructed Non-Energetic Muon ($Q > 40,000$ p.e. and badness < 100 and $\Delta Q < 10^6$ p.e.)
Whole volume of the detector is vetoed for 2 msec, and then cylindrical volume around muon track within 3 m is vetoed for 2 sec. The cylindrical vetoed is only applied to the delayed event.

Where Q means the total charge sum of ID 17 inch PMTs for each muon event, ΔQ means the residual charge. The badness is the grade of the muon reconstruction. The 9.7% of runtime in the fiducial volume (5.5 m fiducial radius) is vetoed by the spallation cut.

5.4.3 Livetime

The livetime is calculated using runtime and deadtime and veto information for each run. In order to consider the overlap of each veto in time and volume, the simple MC simulation is used. The MC events are distributed uniformly for the position and time in the fiducial volume and runtime, so the ratio of livetime/runtime is given by

$$\frac{\text{livetime}}{\text{runtime}} = \frac{\text{number of events (R < 5.5 m) with applying all cut}}{\text{number of events (R < 5.5 m)}} \quad (5.12)$$

The uncertainty of this calculation is verified by the statistic of the generated events. About 9.2×10^8 events were generated, and the vetoed events were about 10% of the total generated events. The error for the ratio of the vetoed events to the total generated events is $\sim 1.0 \times 10^{-5}$. Therefore, the uncertainty of the calculation is 0.001%. Figure 5.9 shows the ratio of livetime to runtime for each run except for the bad run. The livetime for almost all runs are less than 24 hours. The total livetime from March 9, 2002 to January 11, 2004 (run220 - run3206) is 515.1 days.

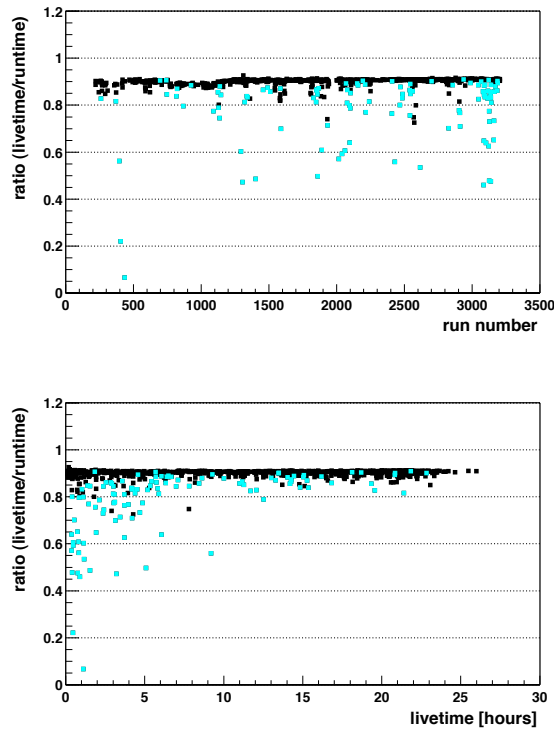


Figure 5.9: Ratio of livetime/runtime for each run. The sky blue markers indicate half-bad runs. The small ratio indicates the noisy run, which has much noisy period. The average efficiency for the runtime is about 90%.

The total systematic uncertainty for the livetime is addressed with a quadratic sum of uncertainty of the runtime $6 \times 10^{-6}\%$, the deadtime finding error 0.06% and the uncertainty of the calculation 0.001% ,

$$\sqrt{(6 \times 10^{-6})^2 + 0.06^2 + 0.001^2} \simeq 0.06\%.$$

5.5 Detection Efficiency and Systematic Uncertainties

The KamLAND data-set is classified according to the status of the electronics and the PMTs. In the KamLAND, the FEE (Front-End Electronics) was upgraded² in January 10, 2003, in order to reduce the waveform undershoot caused by combination of transformer AC coupling, signal clipping, and second AC coupling. In the upgraded FEE, the transformer was removed, and AC coupling was tuned to minimize the overshoot amplitude. The gain of the 20 inch PMTs were tuned in February, 2003, and completed in February 27. The combined data using 17 inch PMTs and 20 inch PMTs were used after that, and increased the photo-cathode coverage from 22% to 34%, which has the advantage of the better energy resolution.

The data-set is named ‘period I’, ‘period II’ and ‘period III’, tentatively. The period I is before FEE upgrade, and the period II and III are after FEE upgrade. The period I and II have only 17 inch PMT runs, and the period III has 17 inch and 20 inch PMT runs. In the period III, when there are many bad channels for the 20 inch PMTs (only 20 inch bad-run), that run belongs to period II. Table 5.4 shows the summary of data-set.

Table 5.4: Summary of data-set

	period I	period II	period III
electronics status	before FEE upgrade	after FEE upgrade	
PMT status	17 inch		17 inch + 20 inch
date	March 9, 2002 ↓ January 10, 2003	January 10, 2003 ↓ February 27, 2003	February 27, 2003 ↓ January 11, 2004
run	220 - 1892	1896 - 2181	2194 - 3206
livetime (day)	218.40	38.87	257.87
energy resolution (% / $\sqrt{E(\text{MeV})}$)	7.3		6.2

²Actually, the date January 10 was the start of FEE upgrade, i.e.
January 10 : replace 50% of 17 inch boards with modified boards
January 11 : replace rest of 17 inch boards with modified boards
January 12 : replace OD, neck boards with modified boards
January 13 : fill 20 inch slots with modified boards.

The selection cuts for $\bar{\nu}_e$ events are the following (i) fiducial volume ($R < 5.5$ m), (ii) time correlation ($0.5 \mu\text{sec} < \Delta T < 1000 \mu\text{sec}$), (iii) vertex correlation ($\Delta R < 2$ m), (iv) delayed energy ($1.8 \text{ MeV} < E_{\text{delayed}} < 2.6 \text{ MeV}$). The total efficiency from cuts (i)-(iv) is $(89.8 \pm 1.5)\%$. The detail of the $\bar{\nu}_e$ detection efficiency is summarized in Table 5.5 and Table 5.6. The effect of (i) on the delayed vertex is included in (iii). Systematic uncertainties for the reactor $\bar{\nu}_e$ detection are summarized in Table 5.7 and Table 5.8.

Table 5.5: $\bar{\nu}_e$ detection efficiency (period I + II)

	0.9 MeV threshold (LAT)	2.6 MeV threshold (HAT)
space correlation ($\Delta R < 200$ cm)	91.32%	91.32%
time correlation ($0.5 < \Delta T < 1000 \mu\text{sec}$)	98.89%	98.89%
trigger efficiency	99.99%	-
delayed energy	99.98%	99.98%
neutron capture on proton	99.48%	99.48%
total	89.81%	89.82%

Table 5.6: $\bar{\nu}_e$ detection efficiency (period III)

	0.9 MeV threshold (LAT)	2.6 MeV threshold (HAT)
space correlation ($\Delta R < 200$ cm)	91.32%	91.32%
time correlation ($0.5 < \Delta T < 1000 \mu\text{sec}$)	98.89%	98.89%
trigger efficiency	99.99%	-
delayed energy	99.99%	99.99%
neutron capture on proton	99.48%	99.48%
total	89.82%	89.83%

Table 5.7: Systematic uncertainties of $\bar{\nu}_e$ detection (period I + II)

	0.9 MeV threshold (LAT)	2.6 MeV threshold (HAT)
-efficiencies-		
space correlation ($\Delta R < 200$ cm)	1.6%	1.6%
time correlation ($0.5 < \Delta T < 1000$ μ sec)	0.05%	0.05%
trigger efficiency	0.002%	-
livetime calculation	0.06%	0.06%
-event selection and reconstruction-		
flasher event cut	$< 0.01\%$	$< 0.01\%$
noise event cut	$< 0.0002\%$	$< 0.0002\%$
fiducial cut	4.71%	4.71%
analysis energy threshold	-	2.14%
-reactor $\bar{\nu}_e$ -		
distance	$< 0.1\%$	$< 0.1\%$
thermal power		
Japanese reactors	2.0%	2.0%
Korean reactors	0.34%	0.34%
other reactors	0.52%	0.52%
chemical composition	$< 1.0\%$	$< 1.0\%$
$\bar{\nu}_e$ spectra	2.29%	2.54%
time lag	0.01%	0.01%
long-lived nuclei	0.34%	0.02%
-number of target and cross section-		
number of target protons	$< 0.1\%$	$< 0.1\%$
cross section	0.2%	0.2%
total	5.96%	6.42%

Table 5.8: Systematic uncertainties of $\bar{\nu}_e$ detection (period III)

	0.9 MeV threshold (LAT)	2.6 MeV threshold (HAT)
<hr/>		
-efficiencies-		
space correlation ($\Delta R < 200$ cm)	1.6%	1.6%
time correlation ($0.5 < \Delta T < 1000$ μ sec)	0.05%	0.05%
trigger efficiency	0.002%	-
livetime calculation	0.06%	0.06%
<hr/>		
-event selection and reconstruction-		
flasher event cut	$< 0.01\%$	$< 0.01\%$
noise event cut	$< 0.0002\%$	$< 0.0002\%$
fiducial cut	4.71%	4.71%
analysis energy threshold	-	2.33%
<hr/>		
-reactor $\bar{\nu}_e$ -		
distance	$< 0.1\%$	$< 0.1\%$
thermal power		
Japanese reactors	2.0%	2.0%
Korean reactors	0.34%	0.34%
other reactors	0.52%	0.52%
chemical composition	$< 1.0\%$	$< 1.0\%$
$\bar{\nu}_e$ spectra	2.29%	2.54%
time lag	0.01%	0.01%
long-lived nuclei	0.34%	0.02%
<hr/>		
-number of target and cross section-		
number of target protons	$< 0.1\%$	$< 0.1\%$
cross section	0.2%	0.2%
total	5.96%	6.49%

5.5.1 Space Correlation

Space correlation between prompt and delayed events is evaluated with a help of a detector simulation. For delayed events, neutrons around $10 \sim 20$ keV are generated in order to simulate the neutron recoil by the reactor anti-neutrino. The diffusion length of recoiled neutron is evaluated to be ~ 9 cm. The assumed vertex resolution is $30 \text{ cm}/\sqrt{E(\text{MeV})}$ estimated from the source calibration for various energies. Figure 5.10 (a) shows the space correlation between prompt and delayed events, and the events within 200 cm is 99.84%. This result can be checked by the Am-Be calibration using the delayed coincidence of prompt γ -rays and delayed neutrons (Appendix D). The prompt events are 4.4 MeV γ -rays, and the delayed events are 2.2 MeV γ -rays as shown in Figure 5.11. The detection efficiencies in the Am-Be source calibration at various z position are shown in Figure 5.12. The overall efficiency of Am-Be calibration is $99.69 \pm 0.11\%$, and it is almost consistent with that of the MC simulation.

The selection criteria for the delayed vertex in the $\bar{\nu}_e$ selection are the diffusion cut $\Delta R < 2$ m and the fiducial cut $R_{\text{delayed}} < 5.5$ m. The efficiency of those selection is 91.32% in the MC, while it is 1.49% smaller in the Am-Be calibration. The difference is addressed as the systematic error in the $\bar{\nu}_e$ selection, conservatively.

$$(\text{Efficiency of space Correlation}) = 91.32 \pm 1.49\%$$

Moreover, the efficiency is consistent within 2% even if the vertex resolution is 10 cm better or worse. The vertex dependence of the space efficiency is shown in Figure 5.10 (b). The inefficiency of the space correlation is dominated by the escape effect from the fiducial radius.

5.5.2 Time Correlation

Time correlation between prompt and delayed events is directly evaluated using the spallation neutrons. Figure 5.13 shows the time difference from muons to spallation neutron capture candidates. In order to avoid the electronics unstable condition due to the multiple neutrons, high energy muons are not used. The mean capture time is evaluated to be $211.2 \pm 2.6 \mu\text{sec}$ using the fitting by the exponential curve with accidental backgrounds. Therefore, the efficiency of the time correlation is calculated as follows,

$$\begin{aligned} (\text{Efficiency of Time Correlation}) &= \frac{1}{\tau} \int_{0.5\mu\text{sec}}^{1000\mu\text{sec}} e^{-t/\tau} dt \\ &= 98.89 \pm 0.05\%. \end{aligned}$$

Moreover, the events generated with the MC have the mean capture time $\sim 212.5 \mu\text{sec}$, which agrees with the capture time with the spallation neutrons. The uncertainty associated with the time correlation cut is dominated by the upper time cut $< 1000 \mu\text{sec}$.

5.5.3 Delayed Energy

The selection efficiency of the delayed energy cut is $1.8 < E_{\text{delayed}} < 2.6$ MeV (visible energy) is calculated using the energy resolution σ at the neutron capture peak.

$$(\text{Efficiency of delayed energy cut}) = \frac{1}{\sqrt{2\pi}\sigma} \int_{1.8\text{MeV}}^{2.6\text{MeV}} e^{-(E-2.21)^2/2\sigma^2} dE$$

The energy resolutions are different between the period I, II data and the period III data due to the 20 inch PMT commissioning (Table 5.4). Therefore, the efficiencies for the both periods are calculated to be

$$\begin{aligned} \text{period I, II (17 inch PMTs)} &\rightarrow 99.98\% \\ \text{period III (17 inch + 20 inch PMTs)} &\rightarrow 99.99\%, \end{aligned}$$

and the effect of the resolution uncertainties is negligible.

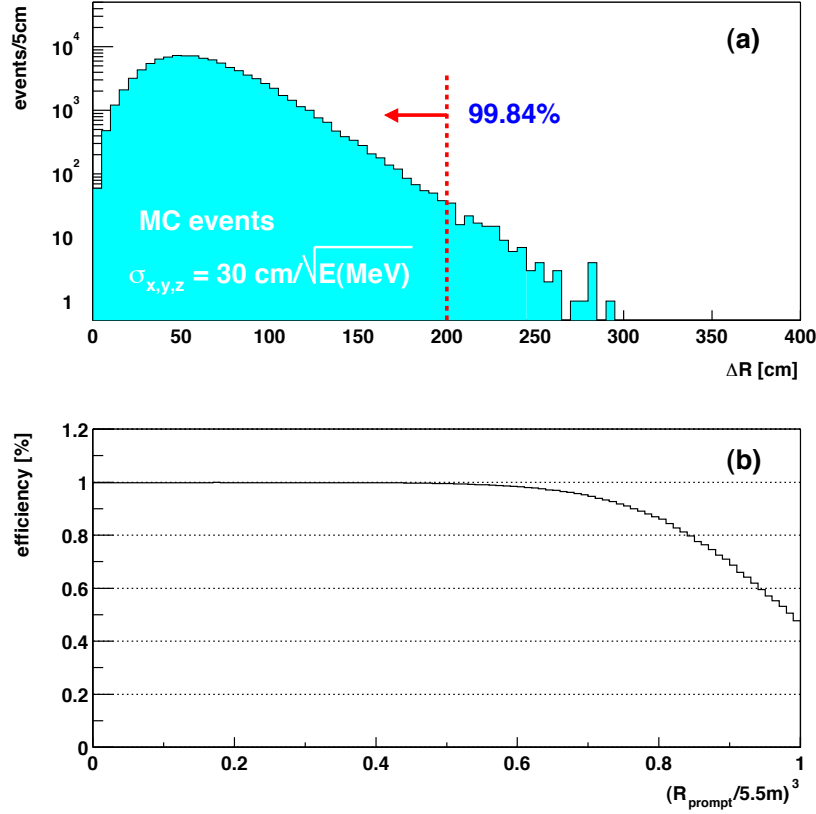


Figure 5.10: (a) Space correlation between prompt and delayed events generated by the MC. The assumed resolution is $\sigma_{x,y,z} = 30 \text{ cm}/\sqrt{E(\text{MeV})}$ estimated from the source calibration for various energies. (b) Efficiency for the delayed vertex is within 2 m from the prompt vertex and within 5.5 m fiducial volume as a function of the prompt vertex.

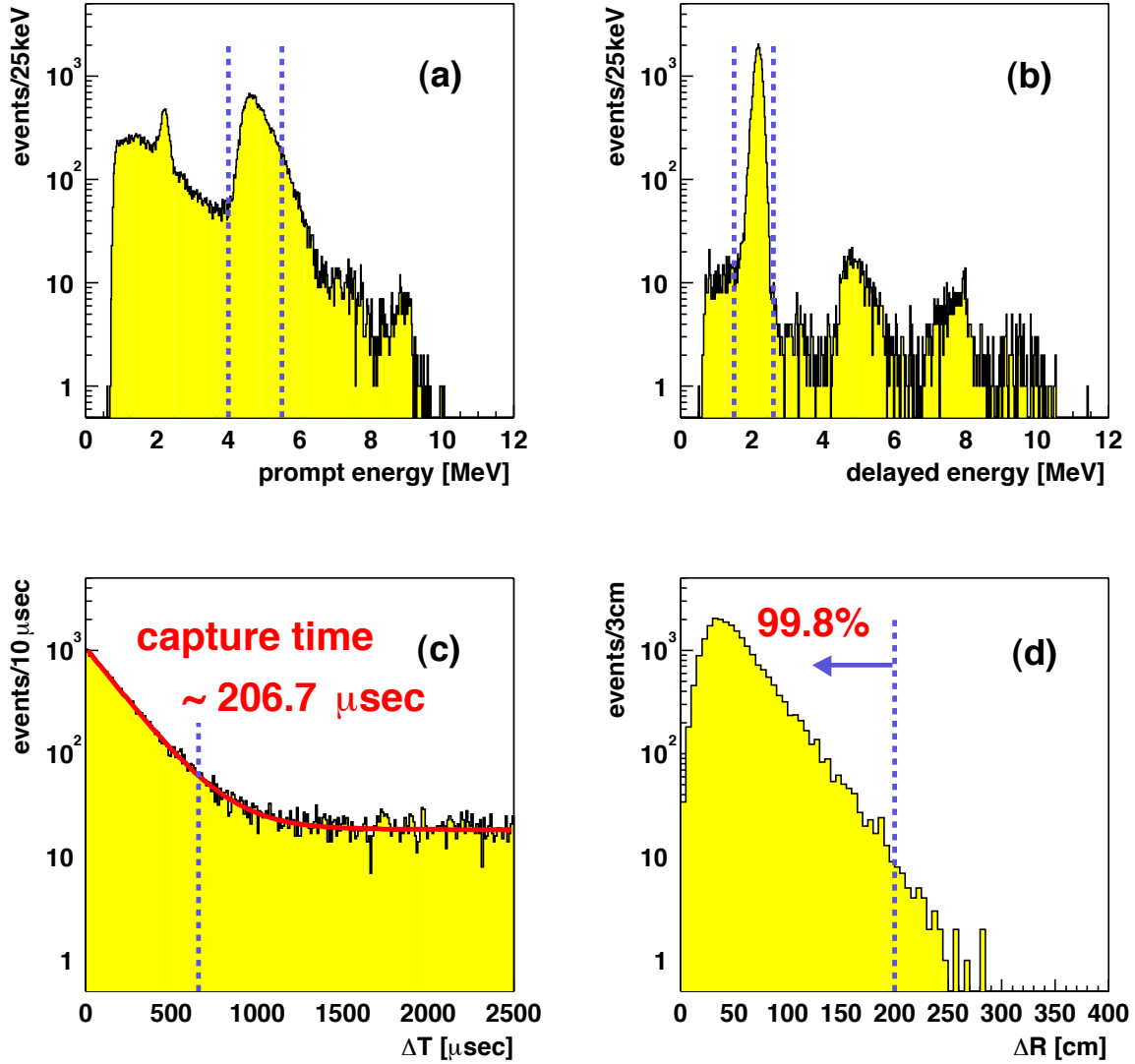


Figure 5.11: Delayed coincidence calibration using the Am-Be source at the center of the detector. The selection cuts for undisplayed parameters are applied. (a) Prompt energy spectrum in gamma-ray energy scale. The peak at ~ 4.4 MeV indicates the γ -ray emission from the first excited state of ^{12}C , and its peak position depends on the light emission from the recoil protons by neutrons or the shadow of the moderator. (b) Delayed energy spectrum in visible energy scale. The accidental coincidence events of 4.4 MeV γ overlap with the γ emission from the thermal neutron capture on ^{12}C . Another neutron capture γ is observed in ~ 8 MeV due to the stainless in the container of source. (c) Time correlation with the exponential fit (capture time $\sim 206.7 \mu\text{sec}$). (d) Space correlation. The efficiency for the 2 m cut is 99.8%.

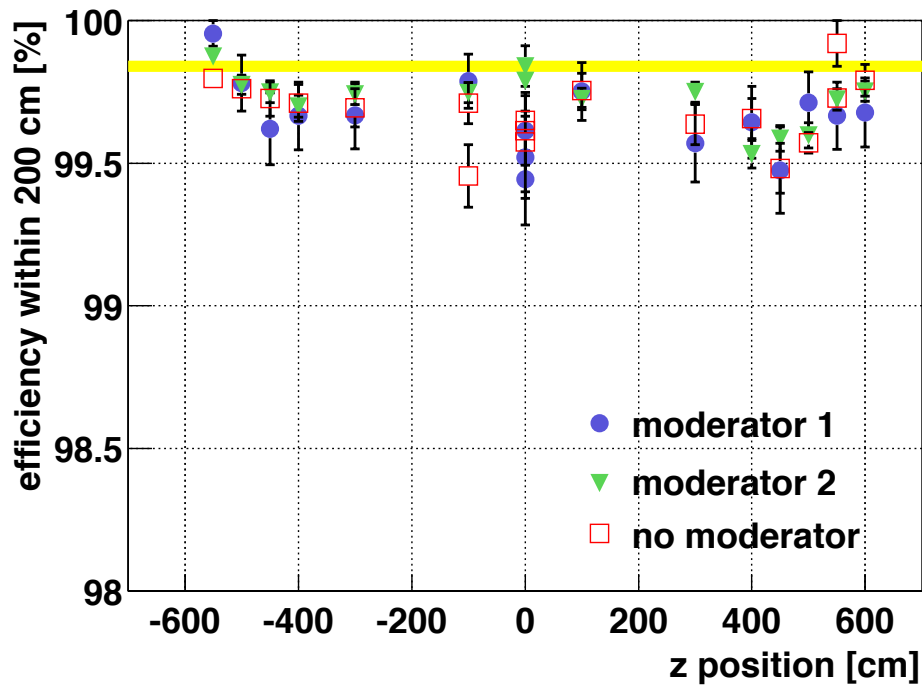


Figure 5.12: Efficiencies of the neutron capture event within 200 cm in the Am-Be source calibration at various z position. There are no significant difference between three sources (Appendix D) with the efficiency. The thick line indicates the prediction of the MC (99.84%). The data of the Am-Be calibration agrees with the prediction of the MC within 0.5%.

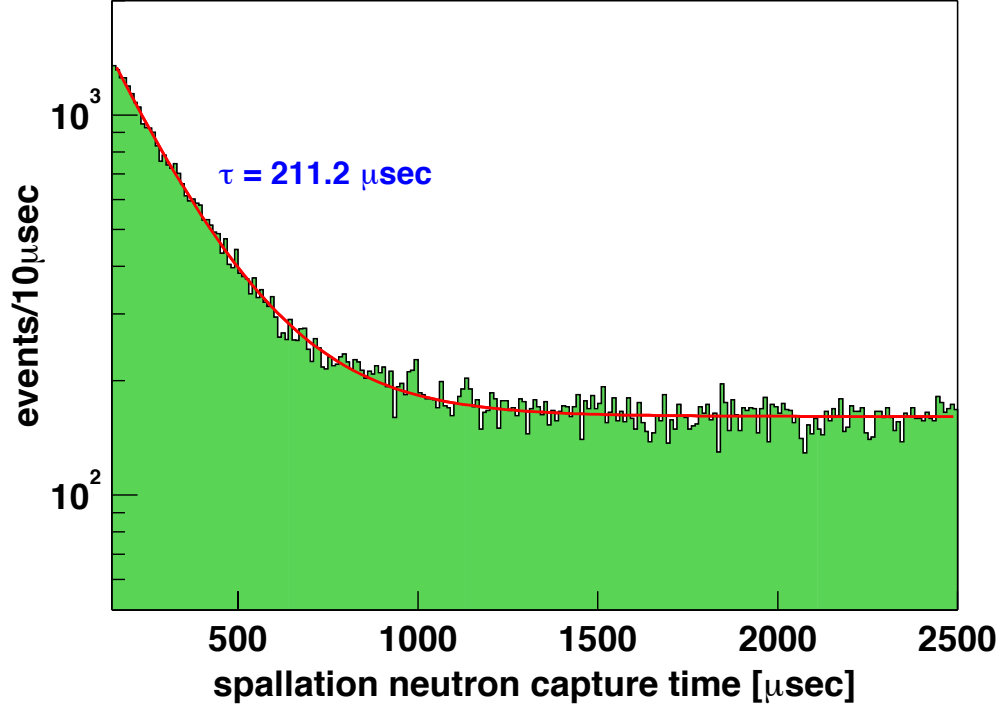


Figure 5.13: Time difference from muons to spallation neutron capture candidates. The neutron candidates are selected by the simple cut, $350 < \text{NsumMax} < 550$ and $\Delta Q < 0$ p.e. in order to avoid the unknown effect of the multiple neutron events (Section 4.2.1). Some events are overlapping to cancel out the time structure of the muon rate. The mean capture time is fitted to be $211.2 \pm 2.6 \mu\text{sec}$.

5.6 Expected Reactor Anti-Neutrino Events

5.6.1 No Oscillation Case

When neutrinos propagate without the neutrino oscillations, the number of reactor $\bar{\nu}_e$ ($N_{expected}$) and its energy spectrum ($n(E_{\bar{\nu}_e})$) is calculated as follows,

$$N_{expected} = \int n(E_{\bar{\nu}_e}) dE_{\bar{\nu}_e} \quad (5.13)$$

$$n(E_{\bar{\nu}_e}) = \int N_p f(E_{\bar{\nu}_e}, t) \sigma(E_{\bar{\nu}_e}) \cdot \epsilon_d dt \quad (5.14)$$

where

$$\begin{aligned} E_{\bar{\nu}_e} &: \text{electron anti-neutrino energy} \\ f(E_{\bar{\nu}_e}, t) &: \bar{\nu}_e \text{ flux} \\ \sigma(E_{\bar{\nu}_e}) &: \text{cross section of the reaction, } \bar{\nu}_e + p \rightarrow e^+ + n \\ \epsilon_d &: \text{detection efficiency.} \end{aligned}$$

and the $\bar{\nu}_e$ flux ($f(E_{\bar{\nu}_e}, t)$) are computed with the total flux from all reactors and all fission nuclei (^{235}U , ^{238}U , ^{239}Pu , ^{241}Pu and long-life nuclei),

$$f(E_{\bar{\nu}_e}, t) = \sum_{i=1}^{N_{reactor}} \sum_{j=1}^{N_{fission}} \frac{r_i^j(t)}{4\pi L_i^2} \cdot F^j(E_{\bar{\nu}_e}) \quad (5.15)$$

where

$$\begin{aligned} N_{reactor} &: \text{number of reactors} \\ N_{fission} &: \text{number of fission nuclei} \\ L_i &: \text{distance from reactor } i \\ r_i^j(t) &: \text{fission rate at a given } t, \text{ from fission nuclei } j, \text{ in reactor } i \\ F^j(E_{\bar{\nu}_e}) &: \bar{\nu}_e \text{ energy spectrum from fission nuclei } j. \end{aligned} \quad (5.16)$$

Considering that the positron angular distribution is essentially isotropic ($\langle \cos \theta \rangle \sim -0.04$), it is sufficiently accurate to use the point $\cos \theta = 0$ [65],

$$\bar{E}_{\bar{\nu}_e} \simeq E_e + \Delta + \frac{1}{M} [E_e(E_e + \Delta) + y^2] \quad (5.17)$$

where $\Delta = M_n - M_p$ and $y^2 = (\Delta^2 - m_e^2)/2$. Therefore, Eq. (5.13), (5.14) are written as a function of E_e using the spectrum correction,

$$N_{expected} = \int n(E_e) dE_e \quad (5.18)$$

$$n(E_e) = \int N_p f(E_{\bar{\nu}_e}, t) \sigma(E_{\bar{\nu}_e}) \frac{dE_{\bar{\nu}_e}}{dE_e} \cdot \epsilon_d dt \quad (5.19)$$

$$\frac{dE_{\bar{\nu}_e}}{dE_e} = 1 + \frac{2E_e + \Delta}{M}. \quad (5.20)$$

Actually, the time integral is approximated by the sum of livetime for each run, supposing the fission rates is constant for that run. The resolution effect is included using convolution integral,

$$n'(E'_e) = \int n(E_e) \frac{1}{\sqrt{2\pi}\sigma} e^{-\frac{(E_e - E'_e)^2}{2\sigma^2}} dE_e \quad (5.21)$$

where σ is $7.3\% \times \sqrt{E(\text{MeV})}$ and $6.2\% \times \sqrt{E(\text{MeV})}$ for period I, II and period III, respectively. The expected number of events in the no oscillation case, is 365.2 events at 2.6 MeV energy threshold for the livetime 515.1 day. This number should be compared with the observed number of events in order to test the neutrino oscillation. The energy threshold effect is included in the systematic uncertainty for each period. From the energy scale error at 2.6 MeV (Section 3.6.5), the uncertainties for period I, II and III are evaluated to be 2.14% and 2.33%, respectively.

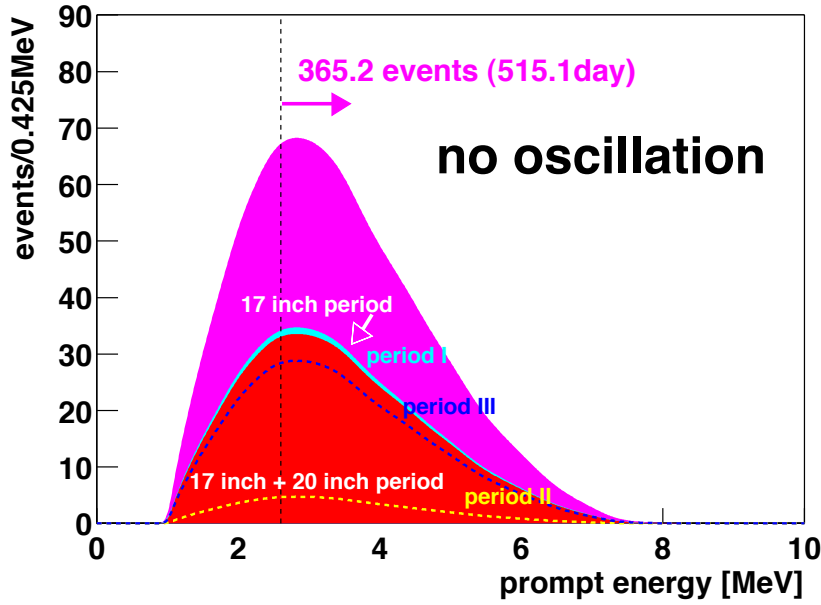


Figure 5.14: Expected spectrum in the no oscillation case. The expected number of events in the no oscillation case, is 365.2 at 2.6 MeV threshold. The expected numbers for period I, II and III are 185.4, 25.4 and 154.5, respectively.

5.6.2 Oscillation Case

In oscillation case, the expected flux is modified by including the neutrino survival probability $P(E_{\bar{\nu}_e}, L_i)$ which is a function of the oscillation parameters,

$$f(E_{\bar{\nu}_e}, t) = \sum_{i=1}^{N_{reactor}} \sum_{j=1}^{N_{fission}} \frac{r_i^j(t)}{4\pi L_i^2} \cdot F^j(E_{\bar{\nu}_e}) P(E_{\bar{\nu}_e}, L_i). \quad (5.22)$$

The expected number of events and energy spectrum depend on the survival probability $P(E_{\bar{\nu}_e}, L_i)$, and they should be compared with the observed data.

5.7 Final Sample

5.7.1 Selection Criteria for Electron Anti-Neutrinos

The $\bar{\nu}_e$ events are selected after the data reconstruction, described in Chapter 3. The delayed coincidence method is used for $\bar{\nu}_e$ detection, and its detection efficiency and systematic uncertainties are estimated in Section 5.5. In this thesis, the prompt energy threshold is decided as 2.6 MeV (HAT) to avoid background uncertainties such as geo-neutrinos and (α, n) . Based on the study of the background and efficiency, the selection cuts for $\bar{\nu}_e$ events are decided as follows,

1. Delayed Coincidence

(a) Time correlation, $0.5 \mu\text{sec} < \Delta T < 1000 \mu\text{sec}$

Neutron capture time is evaluated to be $211.2 \pm 2.6 \mu\text{sec}$ from the neutrons after muons. Therefore, 99.89% of neutron is captured within the time window $0.5 \mu\text{sec} < \Delta T < 1000 \mu\text{sec}$, and the systematic error is 0.05%.

(b) Space correlation, $\Delta R < 2 \text{ m}$

Diffusion of neutron and positron and γ -rays are estimated by the MC simulation, and 91.32% of neutron is captured within 2 m distance and 5.5 m fiducial radius. It gives 1.6% systematic uncertainty.

(c) Prompt energy window, $2.6 < E_{\text{prompt}} < 8.5 \text{ MeV}$

The energy scale error at the 2.6 MeV threshold gives 2.14% and 2.33% systematic errors for period I + II and period III, respectively.

(d) Delayed energy window, $1.8 \text{ MeV} < E_{\text{delayed}} < 2.6 \text{ MeV}$

The detection efficiency is evaluated to be 99.98% and 99.99% for period I + II and period III, respectively.

2. Fiducial Cut

(a) Fiducial radius, $R < 5.5 \text{ m}$

The effect from escape of the delayed vertex ($R_{\text{delayed}} > 5.5 \text{ m}$) near the fiducial volume edge is included in 1b.

3. Spallation Cut

Spallation products accompanying neutrons are eliminated using the following cuts. The overall spallation cut efficiency for ${}^8\text{He}/{}^9\text{Li}$ is 98.7%, and the livetime efficiency is 90.3%.

(a) **Low Charge Muon ($Q \leq 40,000$ p.e.)**

Whole volume of the detector is vetoed for 2 msec

(b) **Energetic Muon ($Q > 40,000$ p.e. and $\Delta Q \geq 10^6$ p.e.)**

Whole volume of the detector is vetoed for 2 sec

(c) **Miss Reconstructed Muon ($Q > 40,000$ p.e. and badness ≥ 100)**

Whole volume of the detector is vetoed for 2 sec

(d) **Well Reconstructed Non-Energetic Muon ($Q > 40,000$ p.e. and badness < 100 and $\Delta Q < 10^6$ p.e.)**

Whole volume of the detector is vetoed for 2 msec, and then cylindrical volume around muon track within 3 m is vetoed for 2 sec. The cylindrical veto is only applied to the delayed event.

4. Multiple neutron cut

(a) **Single Neutron, $N_{\text{delayed-neutron}} = 1$**

The multiple neutron events can be caused by the spontaneous fission of ${}^{238}\text{U}$ (SF branch : 5.45×10^{-5}) or NC reaction of atmospheric neutrinos. The upper limit of ${}^{238}\text{U}$ decay rate is estimated from the ${}^{234}\text{Pa}$ decay rate. The spontaneous fission of ${}^{238}\text{U}$ is calculated to be less than 1.8 events for the livetime 515.1 day. The contribution from atmospheric neutrinos is evaluated to be less than 0.5 events. The inefficiency from this cut is equivalent to the probability of the accidental coincidence for the events which has uniform distribution for time and space. It is estimated to be $< 0.01\%$ for 5.5 m fiducial volume.

5.7.2 Event Reduction

The $\bar{\nu}_e$ events are selected using the following reduction procedure,

1. Bad-run and Deadtime Reduction \sim reduction factor 0.95
runtime $597.7 \rightarrow 570.3$ day (1.43×10^9 events)
2. Noise and Flasher Cut \sim reduction factor 0.81
 $1.43 \times 10^9 \rightarrow 1.16 \times 10^9$ events
3. Muon Separation \sim reduction factor 0.98
 $1.16 \times 10^9 \rightarrow 1.14 \times 10^9$ events
4. Muon Veto \sim reduction factor 0.99
 $1.14 \times 10^9 \rightarrow 1.13 \times 10^9$ events
5. Delayed Coincidence Selection (HAT) \sim reduction factor 1.1×10^{-5}
 $1.13 \times 10^9 \rightarrow 12,766$ events

6. Fiducial Cut \sim reduction factor 0.046
12,766 \rightarrow 593 events
7. Spallation Cut \sim reduction factor 0.44
593 \rightarrow 261 events
8. Multiple Neutron Cut and Upper Prompt Energy Cut \sim reduction factor 0.99
261 \rightarrow 258 events

Background reduction by the delayed coincidence is illustrated in Figure 5.15. The ^{208}Tl γ is a source of accidental backgrounds, and it is efficiently suppressed by the fiducial cut. Figure 5.16 shows the prompt energy and delayed energy distribution, illustrating reduction of the delayed coincidence events by the fiducial cut, spallation cut, multiple neutron cut and upper prompt energy cut. The delayed coincidence selection is the most effective in the event reduction. After the spallation cut, the remaining candidates below 20 MeV are 261 events. After the multiple neutron and upper energy cut, the remaining candidates are 258 events.

The vertex distribution of the delayed coincidence events is shown in Figure 5.17. The final samples have almost uniform distribution. The profiles of $\bar{\nu}_e$ candidates are shown in Figure 5.18 and 5.19. Their correlation is clear in all parameters. The mean neutron capture energy is 2.218 ± 0.010 MeV by the Gaussian fit. Its deviation from the real capture energy is only 0.3%. It demonstrates the stability of the overall energy scale.

Reconstruction qualities of $\bar{\nu}_e$ candidates are checked with the various parameters described in Section 3.8.3. Figure 5.17 shows the overall badness of $\bar{\nu}_e$ candidates. There is no event which has very bad reconstruction quality for both prompt event and delayed event. The worst event of all candidates (Delayed Badness = 1.94^3) is not so strange as shown in Figure 5.21. Moreover, correlation coefficients of $\bar{\nu}_e$ candidates between prompt event and delayed event for hit channel, time and charge distribution are tested as shown in Figure 5.22. The coefficients of neutrino candidates obviously have different distributions from the electronics ringing events, so that the neutrino candidates are not fake events such as the electronics ringing events.

After September 2002, a large number of Japanese nuclear reactors were off, as shown in Figure 5.23 (a). The decrease of the expected $\bar{\nu}_e$ flux is more than a factor of two in the no oscillation case. A correlation between the observed rate and the expected rate is the useful information for the background estimation as demonstrated in the other reactor $\bar{\nu}_e$ experiments. Figure 5.23 (b) shows the correlation in KamLAND, using the binning with approximately equal $\bar{\nu}_e$ flux. The slope indicates the reactor correlated signal and the intercept tells the reactor independent constant background rate. The fitted background rate is consistent with the expected background 17.8 ± 7.3 events given in Chapter 4, within the fitting error. Moreover, its intercept constrain other sources of $\bar{\nu}_e$ such as a geo-reactor at the Earth's core [94]. The typical 3 TW geo-reactor scenario is comparable to the expected background 17.8 ± 7.3 events. However, its contribution gives the minimal impact on the reactor $\bar{\nu}_e$ analysis. Thus, in this thesis, only the contribution from known $\bar{\nu}_e$ sources is considered.

³It can be caused by the electronics noise at ~ 25 nsec after the last event. For such a event, the delayed energy becomes a little larger, but the inefficiency due to its energy shift is negligibly small.

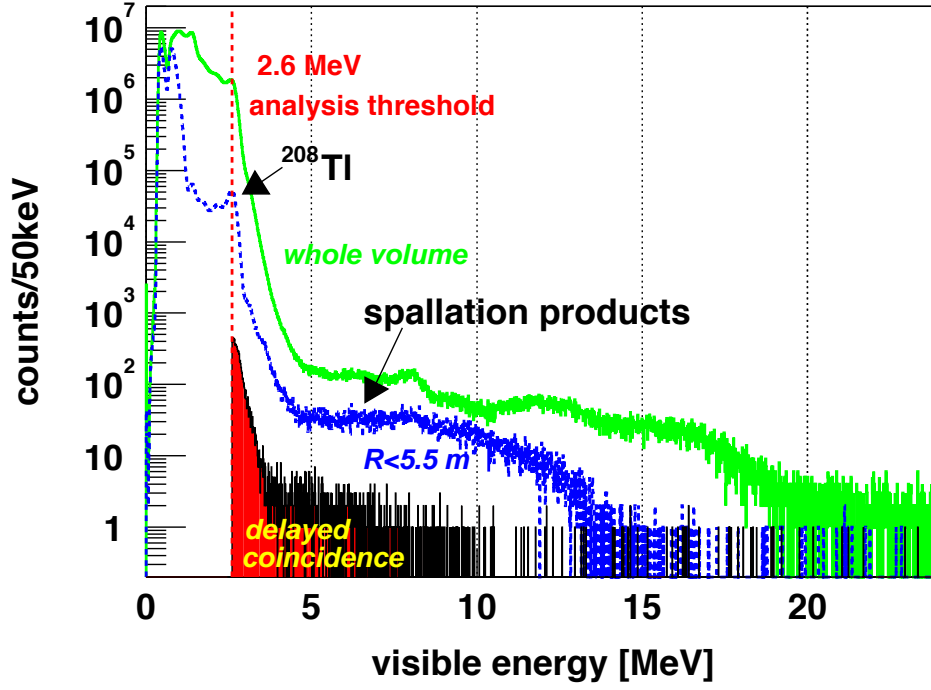


Figure 5.15: Visible energy spectrum for the single events and the delayed coincidence in the whole volume. The dashed line means the single events within 5.5 m fiducial radius, and it has the peak coming from ^{208}Tl γ , which is the source of accidental backgrounds. The red shaded histogram means the delayed coincidence events in the whole volume. The event reduction factor for the delayed coincidence selection is 1.1×10^{-5} .

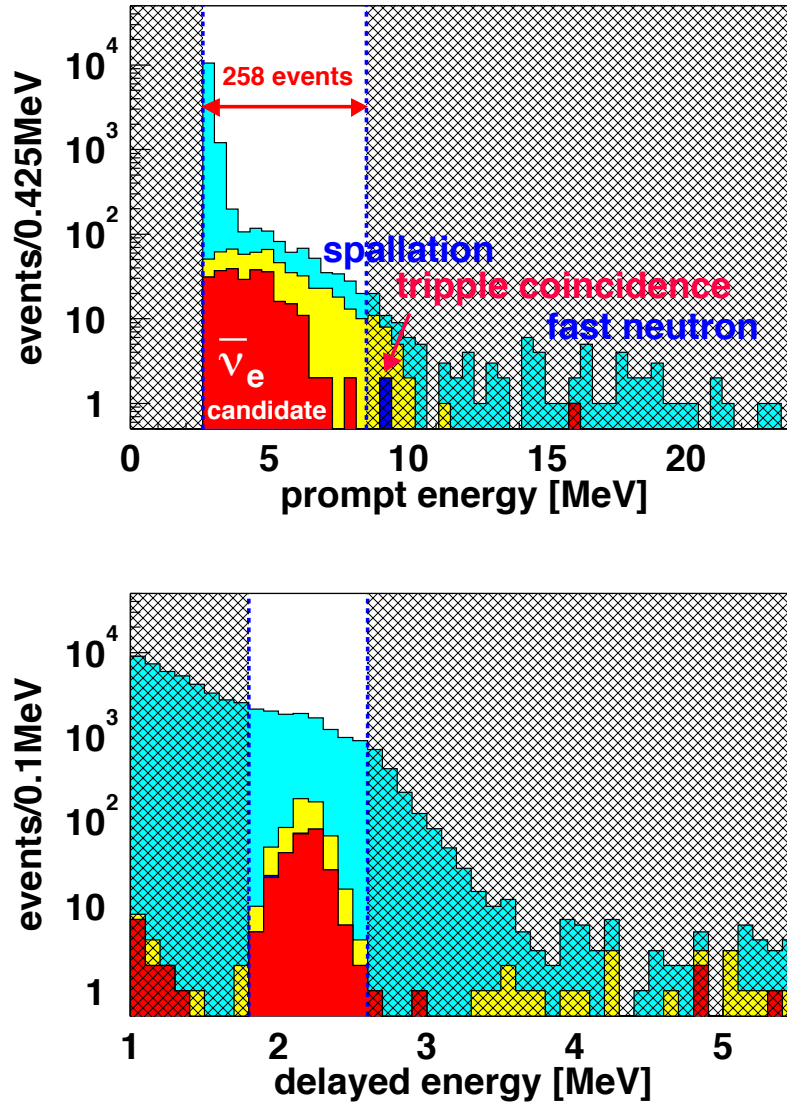


Figure 5.16: Prompt energy and delayed energy distribution, illustrating the reduction of the delayed coincidence events by the fiducial cut, spallation cut, multiple neutron cut and upper prompt energy cut. There are no multiple neutron events in the prompt energy window. The final sample is 258 events for the livetime 515.1 day.

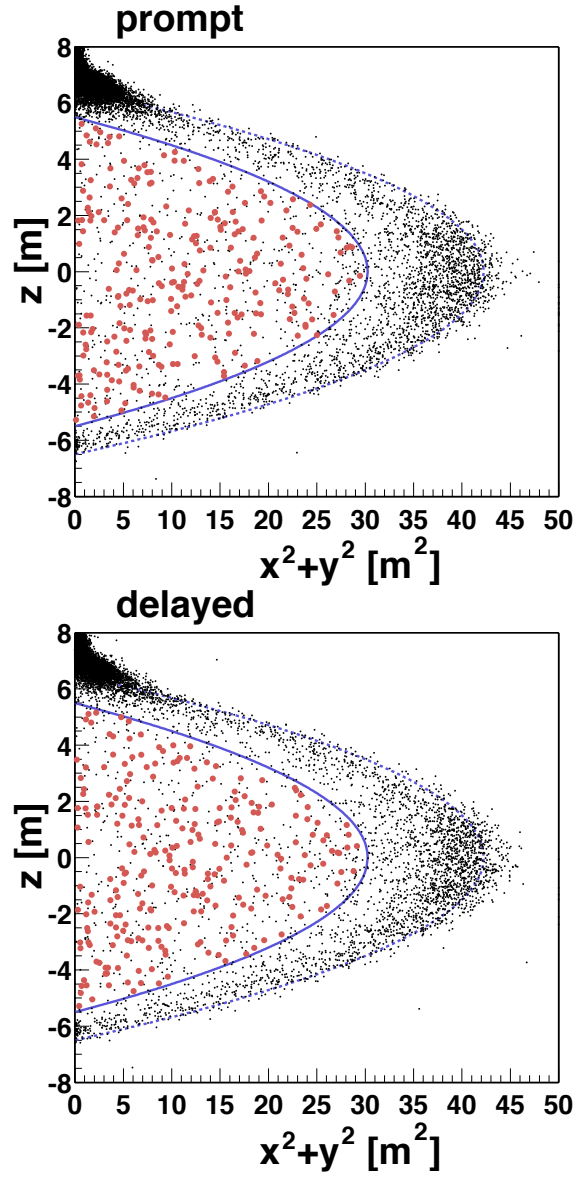


Figure 5.17: Vertex distribution of the delayed coincidence events. The regions with event rates higher than other regions are seen at around $z \sim \pm 6.5$ m and around balloon surfaces. The red markers mean after the fiducial cut, spallation cut, multiple neutron cut and upper prompt energy cut. The final samples distribute almost uniformly.

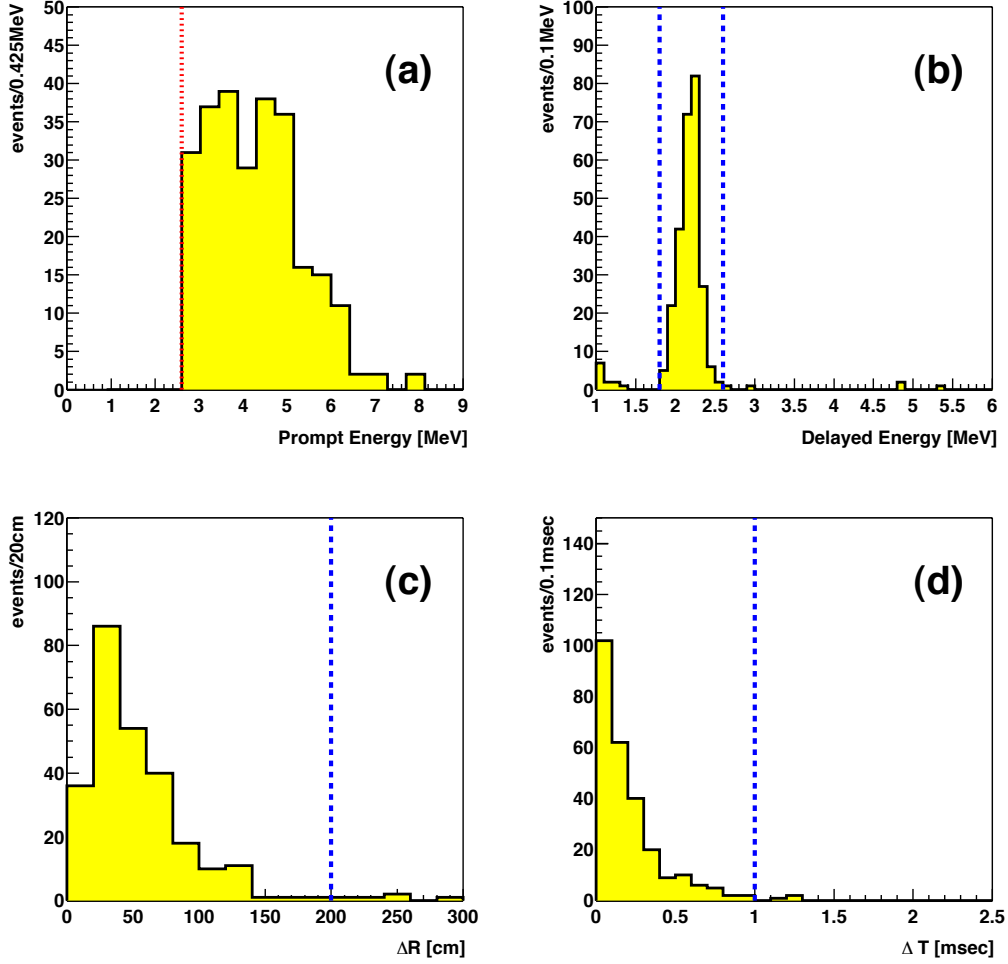


Figure 5.18: Profiles of $\bar{\nu}_e$ candidates. The selection cuts for undisplayed parameters are applied.

- (a) Prompt Energy (HAT)
- (b) Delayed Energy (HAT)
- (c) Space Correlation (HAT)
- (d) Time Difference (HAT)

(c) and (d) shows the correlation of space and time. The accidental backgrounds are suppressed effectively by (b), (c) and (d).

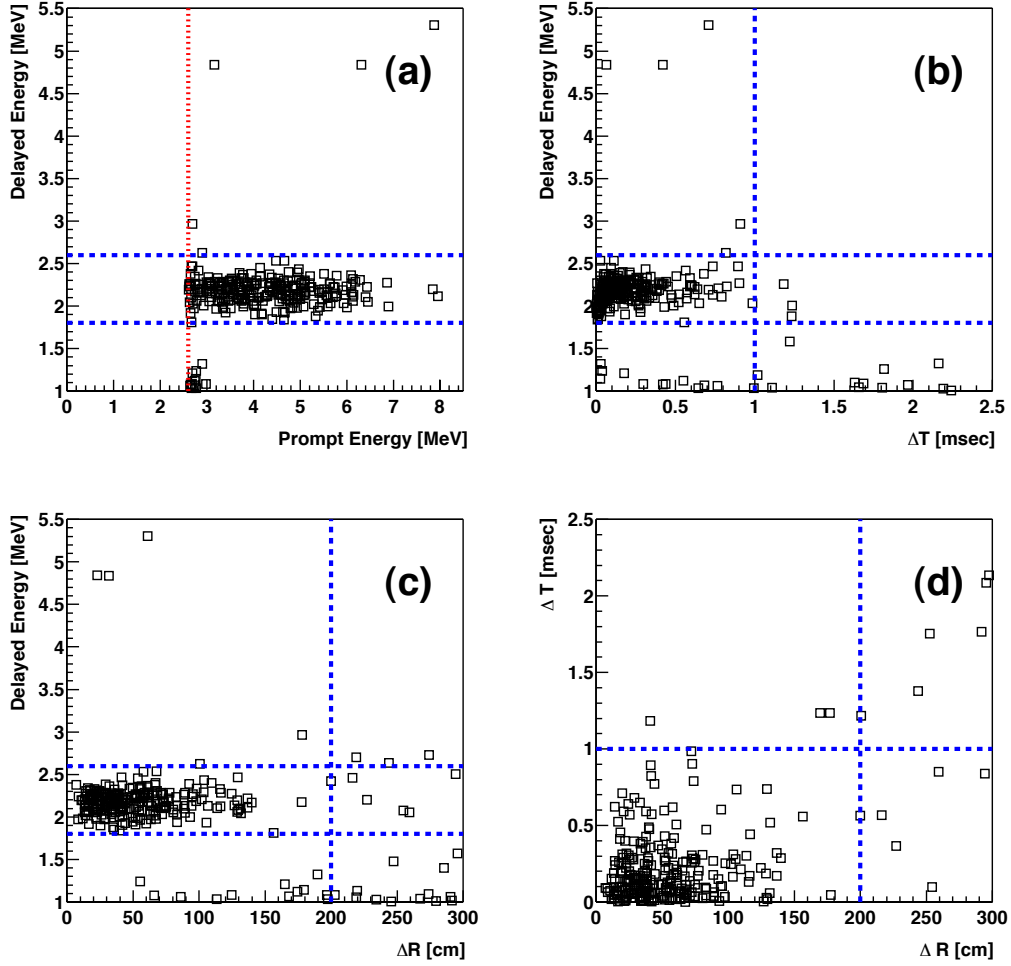


Figure 5.19: Profiles of $\bar{\nu}_e$ candidates. The selection cuts for undisplayed parameters are applied.

- (a) Prompt Energy vs Delayed Energy (HAT)
- (b) Time Difference vs Delayed Energy (HAT)
- (c) Space Correlation vs Delayed Energy (HAT)
- (d) Space Correlation vs Time Difference (HAT)

Events around 5 MeV in the delayed energy are the carbon capture candidates. The accidental events are concentrated at $E_{prompt} \sim 2.6$ MeV.

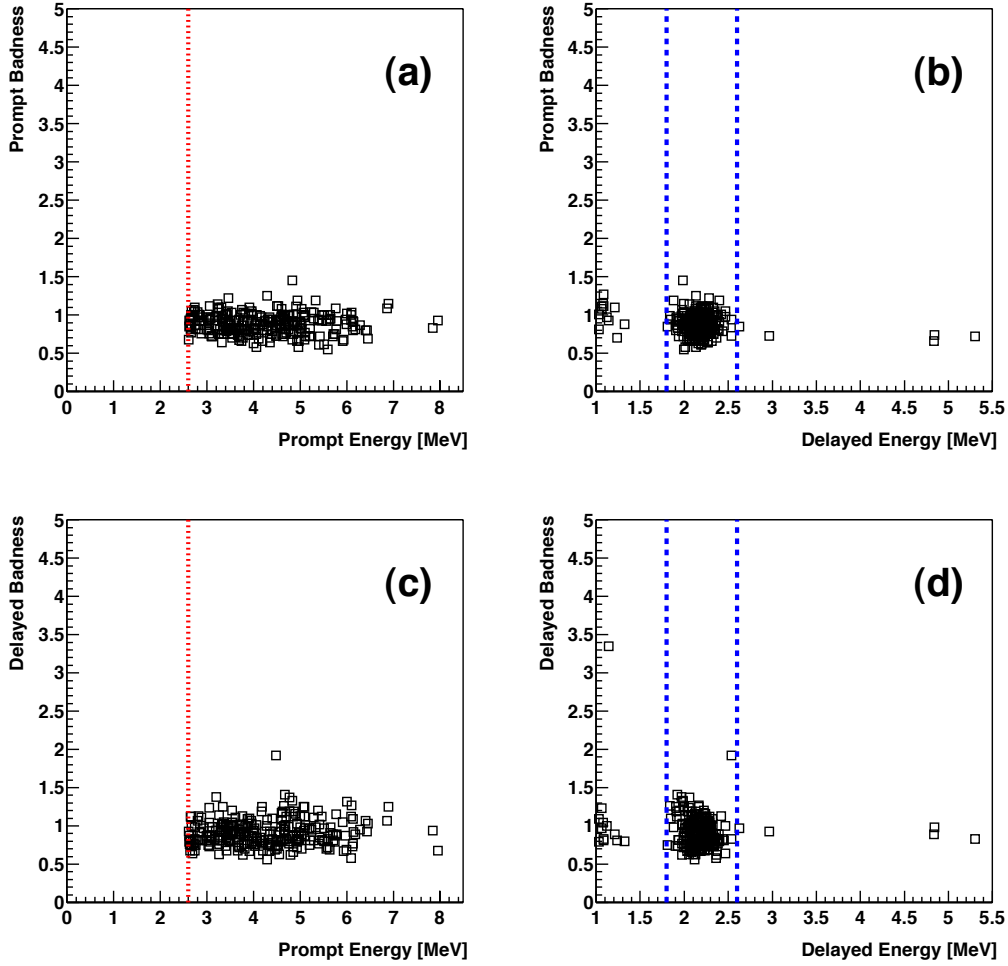


Figure 5.20: Badness of $\bar{\nu}_e$ candidates. The selection cuts for undisplayed parameters are applied.

- (a) Prompt Energy vs Prompt Badness (HAT)
- (b) Delayed Energy vs Prompt Badness (HAT)
- (c) Prompt Energy vs Delayed Badness (HAT)
- (d) Delayed Energy vs Delayed Badness (HAT)

There is no event which has very bad reconstruction quality for both prompt event and delayed event.

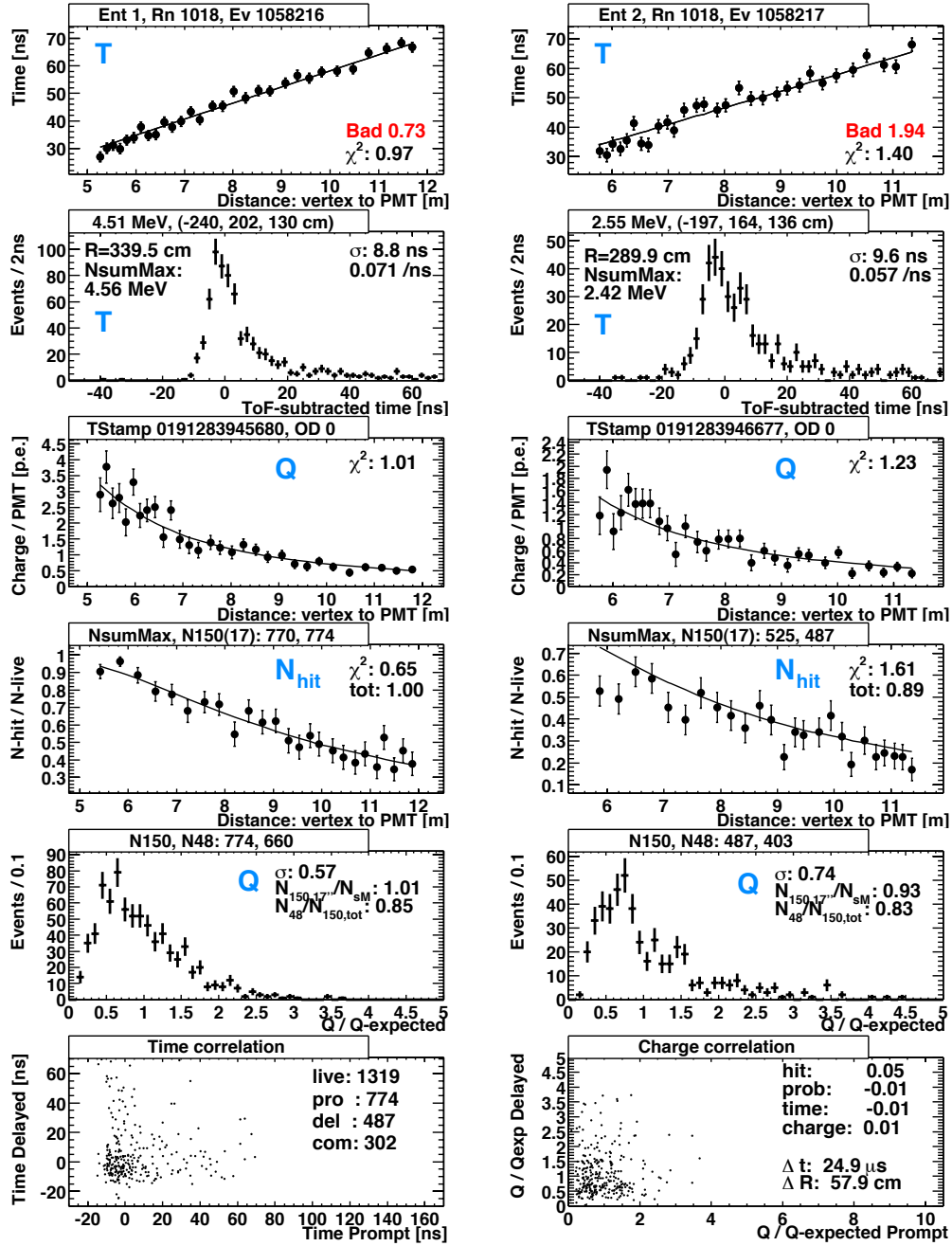


Figure 5.21: Reconstruction quality of the worst event of all candidates (Delayed Badness = 1.94). However, the various correlation data agree with their expectations within the errors.

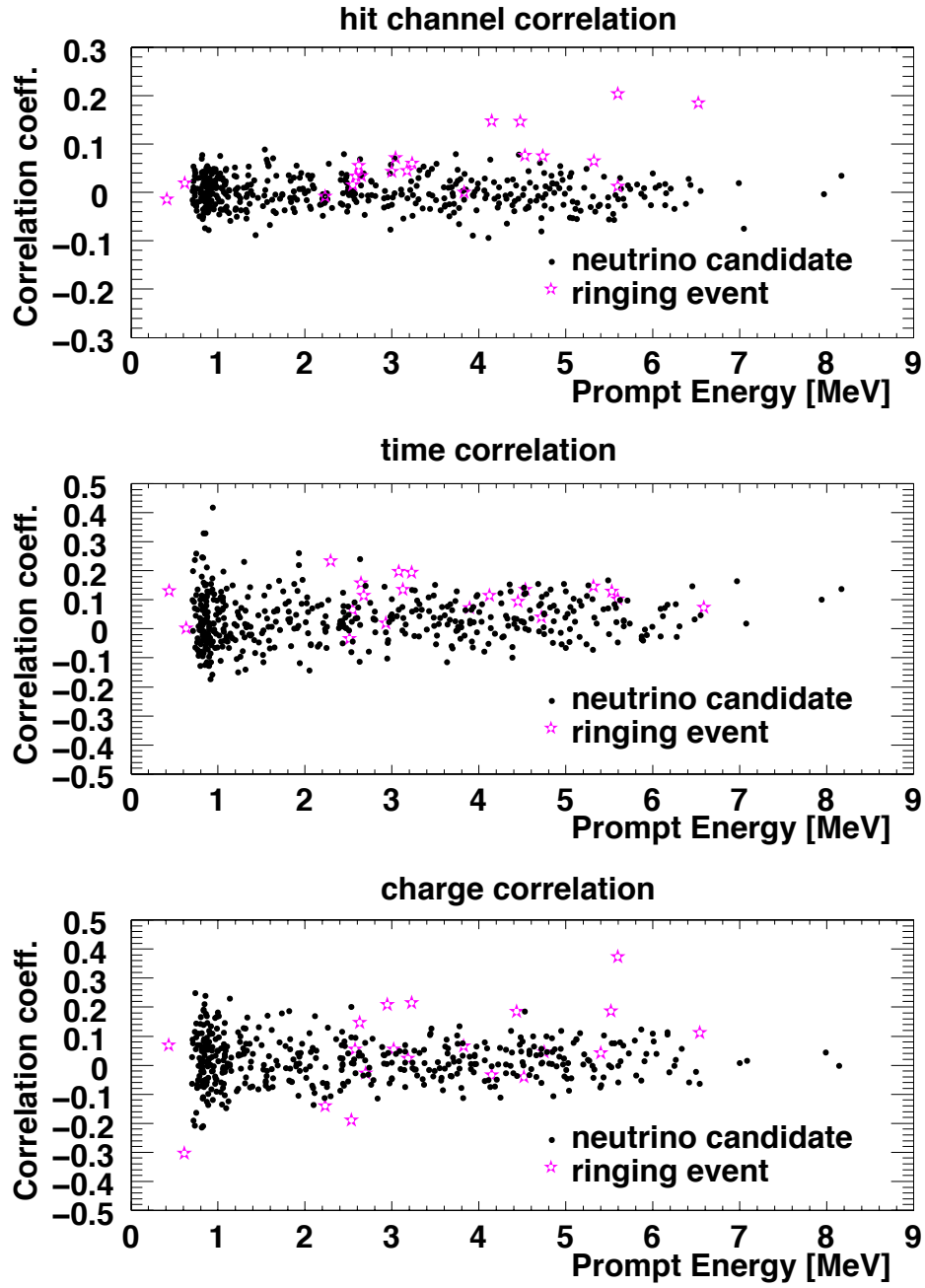


Figure 5.22: Correlation coefficients of $\bar{\nu}_e$ candidates between prompt event and delayed event for hit channel, time and charge distribution. The black and pink dots indicate the neutrino candidate and ringing event, respectively. The coefficients of neutrino candidates have different distributions from the electronics ringing events. That means the neutrino candidates selected by the delayed coincidence are not fake events such as the electronics ringing events.

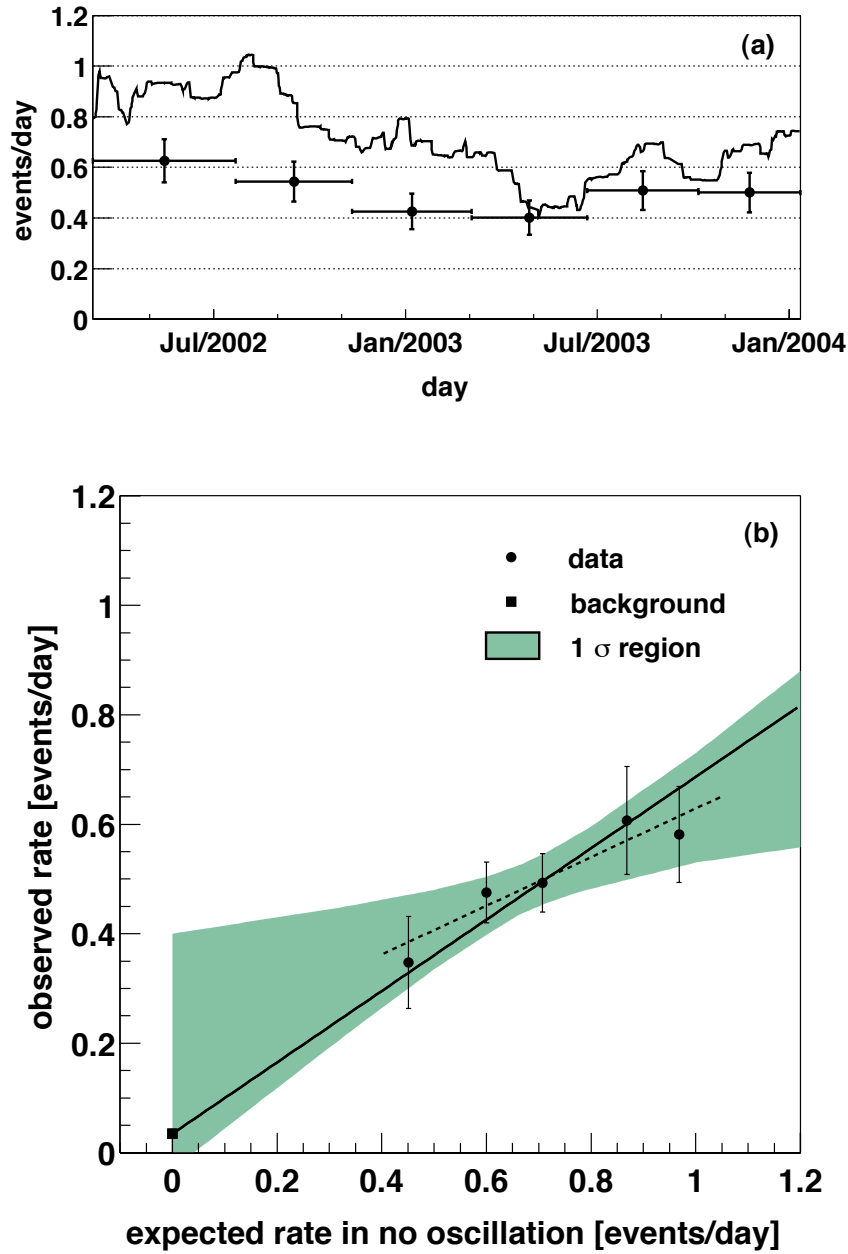


Figure 5.23: (a) Expected time variation of the reactor $\bar{\nu}_e$ flux in the no oscillation case. There is a correlation between the observed rate and the expected rate. (b) Observed $\bar{\nu}_e$ rate versus expected rate in the no oscillation. Data points corresponds to intervals of approximately equal $\bar{\nu}_e$ flux. The dashed line indicates the best-fit, the 1 σ C.L. region is in the shaded region. The solid line is a fit constrained to the expected background.

Chapter 6

Significance of Neutrino Oscillation

6.1 Hypothesis Test

6.1.1 Significance of Neutrino Disappearance

The significance of the disappearance, actually the probability of no disappearance is calculated as follows,

$$Prob(no\ disappearance) = \frac{1}{\sqrt{2\pi}\sigma^2} \int_0^\infty e^{-\frac{(N_{exp}p-x)^2}{2\sigma^2}} \sum_{n=0}^{N_{obs}} P(n, x) dx \quad (6.1)$$

$$P(n, x) = \frac{x^n}{n!} e^{-x} \quad (6.2)$$

where N_{exp} is the mean value of the total expected events $365.2 + 17.8 = 383.0$, σ is the total systematic error $\sqrt{(365.2 \times 0.065)^2 + 7.3^2} = 24.8$ and N_{obs} is the total observed events 258 at the 2.6 MeV analysis threshold. The probability to observe less than or equal to N_{obs} is calculated assuming Gaussian distribution of x around N_{exp} with a standard deviation of σ and a Poissonian for statistical distribution around x . The probability of no disappearance is 0.002%. Thus, the deficit of events is inconsistent with the expected rate for no oscillation $\bar{\nu}_e$ propagation at the 99.998% confidence level, providing strong evidence for $\bar{\nu}_e$ disappearance.

The average survival probability of the reactor $\bar{\nu}_e$ is 0.658 ± 0.044 (stat) ± 0.047 (syst), calculated from the ratio of observed events after the background subtraction versus expected reactor $\bar{\nu}_e$ events ($\frac{N_{obs} - N_{BG}}{N_{expected}}$). As the result indicates the disappearance of $\bar{\nu}_e$, the rate analysis for the oscillation parameter is performed in the context of two-flavor neutrino oscillation. The definition of χ^2 is as follows,

$$\chi^2 = \frac{(R_{observed} - R_{theoretical})^2}{\sigma_{stat}^2 + \sigma_{syst}^2} \quad (6.3)$$

$$= \left(\frac{N_{observed} - N_{BG}}{N_{expected}} - \frac{n_{reactor}}{N_{expected}} \right)^2 / (\sigma_{stat}^2 + \sigma_{syst}^2) \quad (6.4)$$

where

$$N_{expected} : \text{expected number of reactor } \bar{\nu}_e \text{ events for the no oscillation case} \quad (6.5)$$

$$N_{NB} : \text{expected number of background events} \quad (6.6)$$

$$n_{reactor} : \text{expected number of reactor } \bar{\nu}_e \text{ events for each } \Delta m^2 \text{ and } \theta \quad (6.7)$$

$$\sigma_{stat}, \sigma_{syst} : \text{sigma of the ratio } R_{observed}. \quad (6.8)$$

Figure 6.1 shows the excluded region for neutrino oscillation parameters from the KamLAND rate analysis at 2.6 MeV analysis threshold. The solar neutrino solutions, SMA, LOW and VAC are completely excluded at more than 99.9% C.L. and only the LMA solution remains.

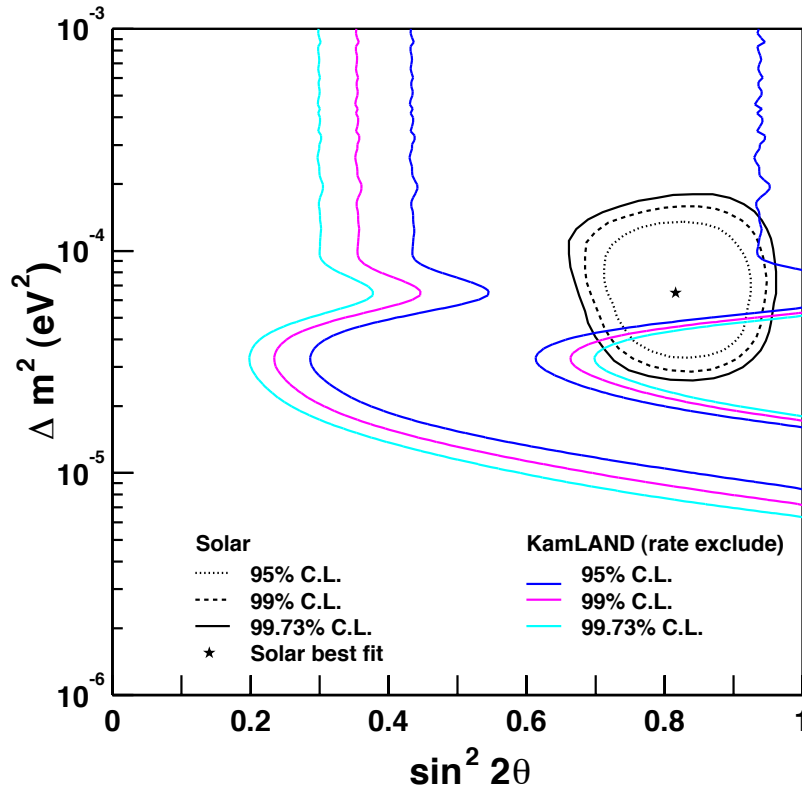


Figure 6.1: Excluded region for neutrino oscillation parameters, using the KamLAND rate analysis above 2.6 MeV analysis threshold. Excluded regions are outside of the solid line, and the blue and pink and sky blue lines indicate 95%, 99%, 99.73% C.L. The black lines indicate the allowed region from solar neutrino experiments.

6.1.2 Significance of Spectral Distortion

The observed energy spectrum is inconsistent with the expected no oscillation shape (Figure 6.4). The significance of the shape distortion is estimated from the comparison with a scaled no oscillation shape. To test how well the observed data agree with predicted probabilities, i.e. no oscillation hypothesis, a χ^2 test is used.

The expected spectrum has energy dependent uncertainties in the $\bar{\nu}_e$ spectrum, the energy scale, the energy resolution and the vertex bias. In the shape distortion analysis, those uncertainties are considered and the expected spectrum is redefined by taking account for these errors. The variation ranges are limited by adding a penalty χ^2 ($\chi^2_{distortion}$) for each error [95]. Various components which may distort the energy spectrum are introduced below,

- Uncertainty in the $\bar{\nu}_e$ spectrum

The uncertainty in the $\bar{\nu}_e$ spectrum is described in Section 5.1 and [90]. The spectrum uncertainty for each isotope is considered (Figure 5.3).

- Uncertainty of the energy scale

This uncertainty is the dominant contribution to the spectrum distortion. The energy scale correction is based on the analysis of Birk's constant and the Cherenkov intensity (Section 3.6.5) using the energy calibration data. This correction has uncertainties related to the two parameters, the Birk's constant and the Cherenkov intensity. The distortion curve from energy scale uncertainties is shown in Figure 6.2. The figure shows differences between the energy scale model at the best fit and a model at 1σ C.L. The distortion effect becomes larger at higher energies.

- Uncertainty of vertex bias

The vertex bias may produce an energy dependence of the fiducial volume. The limit of such dependence is estimated to be less than 2.7% from a comparison of the prompt and delayed event positions of $^8\text{He}/^9\text{Li}$ coincidence events (Section 3.5.3). This distortion effect is smaller than that of other distortion components.

- Uncertainty of energy resolution

The energy resolution is obtained in Section 3.6.5. The $\bar{\nu}_e$ spectrum is calculated using two sets of resolution, $7.3\%/\sqrt{E(\text{MeV})}$ (only 17 inch PMTs) and $6.2\%/\sqrt{E(\text{MeV})}$ (17 inch PMTs and 20 inch PMTs) for the two run periods. However, it has a small position dependence. In Figure 6.2, the contribution of the dependence is shown with a conservative 20% worse energy resolution.

The spectral distortion due to the systematic uncertainties in the background events is also considered. These uncertainties are given in Table 4.1. The distortion from the (α, n) background uncertainty is shown in Figure 6.2. As discussed in Section 4.3.4, the following errors are assigned: 32% scale error for low energy and ~ 4.4 MeV events, 100% scale error for high energy events (at ~ 6 MeV) and 10% quenching error. Most other backgrounds have small contributions to the spectral distortion and are ignored. In the $\bar{\nu}_e$ distortion analysis, the high energy events are addressed using a free parameter. This is a conservative treatment.

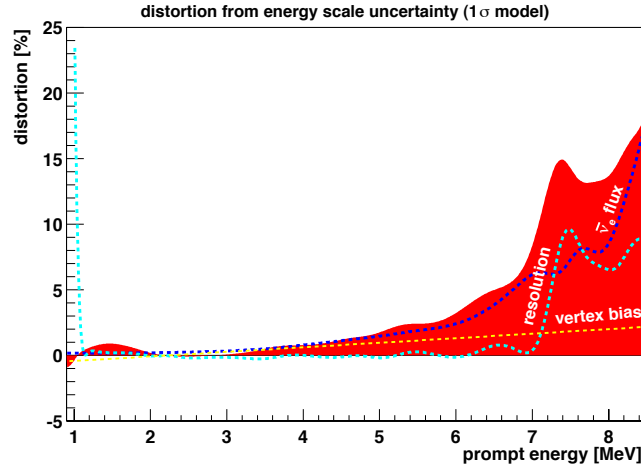


Figure 6.2: Distortion from the energy scale uncertainty in the case of no oscillation. The red shaded curve indicates the effect of varying one of the energy nonlinearity parameters in the model at 1σ . Other distortion components, such as $\bar{\nu}_e$ flux uncertainty, wider resolution (1.2 times of expected resolution conservatively) and a vertex bias (2.7%), are also shown with dashed lines. Each component is normalized at 2.2 MeV to show the contribution to the distortion. For technical reasons (economy with computing time), other distortion components are incorporated in the energy scale uncertainty in the $\bar{\nu}_e$ shape distortion analysis.

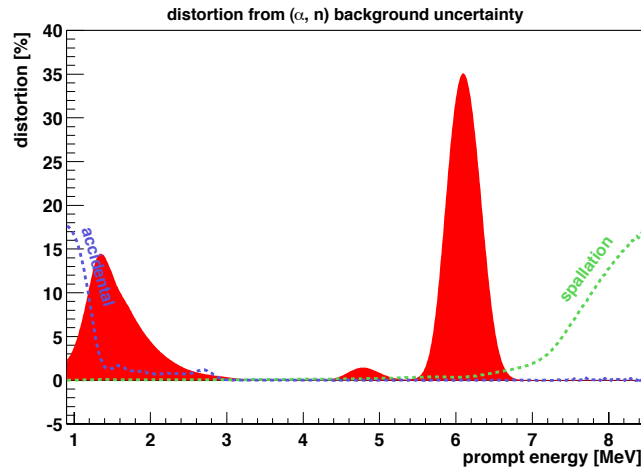


Figure 6.3: Distortion from the (α, n) background uncertainty in the case of no oscillation. The red shaded curve indicates the systematic uncertainty of the (α, n) background. Two other distortion components, the accidental and the spallation background, are also shown with dashed lines. The uncertainties of other distortion components are ignored because of their small contribution.

The definition of χ^2 is as follows,

$$\chi^2 = \chi_{Poisson}^2(S_{normalize}, \alpha_{1\sim 4}, \beta_{1\sim 3}) + \chi_{distortion}^2(\alpha_{1\sim 4}) + \chi_{BG}^2(\beta_{1\sim 3}) \quad (6.9)$$

$$\chi_{Poisson}^2 = 2 \sum_{i=1}^{N_{bin}} \left(n_i \log \frac{n_i}{\mu_i S_{normalize}} + \mu_i S_{normalize} - n_i \right) \quad (6.10)$$

where

n_i : number of observed events in i-th bin

μ_i : number of expected events in i-th bin

$S_{normalize}$: normalization parameter

$\alpha_{1\sim 4}$: distortion effect

($\bar{\nu}_e$ spectrum uncertainty, energy scale uncertainty, finite energy resolution, fiducial volume energy bias)

$\beta_{1\sim 3}$: background systematic components

(low energy (α , n) events, high energy (α , n) events, proton quenching effect)

$\alpha_{1\sim 4}$ and $\beta_{1\sim 3}$ are the parameters that are varied to minimize χ^2 as well as the free normalization parameter $S_{normalize}$. The number of parameters of $\alpha_{1\sim 4}$ and $\beta_{1\sim 2}$ are canceled out by the number of χ^2 to account for the spectrum and backgrounds uncertainty and do not contribute to the total number of degrees of freedom (n.d.f.). β_3 and $S_{normalize}$ are the only free parameters that decrease the n.d.f. The minimum χ^2 is 29.06 for 11 degrees of freedom in $2.6 < E < 8.125$ MeV (13 bins). The probability of no distortion is 0.22%¹. Thus, the observed spectrum shape is inconsistent with the no oscillation shape at 99.78% confidence level, which is the strong evidence for $\bar{\nu}_e$ spectral distortion.

6.2 Null Oscillation Probability

The neutrino oscillation was tested for both disappearance and distortion in the previous section. While the rate and shape contain independent information, their systematic uncertainties have a correlation. To account for the systematic effect, a combined χ^2 is used for the null oscillation hypothesis test. The definition of the χ^2 is as follows,

$$\chi^2 = \chi_{rate}^2 + \chi_{shape}^2 \quad (6.12)$$

$$\chi_{rate}^2 = \frac{(N_{observed} - n_{reactor} - N_{BG})^2}{\sigma_{stat}^2 + \sigma_{syst}^2} \quad (6.13)$$

$$\chi_{shape}^2 = \chi_{Poisson}^2(S_{normalize}, \alpha_{1\sim 4}, \beta_{1\sim 3}) + \chi_{distortion}^2(\alpha_{1\sim 4}) + \chi_{BG}^2(\beta_{1\sim 3}) \quad (6.14)$$

¹When the data are Gaussian distributed variables, χ^2 follows ‘ χ^2 distribution’. ‘ χ^2 distribution’ is defined by

$$f(z; n) = \frac{1}{2^{n/2} \Gamma(n/2)} z^{n/2-1} e^{-z/2}, n = 1, 2, \dots \quad (6.11)$$

where n is the n.d.f., and $\Gamma(x)$ is the gamma function. In this case, the data are Poisson distributed variables, and the corresponding χ^2 distribution is numerically calculated for a comparison. It gave the same significance level as ‘ χ^2 distribution’ for Gaussian distributed variables.

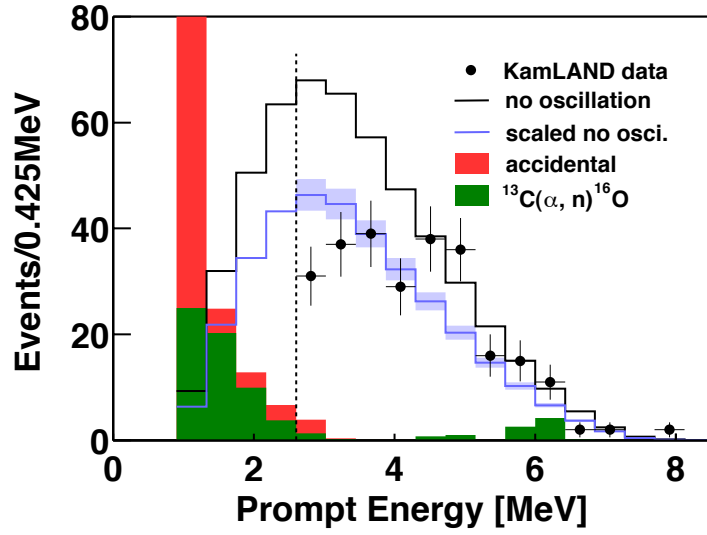


Figure 6.4: Scaled no oscillation spectrum compared with the observed data. The shaded band indicates the systematic error for a scaled no oscillation spectrum.

where $\chi_{Poisson}^2$ is the same as Eq. (6.10).

The χ_{rate}^2 is a penalty term, which cancels out the reduced n.d.f. by the normalization factor $S_{normalize}$. The probability of getting a worse χ^2 than the data is 0.0000052%. From the rate and shape analysis, the observed data is inconsistent with the no oscillation expected rate and shape at 99.999995% confidence level, which is very strong evidence for non-standard $\bar{\nu}_e$ propagation, such as neutrino oscillation.

6.3 Two Generation Neutrino Oscillation Analysis

The oscillation analysis in two generation frame work uses only one flavor-mixing-angle between the electron and a different flavor of anti-neutrinos ($\bar{\nu}_e, \bar{\nu}_x$). This assumption is a good approximation when $\theta_{13} \sim 0$.

The neutrino oscillation gives rise to not only disappearance of $\bar{\nu}_e$ but also to energy spectral distortion, since the survival probability is a function of several parameters, the mixing angle, mass-square difference, energy and travel distance of $\bar{\nu}_e$. These characteristics of neutrino oscillation allow detailed investigation of the oscillation parameter set. To do this, the unbinned maximum likelihood method [96] is used.

In this analysis, several free and variable parameters are used in the χ^2 and chosen to minimize the χ^2 for each oscillation parameter set. The χ^2 consists of a ‘rate evaluation part’ and a ‘shape distortion part’:

$$\begin{aligned}\chi^2(\theta, \Delta m^2) &= \chi_{rate}^2 + \chi_{shape}^2 \\ &= \chi_{rate}^2(\theta, \Delta m^2)\end{aligned}\tag{6.15}$$

$$-2 \ln L_{shape}(\theta, \Delta m^2, \alpha_{1\sim 4}, \beta_{1\sim 3}) + \chi_{distortion}^2(\alpha_{1\sim 4}) + \chi_{BG}^2(\beta_{1\sim 3})\tag{6.16}$$

L_{shape} is the likelihood function relevant for the spectrum distortion and it takes into account experimental distortions, $\alpha_{1\sim 4}, \beta_{1\sim 3}$ in Eq. (6.14).

Result from Shape Only Analysis

The shape only analysis is performed omitting χ_{rate}^2 in Eq. (6.16). The best fit parameters are obtained as

$$\begin{aligned}\sin^2 2\theta &= 0.98, \quad \Delta m^2 = 8.0 \times 10^{-5} \text{ eV}^2 \\ (\beta_1, \beta_2, \beta_3) &= (74, 5, 0)\end{aligned}$$

and the allowed region is shown in Figure 6.5. The LMA I region is favored, and the upper LMA region (LMA II) and the lower LMA region (LMA 0) are disfavored at 91.9% C.L. and 96.0% C.L. respectively. Moreover, no oscillation (zero mixing) is strongly disfavored at 99.988% C.L. by the spectral distortion alone.

Result from Rate + Shape Analysis

The best fit parameters from rate + shape analysis using the full expression in Eq. (6.15) are

$$\begin{aligned}\sin^2 2\theta &= 0.86, \quad \Delta m^2 = 7.9 \times 10^{-5} \text{ eV}^2 \\ (\beta_1, \beta_2, \beta_3) &= (74, 7, 0)\end{aligned}$$

and the allowed region is shown in Figure 6.6. The LMA I region is favored, and the upper LMA region (LMA II) and the lower LMA region (LMA 0) are more strongly disfavored at 98.0% C.L. and 97.5% C.L. respectively. Maximal mixing for LMA I region is allowed at the 62.1% C.L. The no oscillation $\chi^2(0, 0)$ is 45.49 larger than the best fit χ^2 , so the no oscillation hypothesis

is greatly disfavored at 99.99999987% C.L. The (α, n) background events for the 2nd-excited state in the 6 MeV region is found to be 7 events (β_2). The no oscillation spectrum, the best fit oscillation spectrum, accidental and (α, n) backgrounds are shown in Figure 6.7. Next, the goodness of fit is tested, using the same procedure in Section 6.2. The minimum χ^2 for the best fit oscillation parameter is 13.09 for 10 degrees of freedom in $2.6 < E < 8.125$ MeV (13 bins), so the goodness-of-fit is 21.9%. On the other hand, the χ^2 for LMA II is 21.01 for 10 degrees of freedom, so the goodness-of-fit is only 2.1%.

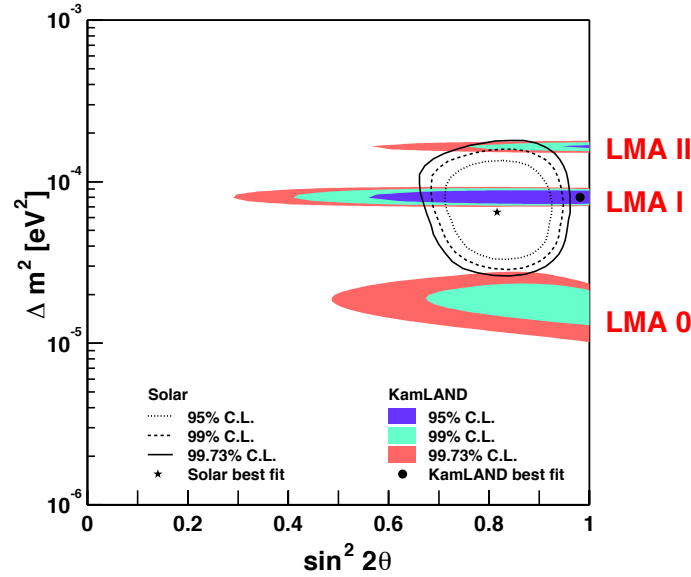


Figure 6.5: Allowed region from shape only analysis for the data set above 2.6 MeV. The best fit parameters are $\sin^2 2\theta = 0.98$ and $\Delta m^2 = 8.0 \times 10^{-5}$ eV². The no oscillation parameter is strongly disfavored at 99.988% C.L.

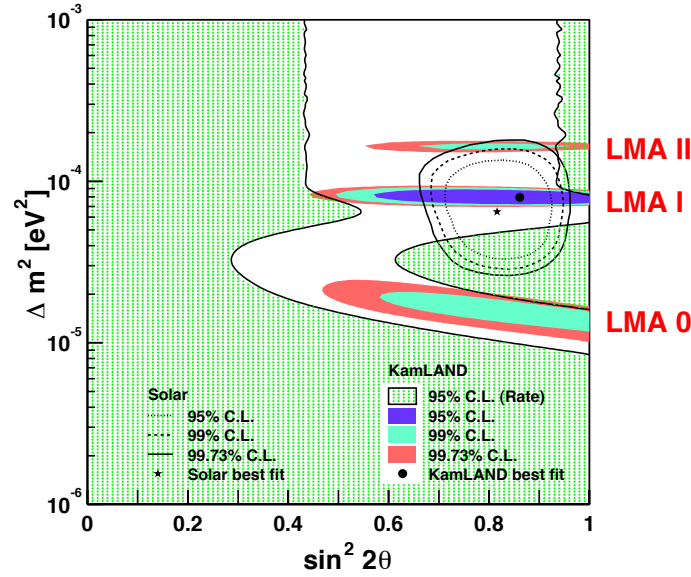


Figure 6.6: Allowed region from rate + shape analysis for the data set above 2.6 MeV. The best fit parameters are $\sin^2 2\theta = 0.86$ and $\Delta m^2 = 7.9 \times 10^{-5} \text{ eV}^2$. The excluded region from rate analysis is also shown.

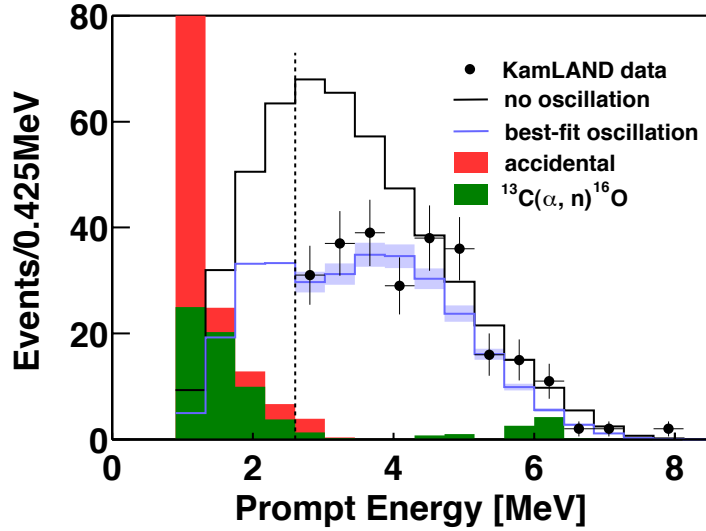


Figure 6.7: No oscillation spectrum and the best fit $(\sin^2 2\theta, \Delta m^2) = (0.86, 7.9 \times 10^{-5} \text{ eV}^2)$ of oscillation spectrum, and the accidental and (α, n) backgrounds. The shaded band indicates the systematic error in the best-fit spectrum. The best fit of (α, n) background events for the 2nd-excited state in the 6 MeV region is 7 events. The upper LMA region (LMA II) and the lower LMA region (LMA 0) are disfavored at 98.0% C.L. and 97.5% C.L. respectively.

6.4 Test for Non-Standard Models of Neutrino Disappearance

6.4.1 Neutrino Decay

Apart from neutrino oscillation, the observed zenith angle dependence of the atmospheric neutrinos can also be accounted for by neutrino decay [7]. Here a similar hypothesis is applied to the KamLAND results. In the context of the Standard Model, neutrinos are stable, because they are massless particles. Assuming neutrinos ($\bar{\nu}_e$, $\bar{\nu}_x$) are mixture of mass eigenstates ($\bar{\nu}_1$, $\bar{\nu}_2$) and only $\bar{\nu}_2$ is unstable, the survival probability of $\bar{\nu}_e$ is

$$P(\bar{\nu}_e \rightarrow \bar{\nu}_e) = \cos^4 \theta + \sin^4 \theta e^{-\alpha L/E} + 2 \sin^2 \theta \cos^2 \theta e^{-\alpha L/2E} \cos(\Delta m^2 L/2E) \quad (6.17)$$

where $\alpha = m_2/\tau_2$ and $\Delta m^2 = m_2^2 - m_1^2$. If $\tau_2 \rightarrow \infty$, Eq. (6.17) becomes Eq. (1.14). If $\Delta m^2 \rightarrow 0$, then the cosine term $\cos(\Delta m^2 L/2E)$ becomes unity, and the survival probability is

$$P(\bar{\nu}_e \rightarrow \bar{\nu}_e) = \left[\cos^2 \theta + \sin^2 \theta e^{-\alpha L/2E} \right]^2. \quad (6.18)$$

Thus, the ‘pure decay’ model has two parameters, the flavor mixing angle θ and the decay constant α related to the lifetime and mass of $\bar{\nu}_2$. A two parameter fit with the observed $\bar{\nu}_e$ spectrum and rate (rate + shape analysis) is performed with the pure decay model as well as the neutrino oscillation model. The best fit parameters are

$$\sin^2 \theta = 1.0, \quad m/\tau = 0.011 \text{ MeV/km}$$

and the allowed region is shown in Figure 6.8.

6.4.2 Neutrino Decoherence

The result of the atmospheric neutrino experiment can be explained by neutrino Decoherence as well as neutrino decay [8]. It is motivated by new physics (e.g., by quantum gravity). If one applies the same idea to explain the KamLAND data, the survival probability of $\bar{\nu}_e$ is expressed as

$$P(\bar{\nu}_e \rightarrow \bar{\nu}_e) = 1 - \frac{1}{2} \sin^2 2\theta \left[1 - e^{-\gamma L} \cos(\Delta m^2 L/2E) \right]^2 \quad (6.19)$$

which is parameterized by $\gamma = \gamma_0 (E/\text{GeV})^n$. Decoherence with $n = -1$ gives a good fit to the zenith angle dependence of ν_μ in Super-Kamiokande. Here the same $n = -1$ is assumed. If $\Delta m^2 \rightarrow 0$, then the cosine term $\cos(\Delta m^2 L/2E)$ becomes unity, and the survival probability is

$$P(\bar{\nu}_e \rightarrow \bar{\nu}_e) = 1 - \frac{1}{2} \sin^2 2\theta (1 - e^{-\gamma_0 L/E})^2 \quad (6.20)$$

Thus, the ‘pure decoherence’ model has two parameters, the flavor mixing angle θ and the decoherence constant γ_0 related to the interaction strength. The two parameter fit with the observed $\bar{\nu}_e$ spectrum and its rate (rate + shape analysis) are performed with the pure decoherence model. The best fit parameters are given by

$$\sin^2 2\theta = 1.0, \quad \gamma_0 = 0.030 \text{ MeV/km}$$

and the allowed region is shown in Figure 6.9.

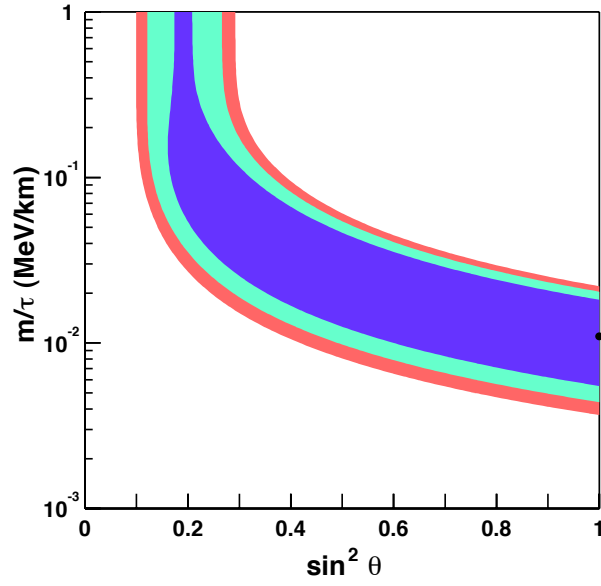


Figure 6.8: Allowed region at 95%, 99%, 99.73% C.L. in pure neutrino decay case as expressed in Eq. (6.18). The best fit parameters are $\sin^2 \theta = 1.0$ and $m/\tau = 0.011$ MeV/km.

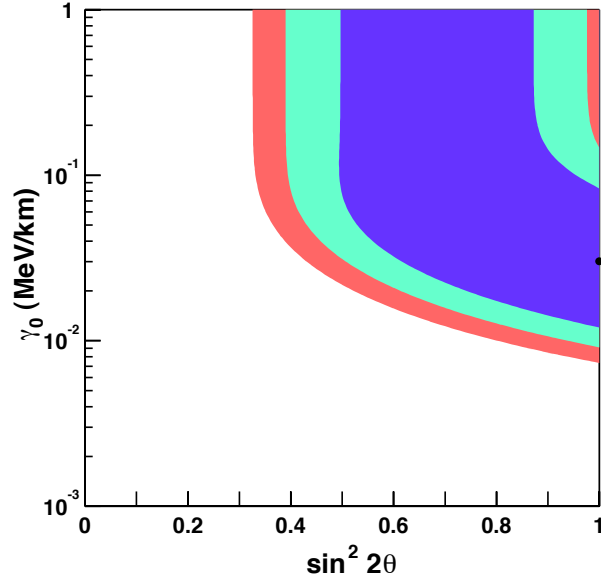


Figure 6.9: Allowed region at 95%, 99%, 99.73% C.L. in pure neutrino decoherence case as expressed in Eq. (6.20). The best fit parameters are $\sin^2 2\theta = 1.0$ and $\gamma_0 = 0.030$ MeV/km.

6.5 Discussion

To illustrate oscillatory behavior of the data, the L_0/E distribution is shown in Figure 6.10. The data and the best-fit spectra are divided by the expected no-oscillation spectrum. The two alternative hypotheses for neutrino disappearance, neutrino decay and decoherence discussed in the previous section, give different L_0/E dependences. These two hypotheses can be compared with the neutrino oscillation hypothesis using the difference of minimum χ^2 in the unbinned maximum likelihood analyses for each hypotheses. The minimum χ^2 of decay and decoherence are 10.7 (3.3 standard deviation) and 12.7 (3.6 standard deviation) larger than neutrino oscillation. That indicates, that the decay and decoherence are strongly disfavored and that oscillation is the most favored neutrino disappearance hypothesis.

The reactor neutrino measurement based on a 766 ton-year exposure of KamLAND to reactor $\bar{\nu}_e$ has observed spectral distortion of reactor $\bar{\nu}_e$ as well as disappearance of neutrinos for the first time. These two indicators of non-standard $\bar{\nu}_e$ propagation are well explained by neutrino oscillation. The next topic for neutrino experiments is to measure the oscillation parameters (e.g., mixing angle and mass difference) in the three generation frame work. The next chapter will discuss the three generation analysis using all the available neutrino data.

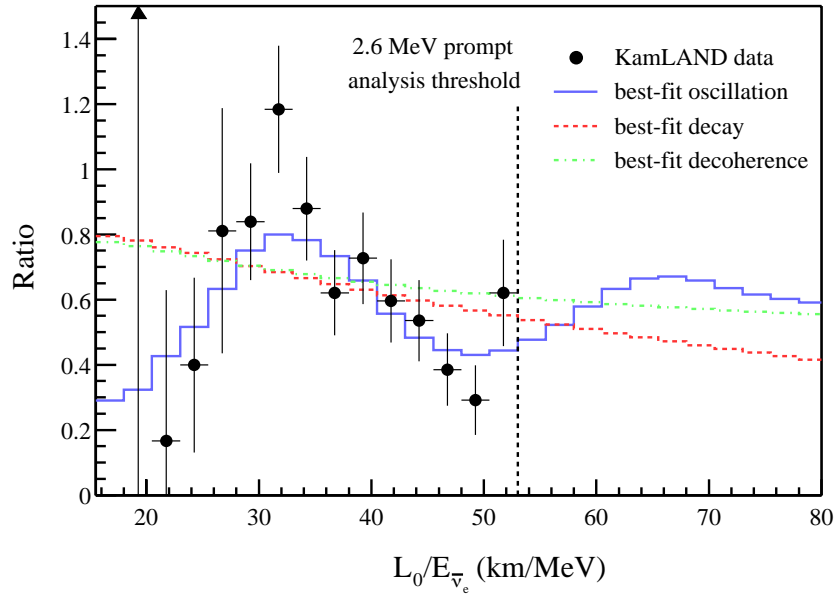


Figure 6.10: Ratio of the observed $\bar{\nu}_e$ spectrum to the expectation for no-oscillation versus L_0/E . For data points, observed energies are converted with a fixed $L_0 = 180$ km. The curves show the corresponding expectation for the best-fit oscillation, best-fit decay and best-fit decoherence models taking into account the individual time-dependent flux variations of all reactors and detector effects.

Chapter 7

Oscillation Analysis

In the context of two-flavor neutrino, the previous chapter discussed the neutrino oscillation parameters as determined by the measurement of the reactor electron anti-neutrino in KamLAND. In addition to the KamLAND data, all current solar neutrino data and the atmospheric neutrino data from Super-Kamiokande and the short baseline (~ 1 km) reactor neutrino data from CHOOZ are analyzed, here.

The neutrino oscillation parameters in the three generation can be determined from a global analysis of the neutrino oscillation experiments. To fix the notation, the neutrino mass-squared difference $\Delta m_{\text{SOL}}^2 \equiv \Delta m_{21}^2 = m_2^2 - m_1^2$ and $\Delta m_{\text{ATM}}^2 \equiv \Delta m_{31}^2 = m_3^2 - m_1^2$ are defined. The simple parameterization of the leptonic mixing matrix (omitting the CP violating angle) is

$$U = \begin{pmatrix} c_{12}c_{13} & s_{12}c_{13} & s_{13} \\ -s_{12}c_{23} - c_{12}s_{23}s_{13} & c_{12}c_{23} - s_{12}s_{23}s_{13} & s_{23}c_{13} \\ s_{12}s_{23} - c_{12}c_{23}s_{13} & -c_{12}s_{23} - s_{12}c_{23}s_{13} & c_{23}c_{13} \end{pmatrix} \quad (7.1)$$

where $c_{ij} \equiv \cos \theta_{ij}$ and $s_{ij} \equiv \sin \theta_{ij}$, and the notations $\theta_{12} \equiv \theta_{\text{SOL}}$ and $\theta_{23} \equiv \theta_{\text{ATM}}$ are used. It is a good approximation to set $\Delta m_{\text{SOL}}^2 = 0$ in the analysis of atmospheric and K2K data, and to set $\Delta m_{\text{ATM}}^2 = \infty$ for the analysis of KamLAND and solar data, and furthermore, the effect of CP-violating phase can be neglected. For the solar and KamLAND experiments, the oscillations related to the atmospheric oscillation length are completely averaged out and the survival probability is given by

$$P_{ee}^{3\nu} = \cos^4 \theta_{13} P_{e'e'}^{2\nu} + \sin^4 \theta_{13}$$

where $P_{e'e'}^{2\nu}$ is obtained from the modified electron density $N_{e'} \rightarrow N_e \cos^2 \theta_{13}$. As a consequence, KamLAND and solar data constrain Δm_{21}^2 , θ_{12} and θ_{13} . For atmospheric and K2K neutrinos, the solar wavelength is too long to be relevant and the corresponding oscillating phase is negligible. So the atmospheric and K2K data constrains Δm_{31}^2 , θ_{23} and θ_{13} . The mixing angle θ_{13} is the only parameter common to both solar and atmospheric neutrino oscillations, it potentially allows for some coupling between the two. The effect of θ_{13} is to add a $\nu_\mu \rightarrow \nu_e$ contribution to the atmospheric oscillations. Finally, for the CHOOZ reactor experiment, the solar wavelength is unobservable if $\Delta m_{21}^2 \leq 8 \times 10^{-4} \text{ eV}^2$. The CHOOZ data are related to Δm_{31}^2 and θ_{13} .

The above considerations imply that the global analysis factorizes as

$$\chi_{\text{global}}^2 = \chi_{\text{Solar+KamLAND}}^2(\Delta m_{21}^2, \theta_{12}, \theta_{13}) + \chi_{\text{CHOOZ+Atmospheric+K2K}}^2(\Delta m_{31}^2, \theta_{23}, \theta_{13}). \quad (7.2)$$

Thus the three generation oscillation effects in the analysis of solar and KamLAND data are obtained from the study of

$$\chi_{\text{global|marg}}^2 = \chi_{\text{Solar+KamLAND}}^2(\Delta m_{21}^2, \theta_{12}, \theta_{13}) + \chi_{\text{CHOOZ+Atmospheric+K2K|marg}}^2(\theta_{13}) \quad (7.3)$$

where $\chi_{\text{CHOOZ+Atmospheric+K2K|marg}}^2$ is the χ^2 analysis of CHOOZ, Atmospheric and K2K data after marginalization over Δm_{31}^2 and θ_{23} .

7.1 Global Analysis

7.1.1 Solar Neutrino Experiments

In the context of three-flavor neutrino oscillation, the solar data constrains Δm_{21}^2 , θ_{12} and θ_{13} . First, a traditional global two generation analysis is performed, and it gives the result of the three generation analysis when θ_{13} is fixed to zero. Next, the analysis is extended to the three flavor oscillation, and the result constrains the three oscillation parameters, Δm_{21}^2 , θ_{12} and θ_{13} .

Two Generation Analysis

A deficit of solar neutrinos have been observed by all current solar neutrino data except the SNO NC measurement. In this analysis, the solar neutrino rates of Homestake, SAGE, GALLEX, GNO, SNO CC and SNO NC as well as the 1496 days of Super-Kamiokande-I data, including the zenith angle spectra are considered.

The definition of χ^2 for the solar neutrino data is as follows,

$$\chi^2 = \chi_{rate}^2 + \chi_{shape}^2 \quad (7.4)$$

$$\chi_{rate}^2 = \sum_{i,j=1}^{N_{obs}} (R_i^{observed} - R_i^{theoretical}) V_{ij}^{-1} (R_j^{observed} - R_j^{theoretical}) \quad (7.5)$$

$$\chi_{shape}^2 = \sum_{i=1}^{N_{bin}} \frac{\{R_i(\text{Data}) - (\beta \cdot R_i^{osc}({}^8\text{B}) + \eta \cdot R_i^{osc}(\text{hep})) / f_i^{corr}(\epsilon_s^2, \epsilon_r^2, \epsilon_b^2)\}^2}{\sigma_i^2 + \epsilon_s^2 + \epsilon_r^2 + \epsilon_b^2} \quad (7.6)$$

where the parameters are following,

- N_{obs}

The number of flux measurements, which is 5 in this analysis (combined Ga rate, Cl rate, SK rate, SNO CC rate, SNO NC rate).

- $R_{observed}$

The ratio of the observed flux to the SSM BP2000 prediction for each measurement.

- $R_{theoretical}$

The ratio of the expected flux with neutrino oscillation to the SSM prediction for each measurement.

- V_{ij}

The error matrix combining the cross section, SSM, and experimental errors,

$$V_{ij} = (\sigma_{ij}^{CS})^2 + (\sigma_{ij}^{SSM})^2 + (\sigma_{ij}^{exp})^2 \quad (7.7)$$

where

$(\sigma_{ij}^{CS})^2$: the error of the effective cross section

$(\sigma_{ij}^{SSM})^2$: the error of the SSM rate prediction
 $(\sigma_{ij}^{exp})^2$: the error for each flux experiment

- N_{bin}

The number of SK bins, which is 7 (zenith angle) \times 6 (energy) in this analysis.

- $R_i(\text{Data}), R_i^{osc}({}^8\text{B}), R_i^{osc}(\text{hep})$

The observed and expected ratio of oscillation to the SSM prediction for each bin.

$$R_i(\text{Data}) = \text{Data}_i / ({}^8\text{B}_i + \text{hep}_i) \quad (7.8)$$

$$R_i^{osc}({}^8\text{B}) = {}^8\text{B}_i^{osc} / ({}^8\text{B}_i + \text{hep}_i) \quad (7.9)$$

$$R_i^{osc}(\text{hep}) = \text{hep}_i^{osc} / ({}^8\text{B}_i + \text{hep}_i) \quad (7.10)$$

where Data_i are the observed rates, and ${}^8\text{B}_i$ (hep_i) and ${}^8\text{B}_i^{osc}$ (hep_i^{osc}) are the expected rates and oscillated rates of ${}^8\text{B}$ (hep) neutrinos in bin i respectively.

- β, η

The free flux scaling parameters for the shape analysis. Those parameters are varied freely to minimize the χ^2 .

- f_i^{corr}

The correction factor for the correlated error.

$$f_i^{corr} = (1 + s_i \cdot \epsilon_s)(1 + r_i \cdot \epsilon_r)(1 + b_i \cdot \epsilon_b) \quad (7.11)$$

where s_i, r_i, b_i are the spectrum uncertainty from SK energy scale, SK energy resolution, ${}^8\text{B}$ neutrino spectrum, respectively. $\epsilon_s, \epsilon_r, \epsilon_b$ are varied to minimize the χ^2 .

The χ_{rate}^2 indicates the flux constraints of the 5 measurements, and the χ_{shape}^2 is the shape constraints of the SK zenith angle spectra including the shape deformation from various uncertainties. Figure 7.1 shows the allowed region from solar data at 95%, 99%, 99.73% C.L. in two generation analysis. The best fit parameters are

$$\sin^2 \theta = 0.28, \quad \Delta m^2 = 6.0 \times 10^{-5} \text{ eV}^2$$

The allowed region from the solar neutrino experiments is consistent with the KamLAND result in the two flavor oscillation (Section 6.3).

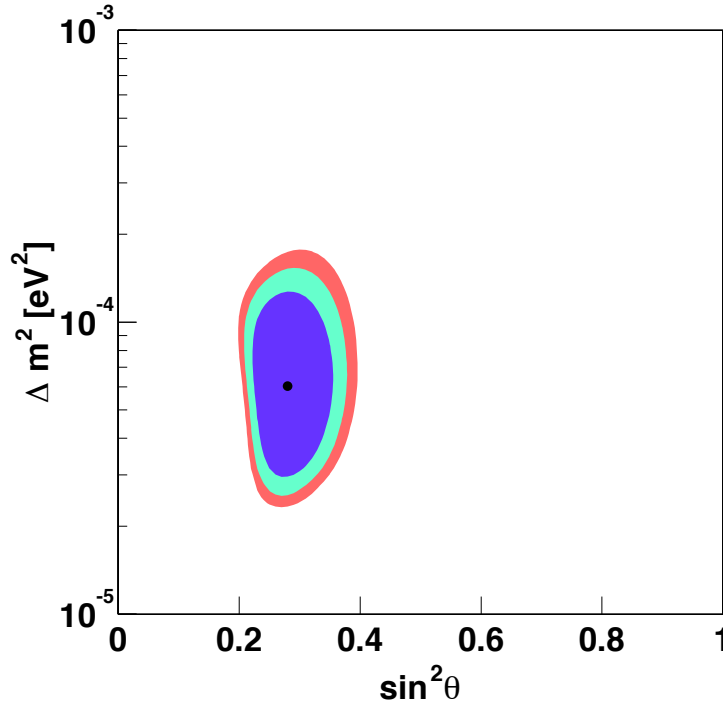


Figure 7.1: Allowed region from solar data at 95%, 99%, 99.73% C.L. in two generation analysis. The best fit parameters are $\sin^2 \theta = 0.28$ and $\Delta m^2 = 6.0 \times 10^{-5} \text{ eV}^2$, using the solar neutrino rates of Homestake, SAGE, GALLEX, GNO, SNO CC and SNO NC as well as the 1496 days of Super-Kamiokande-I data, including the zenith angle spectra. The LMA I region is favored, while the upper LMA region (LMA II $\sim 2 \times 10^{-4} \text{ eV}^2$) and the lower LMA region (LMA 0 $\sim 2 \times 10^{-5} \text{ eV}^2$) from KamLAND only analysis are disfavored. The allowed region is consistent with the two flavor analysis of the KamLAND result.

Three Generation Analysis

A well-approximated calculation of the conversion probability for solar neutrinos in the framework of three neutrino mixing is given in [97]. The survival amplitude for ν_e at a detector on the earth is

$$A_{ee} = \sum_{i=1}^3 A_{ei}^S A_{ie}^E e^{-im_i^2(L-r)/2E} \quad (7.12)$$

where A_{ei}^S is the amplitude of the $\nu_e \rightarrow \nu_i$ transition (ν_i : the i -mass eigenstate) from the production point to the sun surface, A_{ie}^E is the amplitude of the $\nu_i \rightarrow \nu_e$ transition from the earth surface to the detector. L is the distance between the center of the sun and the surface of the earth, and r is the distance between the neutrino production point and the surface of the sun. Using the mass hierarchy, i.e. $\Delta m_{32}^2 \gg 2\sqrt{2}G_F N_e E_\nu \sin^2 2\theta_{13}$ for time evolution of neutrinos both in the sun and in the earth, the three flavor evolution equations decouple into

an effective two-flavor-problem for the intermediate basis [98, 99]

$$\nu_{e'} = \cos \theta_{12} \nu_1 + \sin \theta_{12} \nu_2 \quad (7.13)$$

$$\nu_{\mu'} = -\sin \theta_{12} \nu_1 + \cos \theta_{12} \nu_2 \quad (7.14)$$

with substitution of N_e with the effective density

$$N_{e'} \rightarrow N_e \cos^2 \theta_{13} \quad (7.15)$$

while for the evolution of the third state $\nu_{\tau'} = \nu_3$ there are no matter effects. Thus, the survival amplitude can be simplified to

$$A_{ee} = \cos^2 \theta_{13} \sum_{i=1}^2 A_{e'i}^S A_{ie'}^E e^{-im_i^2(L-r)/2E} + \sin^2 \theta_{13} e^{-im_3^2(L-r)/2E}. \quad (7.16)$$

After averaging out the interference terms due to the higher mass difference $\Delta m_{32}^2 \sim \Delta m_{31}^2$, the survival probability is written as

$$P_{ee}^{3\nu} = \cos^4 \theta_{13} P_{e'e'}^{2\nu} + \sin^4 \theta_{13} \quad (7.17)$$

where $P_{e'e'}^{2\nu}$ is the two flavor survival probability in the $(\Delta m_{21}^2, \theta_{12})$ parameter space but with the modified matter density in Eq. (7.15).

The fitting procedure is the same as in the two generation analysis, but the survival probability is modified. As there is an additional parameter $\sin^2 \theta_{13}$, there are three fitting parameters. The best fit parameters are

$$\sin^2 \theta_{12} = 0.28, \quad \sin^2 \theta_{13} = 0.04, \quad \Delta m_{21}^2 = 6.6 \times 10^{-5} \text{ eV}^2$$

and the allowed region for various $\sin^2 \theta_{13}$ is shown in Figure 7.2. The shaded dots indicate the local minima in each plane. A slightly negative correlation between $\sin^2 \theta_{13}$ and $\sin^2 \theta_{12}$, and a slightly positive correlation between $\sin^2 \theta_{13}$ and Δm_{21}^2 can be seen in Figure 7.2. An increase in $\sin^2 \theta_{13}$ is compensated by a decrease of $\sin^2 \theta_{12}$ or increase of Δm_{21}^2 . Figure 7.4 (b) shows the allowed region in the $(\sin^2 \theta_{12}, \sin^2 \theta_{13})$ plane.

7.1.2 KamLAND

The survival probability in three generation case is given in Eq. (7.17). The oscillation analysis procedure is the same as shown in Section 6.3. The oscillation parameters are $(\sin^2 \theta_{12}, \sin^2 \theta_{13}, \Delta m_{21}^2)$ for the KamLAND as well as the solar neutrino experiments. The best fit parameters are

$$\sin^2 \theta_{12} = 0.32, \quad \sin^2 \theta_{13} = 0.00, \quad \Delta m_{21}^2 = 7.9 \times 10^{-5} \text{ eV}^2$$

and the allowed region for various $\sin^2 \theta_{13}$ is shown in Figure 7.3. The shaded dots indicate the local minima in each plane. A slightly negative correlation between $\sin^2 \theta_{13}$ and $\sin^2 \theta_{12}$ can be seen in Figure 7.3. An increase in $\sin^2 \theta_{13}$ is compensated by a decrease of $\sin^2 \theta_{12}$. Figure 7.4 (a) shows the allowed region in the $(\sin^2 \theta_{12}, \sin^2 \theta_{13})$ plane. The parameters for larger $\sin^2 \theta_{13}$ are disfavored because they have a smaller spectral distortion as shown in Figure 7.5.

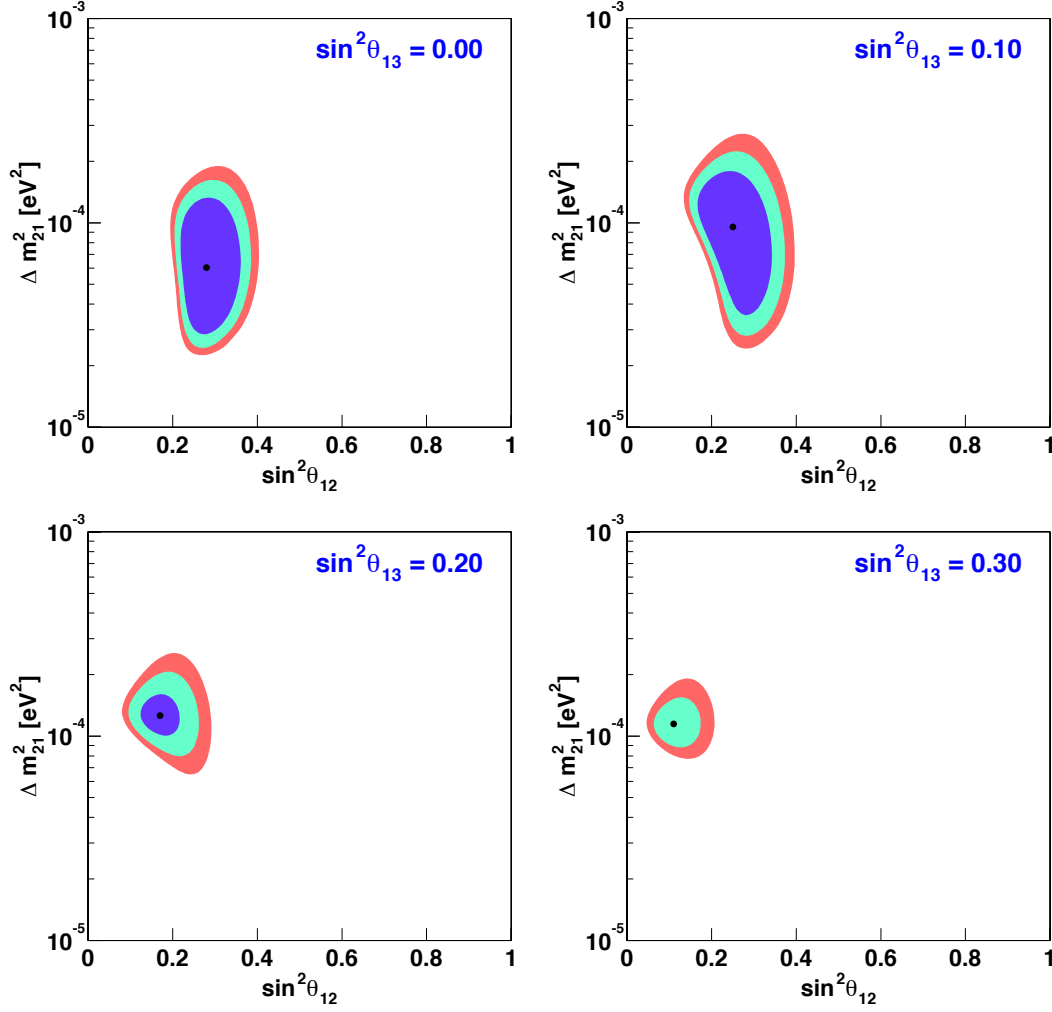


Figure 7.2: Allowed region from solar data in the $(\sin^2 \theta_{12}, \Delta m_{21}^2)$ plane at 95%, 99%, 99.73% C.L. for 3 n.d.f. for various $\sin^2 \theta_{13}$. The best fit parameters are $\sin^2 \theta_{12} = 0.28$, $\Delta m_{21}^2 = 6.6 \times 10^{-5} \text{ eV}^2$ and $\sin^2 \theta_{13} = 0.04$. The black points indicate the local minima in each plane. When the $\sin^2 \theta_{13}$ increases, the lower $\sin^2 \theta_{13}$ and higher Δm_{21}^2 region is favored.

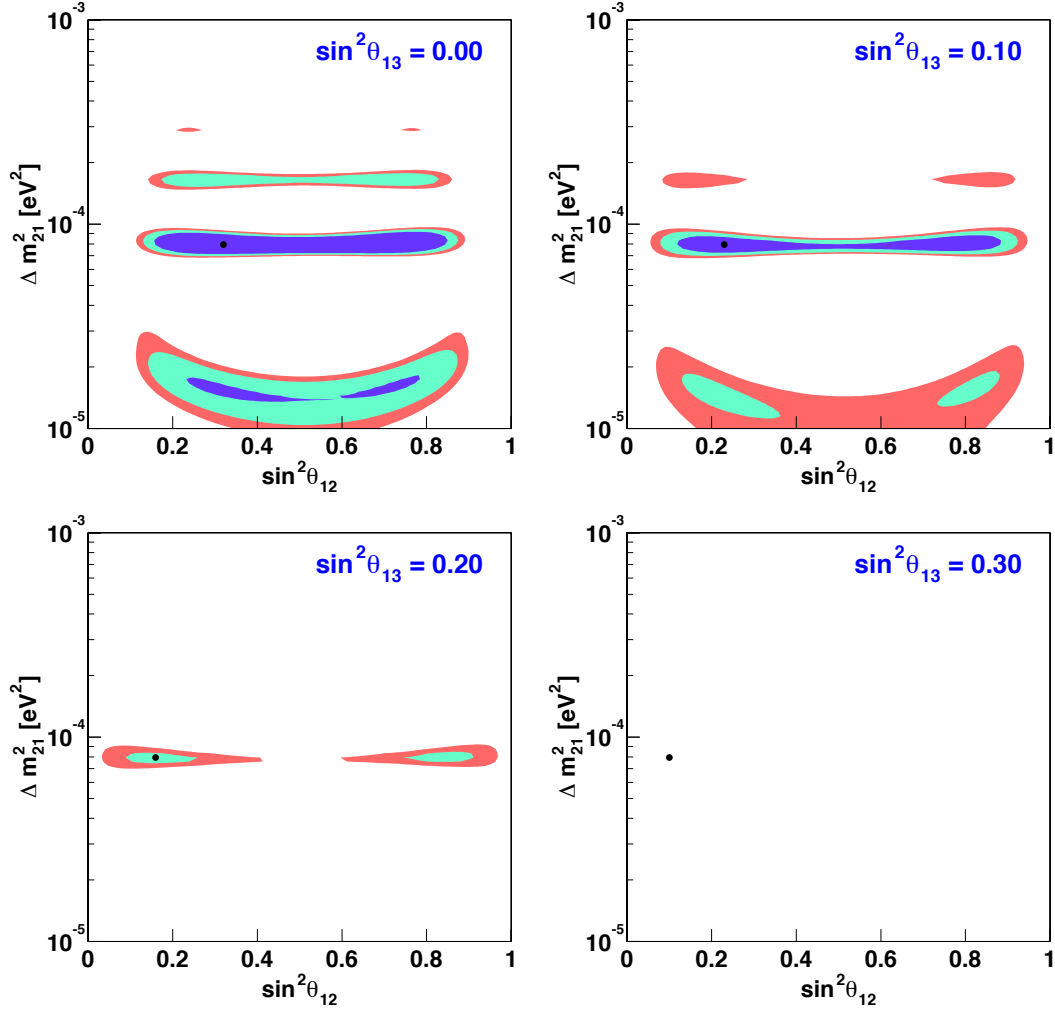


Figure 7.3: Allowed region from KamLAND data in the $(\sin^2 \theta_{12}, \Delta m_{21}^2)$ plane at 95%, 99%, 99.73% C.L. for 3 n.d.f. for various $\sin^2 \theta_{13}$. The best fit parameters in the physical region are $\sin^2 2\theta_{12} = 0.32$, $\Delta m_{21}^2 = 7.9 \times 10^{-5} \text{ eV}^2$ and $\sin^2 2\theta_{13} = 0.00$. The black points indicate the local minima in each plane.

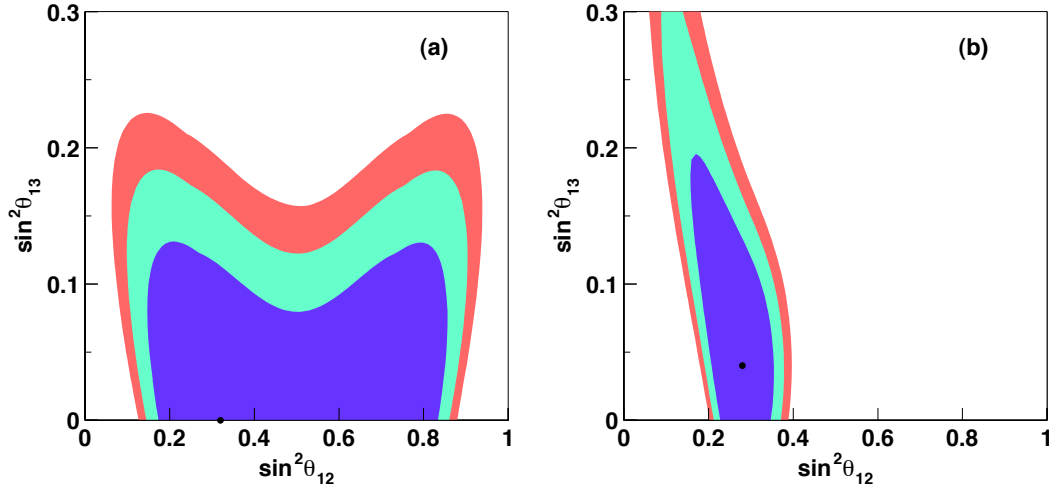


Figure 7.4: Allowed region from (a) KamLAND data and (b) solar data in the $(\sin^2 \theta_{12}, \sin^2 \theta_{13})$ plane at 95%, 99%, 99.73% C.L. for 2 n.d.f.

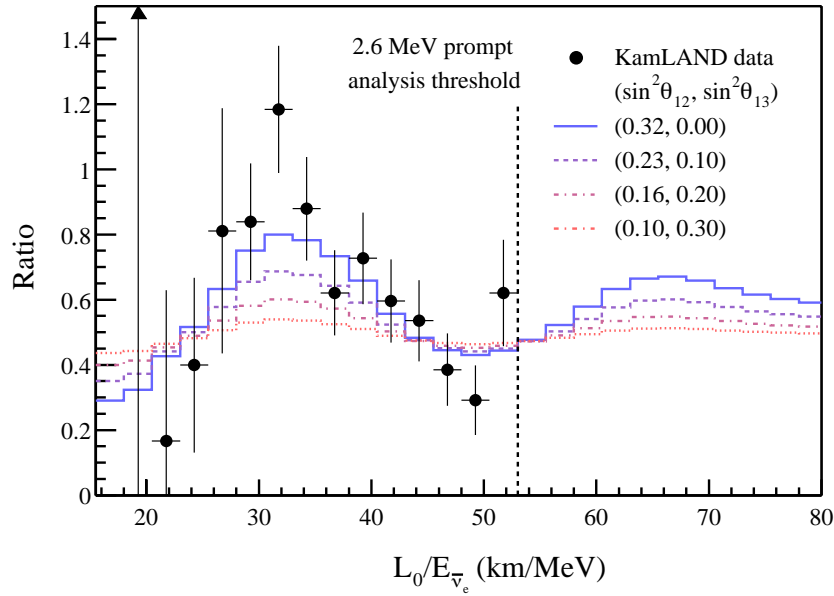


Figure 7.5: Ratio of the observed $\bar{\nu}_e$ spectrum to the expectation for no-oscillation versus L_0/E . For data points, observed energies are converted with a fixed $L_0 = 180$ km. The curves show the corresponding expectation for the oscillation parameter sets, $(\sin^2 \theta_{12}, \sin^2 \theta_{13}) = (0.32, 0.00)$, $(0.23, 0.10)$, $(0.16, 0.20)$, $(0.10, 0.30)$ and $\Delta m_{21}^2 = 7.9 \times 10^{-5} \text{ eV}^2$.

7.1.3 CHOOZ

The CHOOZ experiment [55] has an average value of $L/E \sim 0.3$ km/MeV ($L \sim 1$ km, $E \sim 3$ MeV), and nearly pure neutrino flavor composition and a known intensity to better than 2%. It is ideally suited for a definitive test of $\bar{\nu}_e \rightarrow \bar{\nu}_x$ oscillation down to 10^{-3} eV². The $\bar{\nu}_e$ are detected via the inverse beta decay reaction $\bar{\nu}_e + p \rightarrow e^+ + n$, the same method as used in the KamLAND experiment.

The Chooz power station has two pressurized water reactors with a total thermal power of 8.5 GW. A summary of the data taking is presented in Table 7.1. The reactor ON-OFF information had two beneficial consequences. First, there was enough reactor OFF data to precisely determine the amount of background. Second, the experiment measured the neutrino interaction yield as a function of the reactor power. By fitting the slope of the measured yield to the reactor power, the neutrino interaction yield at full power can be estimated, and that can be compared to the no oscillation hypothesis and to the oscillation hypothesis.

Table 7.1: Summary of the Chooz data acquisition cycle from April 1997 to July 1998 [55]

	Time (h)	$\int W dt$ (GWh)
Run	8761.7	
Live time	8209.3	
Dead time	552.4	
Reactor 1 only ON	2058.0	8295
Reactor 2 only ON	1187.8	4136
Reactors 1 and 2 ON	1543.1	8841
Reactors 1 and 2 OFF	3420.4	

For each run, the expected number of neutrino candidates depends linearly on the reactor power, and the backgrounds are assumed to be independent of power. The expected $\bar{\nu}_e$ yield can be expressed as

$$\overline{N}_i(E_j) = (B(E_j) + W_{1i}^*(E_j)X_1(E_j) + W_{2i}^*(E_j)X_2(E_j))\Delta t_i \quad (7.18)$$

where W_{ki}^* is the effective thermal power and

$$W_{ki}^* = W_{ki}(1 + \eta_{ki})\frac{L_1^2}{L_k^2} \quad (7.19)$$

i : run number

Δt_i : corresponding live time

X_k : distance independent positron yield per reactor power

W_{ki} : thermal power of the two reactors

η_{ki} : correction factor of neutrino interaction yield depending on the fissile isotope composition of the reactor core and positron efficiency correction

L_k : distance to each reactor

The fitted yields are listed in Table 7.2 and compared to the expected yield in the absence of neutrino oscillation. The expected parameters X_1 , X_2 are slightly correlated, such correlation is always negative because an increase of reactor 1 yield corresponds to a decrease in the reactor 2 yield at given candidate and background rates.

Table 7.2: Observed positron yields by fitting (X_1 and X_2) and expected yields (\tilde{X}) for no oscillation [55]

E_{e^+} MeV	$X_1 \pm \sigma_1$ (counts/day/GW)	$X_2 \pm \sigma_2$ (counts/day/GW)	\tilde{X}	σ_{12} (counts/day/GW) ²
1.2	0.151 ± 0.031	0.176 ± 0.035	0.172	$-2.2 \cdot 10^{-4}$
2.0	0.490 ± 0.039	0.510 ± 0.047	0.532	$-1.5 \cdot 10^{-4}$
2.8	0.656 ± 0.041	0.610 ± 0.049	0.632	$-3.5 \cdot 10^{-4}$
3.6	0.515 ± 0.036	0.528 ± 0.044	0.530	$-3.3 \cdot 10^{-4}$
4.4	0.412 ± 0.033	0.408 ± 0.040	0.379	$-2.0 \cdot 10^{-4}$
5.2	0.248 ± 0.030	0.231 ± 0.034	0.208	$-0.7 \cdot 10^{-4}$
6.0	0.102 ± 0.023	0.085 ± 0.026	0.101	$-1.3 \cdot 10^{-4}$

The definition of χ^2 is as follows,

$$\begin{aligned}
\chi^2 = & \sum_{i=1}^{14} \sum_{j=1}^{14} (X_i - \alpha \bar{X}(gE_i, L_i, \theta, \Delta m^2)) V_{ij}^{-1} (X_j - \alpha \bar{X}(gE_j, L_j, \theta, \Delta m^2)) \\
& + \left(\frac{\alpha - 1}{\sigma_\alpha} \right)^2 + \left(\frac{g - 1}{\sigma_g} \right)^2
\end{aligned} \tag{7.20}$$

where α is the absolute normalization constant, g is the energy scale calibration factor ($\sigma_\alpha = 2.7\%$ and $\sigma_g = 1.1\%$), $L_{i,j} = L_1$ for $i, j \leq 7$ and $L_{i,j} = L_2$ for $i, j > 7$. The variance and covariance matrix off-diagonal elements are listed in Table 7.2. Figure 7.6 shows the excluded region of neutrino oscillation parameters from CHOOZ. The parameter θ_{12} is ignored because its effect is suppressed by the much smaller parameter Δm_{21}^2 than Δm_{31}^2 . The CHOOZ result gives a good limit for θ_{13} in the $\Delta m_{31}^2 > 1.0 \times 10^{-3}$ region, however, there is no limit in the lower Δm^2 region.

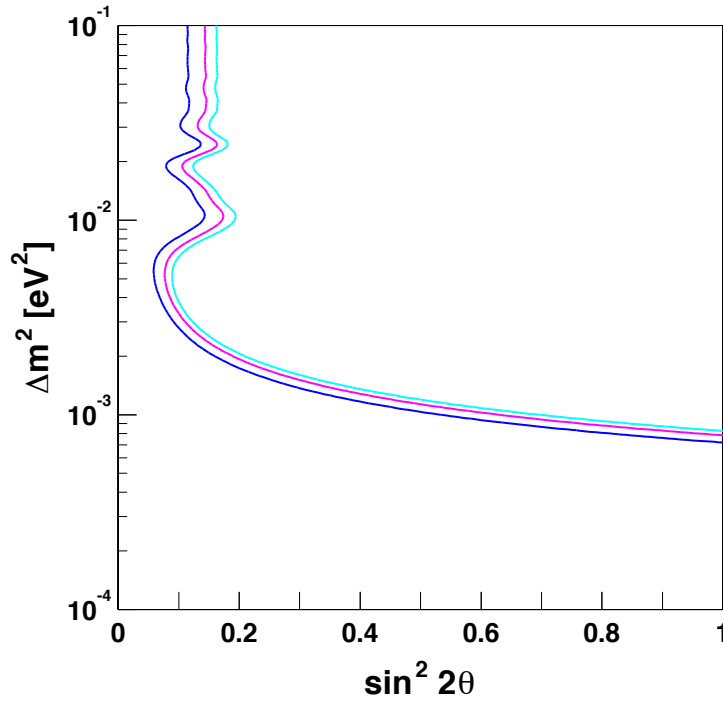


Figure 7.6: Excluded region of neutrino oscillation parameters from CHOOZ. Excluded regions are inside of solid line, and the blue and pink and sky blue lines indicate 95%, 99%, 99.73% C.L. The oscillation parameter θ and Δm^2 are approximated to be θ_{13} and Δm_{31}^2 because the effect from the θ_{12} is weakened due to the small L/E in the CHOOZ experiment. Thus, the determination θ_{13} is not affected by the θ_{12} uncertainty in the CHOOZ result.

7.1.4 Supernova 1987A

On February 23, 1987, the Kamiokande II [100] and Irvine Michigan Brookhaven (IMB) [101] detectors observed neutrino signals from a $20M_\odot$ Type II supernova in the Large Magellanic Cloud, the so called ‘SN1987A’. The core collapse supernova occurs when the iron core of a massive star collapses under its own gravitation. When the density in the core becomes as high as the degeneracy pressure of neutrons, a shock wave is produced, and leads to a supernova explosion. The very high density star under gravitational collapse is an ideal candidate to investigate the neutrino oscillation in three generation scheme.

From the analysis of the supernova collapse, almost all ($\sim 99\%$) of the gravitational binding energy is radiated away in the form of neutrinos. The total amount of binding energy E_b is approximately 10^{53} ergs, and its energy is divided up among all flavors of neutrinos and anti-neutrinos, however the individual neutrino energy distributions are very different (Appendix F). Typically, the average supernova neutrino energies are

$$\langle E_{\nu_e} \rangle \sim 10 - 12 \text{ MeV} \quad (7.21)$$

$$\langle E_{\bar{\nu}_e} \rangle \sim 14 - 17 \text{ MeV} \quad (7.22)$$

$$\langle E_{\nu_x} \rangle \sim \langle E_{\bar{\nu}_x} \rangle \sim 24 - 27 \text{ MeV} \quad (7.23)$$

and their spectra are expressed in a ‘pinched’ Fermi-Dirac distribution [102],

$$F(E_\nu) \propto \frac{E_\nu^2}{1 + e^{E_\nu/T - \eta}} \quad (7.24)$$

where η is an effective ‘chemical potential’, and T is the neutrino temperature. The correlation between the average energy and temperature for each neutrino is given by $\langle E_\nu \rangle \sim 3T$.

In a water Cherenkov detector, the reaction $\bar{\nu}_e + p \rightarrow e^+ + n$ dominates other scattering processes $\nu + e^- \rightarrow \nu + e^-$ at neutrino energy around 10 MeV. Figure 7.7 shows the observed supernova candidates, 11 events for Kamiokande II, and 8 events for IMB detector. Most of the events are concentrated in the first 2.7 sec. In both detectors, the detection efficiency has an energy dependence due to the trigger threshold as described in [103].

As a consequence of the extremely high matter density in the supernova, the three neutrino and three anti-neutrino eigenstates have two level crossings at higher and lower density (Figure 7.8). An important consequence is that the resonance flavor conversion of $\bar{\nu}_e$ can occur by the MSW effect if the mass hierarchy is inverted and ‘H’ resonance is adiabatic. The conversion effects in the anti-neutrino channel are expressed by the probability $P_{ee} \equiv P(\bar{\nu}_e \rightarrow \bar{\nu}_e)$, the total survival probability from the production point to the detector. The earth matter effect is included in P_{ee} . The $\bar{\nu}_e$ flux arriving at a detector is

$$F_{\bar{\nu}_e} = P_{ee} F_{\bar{\nu}_e}^0 + (1 - P_{ee}) F_{\bar{\nu}_x}^0 \quad (7.25)$$

where $F_{\bar{\nu}_e}^e$ and $F_{\bar{\nu}_e}^x$ are the original fluxes of the electron anti-neutrino and muon, tau anti-neutrino. In this work, the calculation of the electron anti-neutrino survival probability is based on a simple analytical method, assuming a ‘power-law’ potential ($V \propto r^{-3}$) as described in [104]. In order to consider the earth matter effect, the probability $P_E(\bar{\nu}_2 \rightarrow \bar{\nu}_e)$ is also calculated analytically, assuming the total pathlength in the mantle, $L_{\text{Kam}} = 3,900$ km and $L_{\text{IMB}} = 8,400$ km, and their density, $d_{\text{Kam}} = 3.4$ g/cm³ and $d_{\text{IMB}} = 4.6$ g/cm³ for the Kamiokande II and IMB detector.

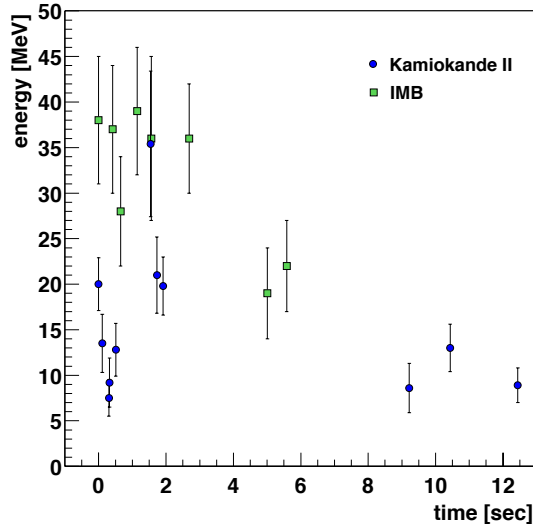


Figure 7.7: Observed supernova events in Kamiokande II and IMB detector within the first 13 sec. The earliest event in the sample of each detector has been arbitrarily assigned $t = 0$. The effective energy threshold is 7.5 MeV for Kamiokande II and 19 MeV for IMB.

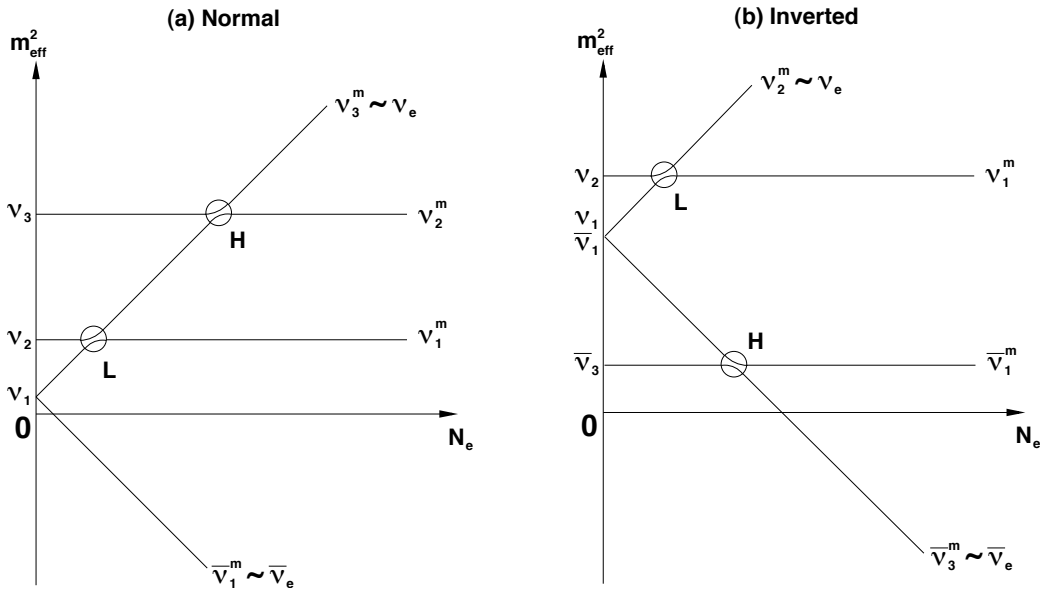


Figure 7.8: Schematic view of level crossing for the supernova neutrino for the case of (a) normal and (b) inverted mass hierarchies. The symbol 'H' and 'L' indicate the resonance points at higher and lower density, respectively.

In order to perform the oscillation analysis, the maximum likelihood method is used [103]. The likelihood function L is

$$L = C \exp \left(- \int_0^\infty n(E) dE \right) \prod_{i=1}^{N_{obs}} n(E_i) \quad (7.26)$$

where N_{obs} is the total number of experimentally observed events and $n(E)$ is the spectrum of detected energies. In the combined analysis of the Kamiokande II and IMB data, the likelihood function is the product of the likelihood functions for each detector.

Figure 7.9 shows the allowed region in the $(T_{\bar{\nu}_e}, \sin^2 \theta_{13})$ plane for the various temperature ratios $\tau \equiv T_{\bar{\nu}_x}/T_{\bar{\nu}_e} = 1.4, 1.7, 2.0$, which is in the range 1.4-2.0 from theoretical prediction, for both the normal and inverted hierarchy cases. It shows that for the inverted hierarchy case, the larger mixing angle $\sin^2 \theta_{13} > 10^{-4}$ is disfavored if the theoretical prediction of the electron anti-neutrino temperature $T_{\bar{\nu}_e}$ is considered. In this analysis, the binding energy E_b is treated as a free parameter. The effective chemical potential η is fixed to zero, and the oscillation parameters $(\sin^2 \theta_{12}, \Delta m_{21}^2, \Delta m_{31}^2)$ are fixed to $(0.28, 7.9 \times 10^{-5} \text{ eV}^2, 2.3 \times 10^{-3} \text{ eV}^2)$, and the uncertainties of those parameters don't change the conclusion¹.

The analysis of the supernova event improved the limit on θ_{13} from the CHOOZ limit for the inverted hierarchy case. However, theoretical models of the supernova have uncertainties, which is difficult to assign reliable errors. In order to get the figures on the result of oscillation analysis, more precise supernova models are needed, therefore the supernova upper limit on θ_{13} is not included in the global three generation analysis for this thesis. When a future galactic supernova occurs, much better information will be obtained.

¹The uncertainties of those parameters are smaller than the uncertainty of the temperature ratio $\tau \equiv T_{\bar{\nu}_x}/T_{\bar{\nu}_e}$. For the mixing angle $\sin^2 \theta_{12}$, the larger angle close to the full mixing is disfavored, because the observed data doesn't agree with the $\bar{\nu}_e - \bar{\nu}_x$ exchanged spectrum.

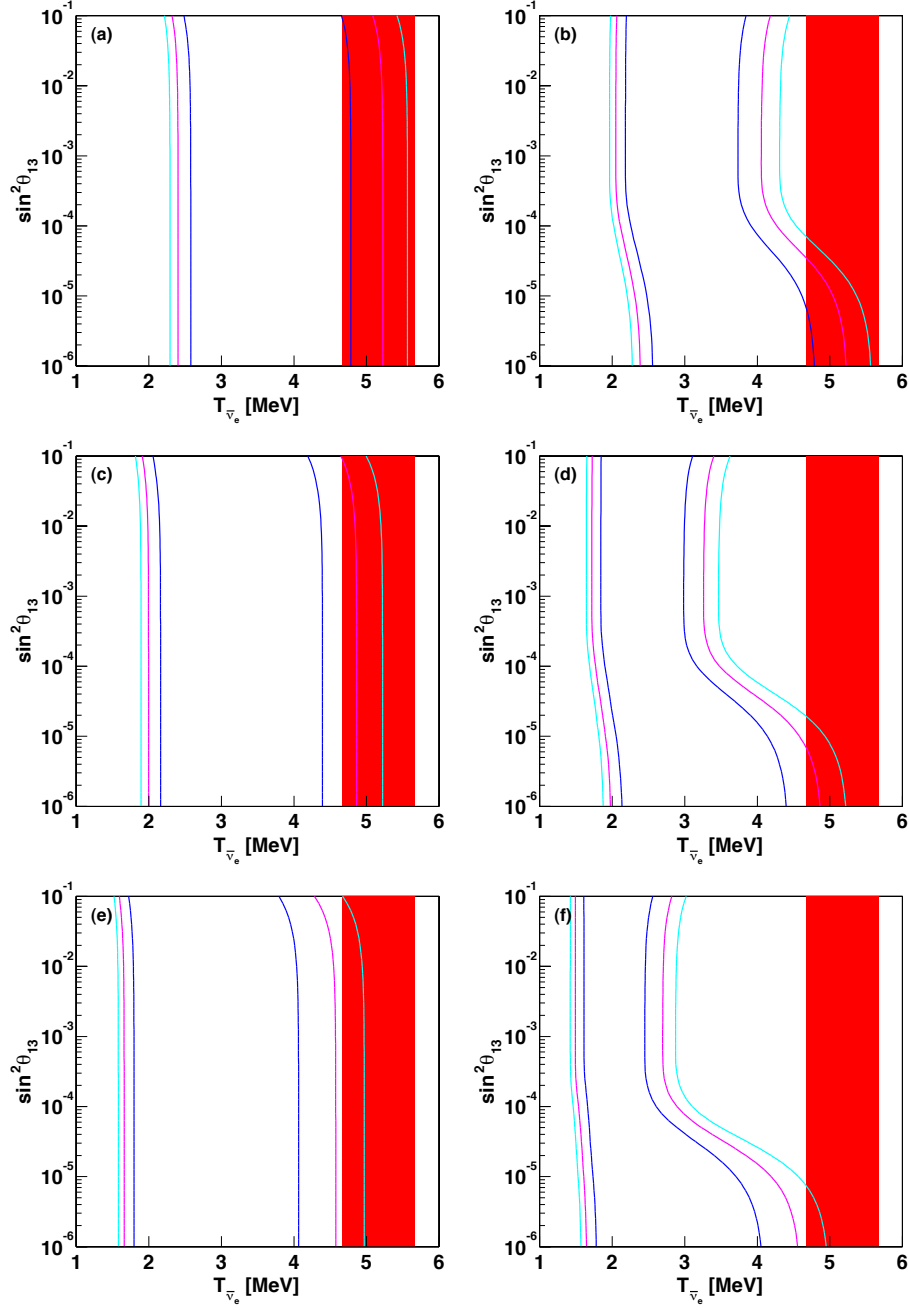


Figure 7.9: Allowed regions in the $(T_{\bar{\nu}_e}, \sin^2 \theta_{13})$ plane for 2 n.d.f from the combined analysis of Kamiokande II and IMB with the supernova 1987A data. The blue and pink and sky blue lines indicate 95%, 99%, 99.73% C.L., and the red shaded region indicates the theoretical prediction of the electron anti-neutrino temperature $T_{\bar{\nu}_e}$. The (a),(c),(e) and (b),(d),(f) indicate the normal and inverted hierarchy case for the temperature ratios $\tau \equiv T_{\bar{\nu}_x}/T_{\bar{\nu}_e} = 1.4, 1.7, 2.0$, respectively.

7.1.5 Global three generation analysis

The most general analysis for the currently known neutrinos is the ‘three generation analysis’. The LSND result is ignored, because that requires the ‘four generation analysis’, which is beyond the scope of this work. All of the oscillation measurements except the LSND and supernova 1987A are summarized below.

- Solar Experiments

Homestake, SAGE, GALLEX, GNO, SK, SNO CC and SNO NC flux measurement and SK zenith energy spectra data are included. The solar neutrino deficit is observed in all experiments, except for SNO NC. In two generation analysis, the allowed region is only LMA region at 3σ C.L. in the combined analysis. For the three neutrino case, these data constrains $(\Delta m_{21}^2, \theta_{12}, \theta_{13})$.

- KamLAND

766.3 ton-year of KamLAND data are included. The data shows a reactor $\bar{\nu}_e$ deficit as well as a spectral distortion at $L/E = 20 - 50$ km/MeV. In the two generation analysis, the allowed region is only LMA I at 95% C.L. For the three neutrino case, the KamLAND data constrains $(\Delta m_{21}^2, \theta_{12}, \theta_{13})$.

- CHOOZ

CHOOZ data from April 7, 1997 to July 20, 1998 are included. The data shows no evidence of a reactor $\bar{\nu}_e$ deficit at $L/E \sim 0.3$ km/MeV. In the two generation analysis, $(\Delta m^2 > 2 \times 10^{-3}$ and $\sin^2 2\theta > 0.15$) region is excluded at 95% C.L. For the three neutrino case, the CHOOZ data constrains $(\Delta m_{31}^2, \theta_{13})$.

- Atmospheric Experiments

Atmospheric neutrino data of SK I (e-like and μ -like) are included. The data shows the correlation of the disappearance of the muon type neutrino with L/E . In the two generation analysis, the best-fit point is $\sin^2 \theta = 0.50$ and $\Delta m^2 = 2.0 \times 10^{-3}$ eV² [105] in the physical region. For the three neutrino case, the atmospheric neutrino data constrains $(\Delta m_{31}^2, \theta_{23}, \theta_{13})$.

- K2K

K2K I and K2K II data are included. The data shows the ν_μ deficit from the accelerator in KEK, as well as the spectral distortion [106]. In the two generation analysis, the best-fit point is $\sin^2 \theta = 0.50$ and $\Delta m^2 = 2.7 \times 10^{-3}$ eV² in the physical region. For the three neutrino case, the K2K data constrains $(\Delta m_{31}^2, \theta_{23}, \theta_{13})$.

For the atmospheric and K2K experiments, the combined analysis from [105] is used, because the constraint on oscillation parameters $(\Delta m_{31}^2, \theta_{23})$, which is not related to KamLAND measurement, is beyond the scope of this thesis. The three generation oscillation parameters of the solar and KamLAND $(\Delta m_{21}^2, \theta_{12}, \theta_{13})$ are limited by CHOOZ + atmospheric + K2K via the constraint on θ_{13} .

Upper Limit on θ_{13}

The small parameter θ_{13} is constrained by solar + KamLAND, and CHOOZ + atmospheric + K2K. The uncertainty of Δm_{31}^2 loosens the limit on θ_{13} in the latter, but not in the former. The CHOOZ limit on θ_{13} depends on the constraint on Δm_{31}^2 by atmospheric + K2K data. Figure 7.10 shows the allowed regions in the $(\sin^2 \theta_{13}, \Delta m_{31}^2)$ plane from CHOOZ data alone and CHOOZ + solar + KamLAND data. The bound on θ_{13} is dominated by CHOOZ in the region around the best fit value of Δm_{31}^2 by atmospheric + K2K. At the lower Δm_{31}^2 , the constraint by KamLAND is dominant.

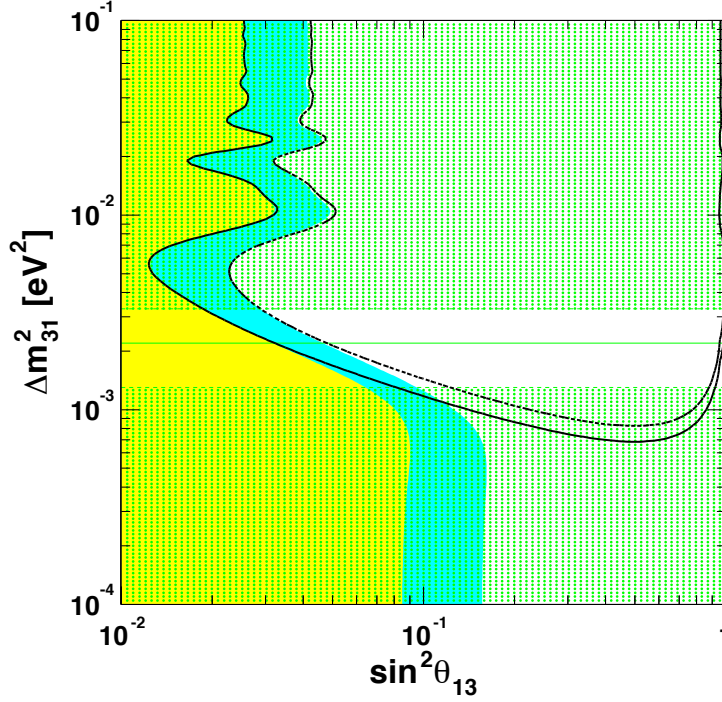
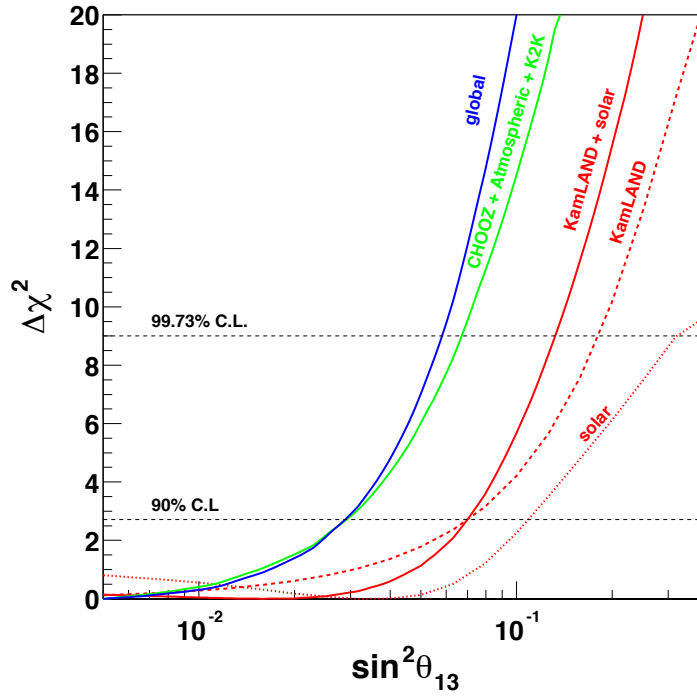


Figure 7.10: Allowed regions in the $(\sin^2 \theta_{13}, \Delta m_{31}^2)$ plane at 90%, 99.73% C.L. for 2 n.d.f. from CHOOZ data alone (lines) and CHOOZ + solar + KamLAND data (colored regions). The green horizontal line and dotted region indicate the best fit value of Δm_{31}^2 and the excluded region at 99.73% C.L. from atmospheric + K2K data [105]. The bound on θ_{13} is dominated by the CHOOZ in the region around the best fit value of Δm_{31}^2 by atmospheric + K2K. At the lower Δm_{31}^2 , the constraint by KamLAND is dominant.

Figure 7.11 shows the $\Delta\chi^2$ profiles projected onto the $\sin^2 \theta_{13}$ axis for different data combinations. The limit of KamLAND data is stronger than that of solar data. The dominated limit on θ_{13} comes from CHOOZ, atmospheric and K2K data. The contribution of solar + KamLAND data is significant, and independent of Δm_{31}^2 value. The limit on $\sin^2 \theta_{13}$ is summarized in Table 7.3.

Table 7.3: Summary of the limit on $\sin^2 \theta_{13}$

	90% C.L.	99.73% C.L.
solar	0.109	0.32
KamLAND	0.070	0.18
solar + KamLAND	0.070	0.13
CHOOZ + atmospheric + K2K	0.029	0.067
global	0.029	0.058

Figure 7.11: $\Delta\chi^2$ profiles projected onto the $\sin^2 \theta_{13}$ axis for solar, KamLAND, solar + KamLAND, atmospheric + K2K + CHOOZ.

Constraint on θ_{12} and Δm_{21}^2

The oscillation parameters θ_{12} and Δm_{21}^2 are measured by the solar neutrino experiments and the KamLAND experiment. As the neutrino consists of three generations, the result from the two flavor oscillation analysis shown in Section 6.3 is not general, only an approximation. In the three neutrino framework, the uncertainty of θ_{13} should be considered for the determination of θ_{12} and Δm_{21}^2 . As discussed in Section 1.5, CP asymmetry from the appearance experiments, detecting $P(\nu_\mu \rightarrow \nu_e)$ and $P(\bar{\nu}_\mu \rightarrow \bar{\nu}_e)$, depends on the oscillation parameters Δm_{21}^2 , θ_{12} , θ_{13} and the CP phase δ . For the precise measurement of the CP effect, the determination of Δm_{21}^2 and θ_{12} is important as well as θ_{13} .

Figure 7.12 shows the projections of the allowed regions onto the $(\sin^2 \theta_{12}, \Delta m_{21}^2)$ plane from KamLAND, solar, and KamLAND + solar. The CHOOZ + atmospheric + K2K constraint on θ_{13} are not included in the left figures, but are included in the right figures. The contour plot of $(\sin^2 \theta_{12}, \Delta m_{21}^2)$ from the global analysis is almost consistent with that of the two generation analysis. This means the allowed region from solar + KamLAND data is stable within the θ_{13} error limited by CHOOZ + atmospheric + K2K data. The $\Delta\chi^2$ profiles onto $\sin^2 \theta_{12}$ and Δm_{21}^2 axis from the global oscillation data are shown in Figure 7.13. The constraint from the solar neutrino experiments is dominant for the limit on θ_{12} , and the constraint from the KamLAND experiments is dominant for the limit on Δm_{21}^2 because of the direct measurement of the oscillatory shape for $\bar{\nu}_e$. The best fit and error (1 n.d.f.) of the neutrino oscillation parameters are summarized in Table 7.4.

Table 7.4: Summary table of the best fit and error (1 n.d.f.) of the oscillation parameters from all neutrino oscillation experiments

Parameter	best fit	2σ	3σ	4σ
Δm_{21}^2 [10^{-5} eV ²]	7.9	7.3-8.7	7.0-9.1	6.7-9.5
$\sin^2 \theta_{12}$	0.28	0.23-0.34	0.21-0.38	0.19-0.43
$\sin^2 \theta_{13}$	0.005	≤ 0.036	≤ 0.058	≤ 0.085

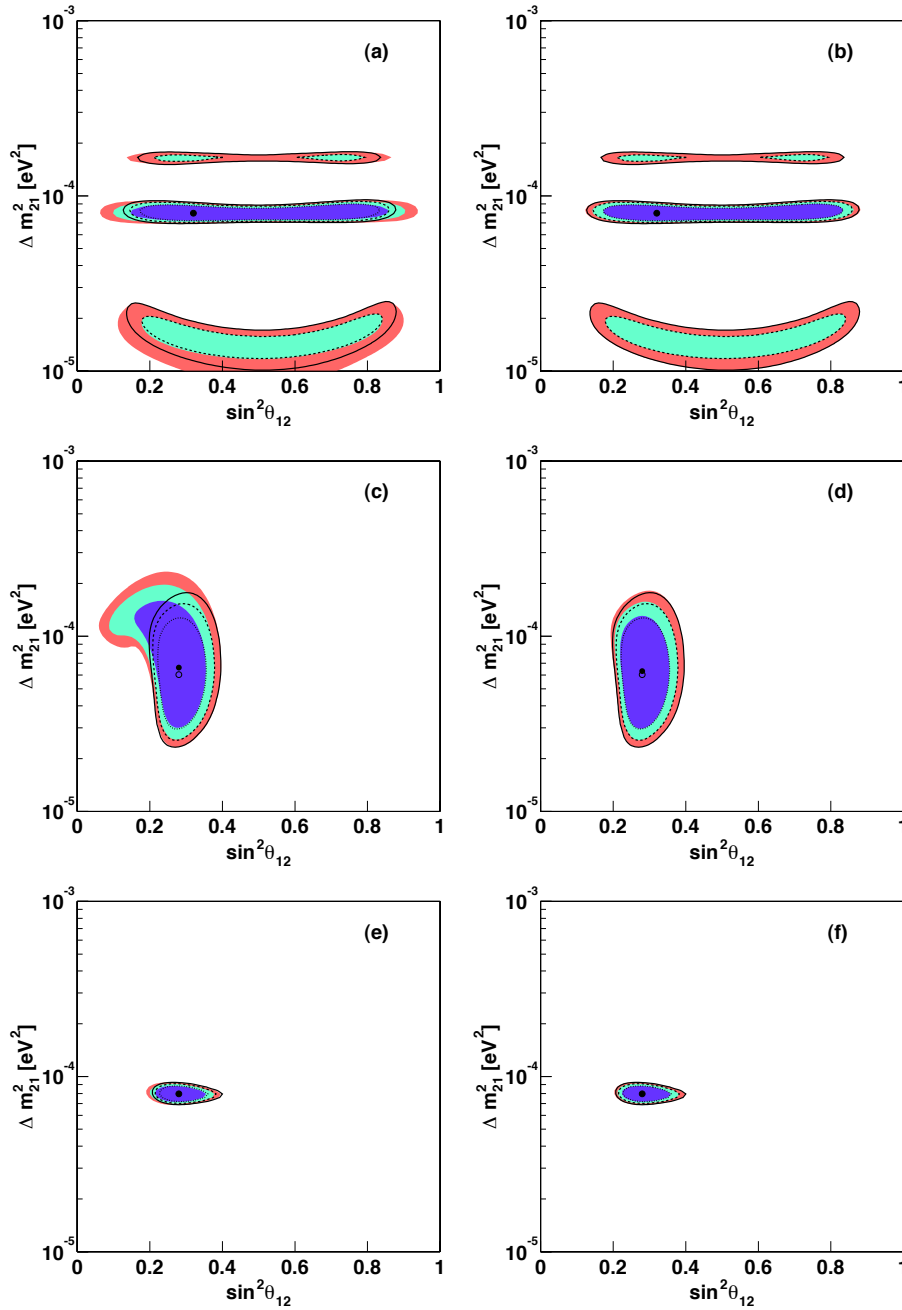


Figure 7.12: Projections of the allowed regions onto the $(\sin^2 \theta_{12}, \Delta m^2_{21})$ plane from KamLAND, solar, and KamLAND + solar at 95%, 99% and 99.73% C.L. for 2 n.d.f., The black lines indicate the allowed regions for the two generation analysis ($\sin^2 \theta_{13} = 0$) at 95%, 99% and 99.73% C.L. for 2 n.d.f. The filled (open) dots indicate the best fit points of 3 (2) generation analysis. The constraint from CHOOZ + atmospheric + K2K data isn't included in (a),(c),(e), but (b),(d),(f).

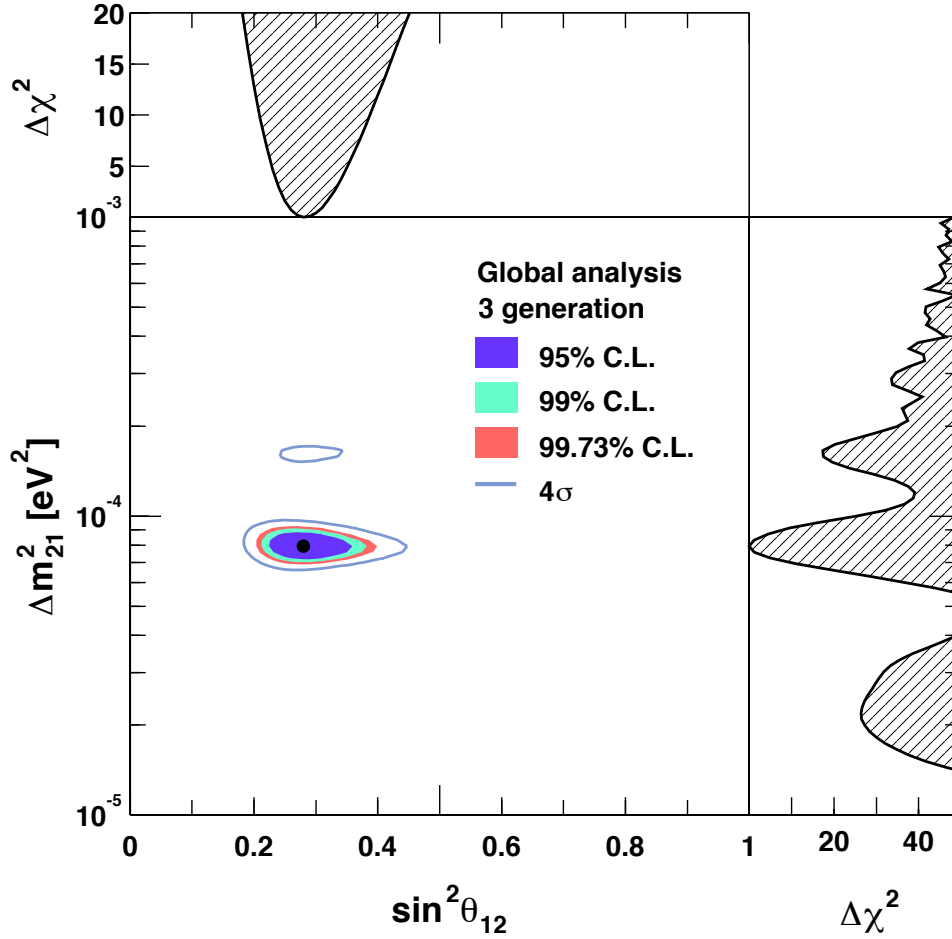


Figure 7.13: Projection of the allowed regions onto the $(\sin^2 \theta_{12}, \Delta m_{21}^2)$ plane from the global oscillation data. $\Delta\chi^2$ profiles projected onto the $\sin^2 \theta_{12}$ and Δm_{21}^2 axis, which constraint are dominated by the solar neutrino experiments (Homestake, SAGE, GALLEX, GNO, SNO, SK) and KamLAND experiment respectively. The LMA II and LMA 0 is excluded at $> 3\sigma$ and $> 4\sigma$ C.L. The contribution of the limit on θ_{13} from CHOOZ + atmospheric + K2K is significant as shown in Figure 7.12.

Chapter 8

Summary

The solar and atmospheric neutrino experiments have reported the deficit of neutrinos possibly due to the neutrino oscillation. However, it was hard to obtain clear oscillatory behavior in their experiments. The primary goal of the Kamioka Liquid Scintillator Anti-Neutrino Detector (KamLAND) is a search for the oscillation of $\bar{\nu}_e$'s emitted from distant power reactors, typically 180 km. The neutrino energy and the distance is good condition to observe the L/E dependence of the LMA neutrino oscillation. The most important element to confirm the neutrino oscillation is detecting the oscillation shape directly using the neutrino energy information.

The data presented in this thesis were collected from March 9, 2002 through January 11, 2004. The total livetime including spallation cuts is 515.1 days. In the absence of anti-neutrino disappearance, we expect 365.2 ± 23.7 (syst) events above 2.6 MeV for the 766.3 ton-year data set. As we observe 258 events, the average $\bar{\nu}_e$ survival probability ($\frac{N_{\text{obs}} - N_{\text{BG}}}{N_{\text{expected}}}$) is $0.658 \pm 0.044(\text{stat}) \pm 0.047(\text{syst})$, confirming $\bar{\nu}_e$ disappearance at 99.998% C.L. After September 2002, a large number of Japanese nuclear reactors were off. A correlation between the observed rate and the expected rate is the useful information for the background estimation as demonstrated in other reactor $\bar{\nu}_e$ experiments. The fitted background rate is consistent with the expected background 17.8 ± 7.3 events.

The neutrino oscillation gives rise to not only the disappearance of $\bar{\nu}_e$ but also the energy spectrum distortion. The scaled no oscillation $\bar{\nu}_e$ spectrum is excluded by χ^2 test at 99.78% C.L independently of the $\bar{\nu}_e$ rate. This is the first evidence for spectral distortion in the $\bar{\nu}_e$ spectrum. Moreover, two alternative hypotheses for neutrino disappearance, neutrino decay and decoherence, are tested. These hypotheses give different L_0/E dependences from the neutrino oscillation hypothesis. The χ^2 of decay and decoherence are 10.7 (3.3 standard deviation) and 12.7 (3.6 standard deviation) larger than neutrino oscillation. That implies, the decay and decoherence are strongly disfavored.

The neutrino oscillation is confirmed, and the next subject is the determination of the neutrino oscillation parameters. The KamLAND data is consistent with the combined result from the solar neutrino experiments (Homestake, SAGE, GALLEX, GNO, SNO, SK) in the conventional two flavor oscillation with CPT invariance. Those data make it possible to measure the oscillation parameters, θ_{12} and Δm_{21}^2 , precisely also in three generation oscillation analysis. In the three generation analysis, θ_{13} uncertainty degrades a precision of the other oscillation param-

eters obtained in two generation frame work. In the CHOOZ experiment, neutrino oscillations were searched at $L/E \sim 0.3$, and the data shows no evidence of the reactor $\bar{\nu}_e$ deficit. However, the CHOOZ result gives a good limit on θ_{13} in the region $\Delta m_{31}^2 > 1.0 \times 10^{-3} \text{ eV}^2$. On the other hand, the atmospheric and K2K data constrains the larger mass splitting Δm_{31}^2 , and the 2 mixing angle θ_{23} , θ_{13} , and those experiment data favor the region of $\Delta m_{31}^2 \sim 2 \times 10^{-3} \text{ eV}^2$. Therefore, the combined result of the CHOOZ, atmospheric and K2K gives strong limit on θ_{13} .

The neutrinos emitted from the very high density star due to the gravitational collapse, so called ‘SN1987A’ neutrinos, were observed in Kamiokande II and IMB. The analysis on supernova improved limit on θ_{13} from the CHOOZ limit for the inverted hierarchy case, which assumes the lightest ν_3 mass. However, theoretical models of the supernova have uncertainties, so the supernova upper limit on θ_{13} is not included in the global three generation analysis for this thesis. For a future galactic supernova, more clear information will be provided.

Finally, the solar neutrino oscillation parameters (Δm_{21}^2 , θ_{12} , θ_{13}) are determined from the solar neutrino experiments, KamLAND, CHOOZ, atmospheric neutrino experiments and K2K. In the global three generation analysis, the uncertainties of Δm_{31}^2 and θ_{23} are considered when θ_{13} is limited. The resultant oscillation parameter set, Δm_{21}^2 , θ_{12} , and θ_{13} , is

$$\begin{aligned}\Delta m_{21}^2 &= 7.9 \times 10^{-5} \text{ eV}^2 \\ \theta_{12} &= 32^\circ \\ \theta_{13} &< 11^\circ \text{ (95\% C.L.)}.\end{aligned}$$

Currently, $\Delta m_{21}^2 = 7.3 \sim 8.7 \times 10^{-5} \text{ eV}^2$, $\theta_{12} = 29^\circ \sim 36^\circ$ are favored at 95% C.L. (1 n.d.f.), and the LMA II and LMA 0 is excluded at $> 3\sigma$ and $> 4\sigma$ C.L., respectively. It was found that the best fit and error of Δm_{21}^2 and θ_{12} don’t change from two generation oscillation analysis. The bounds on θ_{12} and Δm_{21}^2 are dominated by the solar neutrino experiments and KamLAND, respectively. On the other hand, the bound on θ_{13} is dominated by the CHOOZ in the region around the best fit value of Δm_{31}^2 by atmospheric + K2K. At the lower Δm_{31}^2 , the constraint by KamLAND is dominant.

In the near future, the uncertain mixing angle θ_{13} is measured with a $\nu_\mu \rightarrow \nu_e$ appearance search in the accelerator-based long baseline experiment. If $\nu_\mu \rightarrow \nu_e$ appearance is observed, that experiment can test CP violation in the lepton sector. The above oscillation measurement is very important to measure the CP violation effect at a high sensitivity.

Appendix A

Trigger Types

In the beginning of each run, the different trigger types can be enable or disable. The trigger types are as follows,

- ID singles trigger
The ID singles trigger is based on the total ID nsum being above the ID singles trigger threshold. It issues a global acquisition trigger to the ID LBL electronics cards.
- ID prompt trigger
The ID prompt trigger is based on the total ID nsum being above the ID prompt trigger threshold. It issues a global acquisition trigger to the ID LBL electronics cards and opens a 1 ms window for the ID delayed trigger.
- ID delayed trigger
The ID delayed trigger is based on the total ID nsum being above the ID delayed trigger threshold during the window after an ID prompt trigger. It issues a global acquisition trigger to the ID LBL electronics cards.
- ID prescale trigger
The ID prescaled trigger is based on the total ID nsum being above the ID prescaled trigger threshold, but it only issues a global acquisition trigger to the ID LBL electronics cards for a fraction of each second.
- 5 inch trigger
The 5 inch trigger is based on the total 5 inch nsum being above the 5 inch trigger threshold. It issues a global acquisition trigger to the ID LBL electronics cards (note the 5 inch tubes FBE card is in crate 1).
- OD to ID trigger
The OD to ID trigger is based on there being any OD nsum trigger. It issues a global acquisition command to the ID LBL electronics cards.
- OD top, upper side, lower side and bottom singles trigger
Those triggers are based on the total nsum from the OD tubes in each section being above

each singles trigger threshold. They issue a global acquisition trigger to the OD LBL electronics cards.

- ID to OD trigger
The ID to OD trigger is based on there being any ID nsum trigger. It issues a global acquisition command to the OD LBL electronics cards.
- ID calibration forced trigger
The ID calibration forced trigger is based on a trigger input from any triggered calibration device (PLED 1, laser-us 2, laser-jpn 3). It issues a forced acquisition trigger to the ID LBL electronics cards. The PMT signals must arrive around 40 nsec after the trigger command.
- ID calibration global trigger
The ID calibration global trigger is based on a trigger input from any triggered calibration device (PLED 1, laser-us 2, laser-jpn 3). It issues a global acquisition trigger to the ID LBL electronics cards. The PMT signals must arrive around 300 nsec before the trigger command.
- OD calibration forced trigger
The OD calibration forced trigger is based on a trigger input from any triggered calibration device (OD-LED 6). It issues a forced acquisition trigger to the OD LBL electronics cards. The PMT signal must arrive around 40 nsec after the trigger command.
- OD calibration global trigger
The OD calibration global trigger is based on a trigger input from any triggered calibration device (OD-LED 6). It issues a global acquisition trigger to the OD LBL electronics cards. The PMT signals must arrive around 300 nsec before the trigger command.
- Delayed calibration trigger
The delayed calibration trigger is based on a trigger input from any triggered calibration device (PLED 1, laser-us 2, laser-jpn 3, OD-LED 6). delayed by 375 nsec. It does not issue an external trigger. This is used to calculate the occupancy of the calibration device.
- MACRO singles trigger
The MACRO singles trigger is based on the total ID nsum being above the ID singles threshold, this is prescaled to every nth event and issues a short stop to the MACRO electronics 40 μ sec after the trigger condition is met.
- MACRO coincidence trigger
The MACRO coincidence trigger is based on a prompt event with a total ID nsum between 200 and 1050, and a delayed event with a total ID nsum between 340 and 540 within 300 nsec to 500 μ sec. This issues a long stop to the MACRO electronics 200 μ sec after the trigger condition is met.
- MACRO random trigger
The MACRO random trigger is issued every 32 seconds and issues a short stop to the MACRO electronics.

- **MACRO muon trigger**
The MACRO muon trigger is based on the total ID nsum being above 1304 and issues a short stop to the MACRO electronics 130 μ sec after the trigger condition is met.
- **MACRO calibration trigger**
The MACRO calibration trigger is based on a trigger input from any triggered calibration device (PLED 1, laser-us 2, laser-jpn 3). It issues a short stop to the MACRO 20 μ sec after every nth signal the trigger receives from the calibration device.
- **1pps trigger**
The 1pps trigger is based on the GPS 1pps input signal. It does not issue an external trigger.
- **1pps global acquisition trigger**
The 1pps trigger is based on the GPS 1pps input signal. It issues a global acquisition trigger to the ID and OD LBL electronics.
- **GPS trigger**
The GPS trigger is issued at the start of the run and every 32 seconds thereafter. It issues an interrupt to the GPS VME module to capture the time. This trigger can not be disabled.
- **ID history trigger**
The ID history trigger is based on the total ID nsum being above the ID history trigger threshold and is issued every 25 nsec while above threshold up to a maximum of 200 nsec. It does not issue any external triggers.
- **OD top, upper side, lower side and bottom history trigger**
Those triggers are based on the total nsum being above each history threshold and are issued every 25 nsec while above threshold up to a maximum of 200 nsec. They do not issue an external trigger.
- **MACRO to ID trigger**
The MACRO to ID trigger is based on there being any MACRO singles trigger. It issues a global acquisition command to the ID LBL electronics cards. This trigger comes 40 μ sec before the MACRO singles trigger.
- **Supernova trigger**
The supernova trigger is based on there being 8 events with total ID nsum above 772 (board3 version < 12; \sim run 3380) or 1100 (board3 version = 12; run 3381 \sim) in 0.8388608 seconds. There is a 1ms veto around events with total ID nsum above 1250. This sends an interrupt to the DAQ, notifying the shift person so data acquisition is not stopped. It also puts the trigger into a predefined data acquisition state for 1 minute.
- **Disable trigger**
When the trigger buffer is almost full the last trigger issued is a disable trigger until the buffer can be emptied.

- Enable trigger
After a disable trigger when the buffer is empty and other triggers are re-enabled the first trigger issued is an enable trigger.
- Run condition change trigger
When the run condition changes, this trigger is issued to record the timestamp and the run condition.

Table A.1: Trigger types as recorded by the trigger - part I -

trigger-type (HEX)	Function (* Can not occur at the same time)
000:000:001	ID singles trigger
000:000:002	ID history trigger
000:000:004	5 inch trigger
000:000:008	1pps trigger
000:000:010	Acquire trigger: forced acquisition A *
000:000:020	Acquire trigger: forced acquisition B *
000:000:030	Acquire trigger: clock acquisition A *
000:000:040	Acquire trigger: clock acquisition B *
000:000:050	Acquire trigger: test pulser acquisition A *
000:000:060	Acquire trigger: test pulser acquisition B *
000:000:070	Acquire trigger: pedestal acquisition A *
000:000:080	Acquire trigger: pedestal acquisition B *
000:000:090	Acquire trigger: test pulser followed by forced acquisition A *
000:000:0a0	Acquire trigger: test pulser followed by forced acquisition B *
000:000:0b0	Acquire trigger: test pulser no acquisition *
000:000:100	ID prescale trigger
000:000:200	GPS trigger
000:000:400	Delayed calibration trigger
000:000:800	Supernova trigger

Table A.2: Trigger types as recorded by the trigger - part II -

trigger-type (HEX)	Function (# Can not occur at the same time, ** board3 version = 12 only)
000:001:000	ID calibration forced trigger: source 1 #
000:002:000	ID calibration forced trigger: source 2 #
000:003:000	ID calibration forced trigger: source 3 #
000:004:000	ID calibration forced trigger: source 4 #
000:005:000	ID calibration forced trigger: source 5 #
000:006:000	OD calibration forced trigger: source 1 #
000:007:000	OD calibration forced trigger: source 2 #
000:009:000	ID calibration global trigger: source 1 #
000:00a:000	ID calibration global trigger: source 2 #
000:00b:000	ID calibration global trigger: source 3 #
000:00c:000	ID calibration global trigger: source 4 #
000:00d:000	ID calibration global trigger: source 5 #
000:00e:000	OD calibration global trigger: source 1 #
000:00f:000	OD calibration global trigger: source 2 #
000:010:000	Macro singles trigger
000:020:000	Macro coincidence trigger
000:040:000	Macro random trigger
000:080:000	Macro muon trigger
000:100:000	OD top singles trigger
000:200:000	OD upper side singles trigger
000:400:000	OD lower side singles trigger
000:800:000	OD bottom singles trigger
001:000:000	ID delayed trigger
002:000:000	ID prompt trigger
004:000:000	OD to ID trigger
008:000:000	ID to OD trigger
010:000:000	OD top history trigger
020:000:000	OD upper side history trigger
040:000:000	OD lower side history trigger
080:000:000	OD bottom history trigger
400:000:000	Disable trigger
800:000:000	Enable trigger
1000:000:000**	Macro calibration trigger
2000:000:000**	Macro to ID trigger
4000:000:000**	Run condition change trigger
8000:000:000**	1pps global acquisition trigger

Appendix B

Decay chain of ^{238}U and ^{232}Th

B.1 ^{238}U

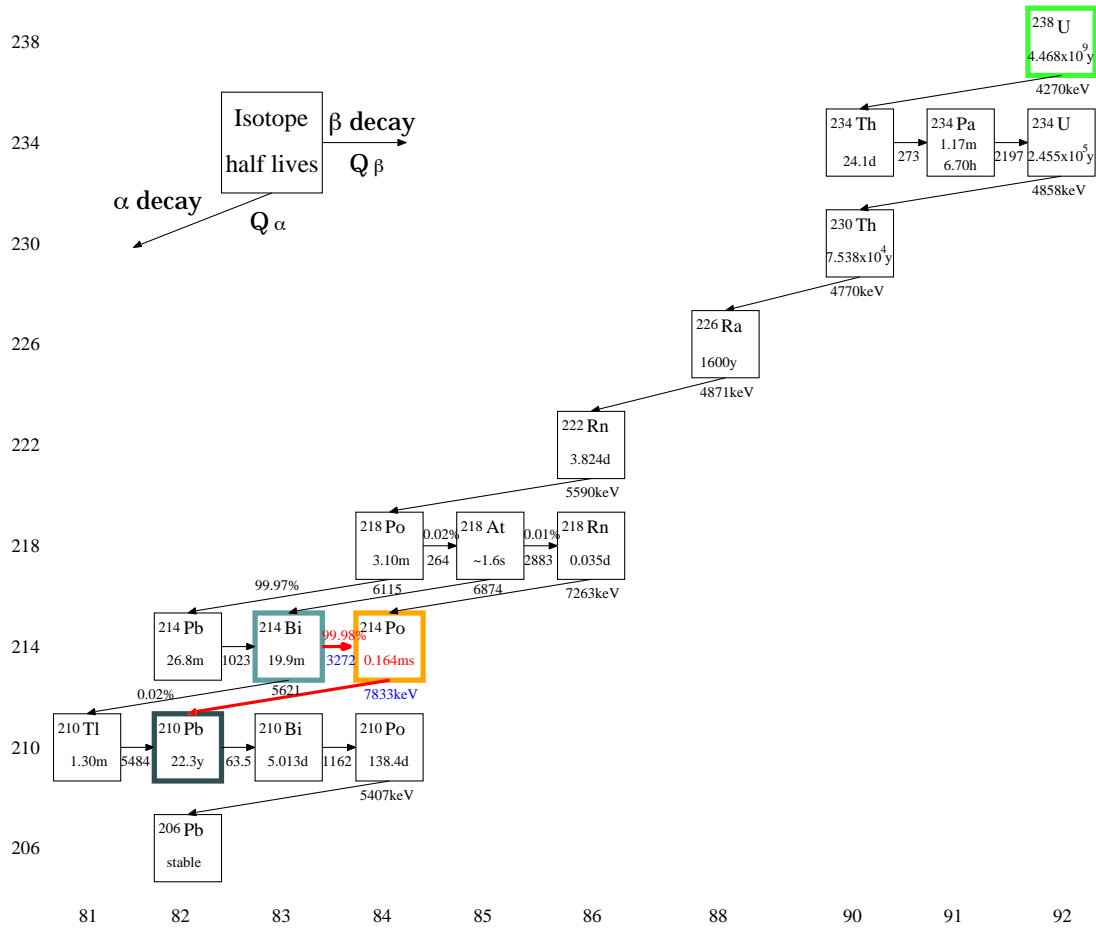
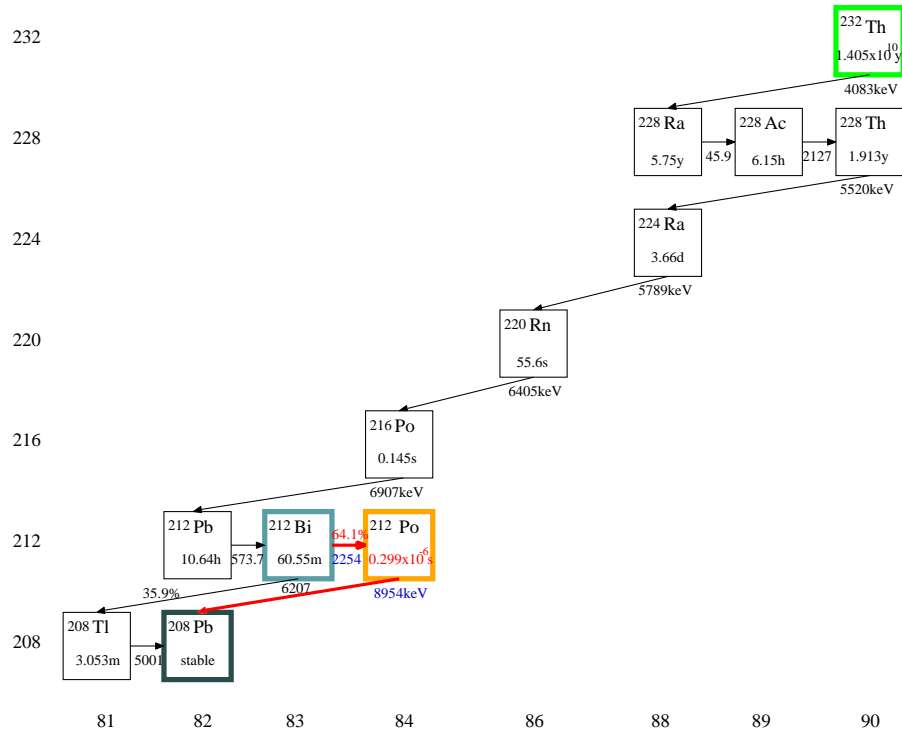


Figure B.1: Decay chain of ^{238}U .

B.2 ^{232}Th Figure B.2: Decay chain of ^{232}Th .

Appendix C

Nuclear Level Diagrams

C.1 ^{203}Hg

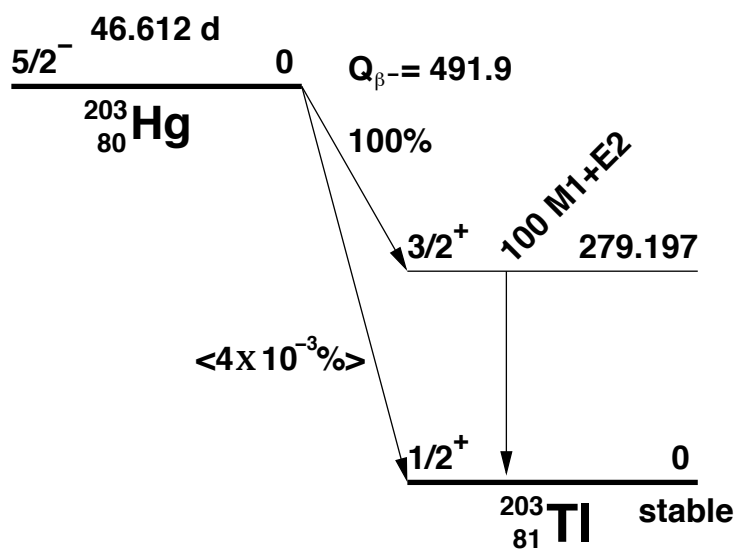
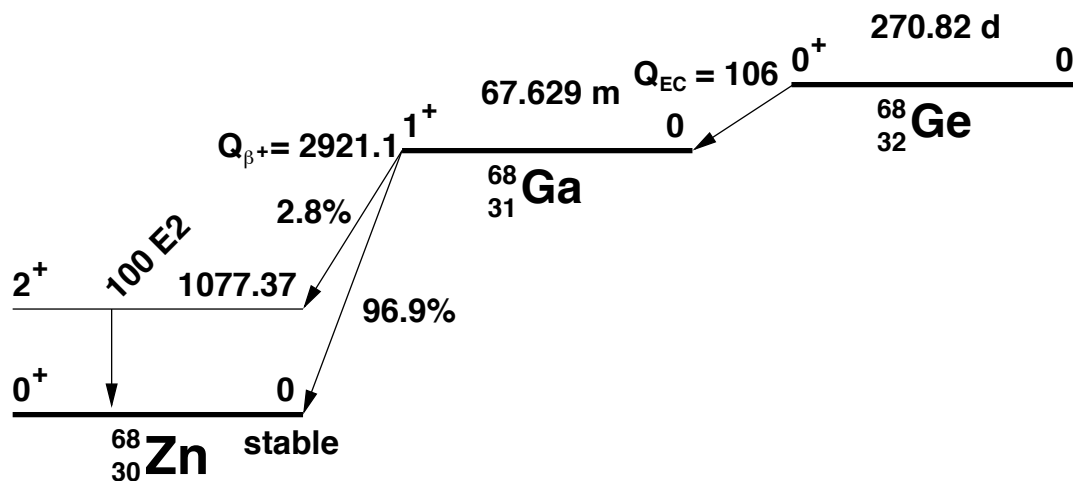
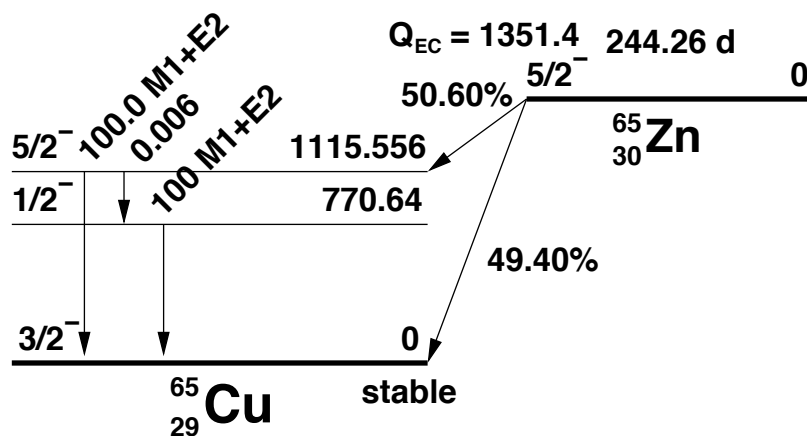
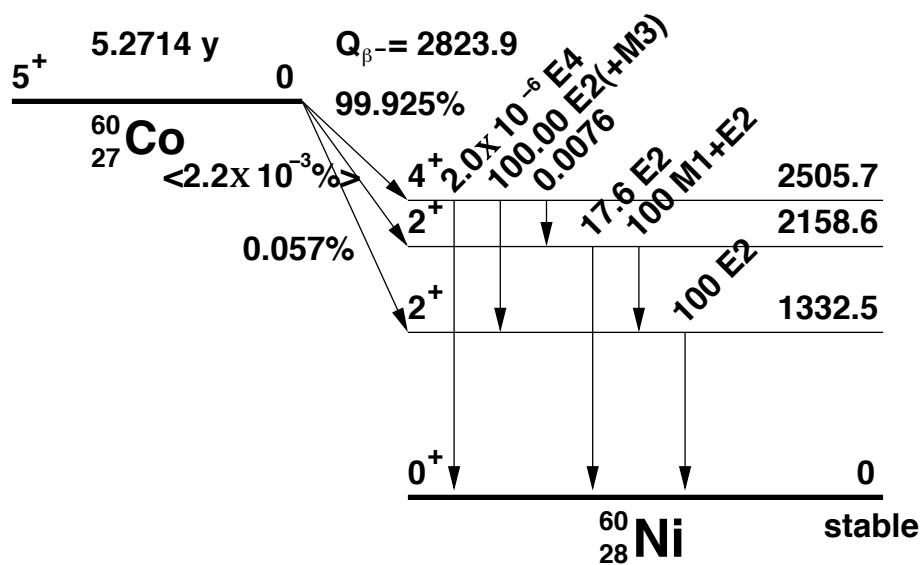


Figure C.1: Level diagram for ^{203}Hg .

C.2 ^{68}Ge Figure C.2: Level diagram for ^{68}Ge .C.3 ^{65}Zn Figure C.3: Level diagram for ^{65}Zn .

C.4 ^{60}Co Figure C.4: Level diagram for ^{60}Co .

Appendix D

Am-Be source

The Am-Be source is commonly used for the calibration with neutrons. The ${}^9\text{Be}(\alpha, n){}^{12}\text{C}$ reaction ($Q = 5.7$ MeV) gives the high neutron yield with radioactive α -emitter, ${}^{241}\text{Am}$ ($\tau_{1/2} = 458$ year). In the KamLAND, the Am-Be source was mainly used for the calibration of neutron diffusion in order to verify the MC result. Another purpose of Am-Be calibration was the energy reconstruction for higher energy range with various γ -rays, so the Am-Be source was packed in the polyethylene moderator to stop the recoil neutrons (Figure D.1). The moderator size were changed for each calibration (Table D.1).

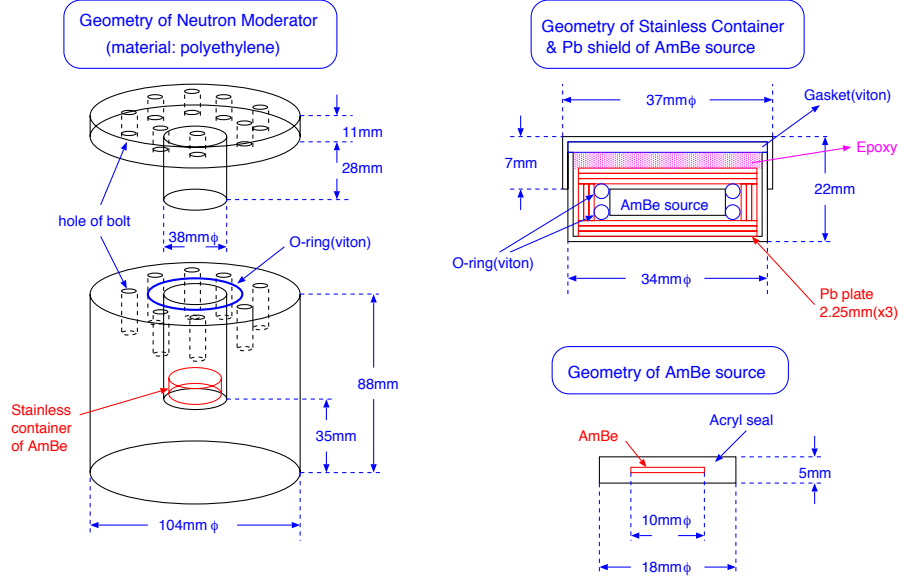
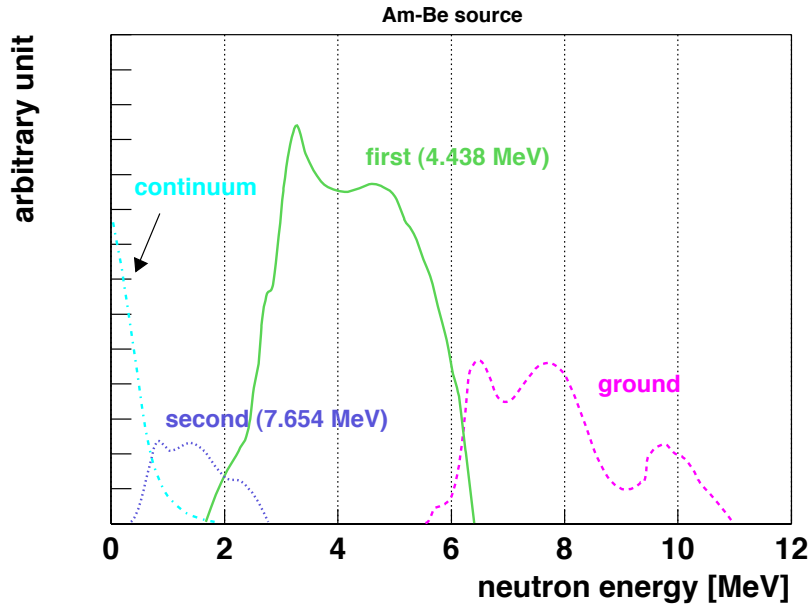


Figure D.1: Geometry of Am-Be source moderator.

Table D.1: Moderator size of Am-Be source in each calibration.

moderator type	date	diameter (mm)	height (mm)
moderator 1	September 2002	104	99
moderator 2	August 2003	76	76
no moderator	April 2004	-	-

The neutron spectrum of a ^{241}Am - ^9Be source have been calculated by using the data on angular distributions [107]. The neutron energy from the first excited state is $2 \sim 6$ MeV, and from the grand state is $6 \sim 11$ MeV. The neutron energies contribute to the energy spectrum of the Am-Be source calibration in the KamLAND. The single γ -rays spectrum from the first excited state are distorted by the neutron energy (Figure D.3). In the low energy, the high energy neutrons from the grand state are observed. There are no gamma-ray peaks from the second and third excited states, 7.654 MeV and 9.641 MeV (Figure D.4), as expected from the small branching ratio to γ -ray emission (Table D.2).

Figure D.2: Primary neutron spectrum of a ^{241}Am - ^9Be source, calculated by [107].

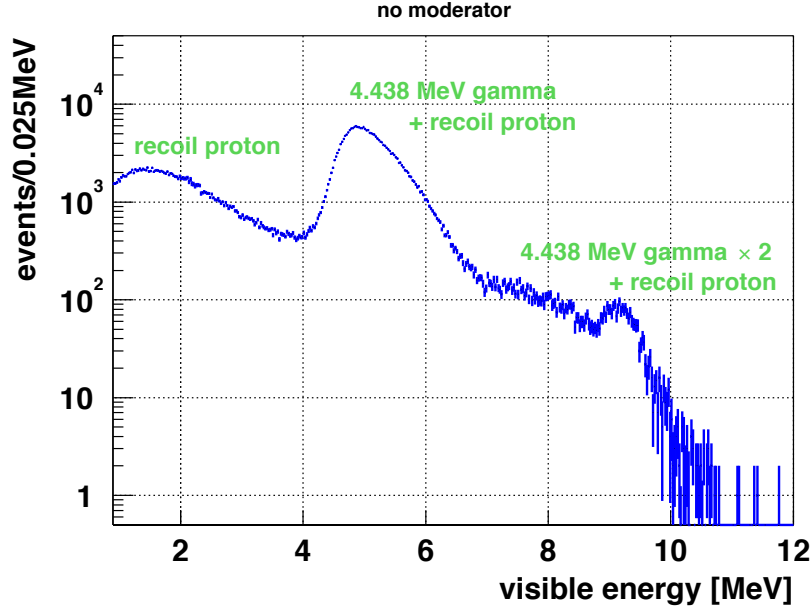
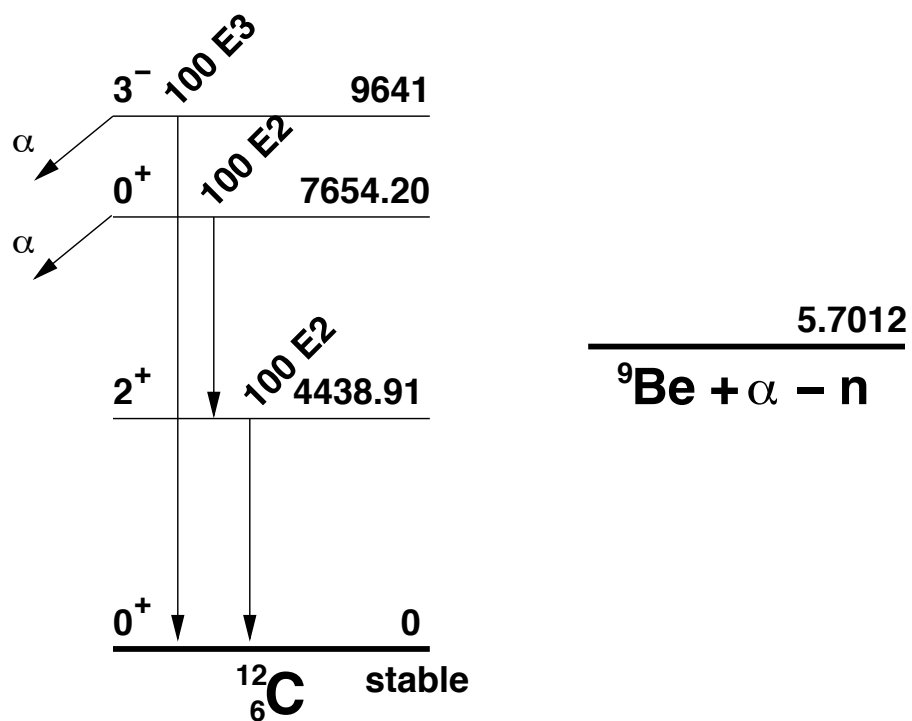


Figure D.3: Prompt energy spectrum of Am-Be source (no moderator) in the visible energy scale after the subtraction of the accidental backgrounds, estimated from the offtime-window. The recoil proton contributes for the spectrum. The peak at ~ 2 MeV are made by the high energy neutrons for the grand state. The single γ -rays from the first excited state 4.438 MeV make the ~ 5 MeV peak, which distorted by the neutrons. Those neutrons can excite ^{12}C and produce the peak at ~ 9 MeV, and when the residual energies of neutrons are ignored, the 4.438 MeV multi-gamma energy is consistent with its peak within 0.6%.

Table D.2: Branchings of decays [108]

level	widths
4.44 MeV	$\Gamma_\gamma = 10.8 \pm 0.6 \text{ meV}$
7.65 MeV	$\Gamma_\pi/\Gamma = (6.8 \pm 0.7) \times 10^{-6}$ $\Gamma_\pi = (60.5 \pm 3.9) \mu\text{eV}$ $\Gamma_{\text{rad}}/\Gamma = (4.13 \pm 0.11) \times 10^{-4}$ $\Gamma = 8.3 \pm 1.0 \text{ eV}$ $\Gamma_{\text{rad}} = 3.7 \pm 0.5 \text{ meV}$
9.64 MeV	$\Gamma_{\text{rad}}/\Gamma \leq 4.1 \times 10^{-7}$ $\Gamma_{\text{rad}} < 14 \text{ meV}$ $\Gamma_{\gamma_0} = (3.1 \pm 0.4) \times 10^{-4} \text{ eV}$

$$\Gamma_{\text{rad}} \equiv \Gamma_\gamma + \Gamma_\pi$$

Figure D.4: Level diagram for ^{12}C and $^9\text{Be} + \alpha - n$.

Appendix E

Analytical calculation of neutrino propagation

The electron neutrino survival probability is the fundamental quantity to calculate in solar neutrino analysis. In the context of three generation neutrino, the survival probability is given by

$$P_{ee}^{3\nu} = \cos^4 \theta_{13} P_{e'e'}^{2\nu} + \sin^4 \theta_{13}$$

where $P_{e'e'}^{2\nu}$ is obtained with the modified electron density $N_{e'} \rightarrow N_e \cos^2 \theta_{13}$. The neutrino propagation in the sun and earth can be calculated by the analytical procedure. For the propagation in the sun, a very accurate and widely used analytical approximation to $P_{ee}^{2\nu}$ is the so-called “Parke’s formula” [109]. For the propagation in the earth, a simple and accurate method for computing the regeneration probability is convenient using the electron density parameterization [110] of the preliminary earth reference model (PREM) [111].

matter effect in the sun

To simplify the problem, only two flavor are considered. In that case, the independent parameter is only one in the MNS matrix. At an electron density, the matter mass eigenstates are

$$|\nu_{1M}\rangle = \cos \theta_M |\nu_e\rangle - \sin \theta_M |\nu_\mu\rangle \quad (\text{E.1})$$

$$|\nu_{2M}\rangle = \sin \theta_M |\nu_e\rangle + \cos \theta_M |\nu_\mu\rangle \quad (\text{E.2})$$

which have eigenvalues $\pm \Delta_M/2$, where

$$\Delta_M = [(\Delta_V \cos 2\theta_V - \sqrt{2}G_F N_e)^2 + \Delta_V^2 \sin^2 2\theta_V]^{1/2} \quad (\text{E.3})$$

and θ_M satisfies

$$\Delta_M \sin 2\theta_M = \Delta_V \sin 2\theta_V \quad (\text{E.4})$$

where $\Delta_V = (m_2^2 - m_1^2)/2E$, $m_{1,2}$ are the neutrino masses, θ_V is the vacuum mixing angle, N_e is number density of electrons, and G_F is the Fermi constant. At resonance, $\Delta_V \cos 2\theta_V =$

$\sqrt{2}G_F N_e$, where the matter mixing angle is $\theta_M = \pi/4$ and the resonant oscillation length is $L_R = L_V/\sin 2\theta_V$, which for small vacuum mixing angle can be many times the vacuum oscillation length. For the situation of current interest, the electron neutrinos are produced above resonance, pass through resonance, and are detected in the vacuum. If the electron density varies slowly, the states which evolve independently in time (the adiabatic states) are

$$e^{-i\frac{1}{2}\int^t \Delta_M dt} |\nu_{1M}(t)\rangle \quad (\text{E.5})$$

$$e^{+i\frac{1}{2}\int^t \Delta_M dt} |\nu_{2M}(t)\rangle. \quad (\text{E.6})$$

It is convenient to use these states, as the basis states, in the region for which there are no transitions (away from the resonance region). As a neutrino goes through resonance these adiabatic states may be mixed, but on the other side of resonance, the neutrino state can still be written as a linear combination of these states. That is, a basis state produced at time t , going through resonance at time t_r , and detected at time t' is described by

$$e^{-i\frac{1}{2}\int_{t_r}^t \Delta_M dt} |\nu_{1M}(t)\rangle \rightarrow \alpha e^{-i\frac{1}{2}\int_{t_r}^{t'} \Delta_M dt} |\nu_{1M}(t')\rangle + \beta e^{+i\frac{1}{2}\int_{t_r}^{t'} \Delta_M dt} |\nu_{2M}(t')\rangle \quad (\text{E.7})$$

$$e^{+i\frac{1}{2}\int_{t_r}^t \Delta_M dt} |\nu_{2M}(t)\rangle \rightarrow -\beta^* e^{-i\frac{1}{2}\int_{t_r}^{t'} \Delta_M dt} |\nu_{1M}(t')\rangle + \alpha^* e^{+i\frac{1}{2}\int_{t_r}^{t'} \Delta_M dt} |\nu_{2M}(t')\rangle \quad (\text{E.8})$$

where α and β are complex number, $|\alpha|^2 + |\beta|^2 = 1$, those parameters give characteristics of the transitions at resonance and are not related to the production and detection of the neutrino state. Hence the amplitude after passage through resonance is

$$A(t) e^{-i\frac{1}{2}\int_{t_r}^{t'} \Delta_M dt} + B(t) e^{+i\frac{1}{2}\int_{t_r}^{t'} \Delta_M dt} \quad (\text{E.9})$$

where

$$A(t) = \cos \theta_V [\alpha \cos \theta_M e^{+i\frac{1}{2}\int_{t_r}^t \Delta_M dt} - \beta^* \sin \theta_M e^{-i\frac{1}{2}\int_{t_r}^t \Delta_M dt}] \quad (\text{E.10})$$

$$B(t) = \sin \theta_V [\beta \cos \theta_M e^{+i\frac{1}{2}\int_{t_r}^t \Delta_M dt} + \alpha^* \sin \theta_M e^{-i\frac{1}{2}\int_{t_r}^t \Delta_M dt}] \quad (\text{E.11})$$

The probability of detecting this neutrino as an electron neutrino is given by

$$P_{\nu_e}(t, t') = |A(t)|^2 + |B(t)|^2 + 2|A(t)B(t)| \cos\left(\int_{t_r}^{t'} \Delta_M dt + \Omega\right) \quad (\text{E.12})$$

with $\Omega = \arg(A^*B)$. Thus, after averaging over the detection position and production position, the survival probability of electron neutrino is given by ‘‘Parke’s formula’’,

$$P(\nu_e \rightarrow \nu_e) = \frac{1}{2} + \left(\frac{1}{2} - P_x\right) \cos 2\theta_M \cos 2\theta_V \quad (\text{E.13})$$

where $P_x = |\beta|^2$, the probability of transition from $|\nu_{1M}\rangle$ to $|\nu_{2M}\rangle$ during resonance crossing. P_x can be solved when the density of electrons varies linearly in the transition region,

$$P_x = \exp \left[-\frac{\pi}{2} \frac{\sin^2 2\theta_V}{\cos 2\theta_V} \frac{\Delta_V}{|(1/N_e)dN_e/dt|_{t_r}} \right] \quad (\text{E.14})$$

Assuming the electron neutrino transitions in matter with exponentially varying density,

$$N_e(x) = N_e(0) e^{-x/r_0} \quad (\text{E.15})$$

P_x is approximated by

$$P_x = \frac{e^{\gamma \cos^2 \theta} - 1}{e^\gamma - 1} \quad (\text{E.16})$$

$$\gamma = 2\pi r_0 \Delta_V \quad (\text{E.17})$$

where $r_0 = R_\odot/10.54$ [112] is derived from a best fit to the SSM profile.

matter effect in the earth

It is essential for the analytical calculation of the earth regeneration effect to parameterize the earth density. This preliminary model elaborated in 1981 still represents the standard framework for the interpretation of seismological data, as far as possible shell aspheric form are neglected. The earth matter density profile $\rho(r)$ is given in Table E.1 of [111].

Table E.1: Coefficients of the electron density parameterization $N_j(r) = \alpha_j + \beta_j r^2 + \gamma_j r^4$ (mol/cm³), for the j -th shell range $[r_{j-1}, r_j]$. The radial distance r is normalized to the earth radius.

j	Shell	$[r_{j-1}, r_j]$	α_j	β_j	γ_j
1	Inner core	$[0, 0.192]$	6.099	-4.119	0.000
2	Outer core	$[0.192, 0.546]$	5.803	-3.653	-1.086
3	Lower mantle	$[0.546, 0.895]$	3.156	-1.459	0.280
4	Transition zone	$[0.895, 0.937]$	-5.376	19.210	-12.520
5	Upper mantle	$[0.937, 1]$	11.540	-20.280	10.410

For each shell j , the density in a polynomial expression is

$$N_j(r) = \alpha_j + \beta_j r^2 + \gamma_j r^4. \quad (\text{E.18})$$

For nonradial neutrino trajectories,

$$N_j(x) = \alpha'_j + \beta'_j x^2 + \gamma'_j x^4. \quad (\text{E.19})$$

where

$$\alpha'_j = \alpha_j + \beta_j \sin^2 \eta + \gamma_j \sin^4 \eta \quad (\text{E.20})$$

$$\beta'_j = \beta_j + 2\gamma_j \sin^2 \eta \quad (\text{E.21})$$

$$\gamma'_j = \gamma_j \quad (\text{E.22})$$

with the trajectory coordinate x and the nadir angle η defined as in Figure . For later purposes, it is useful to split the density as

$$N_j(x) = \overline{N}_j + \delta N_j(x) \quad (\text{E.23})$$

where \overline{N}_j is the average density along the shell code,

$$\overline{N}_j = \frac{\int_{x_{j-1}}^{x_j} dx N_j(x)}{x_j - x_{j-1}} \quad (\text{E.24})$$

and $\delta N_j(x)$ is the residual density variation.

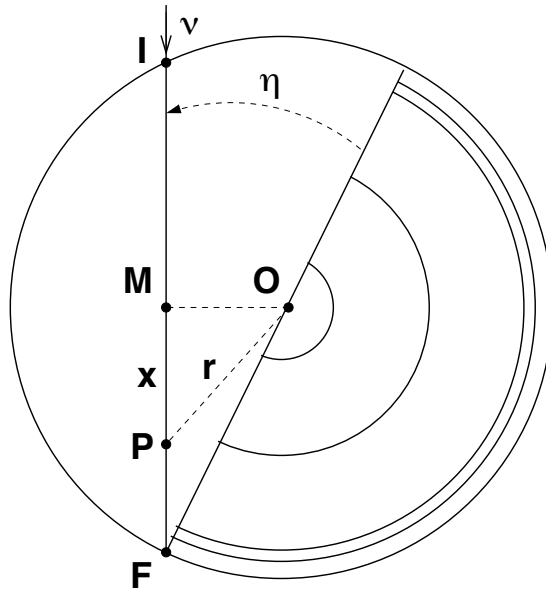


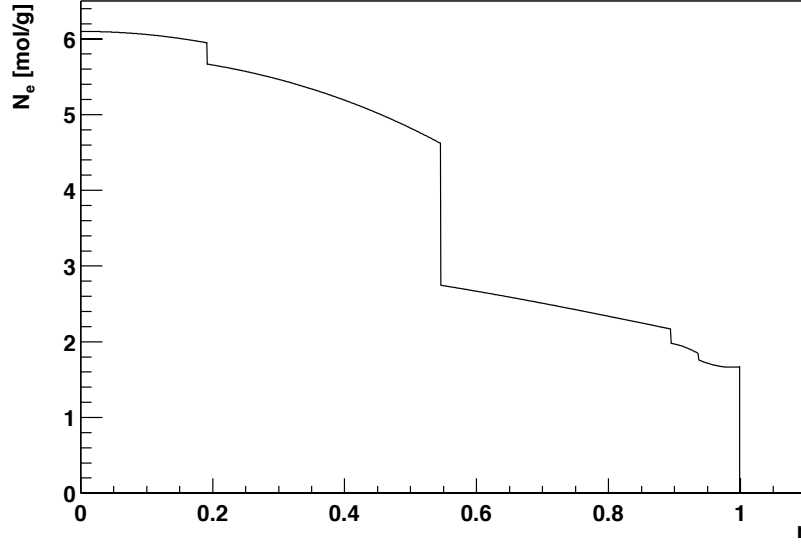
Figure E.1: Section of the earth showing the relevant shell. The geometric definitions used in the text are $I = \nu$ entry point, $F = \nu$ end point (detector), $M =$ trajectory midpoint, $P =$ generic ν position, $x = MP =$ trajectory coordinate, $r = OP =$ radial distance and $\eta =$ nadir angle.

The probability $P_E(\nu_2 \rightarrow \nu_e)$ can be expressed as

$$P_E = |U_{ee} \sin \theta + U_{e\mu} \cos \theta|^2 \quad (\text{E.25})$$

where U is the neutrino evolution operator in the (ν_e, ν_μ) flavor basis. The Hamiltonian $H_j(x)$ along the j -th shell chord traversed by the neutrino is given by

$$H_j(x) = \frac{1}{2} \begin{pmatrix} \sqrt{2}G_F N_j(x) - \Delta_V \cos 2\theta_V & \Delta_V \sin 2\theta_V \\ \Delta_V \sin 2\theta_V & \Delta_V \cos 2\theta_V - \sqrt{2}G_F N_j(x) \end{pmatrix}, \quad (\text{E.26})$$

Figure E.2: Electron density profile $N(r)$ from the parameterization in Table E.1.

and the Hamiltonian can be separated into a constant matrix plus a perturbation

$$H_j(x) = \overline{H}_j + \delta H_j(x) \quad (\text{E.27})$$

where $\overline{H}_j = H_j|_{N \rightarrow \overline{N}}$, and $\delta H_j(x) = G_F/\sqrt{2} \text{diag}[\delta N_j(x) - \delta N_j(x)]$. At the first perturbative order, the evolution operator U_j is given by

$$U_j(x_j, x_{j-1}) = e^{-i\overline{H}_j(x_j - x_{j-1})} - i \int_{x_{j-1}}^{x_j} dx e^{-i\overline{H}_j(x_j - x)} \delta H_j(x) e^{-i\overline{H}_j(x - x_{j-1})} + O(\delta H_j^2) \quad (\text{E.28})$$

$$= \begin{pmatrix} c_j + i s_j \cos 2\overline{\theta}_M & -i s_j \sin 2\overline{\theta}_M \\ -i s_j \sin 2\overline{\theta}_M & c_j - i s_j \cos 2\overline{\theta}_M \end{pmatrix} - \frac{i}{2} \sin 2\overline{\theta}_M \begin{pmatrix} C_j \sin 2\overline{\theta}_M & C_j \cos 2\overline{\theta}_M - i S_j \\ \cos 2\overline{\theta}_M + i S_j & -C_j \sin 2\overline{\theta}_M \end{pmatrix} + O(\delta H_j^2) \quad (\text{E.29})$$

where $\overline{\theta}_M$ is the average mixing angle in matter, defined in Eq. (E.4), and

$$c_j = \cos[\overline{\Delta}_M(x_j - x_{j-1})/2] \quad (\text{E.30})$$

$$s_j = \sin[\overline{\Delta}_M(x_j - x_{j-1})/2] \quad (\text{E.31})$$

$$C_j = \sqrt{2} G_F \int_{x_{j-1}}^{x_j} dx \delta N_j(x) \cos[\overline{\Delta}_M(x - \overline{x})] \quad (\text{E.32})$$

$$S_j = \sqrt{2} G_F \int_{x_{j-1}}^{x_j} dx \delta N_j(x) \sin[\overline{\Delta}_M(x - \overline{x})] \quad (\text{E.33})$$

with $\overline{\Delta}_M = \overline{\Delta}_V \sin 2\theta_V / \sin 2\theta_M$ and $\overline{x} = (x_j + x_{j-1})/2$.

The evolution operator along the total neutrino path \overline{IF} is given by the ordered product of partial evolution operators, $U(x_F, x_I) = \prod_j U(x_j, x_{j-1})$. As the electron density with respect to the trajectory midpoint M is symmetric, the evolution operator can be expressed as

$$U(x_F, x_I) \equiv U(x_F, 0) \cdot U(0, -x_F) = U(x_F, 0) \cdot U^T(-x_F, 0), \quad (\text{E.34})$$

which needs only to calculate from $x_M (= 0)$ to $x_F (= x_I)$.

Appendix F

Supernova Neutrino Emission

The supernova is a phenomenon which the star breaks into the shining brightly and its starlight becomes extinct after a few years. That phenomenon is considered as the explosion in the final stage of the stellar evolution, so called 'supernova explosion'. The supernovae have been broadly categorized into two classes, Type I and Type II according to the absence or presence of the hydrogen line in their spectra. Additionally, Type I supernovae can be further divided into subclasses, Type Ia supernovae have a strong silicon spectral line, and Type Ib supernovae have neither hydrogen nor silicon, but helium lines are present, while Type Ic supernovae have none of hydrogen, silicon and helium lines.

In order to understand the mechanism of supernovae, the process of stellar evolution is very important. The progenitor stars spend the majority of their active existence on the main sequence, fusing hydrogen into helium. The star maintain a stable balance of the pressure from the hydrogen burning and the force of gravity. When the hydrogen in the dense core is depleted, the core begins to collapse under gravity. Consequently, the temperature and pressure of the core increase, and the helium ignites. Once the helium ignites, the pressure becomes high and the star expand. The temperature in the outer envelope has gone down, and the star becomes the 'red giant star'. At this stage, for the case of the light star which contains less than approximately $8M_{\odot}$, the outer envelope is pushed away from the core, and the remaining core is called a 'white dwarf', which is supported against gravity by electron degeneracy. However, for the case of the heavy star which contains more than approximately $8M_{\odot}$, the fusion of helium is followed by the C and O, moreover, Si, Mg, S, and eventually the most stable element Fe will be produced. The Type II supernova is the explosion of the red giant star, which has the enough mass ($> 8M_{\odot}$) to experience stable burning stages until the O + Ne + Mg core or the Fe core is formed. On the other hand, the Type Ia supernova can occur when the carbon in the light star ($< 8M_{\odot}$) ignites in a thermonuclear explosion. Type II, Ib and Ic are believed to be produced by core-collapse.

In the core-collapse supernova, zillions of neutrinos are emitted during a supernova explosion.

The main neutrino interactions in the supernova core are as follows,

$$p + e^- \longleftrightarrow n + \nu_e \quad (\text{F.1})$$

$$n + e^+ \longleftrightarrow p + \bar{\nu}_e \quad (\text{F.2})$$

$$A + e^- \longleftrightarrow A' + \nu_e \quad (\text{F.3})$$

$$e^- + e^+ \longleftrightarrow \nu + \bar{\nu} \quad (\text{F.4})$$

$$\gamma^* \longleftrightarrow \nu + \bar{\nu} \quad (\text{F.5})$$

$$N + N' \longleftrightarrow N + N' + \nu + \bar{\nu} \quad (\text{F.6})$$

$$N + n \longleftrightarrow N + p + l^- + \bar{\nu}_l \quad (\text{F.7})$$

$$N + p + l^- \longleftrightarrow N + n + \nu_l \quad (\text{F.8})$$

$$\nu + N \longleftrightarrow \nu + N \quad (\text{F.9})$$

$$\nu + A \longleftrightarrow \nu + A \quad (\text{F.10})$$

$$\nu + l \longleftrightarrow \nu + l \quad (\text{F.11})$$

where ν indicates all species of neutrinos, A is a heavy nucleus, N is a nucleon (proton or neutron), l is either an electron or a muon (small contribution because the energy available in the system is approximately less than 100 MeV), and γ^* is a plasmon. Figure F.1 shows the neutrino energy spectra for each flavor from the numerical calculation [113], and Figure F.2 shows neutrino processes in each stage of the collapse-driven supernova explosion. The important process for the production of large neutrinos is that the shock wave propagates into the outer core with dissociating nuclei into free nucleons, and neutrinos or anti-neutrinos are produced via the e^- or e^+ capture reaction, or their annihilation reaction. The ν_x and $\bar{\nu}_x$ are emitted from deeper and hotter layer of the supernova, so the mean energy of these neutrinos become higher than that of the ν_e and $\bar{\nu}_e$. The main opacity sources after nuclear dissociation are absorption on free nucleons (Eq. (F.1) and Eq. (F.2)) or scattering off free nucleons (Eq. (F.9)).

The observation of neutrinos burst from the supernova provides knowledge about the temperature of the burst, the time evolution of the star just after the collapse, and the neutrino properties, not only mass, magnetic moment, life time and some other non-standard interactions, but also the neutrino flavor mixing. Actually, neutrino signals observed at the Kamiokande II and IMB from a $20M_\odot$ Type II supernova in the Large Magellanic Cloud, gave many physical hints on the neutrino properties. If the galactic core-collapse supernova occurs, the high statistic observation is possible in the large Super-Kamiokande detector. The rate of the core-collapse supernova in the galaxy is evaluated to be 3 ± 1 / century [114]. The naked-eye supernovae are not visible beyond several kpc due to interstellar dust, however neutrino detectors are sensitive to supernovae throughout the entire galaxy.

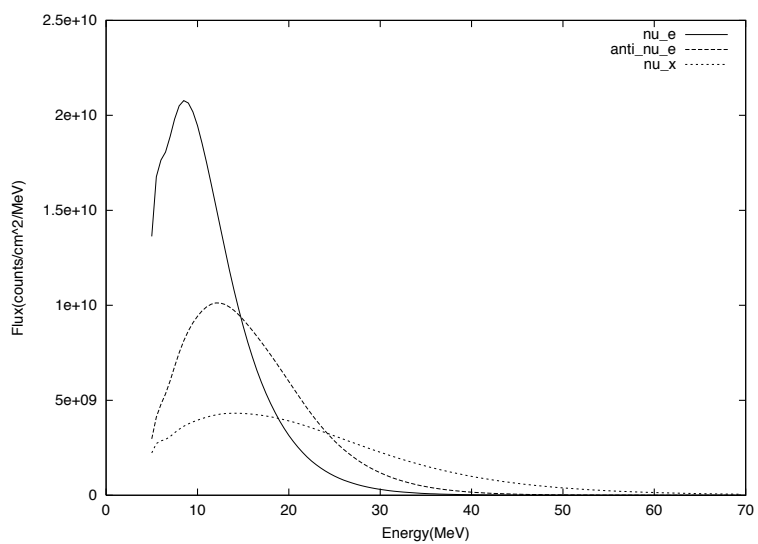


Figure F.1: Energy spectra of ν_e , $\bar{\nu}_e$ and ν_x of the numerical supernova model, which is given by [113]. The solid, dashed and dotted lines are the spectrum of ν_e , $\bar{\nu}_e$ and ν_x , respectively.

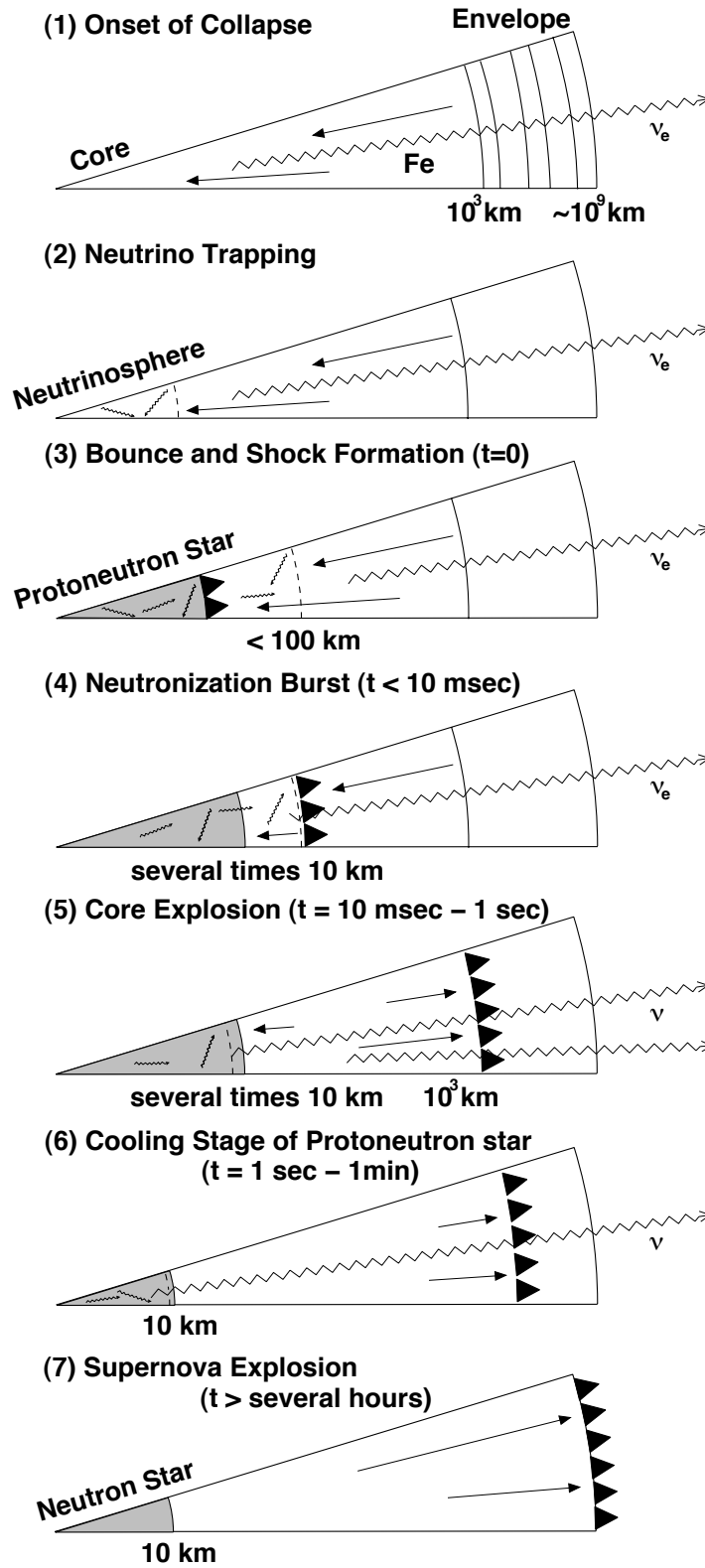


Figure F.2: Schematic view of neutrino processes in each stage of the collapse-driven supernova explosion.

Bibliography

- [1] W. Pauli. Letter to L. Meitner and her colleagues (letter open to the participants of the conference in Tübingen) (1930).
- [2] F. Reines and C. L. Cowan, Jr., Phys. Rev. **92**, 830 (1953).
- [3] R. Davis, Jr., *et al.*, Phys. Rev. Lett. **20**, 1205 (1968).
- [4] Z. Maki, M. Nakagawa and S. Sakata, Prog. Theor. Phys. **28**, 870 (1962).
- [5] Q. R. Ahmad, *et al.*, Phys. Rev. Lett. **89**, 011301 (2002).
- [6] Y. Fukuda, *et al.*, Phys. Rev. Lett. **81**, 1562 (1998).
- [7] V. D. Barger *et al.*, Phys. Rev. Lett. **82**, 2640 (1999).
- [8] E. Lisi *et al.*, Phys. Rev. Lett. **85**, 1166 (2000).
- [9] K. Eguchi *et al.*, Phys. Rev. Lett. **90**, 021802 (2003).
- [10] G. Danby *et al.*, Phys. Rev. Lett. **9**, 36 (1962).
- [11] M. L. Perl *et al.*, Phys. Rev. Lett. **35**, 1489 (1975).
- [12] K. Kodama *et al.*, Phys. Lett. **B504**, 218 (2001).
- [13] T. D. Lee and C. N. Yang, Phys. Rev. **105**, 1671 (1957).
- [14] C. S. Wu, and E. Ambler, R. W. Hayward, D. D. Hoppes and R. P. Hudson, Phys. Rev. **105**, 1413 (1957).
- [15] R. Michael Barnett and Klaus S. Lackner, Howard E. Haber, Phys. Rev. Lett. **51**, 176 (1983).
- [16] The LEP collaborations, the LEP Electroweak Working Group and the SLD Heavy Flavour Group, hep-ex/0212036.
- [17] D. N. Spergel *et al.*, Astrophys. J. Supp. **148**, 175 (2003).
- [18] V. M. Lobashev *et al.*, Phys. Lett. **B460**, 227 (1999).

- [19] K. A. Assamagan *et al.*, Phys. Rev. **D53**, 6065 (1996).
- [20] R. Barate *et al.*, Eur. Phys. J. **C2**, 395 (1998).
- [21] M. Gell-Mann, P. Ramond, and R. Slansky, in Supergravity, Proceedings of the Workshop, Stony Brook, New York, 1979, edited by P. van Nieuwenhuizen and D. Freedman, 315 (North-Holland, Amsterdam, 1979).
- [22] T. Yanagida, in Proceedings of the Workshop on the Unified Theories and Baryon Number in the Universe, Tsukuba, Japan, 1979, edited by O. Sawada and A. Sugamoto, 95 (KEK Report No. 79-18, Tsukuba, 1979).
- [23] R. N. Mohapatra and G. Senjanovic, Phys. Rev. Lett. **44**, 912 (1980).
- [24] S. P. Mikheyev, A. Yu. Smirnov, Sov. J. Nucl. Phys. **42**, 913 (1985).
- [25] L. Wolfenstein, Phys. Rev. **D17**, 2369 (1978), **D20**, 2634 (1979).
- [26] J. N. Bahcall and M. H. Pinsonneault, Phys. Rev. Lett. **92**, 121301 (2004).
- [27] J. N. Bahcall and C. Pena-Garay, New Journal of Physics **6**, 63 (2004).
- [28] J. N. Bahcall, <http://www.neutrinooscillation.org>
- [29] B. T. Cleveland *et al.*, Astrophys. J. **496**, 505 (1998).
- [30] W. Hampel *et al.*, Phys. Lett. **B447**, 127 (1999).
- [31] E. Bellotti, The Gallium Neutrino Observatory (GNO), talk at VIIIth International Conference on Topics in Astroparticle and Underground Physics (TAUP03), Seattle, Sept. 5-9, (2003), GNO collaboration, M. Altmann *et al.*, GNO solar neutrino observations: results for GNO I, Phys. Lett. **B490**, 16 (2000).
- [32] V. Gavrin, Results from the Russian American gallium experiment (SAGE), talk at VIIIth International Conference on Topics in Astroparticle and Underground Physics (TAUP03), Seattle, Sept. 5-9, 2003, SAGE collaboration, J.N. Abdurashitov *et al.*, Measurement of the solar neutrino capture rate by the Russian-American gallium solar neutrino experiment during one half of the 22-year cycle of solar activity, J. Exp. Theor. Phys. **95**, 181 (2002), astro-ph/0204245.
- [33] Y. Fukuda *et al.*, Phys. Rev. Lett. **77**, 1683 (1996).
- [34] Y. Fukuda *et al.*, Phys. Lett. **B539**, 179 (2002).
- [35] S. N. Ahmed *et al.*, Phys. Rev. Lett. **92**, 181301 (2004).
- [36] P. Anselmann *et al.*, Phys. Lett. **B285**, 376 (1994).
- [37] M. Altmann *et al.*, Phys. Lett. **B490**, 16 (2000).
- [38] J. N. Abdurashitov *et al.*, Phys. Lett. **B328**, 234 (1994).

- [39] C. Cattadori, Results from radiochemical solar neutrino experiments, talk at XXIst International Conference on Neutrino Physics and Astrophysics (NU2004), Paris, June 14-19, (2004).
- [40] S. Fukuda *et al.*, Phys. Rev. Lett. **86**, 5651 (2001), Phys. Rev. Lett. **86**, 5656 (2001).
- [41] Y. Fukuda *et al.*, Phys. Lett. **B335**, 237 (1994).
- [42] R. Becker-Szendy *et al.*, Phys. Rev. **D46**, 3720 (1992).
- [43] M. Ishitsuka for the Super-Kamiokande Collaboration, Proceeding of the XVI International Conference on Particles and Nuclei, to be published.
- [44] K. Daum *et al.*, Z. Phys. **C66**, 417 (1995).
- [45] M. Aglietta *et al.*, Europhys. Lett. **8**, 611 (1989).
- [46] W. W. M. Allison *et al.*, Phys. Lett. **B449**, 137 (1999).
- [47] H. Yoshinari for the SK and the K2K collaborations, Eur. Phys. J. **C33**, 829 (2004).
- [48] Y. Ashie *et al.*, hep-ex/0404034.
- [49] M. H. Ahn *et al.*, Phys. Rev. Lett. **90**, 041801 (2003).
- [50] A. Aguilar *et al.*, Phys. Rev. **D64**, 112007 (2001).
- [51] B. Armbruster *et al.*, Phys. Rev. **D65**, 112001 (2002).
- [52] A. O. Bazarko, hep-ex/0210020.
- [53] B. Achkar *et al.*, Nucl. Phys. **B434**, 503 (1995).
- [54] Y. Declais *et al.*, Phys. Lett. **B338**, 383 (1994).
- [55] M. Apollonio *et al.*, Phys. Lett. **B466**, 415 (1999).
- [56] F. Boehm *et al.*, Phys. Rev. **D64**, 112001 (2001).
- [57] A. Osipowicz *et al.*, hep-ex/0109033, L. Bornschein, hep-ex/0309007.
- [58] T. J. Loredo and D. Q. Lamb, Phys. Rev. **D65**, 063002 (2002).
- [59] F. Šimkovic, G. Pantis, J. D. Vergados, and A. Faessler, Phys. Rev. **C60**, 055502 (1999).
- [60] V. A. Rodin, A. Faessler, F. Šimkovic, and P. Vogel, Phys. Rev. **C68**, 044302 (2003).
- [61] P. Vogel and A. Piepke, Phys. Lett. **B592**, 447 (2004).
- [62] Y. Itow *et al.*, hep-ex/0106019.

- [63] A. Suzuki, Talk at XVIII International Conference on Neutrino Physics and Astrophysics, Takayama, Japan, (1998), and its proceedings.
<http://www.awa.tohoku.ac.jp/KamLAND/>
- [64] K. S. Hirata *et al.*, Phys. Rev. **D38**, 448 (1988).
- [65] P. Vogel, Phys. Rev. **D29**, 1918 (1984).
- [66] P. Vogel and J. F. Beacom, Phys. Rev. **D60**, 053003 (1999).
- [67] A. Kurylov, M. J. Ramsey-Musolf and P. Vogel, Phys. Rev. **C67**, 035502 (2003).
- [68] O. Tajima. master thesis, (2000).
- [69] O. Tajima. doctor thesis, (2003).
- [70] T. Mitsui, talk at KamLAND collaboration meeting.
- [71] W. R. Leo, Techniques for Nuclear and Particle Physics Experiment, Springer Verlag, (1987).
- [72] T. Hagner *et al.*, Astroparticle Physics. **14**, 33 (2000).
- [73] C. Galbiati *et al.*, hep-ph/0411002.
- [74] H. Zeldes, B. H. Ketelle and A. R. Brosi, Phys. Rev. **79**, 901 (1950).
- [75] R. A. Meyer *et al.*, Phys. Rev. **C21**, 2590 (1980).
- [76] P. Collon, W. Kutschera and ZT Lu, Annual Review of Nuclear and Particle Science. **54** (2004).
- [77] A. R. Brosi, H. Zeldes and B. H. Ketelle, Phys. Rev. **79**, 902 (1950).
- [78] HH Loosli, Earth Planet. Sci. Lett. **63**, 51 (1983).
- [79] RW Stoenner, OA Schaeffer and S. Katcoff, Science **148/3675**, 1325 (1965).
- [80] HH Loosli and H. Oeschger, Earth Planet. Sci. Lett. **7**, 67 (1969).
- [81] S. Fukuda *et al.*, Nucl. Inst. and Meth. in Physics Res. **A501**, 418 (2003).
- [82] National Nuclear Data Center, <http://www.nndc.bnl.gov>
- [83] R. B. Firestone *et al.*, Table of Isotopes (1995).
- [84] G. W. Kerr *et al.*, Nucl. Phys. **A110**, 637 (1968).
- [85] R. B. Walton *et al.*, Phys. Rev. **170**, 1065 (1957).
- [86] G. Rupak, Nucl. Phys. **A678**, 405 (2000).

- [87] T. K. Gaisser, T. Stanev and G. Barr, Phys. Rev. **D38**, 85 (1988).
- [88] K. Schreckenbach *et al.*, Phys. Lett. **B160**, 325 (1985).
- [89] A. A. HAHN *et al.*, Phys. Lett. **B218**, 365 (1989).
- [90] P. Vogel *et al.*, Phys. Rev. **C24**, 1543 (1981).
- [91] B. Achkar *et al.*, Phys. Lett. **B374**, 243 (1996).
- [92] <http://www.insc.anl.gov/>
- [93] P. Vogel (private communication)
- [94] J. M. Herndon, Proc. Nat. Acad. Sci. **100**, 3047 (2003).
- [95] G. L. Fogli *et al.*, Phys. Rev. **D66**, 053010 (2002).
- [96] Glen Cowan, Statistical Data Analysis, Clarendon press Oxford, (1998).
- [97] M. C. Gonzalez-Garcia *et al.*, Phys. Rev. **D63**, 033005 (2001).
- [98] T. K. Kuo and J. Pantaleone, Phys. Rev. Lett. **57**, 1805 (1986).
- [99] X. Shi and D. N. Schramm, Phys. Lett. **B283**, 305 (1992).
- [100] K. Hirata *et al.*, Phys. Rev. Lett. **58**, 1490 (1987), K. S. Hirata *et al.*, Phys. Rev. **D38**, 448 (1988).
- [101] R. M. Bionta *et al.*, Phys. Rev. Lett. **58**, 1494 (1987), C. B. Bratton *et al.*, Phys. Rev. **D37**, 3361 (1988).
- [102] H.-T. Janka and W. Hillebrandt, Astron. Astrophys. **224**, 49 (1989).
- [103] B. Jegerlehner *et al.*, Phys. Rev. **D54**, 1194 (1996).
- [104] G. L. Fogli *et al.*, Phys. Rev. **D65**, 073008 (2002).
- [105] M. Maltoni *et al.*, hep-ph/0405172.
- [106] T. Nakaya, Talk at Neutrino 2004, 14-19 June 2004, Paris, <http://neutrino2004.in2p3.fr/>
- [107] A. D. Vijaya and A. Kumar, Nucl. Inst. and Meth. **111**, 435 (1973).
- [108] TUNL Nuclear Data Evaluation Group, Nucl. Phys. **A708**, (2002).
- [109] S. Parke, Phys. Rev. Lett. **57**, 1275 (1986).
- [110] E. Lisi and D. Montanino, Phys. Rev. **D56**, 1792 (1997).
- [111] A. M. Dziewonski and D. L. Anderson, Phys. Earth. Planet. Inter. **25**, 297 (1981).
- [112] E. Lisi *et al.*, Phys. Rev. **D63**, 093002 (2001).

- [113] K. Takahashi, M. Watanabe and K. Sato, Phys. Lett. **B510**, 189 (2001).
- [114] J. F. Beacom, R. N. Boyd and A. Mezzacappa, Phys. Rev. **D63**, 073011 (2001).